

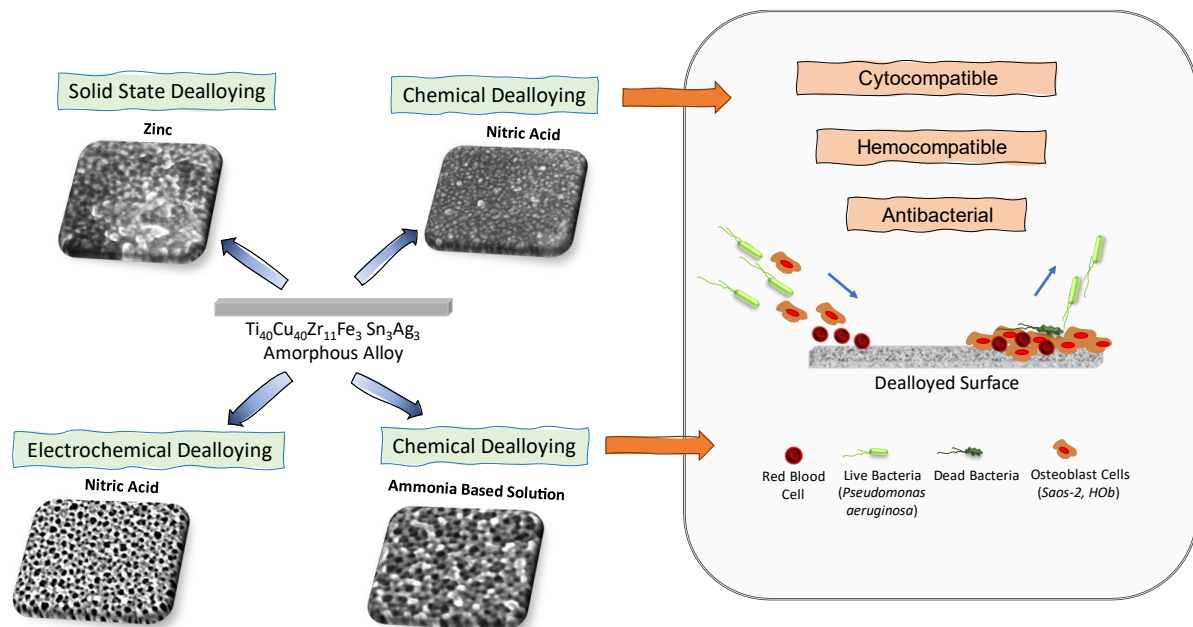


Università degli Studi di Torino

Doctoral School of Sciences and Innovative Technologies

PhD Program in Chemical and Material Sciences XXXVI Cycle

Design of Biocompatible and Antimicrobial Patterned Surfaces Produced by Dealloying of Metallic Glasses



Kirti Tiwari

Supervisor: Prof. Paola Rizzi



Università degli Studi di Torino

Doctoral School of Sciences and Innovative Technologies

PhD Program in Chemical and Material Sciences XXXVI cycle

**Design of Biocompatible and Antimicrobial
Patterned Surfaces Produced by Dealloying of
Metallic Glasses**

Candidate: **Kirti Tiwari**

Supervisor: Prof. **Paola Rizzi**

Jury Members: Prof. **Francesco Turci**

Dipartimento di Chimica

Università degli Studi di Torino, Torino, Italy

Prof. **Francesco Delogu**

Dipartimento di Ingegneria meccanica, chimica e dei materiali

Università di Cagliari, Sardinia, Italy

Prof. **Mariana Calin**

Chemistry of functional materials

Leibniz Institute for Solid State and Materials Research Dresden - IFW
Dresden, Germany

Director of the Doctoral School: Prof. Alberto Rizzuti

PhD Program Coordinator: Prof. Bartolomeo Civalieri

Torino, 2024

Dedicated to all the women in science, my mentors, and my family

Kirti Tiwari

PREFACE

This dissertation, titled "Design of Biocompatible Patterned Surfaces Produced by Dealloying of Metallic Glasses," has been submitted in partial fulfilment of the requirements for the Degree of Doctor of Philosophy in Chemical and Material Science within the XXXVI cycle (October 2020 to March 2024). The research was conducted in the Metallurgy research group under the mentorship of Prof. Paola Rizzi at the Department of Chemistry, University of Turin, Turin, Italy.

This doctoral work is a part of the BIOfilm-RESistant Materials for hard tissue Implant Applications (BIOREMIA) project, funded by the European Union's Horizon 2020 research and innovation programme under the Marie Skłodowska-Curie grant agreement No. 861046, spanning from January 2020 to June 2024. The BIOREMIA project aims to improve the quality of life for patients by minimizing infection rates associated with medical implants. Implant-related infections, often caused by bacterial biofilms, present a significant challenge, leading to implant rejection with substantial economic and social costs. The inherent resistance of biofilm-growing bacteria to antimicrobials underscores the necessity for novel preventive measures.

As an Early Stage Researcher (ESR 7) in the BIOREMIA project, my research objectives are outlined in detail:

Project Description:

Objectives: Design antimicrobial TiO₂, Cu, or Au nanostructured surfaces with direct topological action and enhanced chemical activity to influence antibacterial surface properties. The evaluation of surface microbial adhesion is a key focus.

Tasks:

- (i) **Development of New Ti-Based Amorphous Alloys with Antimicrobial Elements (Ag, Fe, Cu):** This task involves the synthesis and characterization of novel amorphous alloys with a specific emphasis on antimicrobial elements.
- (ii) **Design of Nanoporous Cu/TiO₂ Surfaces from Ti-Based Amorphous Alloys using Dealloying Technique:** This task aims at creating innovative nanopatterned surfaces through the various dealloying techniques with a focus on particular exploration of promising parameters for Ti-based amorphous alloys.
- (iii) **Evaluation of Hierarchical Nanopatterned Surfaces:** This task involves evaluating the surface properties, surface chemistry, contact angle, and biocompatibility of the most promising dealloyed surface. Biocompatibility study involves evaluation of dealloyed samples in cell free systems for antimicrobial activity by analyzing reactive oxygen species, fenton chemistry, free-radical release, surface radical species, hemocompatibility, cytocompatibility, and metal ion release and antimicrobial activity.

Thesis Structure:

- **Chapter I** provides a comprehensive introduction, outlining the main motivation, importance, and a detailed preview of subsequent chapters.
- **Chapter II** focuses on precursor alloy preparation and characterization.
- **Chapters III-IV** delve into chemical dealloying using various electrolytes, with a detailed exploration of the most promising electrolytes, such as nitric acid and ammonia-based solution. Further evaluations, including surface characterization, contact angle, biocompatibility: hemocompatibility, reactive oxygen species, release of metal ion release, cytocompatibility using osteoblast cells (Saos-2 and HOb) and antimicrobial activity using *Pseudomonas aeruginosa* bacteria, are presented.
- **Chapter V** details attempts of electrochemical dealloying using nitric acid to produce a nanostructured copper-depleted surface on the amorphous alloy.
- **Chapter VI** explores solid-state dealloying using zinc to selectively diffuse copper with zinc and further etching the Cu-Zn phase to obtain a nanostructured Ti surface.
- **Chapter VII** provides a comprehensive summary and outlook on the research carried out during this Ph.D.

This thesis endeavors to contribute significantly to the field of biomaterials and surface engineering, offering potential implications for the enhancement of performance and acceptance of medical implants

INDEX

CHAPTER I	1
INTRODUCTION	1
1. Biomaterials	1
2. Requirements of biomaterials	2
2.1. Mechanical properties	2
2.2. Corrosion and wear resistance.....	3
2.3. Biocompatibility	3
2.4. Osseointegration.....	4
3. Current Challenges: Healthcare associated infections	5
3.1. Biofilm	6
3.1.1. Bacteria adhesion	6
3.1.2. Biofilm formation	7
3.2. Biofilm associated risks	8
3.3. Biofilm resistant surfaces	10
3.3.1. Non-adhesive surfaces.....	10
3.3.2. Contact-killing surfaces.....	10
3.3.3. Antimicrobial-releasing coatings	10
3.3.4. Multifunction coatings.....	10
4. Challenges and opportunities of titanium based implants.....	12
4.1. Perspective: New alloy and surface modification	12
5. Amorphous alloys	14
5.1. Composition development: glass formers and biocompatible elements	17
6. Surface modification of titanium alloys	19
6.1. Dealloying	21
6.1.1. Effect of dealloying on the microstructure.....	21
6.1.2. Porosity evolution	21
6.2. Fabrication of np-Ti alloys via dealloying	24
6.2.1. Types of dealloying techniques	24
6.2.1.1. Chemical and electrochemical dealloying	25
6.2.1.2. Liquid melt dealloying	26

6.2.1.3. Solid state dealloying	26
6.2.1.4. Vapor phase dealloying	27
7. Challenges and opportunities	31
CHAPTER II	33
PRECURSOR ALLOY PREPARATION	33
Specific Aim	33
1. Introduction	33
2. Experimental Procedure	35
2.1 Preparation of master alloy and as-quenched ribbons	35
2.2 Characterization of master alloy and as-quenched ribbons.....	36
3. Results and Discussion	37
3.1 Characterization of master alloy.....	37
3.2 Characterization of as-quenched ribbons	40
Conclusion.....	44
CHAPTER III.....	45
CHEMICAL DEALLOYING USING VARIOUS ELECTROLYTES.....	45
Specific Aim.....	45
1. Introduction	46
2. Experimental Procedure	49
2.1 Chemical pseudo-dealloying attempts	49
2.2 Wettability study.....	50
2.3 Hemocompatibility study	50
2.4 Release of reactive oxygen species study	51
2.5 Metal ion release study	51
2.6 In vitro cytocompatibility study	51
2.7 Antimicrobial activity	53
2.7.1 Measuring biofilm formation	53
2.7.2 Measuring bacterial adhesion	53
2.8 Statistical analysis.....	54

3. Results and Discussion	55
3.1 Investigation and characterization of $Ti_{42}Cu_{40}Zr_{8.5}Fe_{2.5}Sn_2Si_2Ag_3$ MA1 ribbons treated using nitric acid	55
3.2 Investigation and characterization of $Ti_{40}Cu_{40}Zr_{11}Fe_3Sn_3Ag_3$ MA2 ribbon treated with various electrolytes	57
3.3 Characterization and biocompatibility testing of <i>pseudo-dealloyed</i> $Ti_{40}Cu_{40}Zr_{11}Fe_3Sn_3Ag_3$ MA2 ribbon	65
3.3.1 Wettability study	65
3.3.2 Hemocompatibility study	65
3.3.3 Release of reactive oxygen species study	66
3.3.4 Metal ion release study	68
3.3.5 In vitro cytocompatibility using Saos-2 and HOB cells	69
3.3.6 Biofilm growth and bacteria adhesion by <i>Pseudomonas aeruginosa</i>	74
Conclusion	78
CHAPTER IV	80
CHEMICAL DEALLOYING USING AMMONIA BASED SOLUTION	80
Specific Aim	80
1. Introduction	81
2. Experimental Procedure	83
2.1. Synthesis of samples using ammonia-based solution	83
2.2. Characterization of treated samples	84
2.3. Wettability study	85
2.4. Hemocompatibility study	85
2.5. Metal ion release study	86
2.6. Release of reactive oxygen species study	86
2.7. Antibacterial activity	87
2.7.1. Measuring biofilm formation	87
2.7.2. Measuring bacteria adhesion	88
2.8. In vitro cytocompatibility study	88
2.9. Statistical analysis	90
3. Results and Discussion	91
3.1. Surface modification by chemical <i>pseudo-dealloying</i>	91
3.1.1. Ammonia based diluted solution	91
3.1.1.1. XPS analysis of sample treated using diluted solution	93
3.1.2. Ammonia-based concentrated solution	97

3.2. Investigating the role of ammonium hydroxide and hydrogen peroxide	99
3.3. <i>Pseudo-dealloying</i> mechanism with ammonia-based solution	102
3.4. Wettability study	105
3.5. Hemocompatibility study	107
3.6. Metal ion release and release of reactive oxygen species study	109
3.7. Biofilm formation and bacterial adhesion study with <i>Pseudomonas</i> <i>aeruginosa</i> (PAO1)	110
3.8. In vitro cytocompatibility assessment with Saos-2 and HOb cells	112
3.9. Converging insights from the studies to illuminate common ground	117
Conclusion	120
CHAPTER V	122
ELECTROCHEMICAL DEALLOYING USING NITRIC ACID	122
Specific Aim	122
1. Introduction	123
2. Experimental Procedure	125
3. Results and Discussion	126
3.1 Electrochemical surface treatment using nitric acid	126
3.2 Surface characterization using XPS	130
Conclusion	133
CHAPTER VI	134
SOLID STATE DEALLOYING	134
Specific Aim	134
1. Introduction	135
2. Experimental Procedure	138
2.1 Sample preparation	138
2.1.1 Electrodeposition of Zn	138
2.1.2 Heat treatment	138
2.1.3 Selective corrosion	138
2.2 Sample characterization	138

3. Results and Discussion	139
3.1. Electrodeposition of pure zinc on the substrate.....	139
3.2. Heat treatment of electrodeposited zinc	142
3.3. Selective etching.....	146
Conclusion.....	148
CHAPTER VII	149
SUMMARY AND OUTLOOK.....	149
LIST OF PUBLICATIONS AND PATENTS.....	151
ACKNOWLEDGEMENTS.....	153
BIBLIOGRAPHY.....	I

Chapter I

INTRODUCTION

1. Biomaterials

Biomedical materials, in the form of implants (such as sutures, bone plates, and joint replacements) and medical devices (including pacemakers, artificial hearts, and blood tubes), play a pivotal role in the field of medicine [1] as shown in Figure 1.1. They are essential for the restoration and replacement of damaged or degenerated tissues and organs, ultimately enhancing the quality of life for patients. The primary criterion guiding the selection of biomaterials is their compatibility with the human body. For a biomaterial to be suitable for implantation, it must exhibit specific key characteristics to ensure prolonged biocompatibility within the body, preventing adverse reactions [2]. The predominant classes of materials used in biomedical applications encompass metals, polymers, ceramics, and composite materials. These categories are employed individually or in combination to craft a wide array of implantation devices available today. Biomaterials hold an increasingly pivotal role within the medical domain. They are characterized as biocompatible materials, fabricated from metals, ceramics, polymers, or composites thereof, specifically designed for integration into the human body [3]. The overarching purpose of biomaterials is to enhance, support, or substitute damaged tissues through the implantation of medical devices or the construction of artificial organs. These biomaterials may be organic or inorganic, originating from natural or synthetic sources, always adhering to the fundamental requirement of being non-toxic and compatible with human tissues. Metals and their alloys constitute a prevalent choice in the realm of biomedicine. Materials like stainless steels, Co-Cr alloys, NiTi shape memory alloys, commercially pure titanium (cp-Ti), and Ti-alloys are favored due to their exceptional mechanical strength, capable of withstanding the physiological loads imposed by the human body. Nonetheless, the release of potentially toxic elements such as Cobalt (Co), Chromium (Cr), and Nickel (Ni) from these metallic materials can compromise human health. Consequently, among metallic options, Ti and Ti alloys emerge as the most suitable materials for orthopedic and dental implants. They possess biocompatibility, exemplary resistance to corrosion, and commendable mechanical properties, rendering them highly favored for these applications [4].

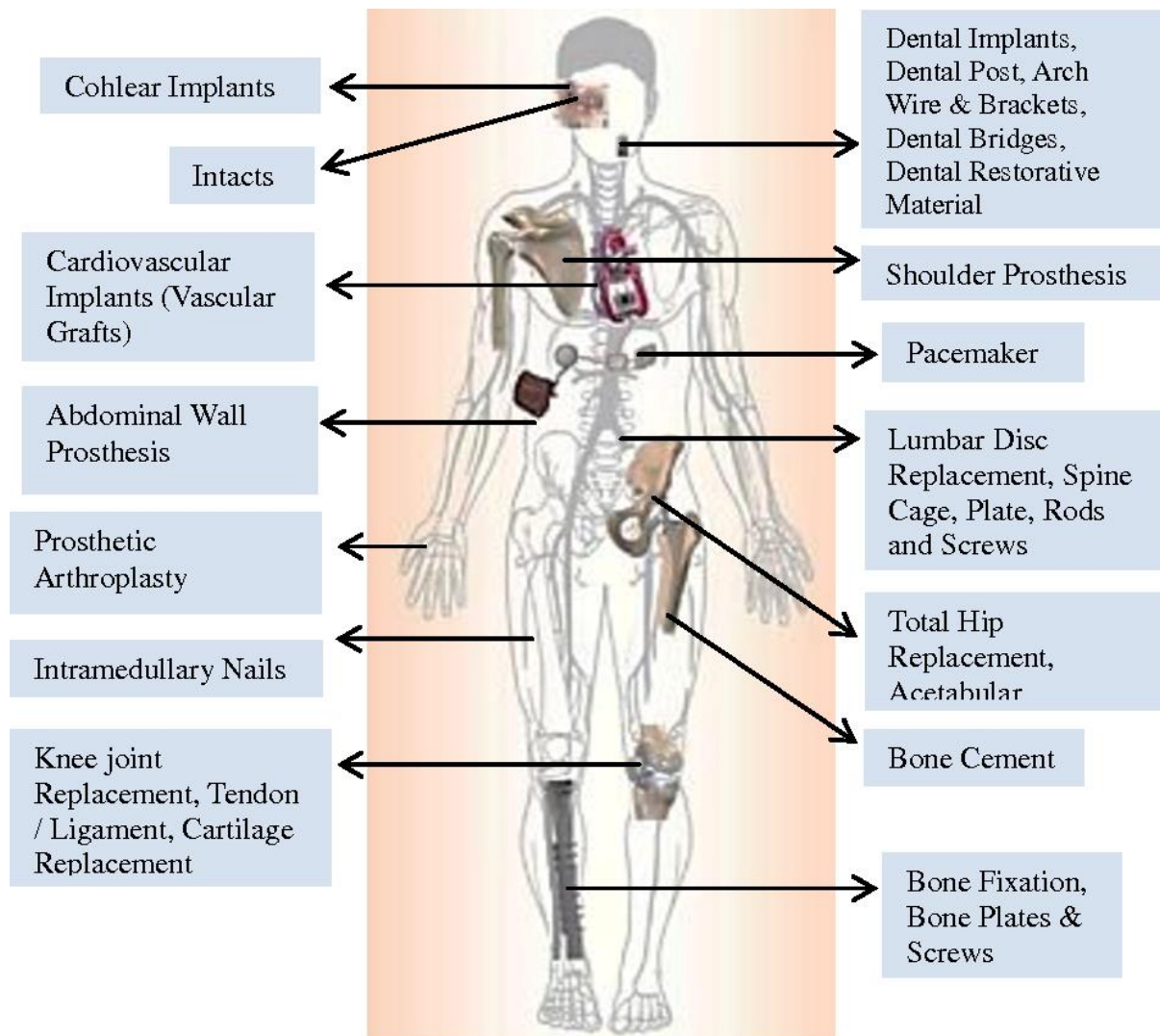


Figure 1.1. Types of implants and their application specific to human anatomy [1].

2. Requirements of biomaterials

Biomaterials must exhibit essential attributes that ensure the longevity of implants within the body while avoiding any rejection response. Failures in implants can often be attributed to one or more deficiencies in material properties, which may subsequently necessitate revision surgeries and pose health risks to patients.

2.1. Mechanical properties

Mechanical properties, like hardness, modulus, tensile strength, strain, fracture resistance, and fatigue strength, dictate material selection for medical implants (Table 1.1). Fatigue strength is particularly vital, as it prevents fractures caused by cyclic loading, averting implant failure and revision surgeries. Material strength is essential for long-term implant reliability, necessitating a modulus akin to bone tissue to counteract stress-shielding-induced implant loosening.

Consequently, a low Young's Modulus, mirroring bone, and high strength stand as critical material attributes for crafting enduring implants, ensuring their stability over time without the need for revisions.

Table 1.1: mechanical properties of metallic biomaterials [5].

Material	Young's Modulus E (GPa)	Yield Strength (MPa)	Tensile Strength (MPa)	Fatigue Limit (MPa)
Stainless steel	190	221–1213	586–1351	241–820
Co-Cr alloys	210–253	448–1606	655–1896	207–950
Ti	110	485	760	300
Ti-6Al-4V	116	896–1034	965–1103	620
Human Cortical bone	15–30	30–70	70–150	-

2.2. Corrosion and wear resistance

The lifespan of medical implants is determined by the material's ability to resist wear and corrosion. Implants with low wear and corrosion resistance can release metal ions or particles into the body, triggering immune responses, toxic reactions, and allergies. Additionally, low wear resistance can lead to implant loosening, as the debris generated can cause inflammation and damage healthy bone. Hence, developing materials with high wear and corrosion resistance is crucial for ensuring the durability of implants in the human body [5].

2.3. Biocompatibility

Biocompatibility is a complex property influenced by various factors, including the chemical and physical characteristics of materials, surface properties, implant design, and intended function. It is dynamic, as it can change with host responses over time. Biocompatibility refers to a material's ability to interact with a biological system without causing harm and with an appropriate response for a specific application. The choice of suitable materials and host responses play a significant role. In the medical field, bioactive materials are commonly used, as they can enhance biological responses by promoting bone tissue formation around implants. Two main concerns related to biocompatibility are the formation of fibrous tissue around soft tissue implants and the risk of thrombosis, which involves blood coagulation and platelet adhesion on the implant's surface [6].

2.4. Osseointegration

Osseointegration is a crucial process for dental and orthopedic implants, as it enables the formation of new bone and facilitates bone healing. When an implant surface cannot effectively integrate with the surrounding bone and tissues, it leads to the development of fibrous tissue around the implant, ultimately causing implant loosening. Improving the implant surface properties can enhance bone formation, and this depends on factors like surface chemistry, topography, and roughness. Having an appropriate implant surface is essential for achieving a strong integration between the implant and the adjacent bone tissue [7].

Table 1.2. Comparison of metallic biomaterials used in the human body [5].

Metals and alloys	Selected examples	Advantages	Disadvantages	Principal applications
Ti-based Alloys	Cp-Ti, Ti-Al-V, Ti-Al-Nb, Ti-13Nb-13Zr, Ti-Mo-Zr-Fe	High biocompatibility. Low Young's modulus excellent corrosion resistance, low density	Poor tribological properties, Toxic effect of Al and V on long term	Bone and joint replacement, fracture fixation, dental implants, pacemaker encapsulation
Cobalt and Cr alloys	Co-Cr-Mo, Cr-Ni-Cr-Mo	High wear resistance	Allergy consideration with Ni, Cr and Co much higher modulus than bone	Bone and joint replacement, dental implants, dental restorations, heart valves
Stainless steels	316L stainless steel	High wear resistance	Allergy consideration with Ni, Cr and Co much higher modulus than bone	Fracture fixation, stents, surgical instruments
Others	Ni-Ti	Low Young's modulus	Ni cause allergy	Bone plates, stents, orthodontic wires
	Platinum and Pt-Ir	High corrosion resistant under extreme voltage		Electrodes

	potential and charge transfer conditions		
Hg-Ag-Sn amalgam	Easy <i>in situ</i> formability to a desired shape susceptible to corrosion in the oral environment	Concerns related to Hg toxicity	Dental restorations

3. Current Challenges: Healthcare associated infections

Biomaterial-associated infection (BAI) occurs as a result of the interplay between an implanted material and the surrounding tissue due to contamination during a surgical procedure. Bacteria have the capacity to adhere to the surface of the implant and subsequently infiltrate the adjacent tissue. Conversely, bacteria originating from colonized tissue can migrate towards the implanted material and initiate an infection within it (Figure 1.2) [8].

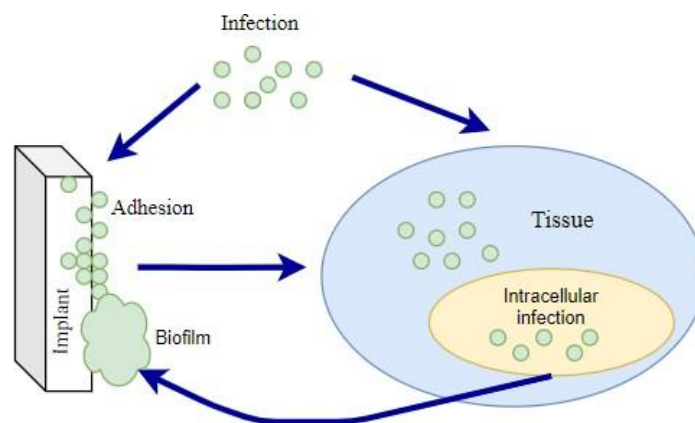


Figure 1.2. A schematic representation of the pathogenesis of biomaterial-associated infection. Bacteria contaminating the surgical site enter the tissue surrounding the implant and may become internalized by host cells or adhere to the implant and eventually develop a biofilm, adapted from [8].

Biomaterial-associated infections have been a concern for several decades, particularly with artificial prosthetic devices. These infections can occur shortly after surgery, during hospitalization, or even years later due to bacteria entering the bloodstream. Infection management typically involves antibiotics, with some patients making a full recovery, but severe cases may require surgical replacement or result in serious consequences. Infections become less likely over time as host tissues adapt. Revision surgeries carry a higher risk of infection than primary implantation procedures. Certain implants, such as those in the hip or knee, are more prone to bacterial reactions due to their limited exposure to bacteria, triggering strong immune responses and potential inflammation. In cases of inadequate immune

responses, chronic inflammation, and possible tissue death, revision surgery may become necessary (Figure 1.3) [9].

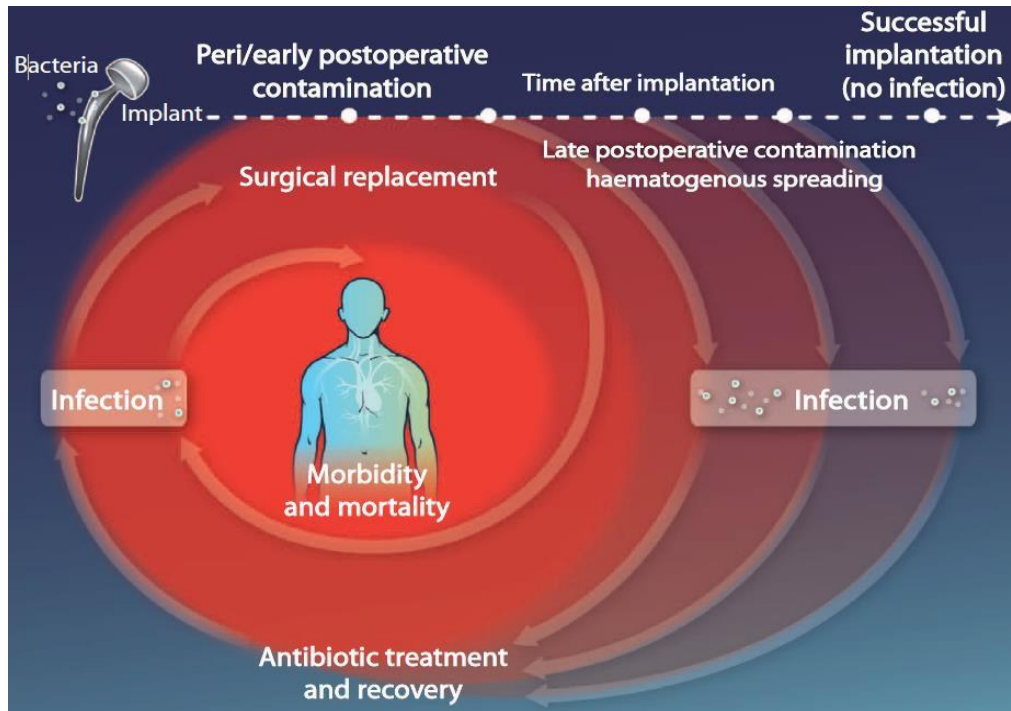


Figure 1.3. Patient risk factors for developing a biomaterial-associated infection [9].

3.1. Biofilm

Biofilm formation caused by bacterial adhesion on implants is a significant issue for human health. These biofilm-associated infections not only impact the functionality and lifespan of the medical device but also contribute to device failure. Consequently, this increases the need for revision surgeries, and in some cases, these infections can have fatal consequences.

3.1.1. Bacteria adhesion

The formation of biofilms on biomaterial surfaces involves a two-phase process. The first phase is an instantaneous and reversible physical interaction, followed by a time-dependent and irreversible molecular and cellular phase. Bacterial adhesion to the surface begins with physical forces such as Van der Waals attraction, Brownian motion, gravitational forces, hydrophobic interactions, and surface electrostatic effects. These interactions occur at both short-range (distances < 5 nm with involvement of hydrogen bonding, ionic and dipole interactions, and hydrophobic interactions) and long-range (distances > 50 nm between cells and surfaces), facilitating the adhesion of cells to the substrate (Figure 1.4). The second phase involves a reaction between the substrate's surface and the bacterial surface, potentially leading to biofilm formation and nutrient provision [10].

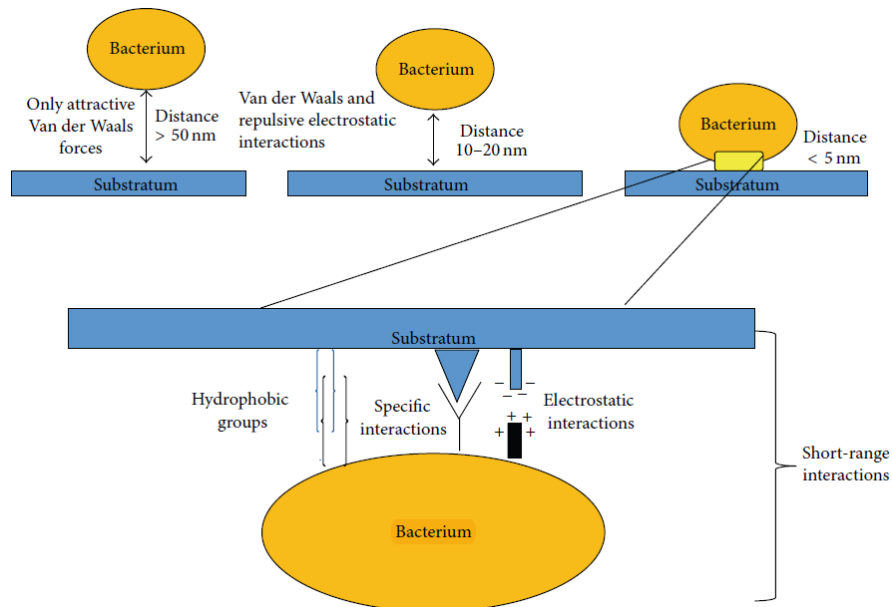


Figure 1.4. Phase one of bacterial adhesion [10].

3.1.2. Biofilm formation

Biofilms are intricate collections of microorganisms that adhere to various surfaces. They consist of cells growing within multicellular aggregates embedded in an extracellular matrix made up of extracellular polymeric substances (EPSs). This matrix is primarily produced by bacteria and typically comprises a mix of proteins, polysaccharides, lipids, and DNA. The development of biofilms is a stage specific and follows a stepwise process (Figure 1.5 a), (1) planktonic cell; (2) reversible attachment to the surface; (3) irreversible attachment to the uncoated or protein coated surface; (4) formation of microcolonies through cell division and extracellular matrix production; (5) formation of a mature three-dimensional biofilm architecture showing pores for the passage of water. Cell detachment from the biofilm: (6) an active process leaving planktonic cell; (7) a passive process that can be shed through mechanical disruption. The adherence of planktonic bacteria to the implant surface is followed by bacterial proliferation, interactions, and accumulation into multi-layered clusters. These clusters can release planktonic cells that detach from the biofilm, initiating the process anew. The formation of bacterial microcolonies is driven by intercellular adhesion and attachment to a polymeric substrate integrated into an extracellular matrix. This matrix includes proteins, exopolysaccharides like staphylococcal polysaccharide intercellular adhesin (PIA), extracellular DNA (eDNA), and enzymes. As a result, a three-dimensional biofilm architecture is established, allowing some bacteria to detach, and spread across the implant surface, facilitating the biofilm's extension (Figure 1.5 b) [11].

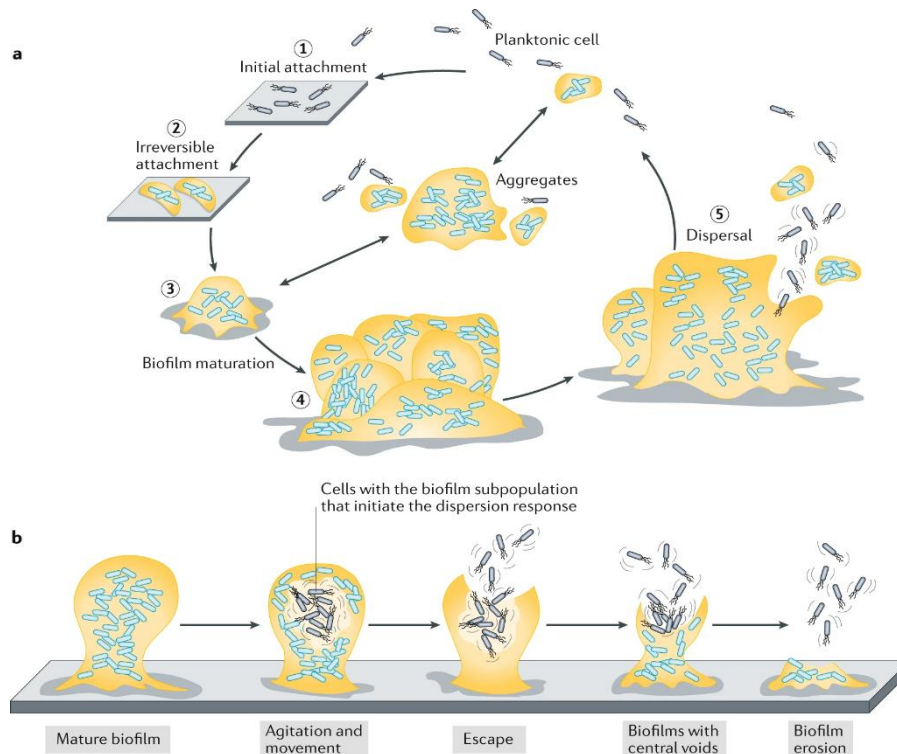


Figure 1.5. Schematic of biofilm formation and dispersion based on the *in vitro* analysis (a) stages of biofilm formation (b) detailed scheme of bacteria dispersion from mature biofilm [11].

3.2. Biofilm associated risks

The National Institutes of Health (NIH) have reported that a significant portion of microbial (65 %) and chronic (80 %) infections can be attributed to the formation of biofilms. These infections are particularly problematic in the context of medical implants, where hospital-acquired infections related to medical devices have been on the rise in recent years. Biofilms are especially concerning in healthcare-associated infections (HAIs) as they develop on the surfaces of medical devices such as intravascular catheters, urinary catheters, and orthopedic implants. The main challenges posed by biofilm formation are their resistance to both the immune system and antimicrobial agents, which has been identified as one of the top health issues by the World Health Organization (WHO), predicting that antimicrobial resistance will be responsible for 10 million deaths annually matching the global death toll of cancer at a cost of 100 trillion dollars to the global economy. The resistance of biofilms to antimicrobial agents is attributed to various factors, including DNA exchange, physiological changes, and the protective extracellular matrix that surrounds the microorganisms within the biofilm. Mature biofilms, which have been present for more than seven days, can be 100 to 1000 times more tolerant to antimicrobials compared to planktonic cells. Nosocomial infections, responsible for 1.7 million cases per year and 99,000 deaths annually, with 60 % to 65 % linked to biomedical implants, represent a significant concern. It is projected that by 2050, infections caused by infectious biofilms will surpass cancer as a leading cause of death. This highlights the urgent need to address antimicrobial resistance and prevent the devastating consequences. Antibiotic

resistance is a natural response resulting from continuous exposure to these drugs. Antibiotic resistance has been steadily increasing over the years, emphasizing the importance of prudent antibiotic use and the development of alternative strategies to combat biofilm-related infections. Impact of antimicrobial resistance. Two teams from Europe modeled the increase in the rates of antimicrobial resistance (AMR) based on the information available in 2014, each using their own methodology, to understand the impact of AMR would have on the world population and the economic output shown in Figure 1.6 (a-c) [12].

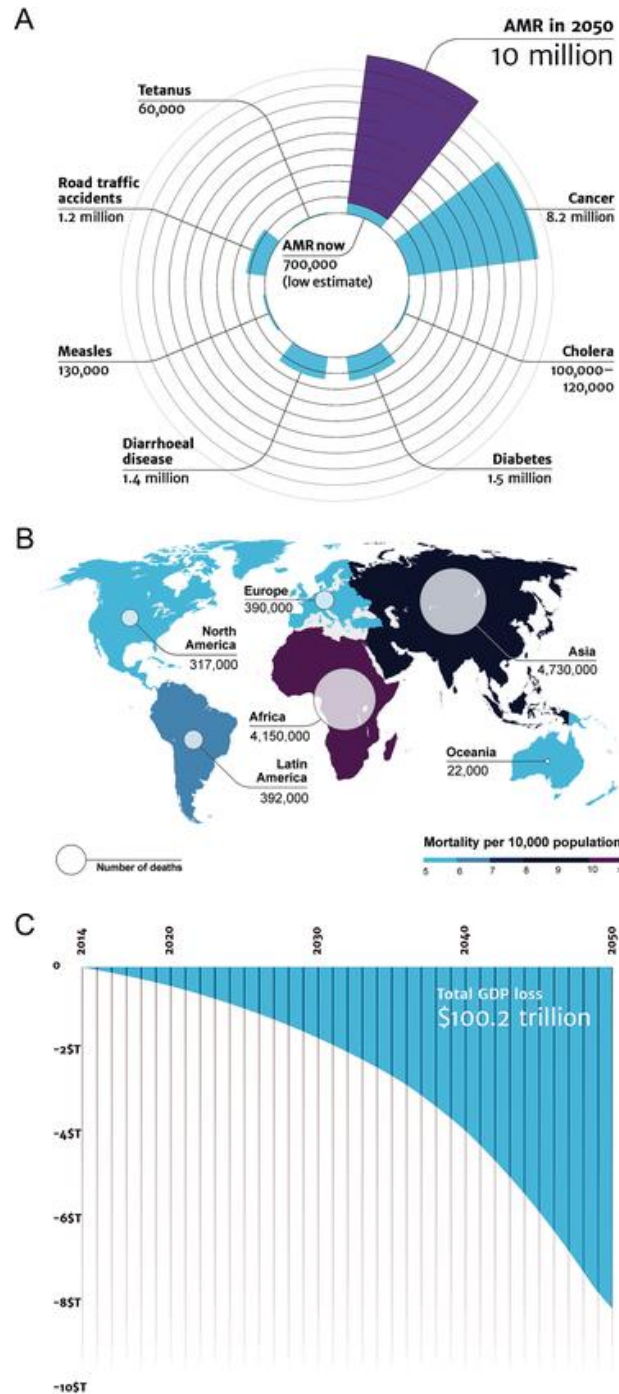


Figure 1.6. (a) Deaths attributable to AMR every year compared to other major causes of death. The estimated number of AMR will increase to 10 million by 2050, approaching the total

number of deaths caused by all diseases today. (b) Deaths attributable to AMR in different parts of the world by 2050. There is a tendency for reduced mortality on continents with better economic conditions and more stringent antibiotic management. (c) The impact of AMR on the world's economy between 2014 and 2050 (in trillions of US dollars) predicts an exponentially loss in gross domestic product (GDP) attributable to combating AMR [12].

3.3. Biofilm resistant surfaces

The type of antibacterial coating must be selected in function of the purpose of the biomaterial. Different biofilm resistant surfaces are illustrated in Figure 1.7 [9].

3.3.1. Non-adhesive surfaces

Non-adhesive surfaces or bacterial repelling surfaces are capable of inhibiting the interaction between the material surface and the bacterial body. There are different ways of achieving this type of surface, for instance the surface can be modified physically with a micro-nano structure, or the hydrophobicity could be adjusted using chemical methods. By doing this the surface can effectively reduce the initial attachment of bacteria and the formation of biofilm, achieving an efficient antibacterial effect.

3.3.2. Contact-killing surfaces

Contact-killing bacteria is a useful added functionality for all applications requiring non-adhesive surfaces. One of the ways bacteria are killed by physical mechanism in which the cell walls is broken. This involves the incorporation of antimicrobial agents or technologies directly into the material, ensuring that any microbes coming into contact with the surface are swiftly neutralized.

3.3.3. Antimicrobial-releasing coatings

These coatings release antibacterial agents, such as antibiotics, bioactive molecules, and inorganic antimicrobial agents, to the surrounding tissues. A number of antibiotics have been incorporated in bioceramics or biodegradable polymer coatings. These methods possess a broad antibacterial spectrum, it is difficult to achieve optimum release kinetics with minimum harmful effects on cellular functions and tissue integration. Inorganic antimicrobial agents can also be used, Ag is one of the most commonly used. Silver possesses a broad antibacterial spectrum and high biocompatibility. It is not prone to antibiotic resistance. Other agents being studied are Cu, F, Ca, Mn and Zn. This sort of coating is highly suitable in revision surgery after a biomaterial-associated infection, in order to clear the infection from surrounding tissues.

3.3.4. Multifunction coatings

These coatings are the most efficient since they combine several antimicrobial mechanisms. They are a mixture of the previously described coatings.

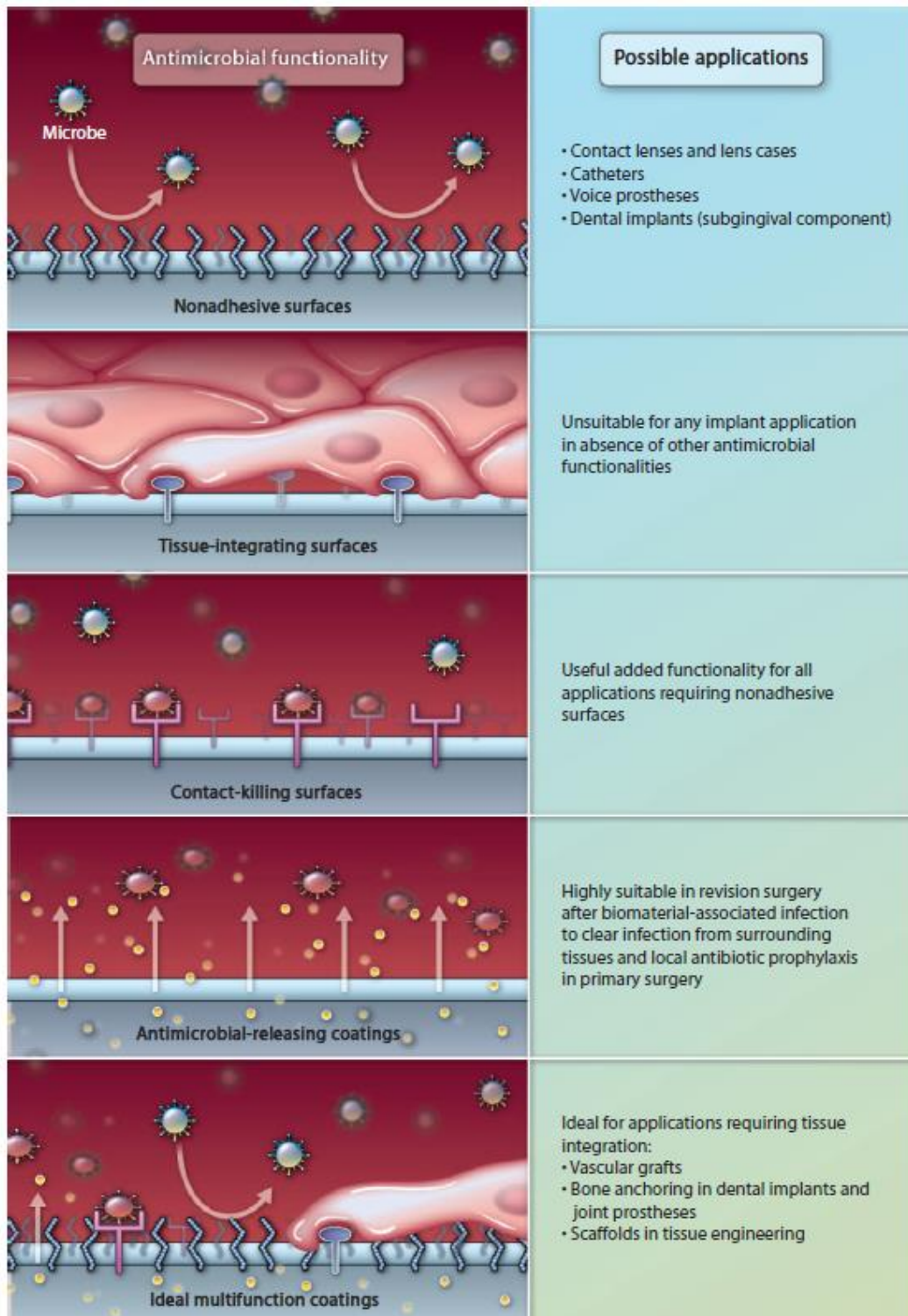


Figure 1.7. A schematic representation of different antimicrobial functionalities that can be added to the surface of a biomaterial implant or device, together with their possible application [9].

4. Challenges and opportunities of titanium based implants

Ti and its alloys are commonly utilized as implant materials in orthopedic and dental applications because of their outstanding biocompatibility, resistance to corrosion, and mechanical properties [13]. Nevertheless, there are certain issues that need to be addressed, such as the discrepancy in elastic modulus between Ti implants and natural bone, the potential release of harmful metal ions, and the absence of bioactivity and osteoinductivity [14]. To overcome these challenges, various research studies have focused on modifying the characteristics of Ti-based implant materials and applying surface modification techniques to enhance the biological performance of Ti implants. These approaches are designed to (1) improve the integration of implants with bone tissue, (2) enhance antibacterial capabilities as shown in Figure 1.8 [15].

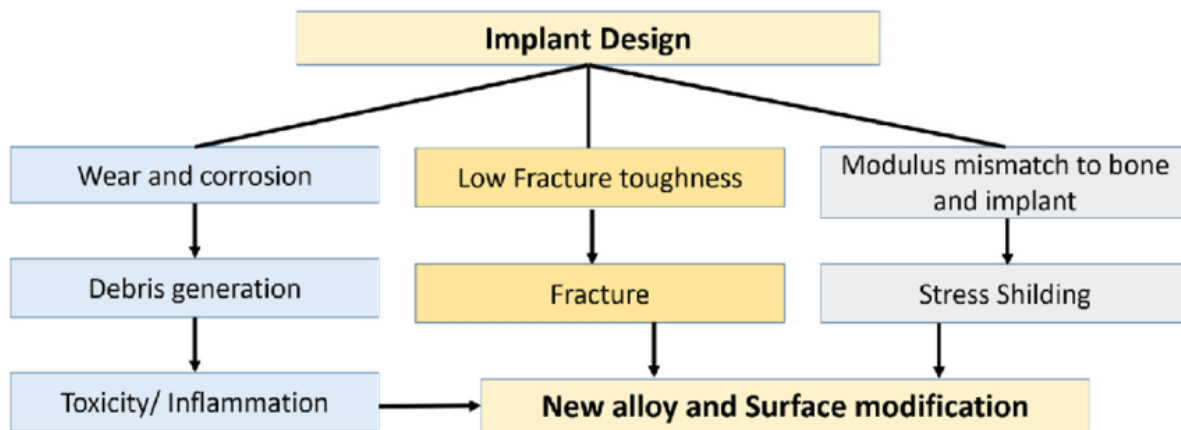


Figure 1.8. Challenges of implants and the possible solution [15].

4.1. Perspective: New alloy and surface modification

The Ti alloys have significantly influenced the performance of medical implants. While conventional Ti alloys possess advantageous traits, they are limited in terms of mechanical strength, elasticity, and wear resistance. This opens the avenue for exploring amorphous alloys as an alternative implant material. Amorphous alloys, characterized by disordered atomic structures, exhibit exceptional mechanical properties, including high strength, elastic limits, superior hardness, and corrosion resistance. Incorporating amorphous alloys into implant design holds promise for augmenting implant durability and lowering failure rates. Recent investigations have revealed that amorphous alloys, owing to their unique atomic arrangement, offer heightened fracture toughness and wear resistance compared to traditional crystalline Ti alloys (Figure 1.9). These attributes are pivotal in maintaining implant structural integrity under load-bearing conditions and mitigating wear-induced debris that can trigger adverse biological reactions. Additionally, amorphous alloys corrosion resistance reduces the risk of implant degradation, ultimately extending implant service life. By precisely tailoring amorphous alloy

composition, researchers strive to match or surpass the properties of existing Ti alloys, providing a potential solution to alloy-related implant complications [16].

Another critical challenge contributing to Ti implant issues is the interaction between implant surfaces and the host tissue environment. Surface characteristics significantly influence cytocompatibility, osseointegration, and susceptibility to biofilm formation—a key factor in implant-related infections. Modifying the surface properties of Ti implants through dealloying techniques offers innovative solutions. Dealloying methods encompass chemical, electrochemical, and solid-state processes, selectively removing elements from the alloys surface to create nanoporous (np) or nanotextured structures [17]. These structures, boasting increased surface area, can promote osseointegration by facilitating cell adhesion, nutrient diffusion from the surrounding tissue to the cells on the surface of the biomaterial, and mechanical interlocking with host bone. Moreover, surface chemistry alterations through dealloying can hinder bacterial biofilm formation, which is a prominent cause of implant-associated infections. The controlled nature of dealloying enables precise customization of surface properties, which can help in addressing patient-specific needs and reducing implant failure risks due to adverse reactions or infections.

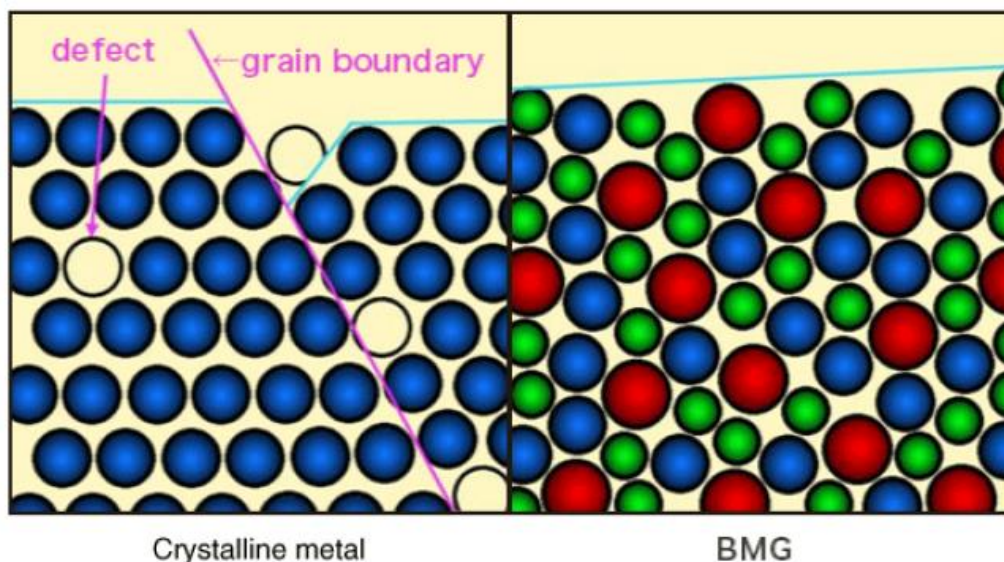


Figure 1.9. On the left, schematic illustration of a typical metal structure: short and long range order of the atoms. Crystalline metals generally have grain boundaries and defects (interstitial element and dislocations). On the right, amorphous metallic structure with at least 3 atomic species with neither long nor short range ordering [18].

5. Amorphous alloys

The history of amorphous alloys dates back to 1960 (Figure 1.10) with the discovery of $\text{Au}_{75}\text{Si}_{25}$ amorphous alloy by Duwez at Caltech. This discovery was revolutionary as it went against the traditional understanding that all metals crystallize when cooled [19]. In the following decades, researchers continued to explore the properties of amorphous alloys, and in the late 1980s, a breakthrough occurred when a multicomponent amorphous alloys with rare earth materials was created by Inoue and co-workers at Tohoku University [20]. This opened new possibilities for development of a wide range of amorphous alloys. The discovery of Vitreloy 1, a multicomponent alloy made of $\text{Zr}_{41.2}\text{Ti}_{13.8}\text{Cu}_{12.5}\text{Ni}_{10.0}\text{Be}_{22.5}$ by Johnson and Atakan Peker at Caltech in the 1990s, sparked a new wave of research in development of amorphous alloys and their potential applications in various industries, such as aerospace, automotive, electronics, and medical devices [21].

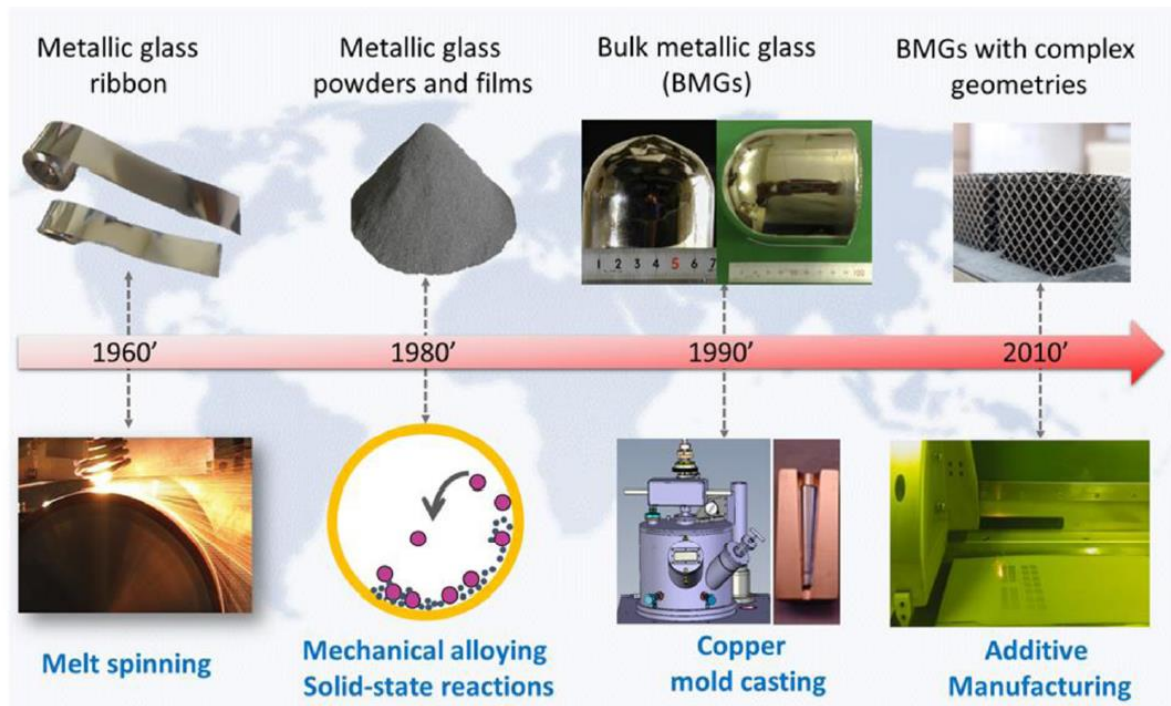


Figure 1.10. Development of amorphous alloy with advances in their fabrication techniques since 1960 [22].

Amorphous alloys, also known as metallic glasses, lack a crystalline structure and are produced through rapid quenching of molten metal. These alloys exhibit short-range atomic order, typically involving the preferential alignment of 2-3 nearest neighboring atoms, known as short-range order. In a medium-range, amorphous alloys display random, dense atomic packing due to distinct atomic sizes. The atomic structure of metallic glasses, whether core-like FCC or icosahedral packing, remains imprecise and can only be understood statistically. These structures lack grain boundaries. The formation of an amorphous or crystalline structure depends on the cooling rate. Slow cooling leads to the eventual formation of a crystalline

structure. Achieving an amorphous structure requires extremely rapid cooling rates to prevent nucleation. The critical cooling rate necessary to avoid nucleation can be determined from a characteristic time-temperature-transformation (TTT) diagram in Figure 1.11. The TTT diagrams involve the computation of the duration required for the transition from a liquid to a solid state at specific temperatures held constant (isothermally) [23].

In binary alloy systems, achieving a fully amorphous structure typically requires rapid cooling rates. This swift cooling prevents the atoms within the molten material from organizing into a crystalline lattice, preserving the disordered atomic arrangement even at lower temperatures. Below the glass-transition temperature, the supercooled liquid solidifies into a glass. However, this high cooling rate constraint limits metallic glasses to forms like powders, wires, and ribbons, typically with dimensions less than 100 μm . This size limitation has posed challenges for the practical use of metallic glasses and the exploitation of their exceptional properties.

To address this issue, scientists have dedicated significant efforts to reduce the critical cooling rates (R_C) required for metallic glass formation. The primary objective is to stabilize the supercooled liquid by shifting the crystalline transformation point to longer times (R_{C2}). This involves considering both thermodynamic and kinetic factors. Two main approaches have been proposed:

1. Purification of Melts: Professor Turnbull from Harvard University introduced the fluxing technique, which involves repeatedly melting and solidifying a Pd-Ni-P alloy in a B_2O_3 flux. This process effectively removes impurities that act as nuclei for crystallization. The purified melt can achieve substantial undercooling, significantly reducing the critical cooling rate needed for glass formation. This approach has successfully produced centimeter-sized bulk metallic glasses (BMGs), with dimensions exceeding 1 mm in the smallest dimension.

2. Designing Alloy Compositions: Professors Inoue from Tohoku University and Johnson from Caltech have made notable contributions in enhancing the critical casting thickness of metallic glasses through careful alloy design. Inoue and colleagues established three key empirical rules that must be adhered to in order to create BMGs: (1) employing a multicomponent system consisting of more than three elements, (2) ensuring a significant difference in atomic size ratios of over 12 % among the three main constituents to achieve low free volume and high packing density, and (3) having negative heats of mixing among the three primary elements [22].

The concept of free volume is a pivotal consideration when working with metallic glasses, particularly bulk metallic glasses (BMGs). Free volume refers to the unoccupied and accessible space found within the disordered arrangement of atoms in an amorphous solid. This state is thermodynamically unstable and characteristically contains a significant amount of unoccupied space within the structure. However, over time, this free space tends to diminish as the material strives to attain a state of equilibrium. As the free volume gradually decreases, the atomic density within the material increases with time. This evolution of available free volume has a direct impact on the potential atomic movements within the material and significantly influences the properties, encompassing both mechanical and chemical attributes [24].

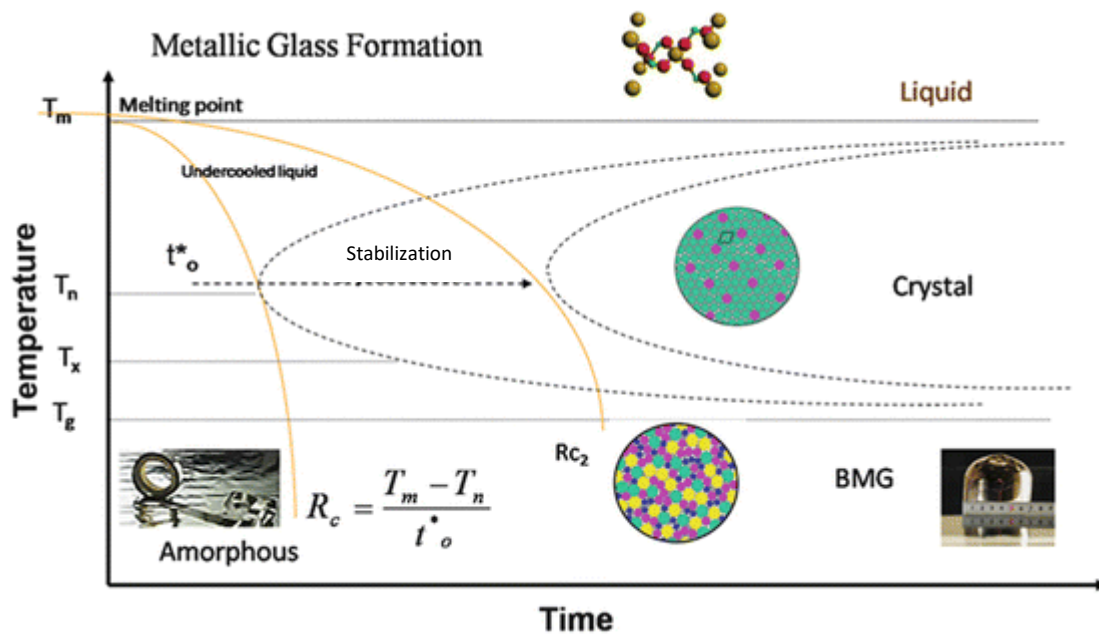


Figure 1.11. Schematic representation of T-T-T diagram [23].

The critical cooling rate required for the formation of glass varies among distinct alloy systems and compositions. Moreover, various metallurgical methods involving molten materials yield diverse cooling rates. Rapid cooling techniques, such as melt-spinning, achieve solidification rates in the range of approximately 10^4 to 10^8 Kelvin per second (K/s) to prevent nucleation and growth of stable phases. In the melt-spinning process, molten material is expelled through an orifice and solidifies on a chilled substrate, resulting in the production of ribbons. A Cu wheel is employed to expedite the dissipation of heat from the ribbon as rapidly as possible. Typically, these ribbons exhibit dimensions of millimeters-centimeters in width and 10-800 micrometers in thickness (Figure 1.12 (a)) [25,26].

On the other hand, slow cooling processes, such as Cu mold casting, yield cooling rates within the range of 10^3 to 1 K/s. This method is utilized for the production of bulk metallic glasses. In this approach, the molten alloy is poured into a Cu mold, which efficiently conducts heat, leading to steep temperature gradients and subsequent solidification. Different molds with varying internal diameters can be employed, resulting in the production of samples with differing diameters (Figure 1.12 (b)) [27].

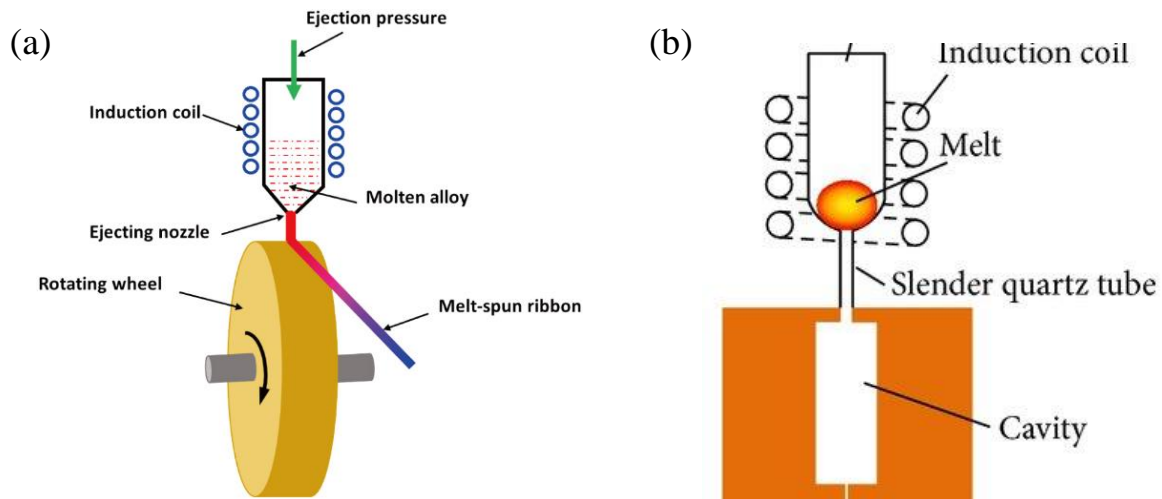


Figure 1.12. (a) Melt spinning [26] and (b) Copper mold casting [27].

5.1. Composition development: glass formers and biocompatible elements

To enhance the glass-forming ability (GFA) i.e., the tendency of the formation of amorphous alloy, additional elements with better glass-forming capabilities are required. Elements such as Be, B, Si, P, Cr, Fe, Co, Ni, Cu and In simultaneously satisfy two main requirements for good glass formers (negative ΔH_{mix} and atomic size difference $|r_{\text{A}} - r_{\text{Ti}}|/r_{\text{Ti}} > 12\%$). However, only B, Si, P and In are also fully biocompatible creating a huge limitation for possible compositions. If only negative heat of mixing is considered together with biocompatibility, in addition to already mentioned B, Si, P and In, five other elements can be included as optional: Mo, Pd, Sn, Pt and Au. Developing amorphous alloy for medical use requires achieving high GFA without using harmful alloying elements. Metal toxicity depends on their chemical state and ion concentration released by implants into the body. Various mechanisms like corrosion, wear, and electrochemical processes, including stress and fretting corrosion, release of metallic ions is responsible for implant failures. Recent studies have identified metals like Ni, Co, Cr, Fe, Mo, V, and Mn responsible for adverse tissue reactions, while Ni, Co, Cr, Al, and V were cytotoxic. Further research revealed Cr, Cu, and Ag as toxic, Ni, Zn, and Co as highly toxic. To develop suitable Ti-based amorphous alloys for implants, one must consider glass formation parameters per empirical rules and the biological safety of alloying elements. Good glass-former elements meeting the rules (negative ΔH of mixing and atomic size mismatch $> 12\%$) include B, Si, P, In, Be, Fe, Co, Ni, and Cu, with Si, In, P, and B being biocompatible. Depending on their impact on Ti's β -transus temperature, alloying elements stabilize either α -Ti (hcp) or β -Ti (bcc) crystal structures. Elements like Fe, Mn, Cr, Co, Ni, Cu, and Si, known as β -eutectoid elements, promote glass formation under non-equilibrium processing conditions due to reduced solid solubility in Ti and the formation of intermetallic compounds with a large negative heat of mixing conditions Figure 1.13 [28].

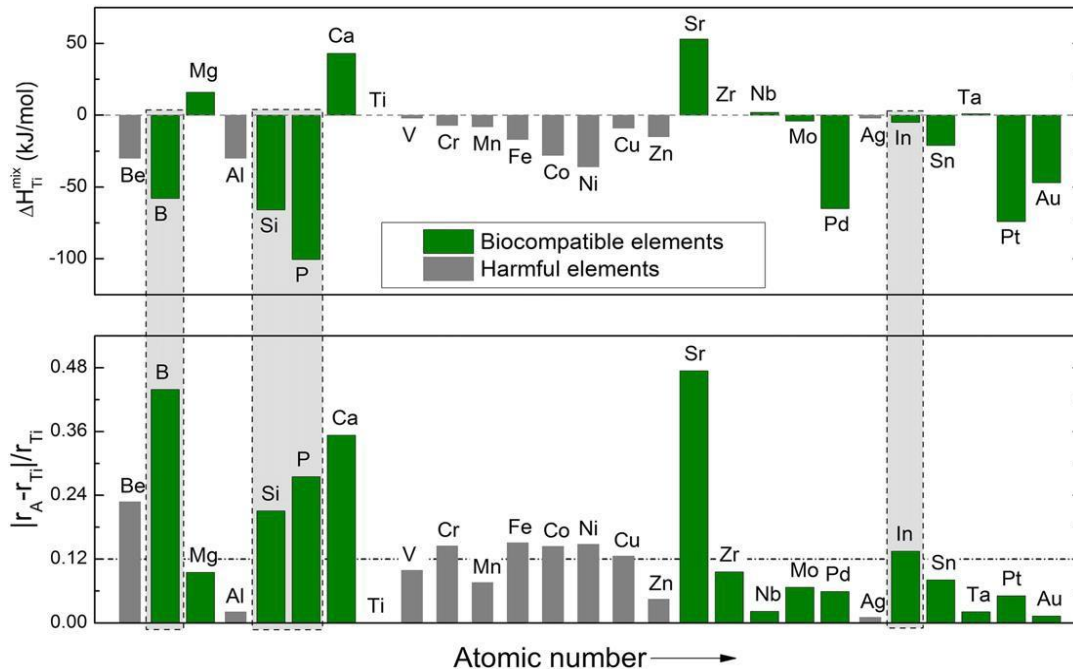


Figure 1.13. Biocompatibility and glass-forming ability of possible alloying additions to Ti-based amorphous alloys [28].

In the past two decades Ti-based amorphous alloys have been developed such as Ti-Cu-Ni, Ti-Cu-Ni-Co, Ti-Cu-Ni-Zr, Ti-Cu-Ni-Zr-Sn, Ti-Cu-Ni-Sn-B-Si, Ti-Cu-Ni-Sn-Be, Ti-Cu-Ni-Zr-Be and Ti-Cu-Ni-Zr-Hf-Si. These alloys have a good GFA. However, they cannot be employed in the medical field since they contain Ni and/or Be, which are toxic elements that can cause allergy and cancer [29–31]. Recently Ti-based amorphous alloys without the presence of Ni (or Be) were created, like Ti-Zr-Cu-Pd-Sn and Ti-Zr-Cu-Pd, which exhibit large GFA, high strength and low Young's modulus. Unfortunately, the high amount of Pd and low content of Ti increase the price of the alloy, limiting their possibility of commercial application. Pang et al. have developed a new Ni-free Ti-based amorphous alloys alloy composition consisting of Ti-Cu-Zr-Fe-Sn-Si. The addition of silver (Ag) was observed to facilitate the formation of icosahedral short-range order in the supercooled melt. This order raises the nucleation barrier for crystalline phases, thereby enhancing the melt's viscosity and the alloy's ability to form glass. Generally, a higher density of atomic packing, such as icosahedral orders, corresponds to better glass-forming ability. The GFA of $Ti_{47}Cu_{38}Zr_{7.5}Fe_{2.5}Sn_2Si_1Ag_2$ amorphous alloy was improved by incorporating 2 at % silver [32]. Wang et al. investigated the GFA of $Ti_{46}Cu_{31.5-x}Zr_{11.5}Co_3Si_1Ag_x$ by varying the silver (Ag) content (x) from 0 to 5 at %. Adding 4 at % of Ag resulted in a fully amorphous state without any crystallites, suggesting that Ag enhances GFA by increasing the temperature gap between crystallization and melting. Zirconium (Zr) and silicon (Si) are recognized for their capacity to enhance glass formability, and numerous amorphous alloys have been developed with substantial Zr and Si contributions. Tin (Sn) was also identified as a good glass former. This can be attributed to the atomic size differences between Ti (0.147 nm), Cu (0.16 nm), Zr (0.128 nm), and Sn (0.14 nm), which introduce size

mismatches and complexity, destabilizing crystalline phases in the melt [33]. Table 1.3 shows the most promising BMG compositions for biomedical application found in the literature.

Table 1.3: Comparison of the most promising BMG compositions for biomedical application in the literature. The BMGs principal characteristics such as: critical diameter, ultimate tensile stress (UTS), plasticity, Young Modulus, biosafety, and corrosion resistance are gathered.

Alloy	ΔT_x (K)	E (GPa)	Testing	Max. Dia. (mm)	Ref.
Ti ₄₀ Zr ₁₀ Cu ₃₆ Pd ₁₄	38	82	c	<5	[34,35]
Ti ₄₀ Zr ₁₀ Cu ₃₄ Pd ₁₄ Sn ₂	50	~91	c, v	<10	[36,37]
Ti ₄₀ Zr ₁₀ Cu ₃₄ Pd ₁₄ Ga ₂	44	93	-	3	[38]
Ti ₄₀ Zr ₁₀ Cu ₃₈ Pd ₁₀ Si ₂	65	80	-	5	[37,39]
Ti ₄₇ Cu ₃₈ Zr _{7.5} Fe _{2.5} Sn ₂ Si ₁ Ag ₂	52	~100	c	7	[32,37]
Ti ₄₅ Cu ₄₀ Zr _{7.5} Fe _{2.5} Sn ₂ Si ₁ Sc ₂	55	97	c	6	[37,40]
Ti ₄₇ Cu ₄₀ Zr _{7.5} Fe _{2.5} Sn ₂ Si ₁	56	~100	c	3	[37,41]

(c) – Cytocompatibility, (v) – in vivo

6. Surface modification of titanium alloys

Surface properties play a crucial role in the long-term performance of implants, alongside biomechanical properties. Ensuring proper osseointegration and preventing wear and corrosion-related particle release is essential to prevent implant failure. Surface modification, which alters surface composition, structure, and morphology while maintaining bulk mechanical properties, is employed to enhance the biofunctionality of implant materials. Titanium and Ti-based alloys, while naturally corrosion-resistant, have bioinert surfaces that hinder bonding with bone tissue. Surface modifications serve two main purposes: improving bone bonding capability and enhancing wear and corrosion resistance of implants. Methods for surface modification fall into four generations as shown in Figure 1.14.

1st generation: Mechanical surface modifications, like grind machining.

2nd generation: Morphological surface modifications, such as grooving, blast, acid etching, and anodic oxidation (TiO₂ nanotubes), which create rough and porous surfaces to promote bone ingrowth.

3rd generation: Physicochemical active surface modifications, including chemical treatments and hydroxyapatite (HA) coating, which encourage chemical bonding between the implant and bone.

4th generation: Biochemical active surface modifications involve immobilizing biofunctional molecules like collagen and peptides.

Commercially, most modified Ti and Ti-based alloys belong to the second generation, focusing on enhancing TiO₂-based coatings, oxide film thickness, porosity, and altering the oxide film structure. Some methods from the third-generation deposit osteoconductive coatings through processes like HA formation or Ca ion implantation. The fourth generation, involving immobilized layers of biofunctional molecules, is still in development due to safety, quality, and durability challenges during storage and dry conditions [42].

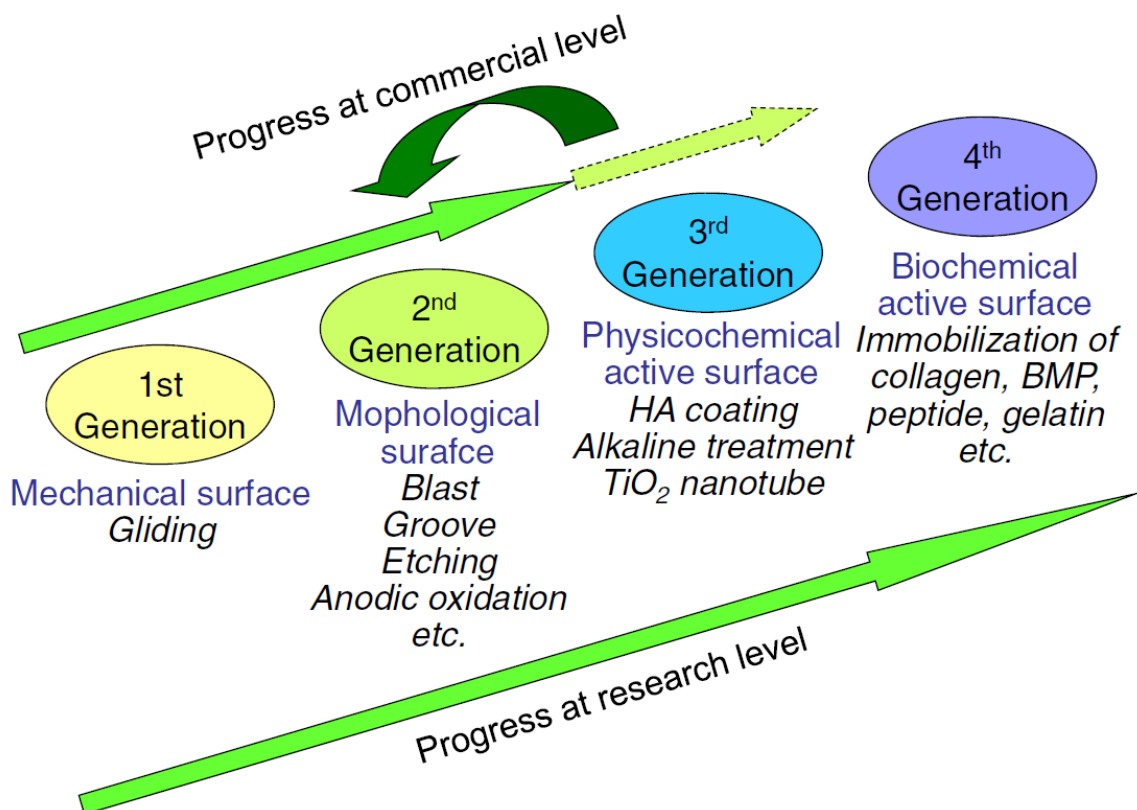


Figure 1.14. History of surface modification techniques to improve hard tissue compatibility regarding the commercial and research level [42].

6.1. Dealloying

Dealloying consists of a simple and effective way to fabricate functional nanostructured materials by selective dissolution of one element from an alloy [43]. During dissolution the remaining components become free to move along the interface between the alloy and the dissolution medium, and if the alloy is in the appropriate composition range, the remaining component(s) reorganizes into a three-dimensional network exhibiting open porosity. Previously dealloying was only considered in the context of corrosion, however now it's considered as a self-organization technique that allows us to fabricate high surface area, bicontinuous np materials [44].

6.1.1. Effect of dealloying on the microstructure

During the dealloying process, diffusion occurs on the initial crystal lattice of the metal, so the grain structure of the parent alloy is preserved. However, this is not the case for dealloying amorphous alloys. Amorphous alloys exhibit an absence of grain boundaries or segregations, this makes them preferred choices for dealloying precursors to prepare homogeneous np metals [45]. The decrease in the surface diffusivity of np metals, caused by the addition of minor alloying noble elements to the dealloying precursor alloys, has consequently resulted in the refinement of the pore structure. It is important to mention that so far there is a lack of insightful understanding of the correlation of the composition of the metallic glass precursors, the pore/ligament size of the np metals and the effect of adding minor elements to the alloy [46].

6.1.2. Porosity evolution

The working model of porosity evolution during dealloying is supported by both kinetic Monte Carlo (KMC) simulations and numerical solutions of the interface evolution equations. The primary driving force is that, at electrochemical potentials above a composition-dependent critical potential V_c , dissolvable atoms are easily solvated and removed from low-coordination sites such as step edges, and the surface sites are rapidly passivated with the remaining more noble species [44,47]. A summary of this model is shown in Figure 1.15.

- (a) rate-limiting step: formation of terrace vacancies which then grow into lateral vacancy clusters.
- (b) dissolution proceeds layer by layer: surface diffusion passivates low-coordination sites with Au leading to surface roughening.
- (c, d) dealloying continues wherein insufficient Au totally passivate the increasing surface area leading to undercutting and bifurcation of ligaments.
- (e) result of this process: bicontinuous porous structure in which ligaments have Au-rich surfaces and Ag-rich interiors.
- (f) coarsening increases the length scale of the initial structure and residual Ag atoms are exposed and dissolved, leaving a final structure with much reduced Ag content [44].

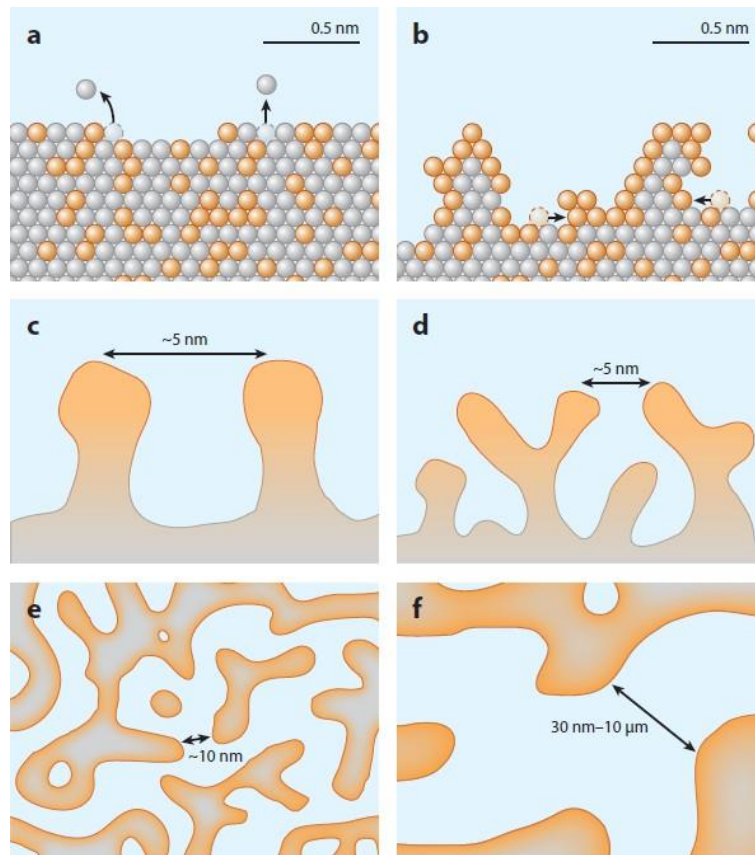


Figure 1.15. Working model for porosity evolution in dealloying in the Ag-Au alloy system (Ag, gray; Au, orange). (a) Terrace Vacancies formation. (b) Surface diffusion passivates low-coordination sites with Au (c, d) Undercutting and bifurcation of ligaments. (e) Bicontinuous porous structure in which ligaments have Au-rich surfaces and Ag-rich interiors. (f) Final structure with much reduced Ag content [44].

The process of porous metal formation, particularly within the realm of amorphous alloys, involves a distinctive dealloying mechanism. Unlike traditional crystalline alloys, where the dissolution of less noble elements and surface diffusion of noble atoms (adatoms) lead to the development of smooth ligaments and porosities. In amorphous alloys the resulting ligaments are notably rough, characterized by a polycrystalline composition comprising several impinged grains. In the absence of a long-range order structure in amorphous precursors, adatoms liberated from the alloy's structure exhibit a tendency to aggregate randomly through surface diffusion. This aggregation forms domains that incrementally grow until they converge, ultimately giving rise to ligaments [48].

Furthermore, the dealloying process in amorphous alloys is shown in Figure 1.16. The steps involved in the process are:

i. Adatom aggregation by surface diffusion:

In the case of amorphous alloys, adatoms (individual atoms) liberated from the alloy's structure are not fixed to an ordered structure, as is the case in crystalline alloys. These adatoms exhibit random aggregation through surface diffusion. Surface diffusion refers to the movement of atoms along the surface of the material.

ii. Formation of randomly aggregated domains:

The adatoms aggregate randomly on the surface, forming domains that gradually grow in size. Unlike in crystalline alloys, where adatoms initially create islands and hillocks, in amorphous alloys, the aggregation leads to the formation of domains.

iii. Domain growth and convergence:

These domains continue to grow until they impinge on each other. The impingement results in the convergence of domains, generating ligaments in the process. Ligaments are elongated structures that are a characteristic feature of porous materials [49].

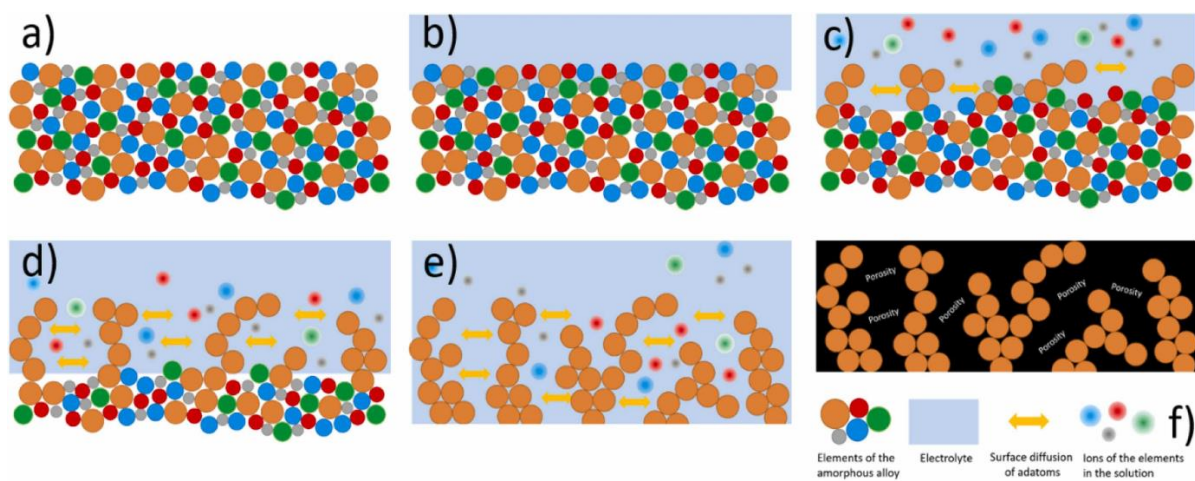


Figure 1.16. Scheme of dealloying in amorphous alloys [49].

6.2. Fabrication of np-Ti alloys via dealloying

This section discusses the potential of dealloying for producing np-TiO_x rich layer on Ti based alloys, for biomedical implant application. A brief summary of the scientific work done by researchers from the early 2000s to 2022 is shown in Figure 1.17. This emphasizes the increase in the focus of researchers towards the improvement of the dealloying technique for application in biomedical field. The focus has been primarily towards crystalline alloys, while other classes of materials like bulk amorphous alloys and shape memory alloys are being explored (shown in Table 1.4). As this research field is gaining momentum, it is necessary to give a direction to it underlining the advances in surface science.

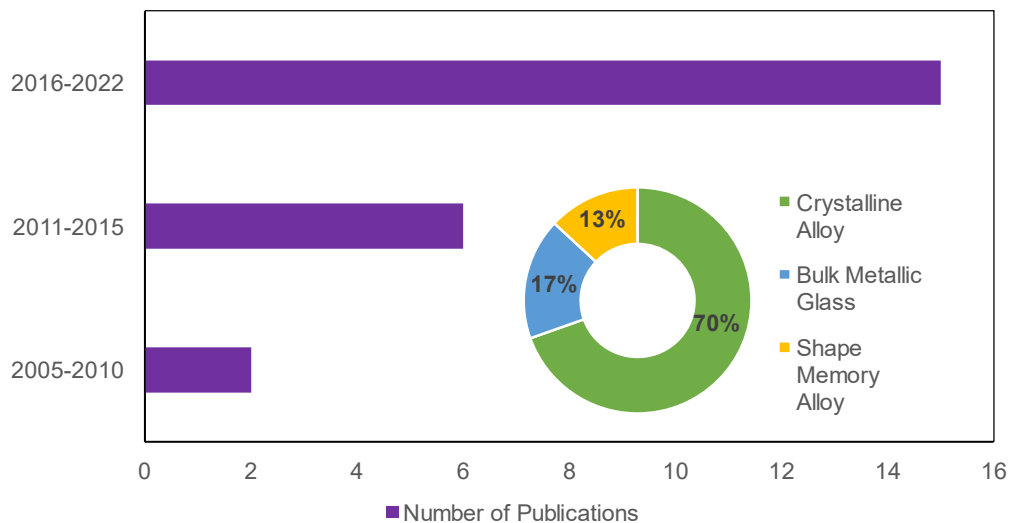


Figure 1.17. Trends in producing np-Ti by dealloying method, from 2005 to 2022, summarizing the number of publications with research focus on the class of materials.

6.2.1. Types of dealloying techniques

A schematic representation shown in Figure 1.18 summarizes the dealloying technique. The precursor alloy here is made up of elements A and B, where B needs to be selectively removed. The choice of dealloying media or electrolyte, denoted here as C, depends on their chemical reactivity towards B. Here, element C is reactive towards B but inert towards A. This leads to the targeted dissolution of B into C from the A-B precursor alloy, leaving behind A with a np-surface. A number of different dealloying techniques have been studied by researchers since the 2000s to explore new options for dealloying media beyond aqueous electrolytes.

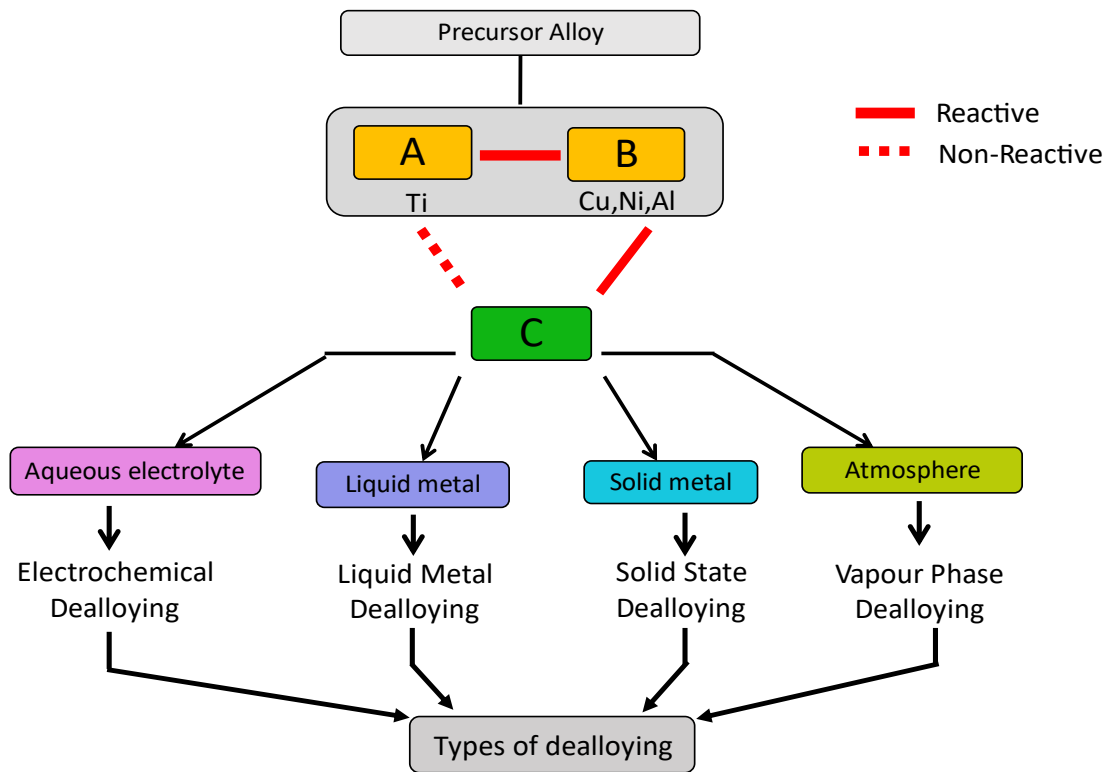


Figure 1.18. Schematic representation of dealloying techniques.

6.2.1.1. Chemical and electrochemical dealloying

Chemical dealloying involves free immersion of precursor alloy in the etching solution as shown in Figure 1.19. It is a spontaneous process which can be performed at an elevated temperature and offers various advantages such as simplicity, affordability, and the possibility of easy scale-up for commercialization [50,51]. The surface morphology of the dealloyed sample can be controlled and optimized by regulating the experimental conditions like concentration and pH (acid/base) of the electrolyte, treatment time and temperature. However, this method is not suitable for alloys with elements having similar chemical properties as it becomes difficult to ensure selective etching [52].

Electrochemical dealloying is another widely used dealloying method (Figure 1.19 a). It is also known as potentiostatic or galvanostatic dealloying because it occurs due to difference in the standard reduction potential of the two alloy elements [53]. These techniques have been widely studied on Au-Ag based alloy, where Ag is less noble than Au and it is selectively dissolved, producing np-Au on the surface [54]. A three-electrode setup with a reference electrode, counter electrode, and sample as the working electrode. The experimental parameters can be optimized by adjusting the electrolyte concentration, temperature, alloy composition and applied potential to tailor the morphology of the sample. This method is also facile and inexpensive but, obviously, precursor alloys containing elements with similar electrode potential values cannot be dealloyed using this method [52,55]. Some examples of elements dealloyed using this technique are Pt, Pd, Ag, Cu, Ni, Al [56–64].

6.2.1.2. Liquid melt dealloying

Liquid metal dealloying (LMD) technique uses metallic melt for dealloying a sample. This method is based on the difference in enthalpy of mixing of elements present in precursor alloy with respect to the liquid melt. The elements selected for liquid melt are based on the theory that at certain dealloying temperature, when precursor alloy is immersed in the liquid melt, the constituent element that has positive enthalpy of mixing with the metallic melt gets diffused into the liquid while that with negative enthalpy of mixing remains on the surface of the alloy. The atoms present on the surface of the sample rearrange and form ligaments and pores via surface diffusion [65,66]. The schematic representation of liquid melt dealloying is shown in Figure 1.19 (b). For better understanding, Ti-Cu alloys can be considered. When a Ti-Cu alloy is immersed in a Mg melt Cu diffuses in the melt, being miscible in Mg, and forms Mg_2Cu phase on the surface whereas Ti does not react with Mg since it is immiscible in Mg. Later, the treated sample is immersed in HNO_3 to selectively etch Mg_2Cu phase producing np-Ti-rich phase on the surface. This technique provides new possibilities for selection of elements for developing precursor alloy and selecting a suitable element for liquid melt. This phenomenon was first explained by Harrison and Wagner in 1959 [67] and then re-addressed by Wada et al. in 2011 [68,69]. This technique can be useful for dealloying less noble elements like Ti, which is prone to oxidation, form a passive oxide film and have positive reduction potential that is challenging to be dealloyed using chemical and electrochemical dealloying routes [70]. However, there are some limitations with this method like maintaining proper working conditions which requires high temperature for preparing metallic melt and this leads to high cost of operation [52]. This technique has been widely used to fabricate porous layers on less noble materials like Ti, Nb, V, Fe, Cr, Mn, Ta, Cu [71–74].

6.2.1.3. Solid state dealloying

Solid state dealloying (SSD) is also referred to as solid metal dealloying (SMD). In this technique, which is like LMD in thermodynamic aspects, one element is selectively removed via solid-state diffusion mechanism into a metal solvent to produce a bi-continuous np-structure as shown in Figure 1.19 (c). Unlike LMD, where heat of enthalpy is an important criterion, SMD is, thus, dependent on the interdiffusion kinetics of the metal solvent with the components of the alloy. Slower transport kinetics and difference in the diffusion coefficients of the solid metals play a vital role for a successful dealloying. The interdiffusion kinetics of metal solvent should be slower with at least one order of magnitude compared to other components of the alloy. Dealloying occurs at the metal-solvent interface and depending on the rate of diffusion and heat of mixing of the concerned element in the metal solvent the reorganization of atoms at the interface is determined. This method requires low processing temperature which is below the melting point of the metal solvent to promote the formation of finer structures [75]. It is also a cost-effective technique which provides a wide window for varying processing time and temperature and enabling more control over the volume fraction

of the components present in the alloy. This is an important criterion as it influences the morphology of the porous networks [76]. SSD was first reported by Wada et al. in 2016 [77] where the authors proposed a new strategy for producing porous structures developed on $(\text{Fe}_{0.8}\text{Cr}_{0.2})_{50}\text{Ni}_{50}$ alloy. It involved atomic diffusion of Ni in Mg occurring at a temperature lower than the melting point of the Mg powder which was used as the dealloying medium. This treatment resulted in the formation of a np-surface with very fine morphology rich in Fe-Cr phases and lower Ni content, composition being $\text{Fe}_{76.3}\text{Cr}_{20.4}\text{Ni}_{3.3}$. Ni_2Mg phase formed due to solid state diffusion was later etched using HNO_3 solution. Currently, thin film substrates are used for studying SSD mechanism. McCue et al. in 2017 [78], developed dense metal composites by solid state dealloying of a binary precursor alloy deposited on solid metal solvent made of Cu and Zr. This study suggested the use of SSD in creating multi-layered films with different compositions of precursor alloy and metal solvent which can be dealloyed simultaneously. The authors studied requirements and kinetics for a solid state dealloying by using thin film of $\text{Ni}_{55}\text{Fe}_{45}$ (750 nm thickness) and $\text{Ti}_{65}\text{Ta}_{35}$ (700-800 nm thickness) alloys deposited on Cu and Zr substrates, respectively. In this design Cu and Zr remain immiscible with Ta and Fe but miscible with Ti and Ni. The dealloying occurred by diffusing the miscible components from the deposited thin film with substrate. Interdiffusion kinetics were studied, and the authors proposed Ti-Ta/Zr as the ideal model for further investigations like finding critical composition for SSD to occur and mechanism of morphology formation. The influence of volume change of metal solvent and the substrate, considering their diffusion kinetics, was also investigated as it is an important parameter. It was concluded that altering the composition of parent alloy interpenetrating metal nanocomposite can be produced where volume fraction of each phase gradually changes upon dealloying. Additionally, it is possible to dealloy thin films with multiple layers of metal solvent which can then be simultaneously dealloyed through the entire layers thus, eradicating the limitations of performing SSD with only one substrate. Recently in 2019, Yao Shi et al. [79] fabricated ultrafine ligaments of np-Ti. Samples were prepared by ball milling Ti-Cu powders with Mg powder followed by heat treatment to form a phase of Mg-Cu, the samples were then chemically etched in 1 M HNO_3 solution to remove Mg-Cu phase and produce np-Ti. This study helped in understanding the formation of dealloyed structures at the sample interface after SSD.

6.2.1.4. Vapor phase dealloying

Vapor phase dealloying is a technique involving evaporation of one or more elements from the precursor alloy to fabricate different surface morphologies as shown in Figure 1.19 (d). This technique uses the difference in the melting and boiling point of the elements present in the alloy as well as the difference in their saturated vapor pressure. The dealloying temperature is maintained below the melting point of the precursor alloy in accordance with the Kirkendall effect [80,81]. This method is quite facile and environment friendly. However, this type of treatment is limited to Zinc (Zn) based alloy systems for dealloying elements like Ni and/or Co [82,83]. This phenomenon often attributed as Kirkendall effect was observed by Balluffi and Alexander back in 1952 [84,85] where the author reported dezincification of brass in vacuum, which led to the formation of close porosities instead of interdiffusion surface rearrangement

which produces bicontinuous open porosity. The authors studied diffusional changes of Ag from vapor phase into a thin gold wire at 1213 K in normal and parallel direction of diffusion. Recently this technique received attention when Zhen Lu et al. [86] developed a prototype of $\text{Co}_5\text{Zn}_{21}$ alloy by mechanically milling powders at room temperature and melt spinning to produce thin ribbons. The ribbons were heated in an inert atmosphere at 773 K and 100 Pa for 5 to 120 min and the resultant dealloyed samples were found to be rich in Co. Additionally Yujun Shi et al. [87] synthesized bulk np-Co with face centered cubic structure from a $\text{Co}_5\text{Zn}_{21}$ alloy foils. The dealloyed surface consists of high surface area $1.06 \text{ m}^2\text{g}^{-1}$ and large pore size distribution with average pore diameter around 400 nm and ligament size $0.36 \pm 0.07 \mu\text{m}$. Jiuhui Han et al. [83] fabricated 3D bicontinuous np-Ni and Ge from Ni-Zn and Ge-Zn precursor alloys with tunable pore size by varying the temperature, time of treatment, Further the author studied the dealloying kinetics for understand effect of alloy composition on the porosity and grain size of the precursors of Ge-Zn. VPD has been attempted for dealloying Mn-Zn, Ni-Zn and Al-Zn alloys for fabricating np-Mn, Ni and Al [88–90].

This technique is being utilized on various materials as it allows the tunability of pore size from micron to nano scale by controlling the dealloying parameters like temperature, time and pressure. Since it does not involve any chemical or electrochemical route of fabrication, the method is versatile which can be used on various alloys without the need to consider their electrical conductivity or chemical stability. Importantly, it is an economical, pollution-free technique and affordable where recovery of the evaporated elements such as Zn in the vacuum system is possible. Thus, this method holds great potential.

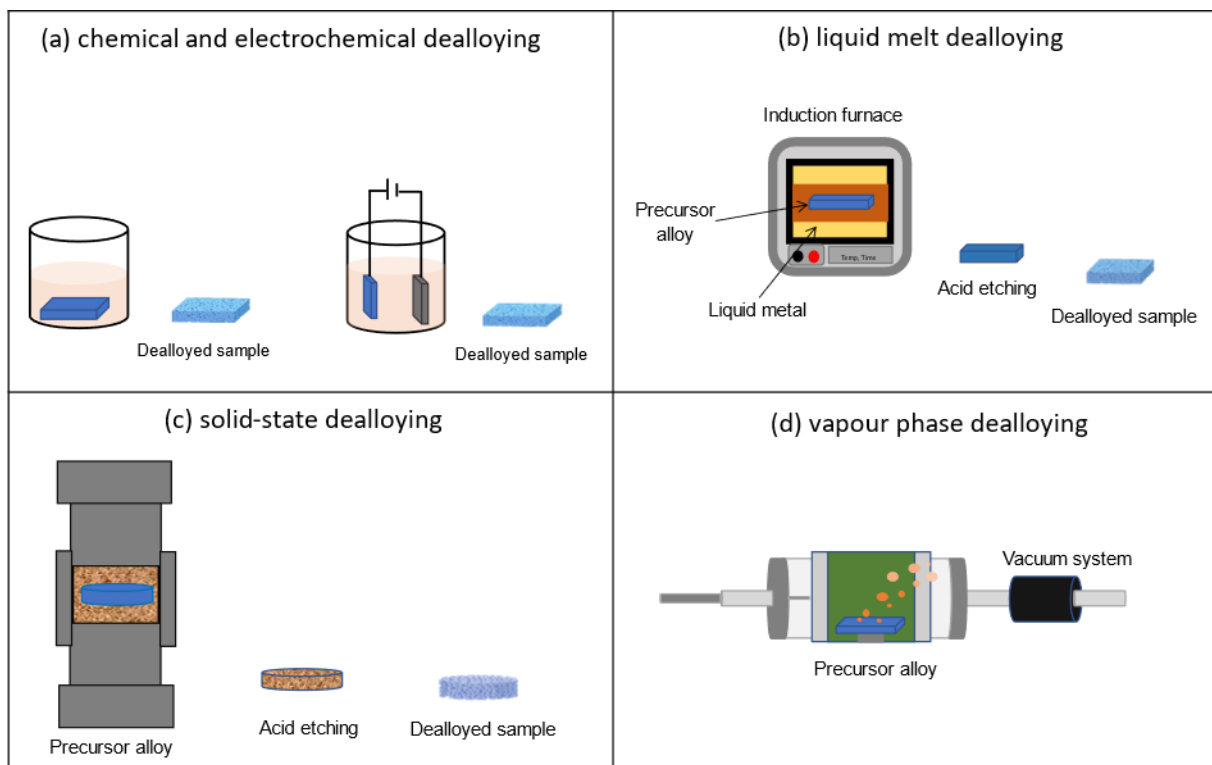


Figure 1.19. Schematic representation of (a) chemical and electrochemical dealloying (b) liquid melt dealloying technique (c) solid-state dealloying technique (d) vapor phase dealloying technique.

Table 1.4. Summary of the Ti based alloys treated using dealloying techniques with the key findings.

	Alloy Type	Dealloying Technique and Media	Key Findings	Ref
Crystalline Alloys	Ti6Al4V	LMD: Mg	low Al on the surface, Studied effect of crucible material on LMD	[91]
	Ti6Al7Nb	LMD: Mg	Tunable pore size, pore shape, and pore depth, reduced Al conc. by 48 % on the surface, improved cytocompatibility and bone formation	[92]
	Ti _x Zr _{(100-x)y} Cu _{100-y}	LMD: Mg	Tunable surface functionality such as, stiffness, strength, Young's modulus, cytocompatible	[93]
	Ti ₂₀ Hf ₂₀ Cu ₆₀ , Ti ₂₅ Hf ₁₀ Cu ₆₀ , Ti ₃₀ Hf ₁₀ Cu ₆₀	LMD: Mg	Developed metal-polymer composites mimicking mechanical behavior of cortical bone	[94]
	Ti _{27.2} Nb ₃ Cu _{69.8} and Ti _{29.2} Fe _{3.9} Cu _{66.9}	LMD: Mg	Tunable phase formation, microstructure, high yield strength and low Young's modulus	[95]
	Ti _{47.5} Mo _{2.5} Cu ₅₀	LMD: Mg	Dendritic microstructure, Elastic modulus near human cortical bone	[96]
	(TiZrCr) ₂₀ Cu ₈₀	LMD: Mg	Dealloyed multicomponent alloy	[97]
	Ti ₅₀ Sc ₅₀	CD: HNO ₃	np-Ti by spinodal decomposition	[98]
	(TiMo) ₃₀ Cu ₇₀ , Ti ₃₀ Cu ₇₀	SSD: Mg	hierarchical structure with improved mechanical properties and bioactive surfaces	[99]

	Ti ₂₀ Cu ₈₀ , Ti ₃₀ Cu ₇₀ , Ti ₄₀ Cu ₆₀ , Ti ₁₅ Zr ₁₅ Cu ₇₀ , and Ti _{22.3} Nb _{7.7} Cu ₇₀	LMD: Mg	np-metal composite with bisphenol F epoxy polymer mimicking the elastic behavior of human bones	[100]
	Ti ₅₀ Cu ₅₀	LMD: Mg	Ti-Mg nanocomposites with low Young's modulus and moderate yield strength	[101]
	Ti ₃₀ Cu ₇₀	SSD: Mg	suggested pore-forming mechanism is a solid-state interdiffusion process, found that elastic modulus in np- α -Ti foam follow linear decay fit with increasing ligament size	[102]
	Ti ₂₅ Nb ₁₅ Cu ₆₀	CD: Nitric Alcohol Solution	np-structure with 24 GPa elastic modulus	[103]
	Ti6Al4V	ECD: NaOH	np-surface with low Al conc., bioactive and cytocompatible surface with high osteogenic activity	[104]
	Ti ₃ Zr ₂ Sn ₃ Mo ₂₅ Nb	ECD: HF + HNO ₃	Dealloying of as-solution treated TLM alloy created a simple np- topography, while in as-cold rolled TLM alloy created a hierarchical micro/np-topography, cytocompatible surfaces	[105]
Amorphous Alloys	Ti ₃₀ Cu ₇₀ , Ti ₄₀ Cu ₆₀ and Ti ₅₀ Cu ₅₀	ECD: HNO ₃	np-Ti oxide layer with mean diameter of pores 50 nm and the thickness of pore walls 100 nm	[106]
	Y ₅₆ Al ₂₄ Co ₂₀ , Ti ₅₆ Al ₂₄ Co ₂₀ , and Y ₂₀ Ti ₃₆ Al ₂₄ Co ₂₀	ECD: HNO ₃	np-interconnected microstructure with amorphous phase	[107]
	Ti ₄₅ Y ₁₁ Al ₂₄ Co ₂₀	CD: H ₂ SO ₄	np- Ti oxide surface with improved passivation behavior in simulated body fluid	[108]
	Ti ₃₀ Cu ₇₀	LMD: Mg	Hierarchical structure	[109]

Shape Memory Alloy	NiTi	CD: nitro dioctyl phthalate + H ₂ O ₂ + HCl + H ₂ SO ₄	Ni depleted np-surface with thickness 130 nm, cytocompatible with dermal mesenchymal stem cells	[110]
	NiTi	CD: FeCl ₃	nanogrid structure, bioactive surface promoting hydroxyapatite growth after 14-day immersion in Hank's solution	[111]
	NiTi	ECD: HNO ₃	hierarchically porous composite of NiTi/ hydrogels with high water retention capacity for antibiofouling performance	[112]

7. Challenges and opportunities

Dealloying technique is a controlled corrosion method for developing self-organized np-morphology with large surface areas. This method, being one of the very old techniques, still finds application in emerging fields like energy storage, sensing, catalysts, and biomedical implants made up of Ti alloys. In the past decades researchers have been able to successfully discover new ways to dealloy Ti-based alloys for production of np-TiO₂ layer. Despite these attempts, it is required that more research is done to find the full potential of this technique. In the current scenario dealloying of Ti faces difficulties of passivation when immersed in chemical solutions due to high stability of TiO₂ layer, hence, etching of other elements becomes difficult. In the case of liquid metal dealloying current work is focused on using Mg melt but it possesses some challenges because handling of Mg is difficult, and it cannot be scaled easily for commercial purposes. Also, the solid-state and vapor-phase dealloying techniques pose certain limitations with the type of dealloying components. These techniques require further optimization and better understanding of the dealloying process in order to tailor the np-structures as per the desired application. The dealloying method can provide new pathways for synthesis of np-Ti-based alloys with multiple components. A. Chuang and J. Erlebacher [113] discussed progress and challenges in integrating dealloying method with additive manufacturing which expands opportunity for scientific community to incorporate these two techniques to make nanocomposites and np-materials with wide selection of elements from the periodic table. The authors further discussed the ongoing research on the dealloying of additively manufactured materials like Au-Ag, Ni-Cu using electrochemical route, while SiC using liquid melt dealloying technique. Several alloys produced with selective laser melting/sintering were treated using dealloying methods. For instance, electrochemical dealloying was used for Cu-Mn, Al-Si, while liquid-melt dealloying was used on Co-Cr-Mn,

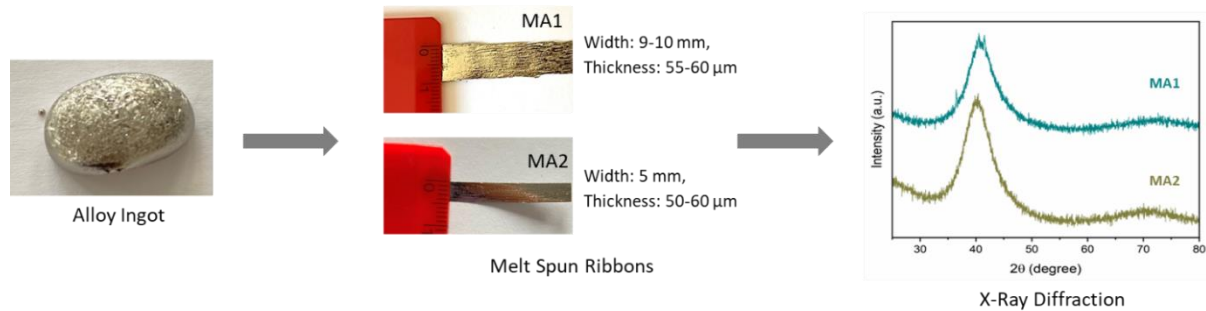
Fe-Cr-Ni and Nb-Ti, and solid-state and vapor-phase dealloying were used on Fe-Ni and Brass respectively.

In the past decades amorphous alloys with compositions containing biocompatible elements such as Ti, Zr, Pd are explored [114–118]. Wang et al. studied the biocompatibility of $\text{Ti}_{41.5}\text{Zr}_{2.5}\text{Hf}_5\text{Cu}_{37.5}\text{Ni}_{7.5}\text{Si}_1\text{Sn}_5$ amorphous alloy and pure Ti, using in vitro cell response and in vivo animal response. The results indicated that the two materials were well integrated with a gap less than 5 μm between bone tissue and implant after one-month post-implantation. However, presence of Ni and high content of Cu was considered concerning [119], and suggested the necessity to evaluate the biocompatibility of $\text{Ti}_{41.5}\text{Zr}_{2.5}\text{Hf}_5\text{Cu}_{37.5}\text{Ni}_{7.5}\text{Si}_1\text{Sn}_5$ amorphous alloy for long-term implantation. Liu et al. studied the cytocompatibility of three different Ti–Zr–Cu–Fe–Sn–Si amorphous alloys and Ti–6Al–4V alloy with mouse pre-osteoblast MC3T3-E1 and found that cell viability in the $\text{Ti}_{47}\text{Zr}_{7.5}\text{Cu}_{40}\text{Fe}_{2.5}\text{Sn}_2\text{Si}_1$ amorphous alloy extracts was slightly higher than that in the Ti–6Al–4V alloy extract [120]. Yang et al. reported that $(\text{Ti}, \text{Zr}, \text{Cu})_{92.5}\text{Fe}_{2.5}\text{Sn}_2\text{Si}_1\text{Ag}_2$ amorphous alloy showed moderate bio-corrosion resistance and good biocompatibility with MC3T3-E1 cells in a direct and indirect in vitro cell culture [121]. Kokubun et al. conducted an in vivo evaluation of $\text{Ti}_{40}\text{Zr}_{10}\text{Cu}_{34}\text{Pd}_{14}\text{Sn}_2$ amorphous alloy and found that it showed biocompatibility and integration to bone tissue, with no abnormal findings or inflammation detected up to three months post-implantation [122]. Despite these advantages, amorphous alloys with high Cu concentration are observed to suffer from wear and localized corrosion and cytotoxicity [123]. Therefore, it is important to modify the surface of the implant material (chemical composition, morphology, and roughness) for improving biocompatibility and reducing the risk of adverse reactions [124–129].

The primary objective of this thesis is to explore and assess the applicability of dealloying techniques on Ti-based multicomponent amorphous alloys, with a specific focus on advancing the use of these techniques for biomedical implant applications. Subsequent chapters of this thesis delve into the detailed findings corresponding to each specific aim for providing a comprehensive exploration of the research objectives.

Chapter II

PRECURSOR ALLOY PREPARATION



Specific Aim

- To develop and characterize amorphous alloy with biocompatible elements (Ti and Zr) and antimicrobial elements (Ag, Fe, and Cu) for potential use as implant materials.

1. Introduction

Amorphous alloys (or metallic glasses) have unique structural characteristics, i.e., they have an amorphous structure free from microstructural defects such as dislocations and grain boundaries, therefore offering an appealing array of properties and processing capabilities for implant applications [130]. Key features of the amorphous state in metals, pertinent to structural implants, encompass high strength and hardness, promising robust load-bearing capacity, wear resistance, and a reduced elastic modulus that, associated with high values of elastic strain limit, can potentially reduce the stress-shielding effects [131,132]. To effectively use amorphous alloys as implanted materials, it is important to design alloys with high GFA, i.e., high capability to form an amorphous phase during solidification even when slow rates of solidifications are used (100 K/s). In fact, metallic glasses with high GFA can be obtained completely amorphous via conventional liquid metal casting with centimeter-sized cross-sections, so perfectly fitting the needs of the implant materials [133,134]. Therefore, it is important to design the right composition that both enable a high GFA and include elements with good biocompatibility [135,136]. In this respect, Calin et al. presented a critical review on biological response of various elements to the human body and their influence on GFA when added to Ti. The list of biocompatible elements includes Zr, Si, and Sn, whereas Cu, Fe and Ag are harmful to the human body [137]. Cu is a good glass former when added to Ti [138], however it poses significant health risks when present in high concentrations [139] such as contributing to the development of osteoporosis, angiogenesis, and coronary heart disease [140,141]. The high Cu fractions are the main reasons for pitting corrosion in Ti-Cu-based and Zr-Cu-based BMGs. This pitting corrosion is a significant concern for the long-term

performance of these materials and can lead to expected early implant failure [142–144]. To overcome this issue, a potential strategy is to focus on enhanced surface oxidation to minimize the release of Cu ions into the physiological environment and reduce the risk of inflammatory reactions or cell death [145]. Nevertheless, the presence of Cu in small amount (1 wt % and 5 wt %) in Ti based alloys shows antibacterial properties [146]. Several studies have reported the synthesis of amorphous alloys based on Ti-Zr-Cu-Pd system with minor additions of Si, Sn, Nb, Ta, and Sc for biomedical applications [147–149]. Moreover, Ti based amorphous alloys without Pd were developed in order to decrease the material costs [150,151]. Y. Liu et al. developed Ti-Cu-Zr-Fe-Sn-Si amorphous alloys, with high GFA proved by a relatively large critical diameters of 3 mm, i.e., the maximum diameter for which an alloy can be obtained completely amorphous by conventional liquid metal casting. These alloys are characterized by a high (Ti + Zr)/Cu ratio (1.25 - 1.42) that was demonstrated to be beneficial in improving bio-corrosion resistance and biocompatibility. Moreover, the presence of different elements with large atomic size mismatch promotes atomic packing density and inhibits constituent elements diffusion, leading to an enhanced resistance to crystallization. The addition of Si and/or Sn elements in the Ti-based amorphous alloy system improved the glass-forming ability for other Ti-based amorphous alloy systems [120]. Recently, Pang et al. reported a new alloy, $\text{Ti}_{47}\text{Cu}_{38}\text{Zr}_{7.5}\text{Fe}_{2.5}\text{Sn}_2\text{Si}_1\text{Ag}_2$ at %, with a critical diameter of 7 mm, displaying Young's modulus around 100 GPa, similar to Ti6Al4V alloy (discussed in chapter 1, section 5.1). This composition shows a good combination of mechanical properties and cytocompatibility with MC3T3-E1 osteoblast cells [152]. Starting from this composition, in the present study, a new amorphous alloy with composition $\text{Ti}_{42}\text{Cu}_{40}\text{Zr}_{8.5}\text{Fe}_{2.5}\text{Sn}_2\text{Si}_2\text{Ag}_3$ and $\text{Ti}_{40}\text{Cu}_{40}\text{Zr}_{11}\text{Fe}_3\text{Sn}_3\text{Ag}_3$ at % were designed. The concentration of Ti, Sn, Si, Zr and Cu was adjusted to enhance the GFA and in particular (i) the (Ti + Zr)/Cu ratio was maintained high (=1.28) and (ii) Sn and Si concentration was increased to potentially extend the supercooled liquid region. Further, characterization of master alloy and amorphous ribbon was performed using X-ray diffraction, scanning electron microscope, differential scanning calorimetry, inductively coupled plasma with optical emission spectroscopy to investigate the structural and thermal properties.





The studies related to ICP-OES, AFM, amorphous ribbon preparation was carried out at Institute of Complex materials, Leibniz-Institute for Solid State and Materials Research Dresden (Leibniz IFW Dresden), Dresden, Germany during my period abroad.

2. Experimental Procedure

2.1 Preparation of master alloy and as-quenched ribbons

Two master alloy (MA) ingots with compositions $Ti_{42}Cu_{40}Zr_{8.5}Fe_{2.5}Sn_2Si_2Ag_3$ at % and $Ti_{40}Cu_{40}Zr_{11}Fe_3Sn_3Ag_3$ at %, named MA1 and MA2 respectively, were prepared by arc melting pure elements under inert atmosphere of argon. Pure elements such as Ti (99.99 %), Cu (99.99 %), Zr (99.5 %), Sn (99.99 %), Si (99.999 %), Fe (99.95 %), Ag (99.99 %) were arc melted 8 times to ensure homogenization. The master alloys were melt-spun to produce metallic glass ribbons using planar flow casting technique using boron nitride (BN) crucible and melted using induction heating. The molten liquid was ejected with an over pressure on a rotating Cu wheel in an argon atmosphere of 1 bar. The produced ribbon samples and selected parameters are described below in Table 2.1.

Table 2.1. Melt spinning parameter of master alloys, $Ti_{42}Cu_{40}Zr_{8.5}Fe_{2.5}Sn_2Si_2Ag_3$ MA1 and $Ti_{40}Cu_{40}Zr_{11}Fe_3Sn_3Ag_3$ MA2.

Ribbon	Temperature (°C)	Over pressure (bar)	Wheel speed (m/s)	Crucible	Crucible to Wheel distance (mm)	Width (mm)	Thickness (μm)	Image
MA1								
Ribbon 1	1000	0.25	25	Boron Nitride (BN)	0.3	10	60-65	
MA2								
Ribbon 1	965	0.3	30	BN	0.25	9	50-55	
Ribbon 2	1050	0.3	30	BN	0.25	2	50-55	
Ribbon 3	1018	0.25	32	Quartz with BN spray coating	0.3	4	50-60	

2.2 Characterization of master alloy and as-quenched ribbons

The structure of $\text{Ti}_{42}\text{Cu}_{40}\text{Zr}_{8.5}\text{Fe}_{2.5}\text{Sn}_2\text{Si}_2\text{Ag}_3$ MA1 and $\text{Ti}_{40}\text{Cu}_{40}\text{Zr}_{11}\text{Fe}_3\text{Sn}_3\text{Ag}_3$ MA2 master alloys and as quenched ribbons was analyzed by X-ray diffraction (XRD) with a Panalytical X'Pert apparatus. The cross section of master alloys was analyzed using Cu K α radiation ($\lambda=1.5418 \text{ \AA}$) in Bragg Brentano geometry. The measurements were made at tension of 40 kV and current of 30 mA. The slit sizes used were 1/4 degree and 5 mm at 600 and 800 counts, respectively. The microstructure of the master alloys was analyzed using scanning electron microscope (SEM) (Tescan Vega 4). The elemental composition of the master alloys was analyzed using Energy Dispersive Spectroscopy (EDS) (Ultim Max 40 mm² Oxford instruments) with a minimum of five measurements for each crystalline phase.

The thermal behavior of the as-cast master alloy was investigated using a high temperature differential scanning calorimetry (SETARAM multidetector). The samples were placed in an Al₂O₃ crucible surrounded with Y₂O₃ powder, 10°C/min of heating rate was maintained during the measurement up to 1550 °C. Constant flow of Helium gas was maintained inside the experimental chamber. The measurement was performed at 10⁻² mbar vacuum pressure.

The structural analysis of as quenched ribbons was performed using XRD at tension of 40 kV and current of 30 mA using a slit size of 1/4 degree, 5 mm with step size of 0.0167 and scan speed of 600 counts.

The thermal properties of the $\text{Ti}_{42}\text{Cu}_{40}\text{Zr}_{8.5}\text{Fe}_{2.5}\text{Sn}_2\text{Si}_2\text{Ag}_3$ MA1 and $\text{Ti}_{40}\text{Cu}_{40}\text{Zr}_{11}\text{Fe}_3\text{Sn}_3\text{Ag}_3$ MA2 ribbon were analyzed using differential scanning calorimeter (DSC Perkin Elmer DSC 8000) at a heating rate of 20 °C/min in Al₂O₃ pan from 50 °C to 650 °C under argon atmosphere.

The elemental composition of the as quenched ribbons was analyzed using Inductively Coupled Plasma with Optical Emission Spectroscopy (ICP OES, iCAP6500 DUO, Thermo Fisher Scientific GmbH).

The surface roughness of samples was analyzed using atomic force microscopy (AFM) under ambient conditions using a Bruker Dimension Icon AFM in tapping mode with a scan rate of 0.5 Hz. A TESPA-v2 probe was used with a resonance frequency of 320 kHz. The AFM data was analyzed using WSxM5.0 Develop 10.0 and/or Gwyddion 2.56. AFM images were acquired at 1 × 1 μm² on three different spots of the samples for calculation of average root mean square (RMS) roughness of the sample surface.

3. Results and Discussion

3.1 Characterization of master alloy

The microstructure and composition of $\text{Ti}_{42}\text{Cu}_{40}\text{Zr}_{8.5}\text{Fe}_{2.5}\text{Sn}_2\text{Si}_2\text{Ag}_3$ MA1 and $\text{Ti}_{40}\text{Cu}_{40}\text{Zr}_{11}\text{Fe}_3\text{Sn}_3\text{Ag}_3$ MA2 alloys were analyzed using SEM and EDS. The SEM image of MA1 in Figure 2.1 (a-b) shows the presence of five distinct crystalline phases: phase 1 with a dendritic shape, phase 2 and phase 3 with a lamella like shape, and two phases in small concentration, i.e., phase 4 in grey scale with rounded morphology and phase 5 with small black crystals. EDS analysis was performed on the identified phases to determine the distribution of Ti, Cu, Zr, Fe, Sn, Ag, Si elements and the results are reported in Table 2.2. Phase 1 is mainly composed of Ti and Cu in almost equal amount (46.8 at % and 43.7 at % respectively) and it can be attributed to the formation of $(\text{Ti,Zr})\text{Cu}$ phase with a small amount of Zr in solid solution (4.0 %) substituting Ti in the unit cell. Similarly, phase 2 contains Ti, Zr and Cu in 29.9, 18.5 and 43.2 at % respectively and it can be related to the formation of the Cu_2TiZr phase. Phase 3, with concentration of Ti, Zr, Sn and Cu of 28.6, 27.9, 17.7, 18.2 at % respectively, can be related to the formation of a $(\text{Ti,Zr})_5\text{Sn}_3\text{Cu}$ phase. Phase 4 is constituted by Ti, Zr, Sn and Si in 42.8, 24.3, 10.5, 17.6 at % respectively and it can be attributed to the formation of $(\text{Ti,Zr})_5(\text{Si,Sn})_3$. Phase 5 contains Ti, Zr and Si in 52.9, 10.6 and 29.6 at % respectively indicating the formation of $(\text{Ti,Zr})_5\text{Si}_3$ titanium silicide.

Three distinct crystalline phases in black, grey, and white scale were observed in MA2 alloy that were related to the same phases described for MA1. In detail, phase 1 is enriched in Ti and Cu in 46.8 and 42.4 at % respectively indicating the formation of $(\text{Ti,Zr})\text{Cu}$ phase, phase 2 is constituted by Ti, Cu, Zr in 36.4, 40.2, 16.2 at % respectively, i.e., Cu_2TiZr phase, phase 3 composed by Ti, Zr, Sn and Cu in 21.7, 35.6, 27.1, 15.1 at % respectively is related to a $(\text{Ti,Zr})_5\text{Sn}_3\text{Cu}$ phase.

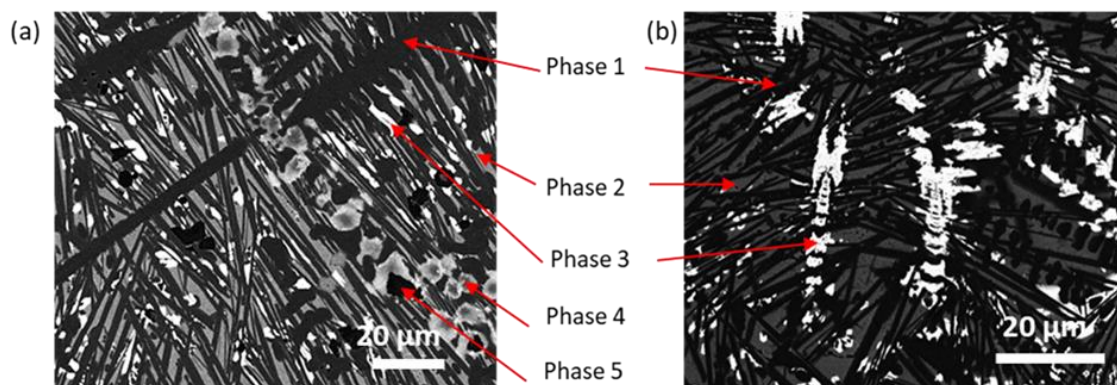


Figure 2.1. SEM back scatter electrons image of (a) $\text{Ti}_{42}\text{Cu}_{40}\text{Zr}_{8.5}\text{Fe}_{2.5}\text{Sn}_2\text{Si}_2\text{Ag}_3$ MA1 and (b) $\text{Ti}_{40}\text{Cu}_{40}\text{Zr}_{11}\text{Fe}_3\text{Sn}_3\text{Ag}_3$ MA2 alloy ingot with identified phases.

Table 2.2. EDS measurement of alloy ingot of $Ti_{42}Cu_{40}Zr_{8.5}Fe_{2.5}Sn_2Si_2Ag_3$ MA1 and $Ti_{40}Cu_{40}Zr_{11}Fe_3Sn_3Ag_3$ MA2 (at %). Data estimated with the error of 0.01-1 %.

Phase	Ti	Fe	Cu	Zr	Ag	Sn	Si
MA1							
1	46.8	1.4	43.7	4.0	3.7	0.6	0.4
2	29.9	1.6	43.2	18.5	5.7	0.8	0.0
3	28.6	0.7	18.2	27.9	1.4	17.7	5.1
4	42.8	0.5	4.2	24.3	1.7	10.5	17.6
5	52.9	0.4	5.7	10.6	0.3	0.6	29.6
MA2							
1	46.8	4.7	42.4	4.0	2.9	0.9	NA
2	36.4	2.1	40.2	16.2	3.9	0.8	NA
3	21.7	0.3	15.1	35.6	0.9	27.1	NA

In order to confirm the phases identified by SEM/EDS analysis, $Ti_{42}Cu_{40}Zr_{8.5}Fe_{2.5}Sn_2Si_2Ag_3$ MA1 and $Ti_{40}Cu_{40}Zr_{11}Fe_3Sn_3Ag_3$ MA2 master alloys were analyzed by XRD, and the patterns are shown in Figure 2.2 (a, b). The patterns of MA1 and MA2 were constituted by the same reflections, indicating the presence of the same crystalline phases in the two master alloys. This is in line with what was observed in the microstructure, where, apart from the three major phases, only two silicides were present in a low amount in MA1 with respect to MA2. Therefore, it can be expected that silicide cannot be detected by XRD due to the low intensity of the diffraction peaks. The XRD patterns in Figure 2.2 (a) confirm the presence of tetragonal TiCu (P4/nmm) [153], hexagonal Cu_2TiZr (P6₃/mmc) [154], and hexagonal Ti_5Sn_3Cu (P6₃/mcm) [155,156] phases. Slight shift in peak positions was observed due to the presence of Zr in substitutional solid solution resulting in changes in the lattice parameter [156]. The peaks corresponding to phases 4 and 5 were not observed in XRD spectra of MA1 alloy due to their presence in low fraction.

High temperature DSC scan of MA1 alloy is shown in Figure 2.2 (b). MA1 shows, during heating at 10 °C/min, four endothermic peaks partially superimposed, showing that the alloy is outside the quinary eutectic point. The first melting event is at 826.8 °C and the liquidus temperature (T_l) is at 1188.6 °C. During solidification an undercooling is observed. The DSC curve of MA2 alloy is very similar, with four endothermic peaks partially superimposed with starting melting temperature of 807.8 °C and T_l of 1094.1 °C. Also, in this case an undercooling is observed during solidification.

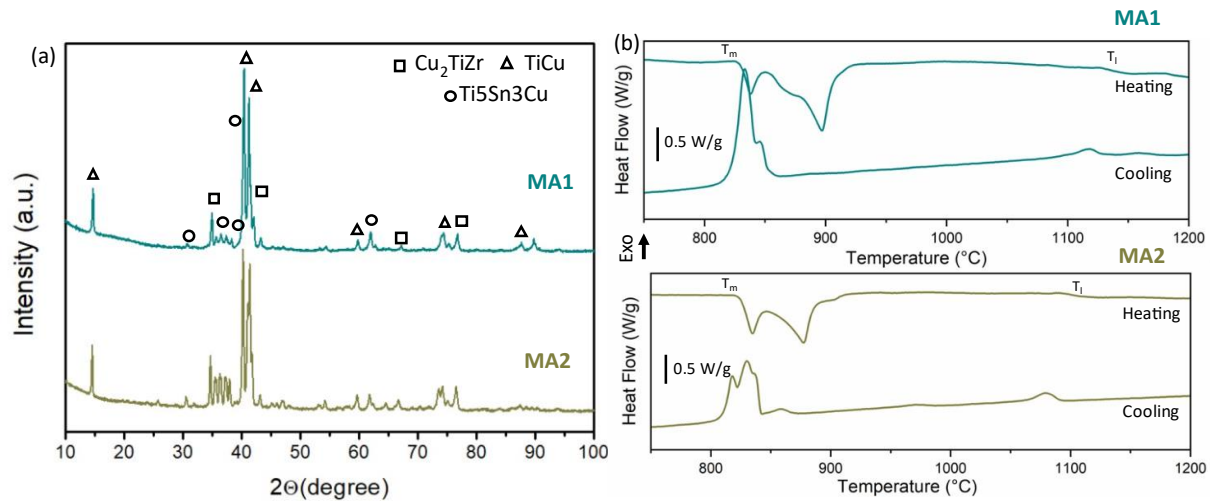


Figure 2.2. Shows (a) XRD patterns and (b) High temperature DSC curve of $\text{Ti}_{42}\text{Cu}_{40}\text{Zr}_{8.5}\text{Fe}_{2.5}\text{Sn}_2\text{Si}_2\text{Ag}_3$ at % (MA1) and $\text{Ti}_{40}\text{Cu}_{40}\text{Zr}_{11}\text{Fe}_3\text{Sn}_3\text{Ag}_3$ at % (MA2) master alloy.

The color map of MA1 alloy in Figure 2.3 (a) showed Ti and Cu were present in phase 1-3 in highest concentration. However, phase 4 consisted mostly of Ti and Zr along with Sn and Si. While phase 5 was rich in Ti and Si with small content of Zr and Sn. In MA2 alloy EDS color map in Figure 2.3 (b) showed presence of Ti and Cu in phase 1-2, whereas phase 3 composed of Zr and Sn. The distribution of each element in the described phases complemented the data obtained using EDS and XRD.

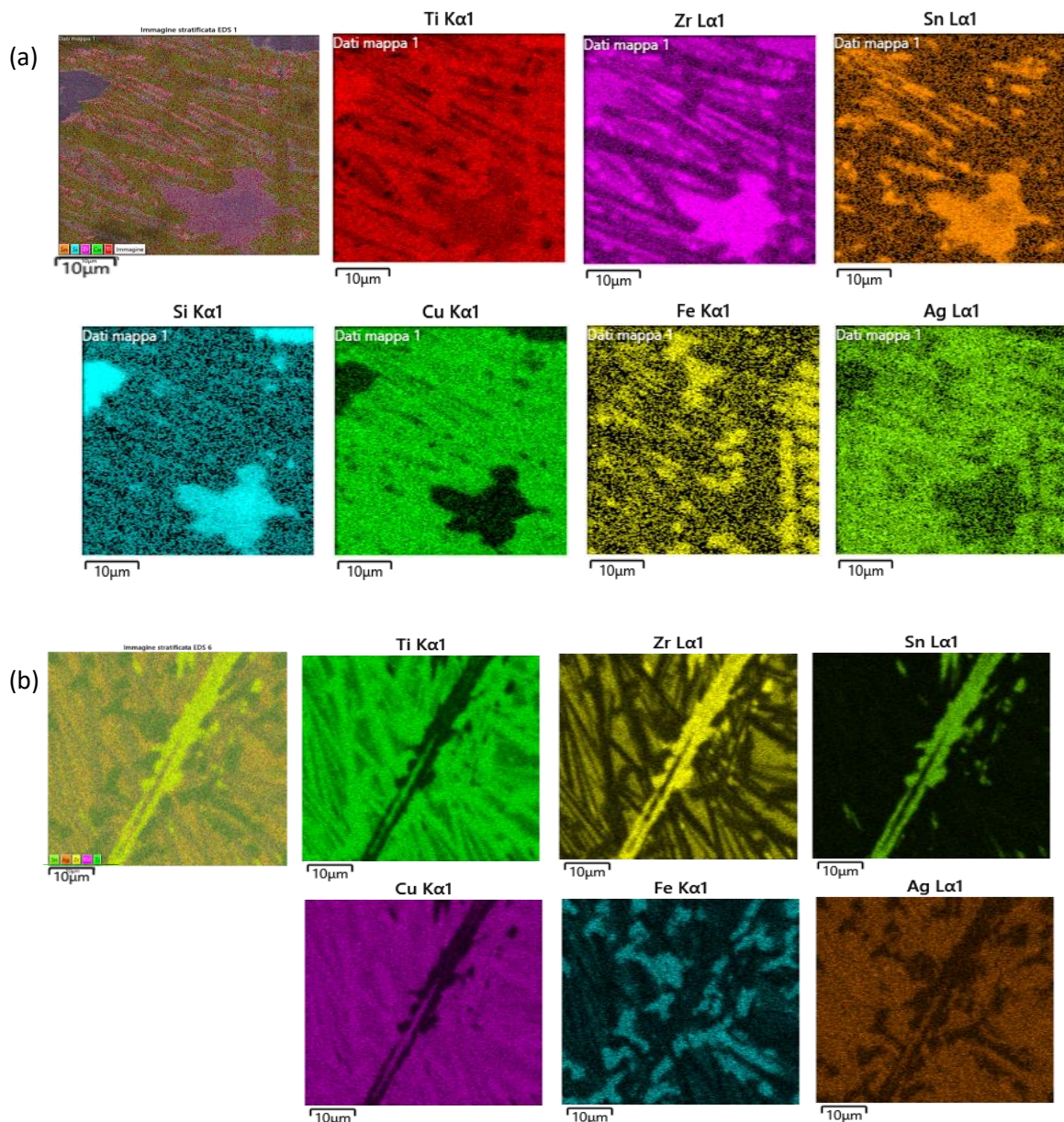


Figure 2.3. EDS color map of (a) $\text{Ti}_{42}\text{Cu}_{40}\text{Zr}_{8.5}\text{Fe}_{2.5}\text{Sn}_2\text{Si}_2\text{Ag}_3$ MA1 and (b) $\text{Ti}_{40}\text{Cu}_{40}\text{Zr}_{11}\text{Fe}_3\text{Sn}_3\text{Ag}_3$ MA2 alloy showing the distribution of the elements in the sample.

3.2 Characterization of as-quenched ribbons

The master alloys were melt-spun into ribbons using planar flow casting technique following parameters mentioned in Table 2.1. Subsequent analysis and comparison of all ribbon samples revealed consistent outcomes for the three ribbons derived from the MA2 composition. As a result, the data presented and discussed in this section pertains specifically to ribbon 3 of MA2.

The composition of as quenched $\text{Ti}_{42}\text{Cu}_{40}\text{Zr}_{8.5}\text{Fe}_{2.5}\text{Sn}_2\text{Si}_2\text{Ag}_3$ MA1 and $\text{Ti}_{40}\text{Cu}_{40}\text{Zr}_{11}\text{Fe}_3\text{Sn}_3\text{Ag}_3$ MA2 ribbons were investigated using inductively coupled plasma optical emission

spectroscopy (ICP-OES). The results reported in Table 2.3 confirm that the composition of the MA1 and MA2 melt-spun ribbons are in accordance with the nominal composition.

Table 2.3. ICP-OES analysis of $\text{Ti}_{42}\text{Cu}_{40}\text{Zr}_{8.5}\text{Fe}_{2.5}\text{Sn}_2\text{Si}_2\text{Ag}_3$ MA1 and $\text{Ti}_{40}\text{Cu}_{40}\text{Zr}_{11}\text{Fe}_3\text{Sn}_3\text{Ag}_3$ MA2 as quenched ribbon samples. Data estimated with the error of 0.01-0.20 %.

	Ti	Cu	Zr	Fe	Ag	Sn	Si
MA 1 [at %]	41.99	40.07	8.35	2.01	2.98	2.02	1.98
MA 2 [at %]	40.10	40.15	10.78	2.99	3.01	2.96	NA

The structure of $\text{Ti}_{42}\text{Cu}_{40}\text{Zr}_{8.5}\text{Fe}_{2.5}\text{Sn}_2\text{Si}_2\text{Ag}_3$ MA1 and $\text{Ti}_{40}\text{Cu}_{40}\text{Zr}_{11}\text{Fe}_3\text{Sn}_3\text{Ag}_3$ MA2 as quenched ribbons were analyzed using XRD. In Figure 2.4 (a) XRD spectra of MA1 showed low intensity crystalline peaks superimposed to the amorphous halo, due to the formation of hexagonal $(\text{Ti,Zr})_5\text{Si}_3$ ($P6_3/mcm$) phase [157]. EDS analysis of the crystalline phases showed the presence of Ti, Zr and Si in 50.2, 13.1, 31.0 at % respectively, confirming presence of $(\text{Ti,Zr})_5\text{Si}_3$ phase as shown in Figure 2.4 (a-c). Whereas MA2 ribbons showed a broad halo with absence of any diffraction peak indicating formation of fully amorphous ribbon.

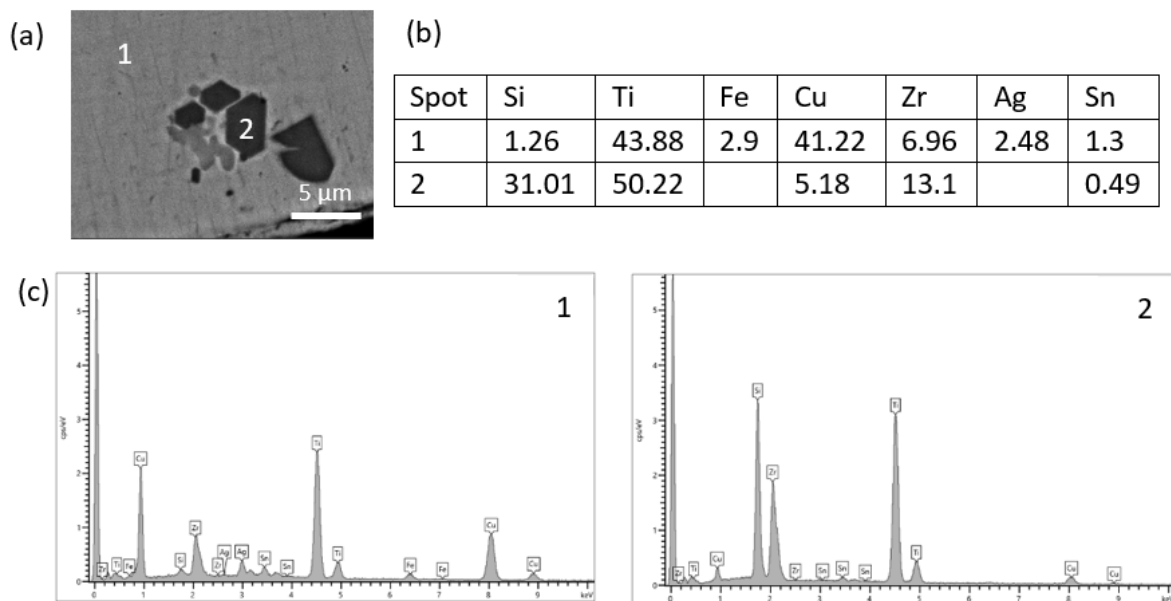


Figure 2.4. (a) SEM micrograph of MA1 ribbon cross section with crystalline phases embedded in amorphous matrix. (b) Table with EDS measurement of spot 1 and 2 observed in SEM micrograph. (c) EDS map of spots 1 and 2.

The thermal stability of $\text{Ti}_{42}\text{Cu}_{40}\text{Zr}_{8.5}\text{Fe}_{2.5}\text{Sn}_2\text{Si}_2\text{Ag}_3$ MA1 and $\text{Ti}_{40}\text{Cu}_{40}\text{Zr}_{11}\text{Fe}_3\text{Sn}_3\text{Ag}_3$ MA2 as-quenched ribbons was determined using DSC analysis as shown in Figure 2.5 (b). The two

DSC curves are nearly identical with MA1 composition showing thermal events at slightly higher temperature compared to MA2. The DSC trace of MA1 shows exothermic thermal events with presence of two crystallization peaks (T_x) with onset temperature of crystallization of T_{x1} at 426 °C and T_{x2} at 525 °C and glass transition temperature (T_g) was observed at 402.5 °C. The temperature interval of supercooled liquid region ΔT_x ($\Delta T_x = T_x - T_g$) was 23.5 °C. In the case of the DSC trace of MA2 two crystallization peaks were observed with onset temperature of crystallization of T_{x1} at 422.5 °C and T_{x2} at 509 °C. Glass transition temperature (T_g) was observed at 382 °C. The ΔT_x was 40.5 °C showing a higher thermal stability of the amorphous phase with respect to the MA1 ribbon. The ΔH value for first and second crystallization peak of MA1 was -22.5 J/g and -70.1 J/g respectively, in accordance with the ΔH values determined for MA2 -22.1 J/g and -70.9 J/g for first and second crystallization event respectively. The reduced glass transition temperature T_g/T_m and T_g/T_l for MA1 were 0.48 and 0.33 respectively and for MA2 were 0.47 and 0.34 respectively suggesting a promising GFA of the alloy compositions.

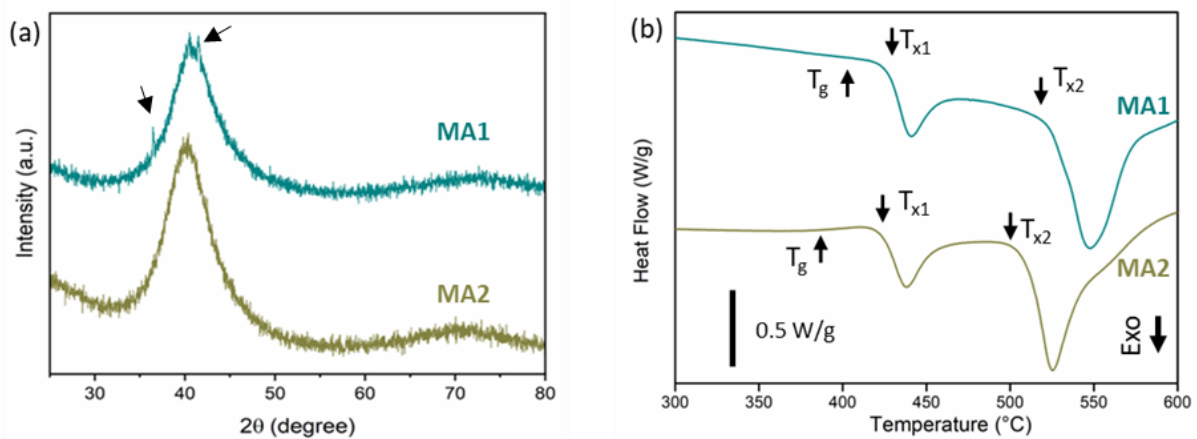


Figure 2.5. (a) XRD graph of as quenched ribbon of $Ti_{42}Cu_{40}Zr_{8.5}Fe_{2.5}Sn_2Si_2Ag_3$ MA1 and $Ti_{40}Cu_{40}Zr_{11}Fe_3Sn_3Ag_3$ MA2 (arrows showing crystalline peaks observed in MA1 ribbon), (b) DSC curve of MA1 and MA2 as quenched ribbon (arrows showing T_g , T_x).

The results obtained from MA2 composition were in agreement with the findings from studies in literature [120,158]. Addition of Sn and/or Si has contributed to beneficial effects for thermal stability and improved GFA due to their negative heat of mixing and atomic size mismatch with Ti [147,159]. However, MA1 composition resulted in formation of partially amorphous ribbons due to presence of titanium silicide $(Ti,Zr)_5Si_3$ phase. The formation of partially amorphous structure in MA1 could be due to incomplete melting of the titanium silicide in the master alloy during planar flow casting, due to the high melting temperature of this phase [160,161]. Due to the formation of partially amorphous ribbon with MA1 composition, only MA2 ribbons were further investigated for dealloying due to their fully amorphous nature, good GFA and thermal stability.

The dealloying treatments were performed on one specific side of the ribbon i.e., airside because morphology of the two sides differs during rapid quenching of the mater alloy. The

wheel side of the ribbon adapts to the roughness of the wheel and the gas that remains entrapped between the liquid melt and the wheel produces air pockets [162]. Compared to the wheel side, the air side has a slightly slower quenching rate, and it results in smooth and wavy morphology on the surface [163] as observed by SEM (Figure 2.6 a-b). The structure of the MA2 amorphous ribbon ($\text{Ti}_{40}\text{Cu}_{40}\text{Zr}_{11}\text{Fe}_3\text{Sn}_3\text{Ag}_3$ at %) was analyzed using XRD. Figure 2.6 (c) shows the XRD pattern with a broad diffraction peak on wheel side and air side, indicating formation of a fully amorphous structure. AFM images of air side of as-quenched ribbon sample is shown in Figure 2.6 (d). The average RMS roughness is 1.7 ± 0.7 nm.

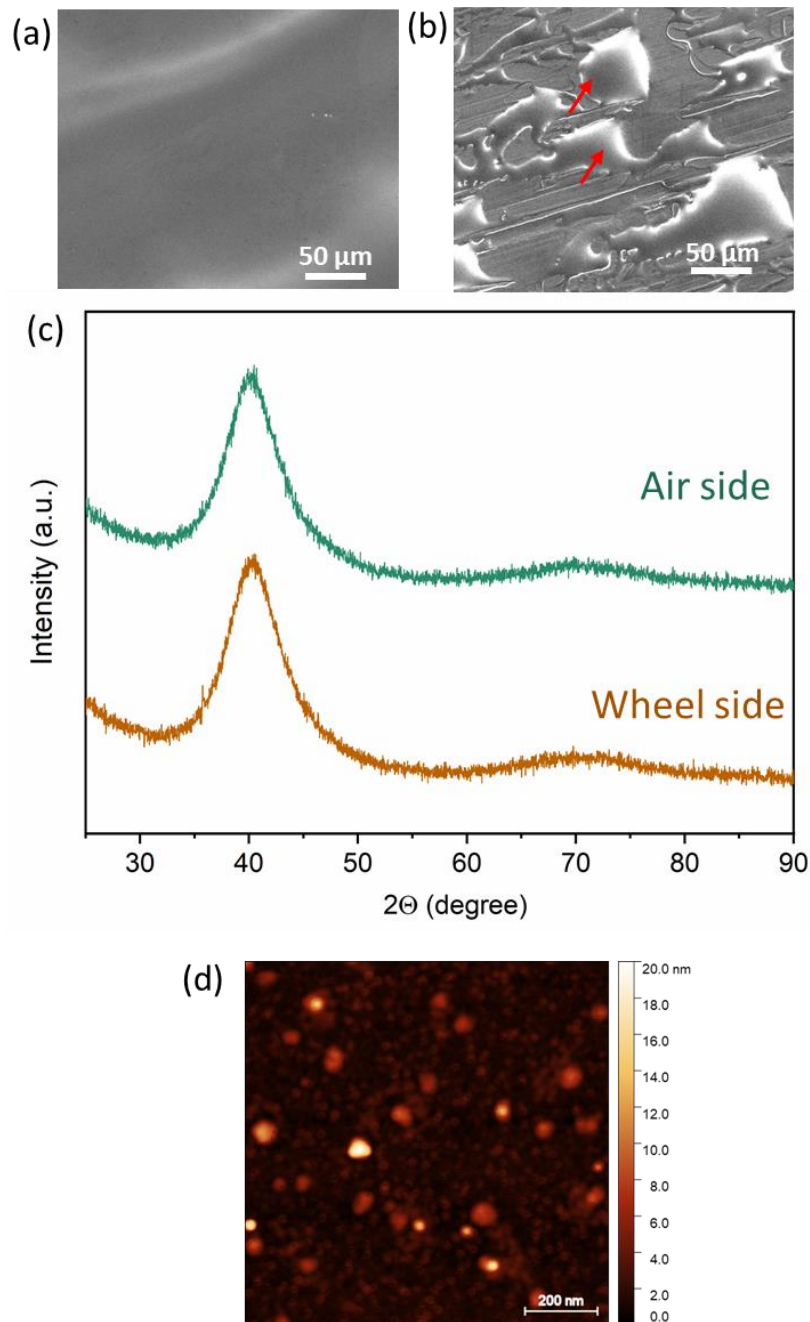


Figure 2.6. SEM micrographs of MA2 as-quenched ribbon showing (a) airside and (b) wheel side (arrows indicating air pockets). (c) XRD pattern air side and wheel side. (d) AFM image of airside of as-quenched ribbon sample with scan size $1 \times 1 \mu\text{m}^2$.

Conclusion

Two alloy compositions were investigated in this study. The $\text{Ti}_{42}\text{Cu}_{40}\text{Zr}_{8.5}\text{Fe}_{2.5}\text{Sn}_2\text{Si}_2\text{Ag}_3$ (MA1) composition consisting of Si resulted in formation of partially amorphous ribbons due to high melting temperature of titanium silicide rich phases which were formed during arc melting treatment. While $\text{Ti}_{40}\text{Cu}_{40}\text{Zr}_{11}\text{Fe}_3\text{Sn}_3\text{Ag}_3$ at % (MA2) composition showed formation of fully amorphous ribbons indicating a promising GFA with $\Delta T_x = 40.5^\circ\text{C}$. The formation of partially amorphous ribbon samples with MA 1 composition shows the possibilities of casting defects due to Si thus it is preferable to use MA 2 composition which resulted in the formation of fully amorphous ribbons.

Further developments regarding surface treatment using dealloying techniques were made on MA1 and MA2 ribbons. Figure 2.7 shows the schematic flow chart of dealloying treatment and parameters applied to the two developed amorphous alloys in this thesis. The results of dealloying treatments will be discussed in the next chapters.

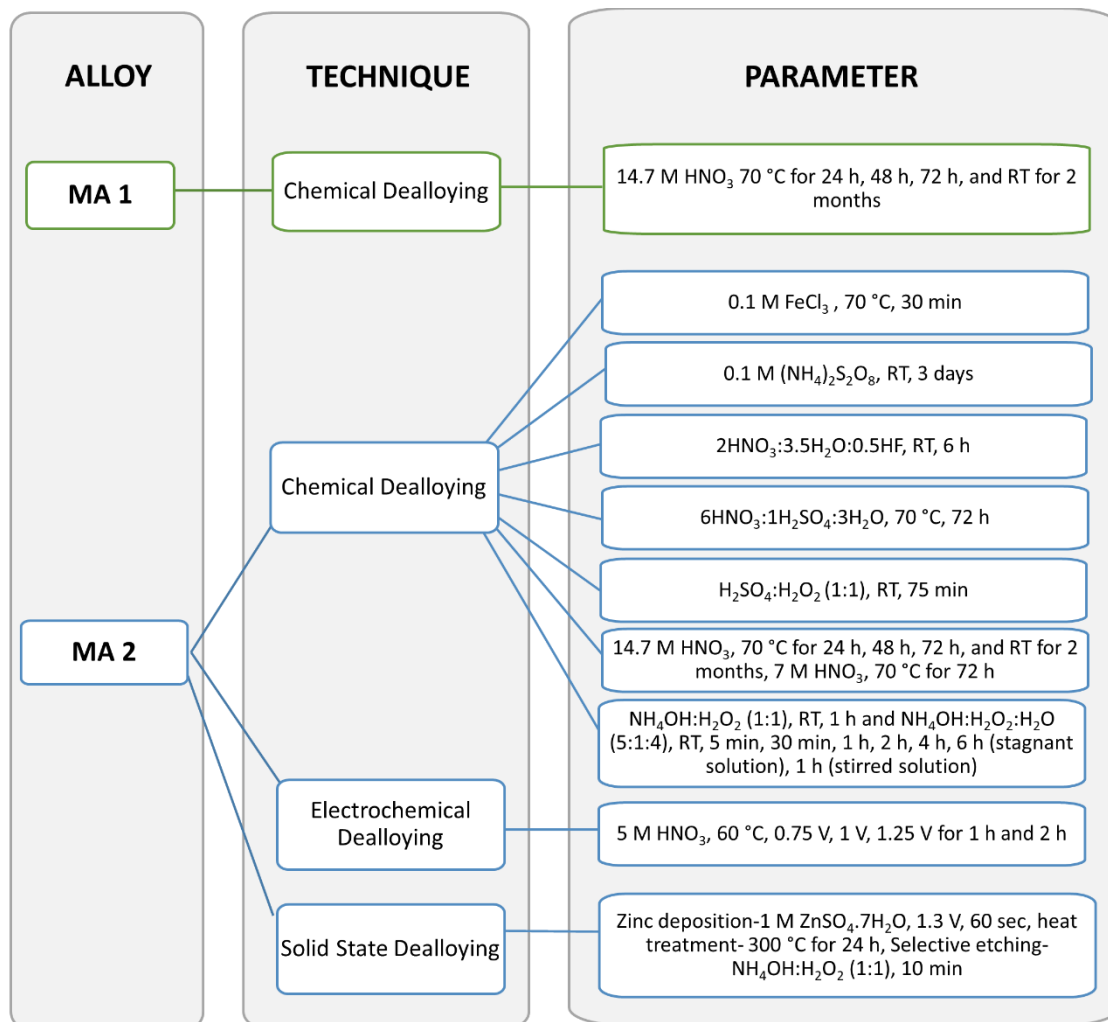
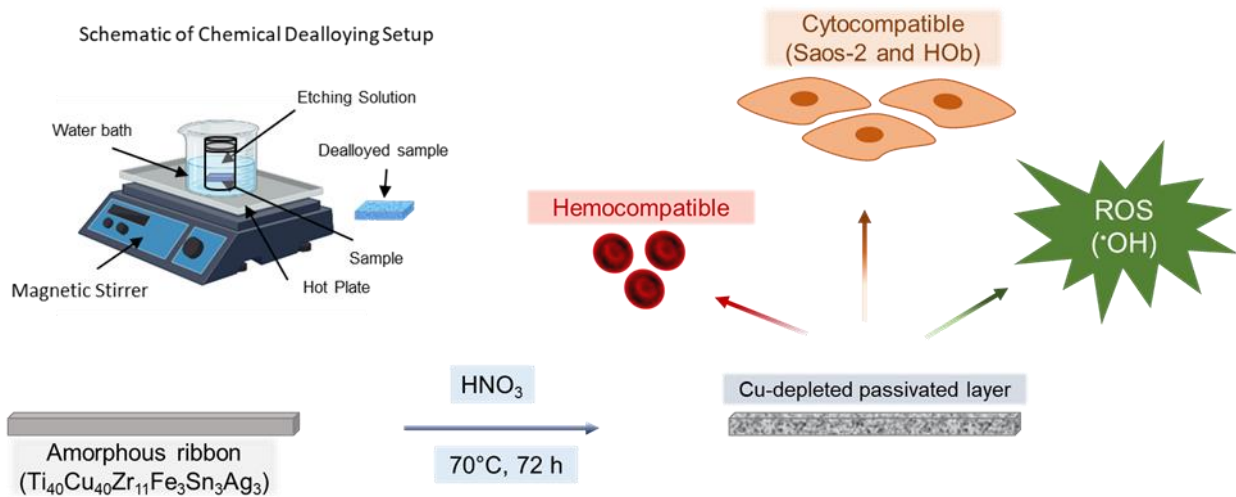


Figure 2.7. Schematic flow chart of dealloying treatment and parameters applied on $\text{Ti}_{42}\text{Cu}_{40}\text{Zr}_{8.5}\text{Fe}_{2.5}\text{Sn}_2\text{Si}_2\text{Ag}_3$ at %, MA1 and $\text{Ti}_{40}\text{Cu}_{40}\text{Zr}_{11}\text{Fe}_3\text{Sn}_3\text{Ag}_3$ at %, MA2.

Chapter III

CHEMICAL DEALLOYING USING VARIOUS ELECTROLYTES



Specific Aim

- To selectively etch Cu from the surface of the $\text{Ti}_{40}\text{Cu}_{40}\text{Zr}_{11}\text{Fe}_3\text{Sn}_3\text{Ag}_3$ at % amorphous ribbons and produce a patterned passivated surface rich in Ti and Zr oxides using chemical dealloying technique.
- Explore potential electrolyte combination for selective Cu etching and optimization of parameters for achieving tunability in surface composition and morphology.
- Analyze the biocompatibility of the treated ribbon samples involving hemocompatibility test, antimicrobial test: reactive oxygen species, biofilm growth and bacteria adhesion using *Pseudomonas aeruginosa*, cytocompatibility test using osteoblast cell lines (Saos-2 and Hob).

1. Introduction

Different strategies can be adopted for increasing the surface resistance to the bacteria adhesion and biofilm formation, such as non-adhesive surfaces, contact killing surfaces and antimicrobial agent releasing surface as discussed in chapter 1, section 3.5. In the present study, two strategies were adopted for developing the alloy and its antimicrobial properties: (i) the concentration of Ag and Fe was increased to enhance of the antibacterial activity by using a contact killing agent strategy and (ii) a modification of the surface morphology was optimized in order to hinder the adhesion of the bacteria to the surface. In this respect, surface modification of Ti-based alloys is widely attempted for increasing cytocompatibility, osseointegration, surface stability and controlled release of metal ion in the human body of implanted materials [164].

Chemical dealloying is a simple and less explored technique which can be used to produce unique morphology and surface properties [44,49]. Additionally, it can selectively remove harmful or undesirable elements such as Cu which is in high concentration in $Ti_{42}Cu_{40}Zr_{8.5}Fe_{2.5}Sn_2Si_2Ag_3$, MA1 and $Ti_{40}Cu_{40}Zr_{11}Fe_3Sn_3Ag_3$, MA2 alloy. While this technique is facile, it faces some challenges such as controlling the dissolution rate of each element in the alloy.

In this respect, it is important to carefully tailor the process parameters such as temperature, time, and composition of the electrolyte [52]. Several attempts have been made in literature to chemically/electrochemically treat Ti-Cu based alloys to etch Cu using ferric chloride, ammonium salts, hydrogen peroxide/sulphuric acid [165]. The reaction of nitric acid with Cu has been discussed widely in the literature [166–169]. S. Zhu et al. reported that dealloying of Cu from a $Ti_{40}Cu_{60}$ at % amorphous alloy, using nitric acid (13.14 M) at 70 °C resulted in the formation of a dealloyed layer with thickness around 3-5 μm . Additionally, the authors reported the formation of a Ti oxide rich layer on the sample surface [170]. In another study by S.L. Zhu et al. it is reported that a np layer on the surface of $Ti_{30}Cu_{70}$ at % amorphous alloy was produced by using 5.36 M of HNO_3 , at 1.0 V, for 3 h at 70 °C. The np layer thickness was 100 nm and it was composed of TiO, Ti_2O_3 , TiO_2 and Cu_2O [171].

The limited penetration depth in dealloying of Ti-Cu based amorphous alloys is usually observed due to the rapid oxidation of the surface which inhibits surface diffusion and removal of atoms. Due to such limitations, the Ti-Cu based systems are not prone to undergo complete dealloying in bulk as observed in gold, silver, and platinum alloys [44,56,172]. Therefore, it is possible to describe the process as *pseudo-dealloying* with a change that remains limited to a surface layer. Our recent work has demonstrated a strategy of electrochemical *pseudo-dealloying* of $Ti_{47}Cu_{38}Fe_{2.5}Zr_{7.5}Sn_2Si_1Ag_2$ metallic glass in an acidic solution to generate np oxide layers which improves the corrosion resistance of the treated surface in a synthetic body fluid compared to untreated surfaces [173].

Amorphous alloys with a combination of compositions (Ti, Cu, Zr) $_{92.5}Fe_{2.5}Sn_2Si_1Ag_2$ [121], $Ti_{47}Cu_{38-x}Zr_{7.5}Fe_{2.5}Sn_2Si_1Ag_2Nb_x$ ($x = 0, 1, 2$ at %) [136], $Ti_{47}Cu_{38-x}Zr_{7.5}Fe_{2.5}Sn_2Si_1Ag_2Pd_x$ (x

= 1, 2, 3, and 4 at %) [148] and $(\text{Ti, Zr, Cu})_{94.5}\text{Fe}_{2.5}\text{Sn}_2\text{Si}_1$ [120] have shown promising cytocompatibility with mouse MC3T3-E1 pre-osteoblast cell line indicating the potential of these compositions for biomedical implant application. It is important to consider the presence of Cu in these compositions. It is known that Cu is crucial for enhancing the glass forming ability of the Ti-based alloys [174,175], whereas its presence in high concentration can cause cytotoxicity, especially in long term implantation.

In a study by Lin et al. [176] the authors investigated ion release, corrosion behavior in hanks solution mimicking cell membrane potential, in vitro cytotoxic effects using mouse bone marrow stem cells and in vivo study on tibias of Sprague-Dawley rats using three different compositions of metallic glasses, $\text{Ti}_{45}\text{Zr}_{40}\text{Si}_{15}$, $\text{Ti}_{45}\text{Zr}_{40}\text{Si}_{10}\text{Cu}_5$, and $\text{Ti}_{45}\text{Zr}_{20}\text{Cu}_{35}$ at % containing different levels of Cu. The result showed that Ti, Zr and Cu ion release and associated cytotoxicity are dependent on the chemical composition of the metallic glasses. The absence or low levels of Cu in MGs exhibit excellent corrosion resistance in Hank's solution and low cytotoxicity. No inflammatory reaction was observed until 12 weeks of in-vivo study. However, the high-Cu metallic glass displays poor in-vitro cell viability (<80 %) due to ion release and pitting corrosion warranting further investigation for long-term biocompatibility.

Ti-based alloys and Cu oxides are known to generate Reactive Oxygen Species (ROS) through a mechanism that involves the Fenton-type reaction [177]. Redox-active metal transition ions, such as copper and iron, are likely responsible for reactivity in ROS generation. Besides chemical composition, other alloy properties such as surface roughness, porosity, mechanical properties, which affect the extent of the exposed surface and the corrosion resistance, may influence ROS generation [178]. The ROS produced by the material can damage bacteria membranes and hinder their attachment to implant surfaces, thus reducing implant rejection due to biofilm formation and increasing the biocompatibility of the material [179,180]. On the other hand, if ROS production is excessive, it may reduce cell adhesion and viability, possibly impairing osseointegration [181]. Indeed, elevated ROS levels can have detrimental effects on osteoblast activity, leading to a reduction in extracellular matrix synthesis and mineralization, and potentially osteoblast cell death.

Demonstrating the safety and cytocompatibility of these alloys is an essential prerequisite for their consideration as potential biomaterials for medical applications [182]. Therefore, in order to assess the biocompatibility of new Ti-based alloys it is of importance to evaluate the ROS production and cytocompatibility and to tailor the material surface morphology and chemistry to control mechanisms of cell damage. One of the requirements for implants in contact with blood is to not cause acute hemolysis, i.e., to be hemocompatible. For instance, 316 L-stainless steel and cp-Ti are considered hemocompatible, recent study comparing the two materials showed that Ti-8Mo-2Fe alloy did not cause hemolysis [183]. Ti-Nb-Zr-Si thin film metallic glass showed enhanced hemocompatibility with respect to the Ti6Al4V specimen [184]. Thus, Ti-based amorphous alloys appear as good candidates in terms of blood compatibility.

In this chapter, chemical *pseudo-dealloying* of $\text{Ti}_{42}\text{Cu}_{40}\text{Zr}_{8.5}\text{Fe}_{2.5}\text{Sn}_2\text{Si}_2\text{Ag}_3$ MA1 and $\text{Ti}_{40}\text{Cu}_{40}\text{Zr}_{11}\text{Fe}_3\text{Sn}_3\text{Ag}_3$ MA2 amorphous alloy is attempted using various electrolytes to improve biocompatibility and induce ROS production for an effective antibacterial activity.

The evolution of surface morphology was investigated for the most promising electrolyte by altering treatment parameters such as time and temperature. Further the wettability and release of ROS, such as hydroxyl radicals, was evaluated in a cell-free system. Additionally, hemocompatibility was measured using sheep's defibrinated blood, and cytocompatibility of the samples was studied using two human osteoblast cell lines (Saos-2 and HOb) to understand the applicability of these materials for implant application.

Surface characterization utilizing AES and FIB was performed at Leibniz-Institute for Solid State and Materials Research Dresden (Leibniz IFW Dresden), Dresden, Germany during my period abroad. The studies related to cytocompatibility were performed in Departament Biologia Cellular, Fisiologia i Immunologia, Universitat Autònoma de Barcelona, Spain during my period abroad. Additionally, the antimicrobial testing was performed in collaboration with School of Biomolecular and Biomedical Science, University College Dublin, Ireland.

2. Experimental Procedure

2.1 Chemical pseudo-dealloying attempts

Surface treatment of $\text{Ti}_{42}\text{Cu}_{40}\text{Zr}_{8.5}\text{Fe}_{2.5}\text{Sn}_2\text{Si}_2\text{Ag}_3$ MA1 ribbons were performed using 14.6 M HNO_3 at RT for 2 months and at 70 °C for 24, 48, 72 h using a water bath.

While $\text{Ti}_{40}\text{Cu}_{40}\text{Zr}_{11}\text{Fe}_3\text{Sn}_3\text{Ag}_3$ MA2 amorphous ribbons were treated using combination of different electrolytes. The electrolytes and parameters for chemical selective dissolution treatment are reported in detail below.

- i. 0.1 M FeCl_3 at 70 °C for 30 minutes (min).
- ii. Sulphuric acid (95 %, H_2SO_4) and hydrogen peroxide (30 %, H_2O_2) in 1:1 volume ratio at room temperature (RT) for 75 min.
- iii. 0.1M solution of ammonium per sulphate $(\text{NH}_4)_2\text{S}_2\text{O}_8$ at RT for 3 days.
- iv. Artificial Sea water at 70 °C for 10 days.
- v. Nitric acid (65 %), hydrofluoric acid (40 %) and deionized water in $2\text{HNO}_3:0.5\text{HF}:3\text{H}_2\text{O}$ vol ratio at 70 °C for 6 h (hours).
- vi. Nitric acid (65 %), sulphuric acid (95 %) and deionized water in $6\text{HNO}_3:1\text{H}_2\text{SO}_4:3\text{H}_2\text{O}$ vol ratio at 70 °C for 72 h.
- vii. 14.6 M HNO_3 at RT for 2 months and at 70 °C for 24, 48, 72 h using a water bath.
- viii. 7 M HNO_3 at 70 °C for 72 h using a water bath.

Before treatment, ribbon samples were ultrasonically cleaned for 5 min in acetone and ethanol followed by air drying and after the treatment samples were rinsed with deionized water for five times and dried at ambient temperature. In the case of samples etched with nitric acid, drying of the samples was performed using oven at 50°C for 12 h to ensure removal of residual electrolyte and water from the sample surface.

The morphology and chemical composition of treated ribbon was characterized using a TESCAN Vega 4, Scanning Electron Microscope (SEM) equipped with Ultim Max 40 mm² Oxford instrument electron dispersive spectroscopy (EDS). TESCAN S 9000 G Field Emission Scanning Electron microscope (FESEM) was used to analyze the morphology of the ribbons. The cross section of the sample was analyzed by in-situ cutting using a focused ion beam (FIB) inside the FESEM (FIB Helios 5 CX, Thermo Scientific). Image J software was used to calculate the pore diameter and ligament size of the treated ribbons.

Auger electron spectroscopy (AES) was used for determining the chemical composition of the sample surface. Additionally surface depth profiling of the samples was performed, using a JEOL JAMP 9500F with Ar ions of 1 keV at 30° angle. The sputtering rate was measured using a reference sample i.e., 6 nm/min (SiO_2 deposited on Si wafer). The AES measurements were

performed with 10 kV and 10 nA beam condition. All sample surfaces were sputter cleaned for 30 seconds (sec) prior to AES measurements to remove adventitious carbon contamination.

2.2 Wettability study

The wettability of the ribbons was analyzed using a Theta Lite optical tensiometer, Biolin Scientific Goniometer. The contact angle was measured on freshly prepared ribbons using 3 μL of deionized water in sessile drop mode after 1 sec of placing the drop. OneAttension software was used to measure the contact angle. This analysis was performed on the air side of the ribbons with a minimum of 3 measurements on each ribbon produced in triplicate.

2.3 Hemocompatibility study

The hemocompatibility of the ribbons (0.4×3 cm) was evaluated according to ISO-10993-4 (2017) standards [35], using defibrinated sheep blood (Microbiol Diagnostics). The blood was diluted with 10 mM phosphate buffer solution (PBS, Merck) in 4:5 ratio and calibrated using a positive control of 0.2 mL diluted blood in 10 mL of deionized water (Merck-Millipore). The absorbance of the positive control was adjusted to 0.9 - 1.0 by adding PBS or blood. The absorbance of the released hemoglobin (Hb) was measured at 540 nm using a UV/vis spectrophotometer (Uvikon, Kontron Instruments). A negative control with 10 mL of PBS and 0.2 mL diluted blood was additionally prepared. Commercially purchased Mg alloy (Mg93/Y4/Nd3 (WE43B, Goodfellow)), and quartz particles (Min-U-Sil 5, U.S. Silica, 200 cm^2/mL , and specific surface area of 5 m^2/g) were used as a positive reference material. Cp-Ti was used as a negative reference material. The samples were sterilized with 70 % ethanol, further washed with deionized water and PBS. The samples were immersed in 10 mL of PBS and pre incubated at 37 °C for 30 min. Further, 0.2 mL of diluted blood was added into test tubes and incubated at 37 °C for 60 min. After incubation, the solution of each tube was centrifuged at 500 g (Centrifuge Rotina 380R) for 5 min. The percentage of hemolysis was calculated using equation 3.1.

$$\% \text{ Hemolysis} = \frac{\text{Abs}(\text{test}) - \text{Abs}(\text{negative control})}{\text{Abs}(\text{positive control}) - \text{Abs}(\text{negative control})} \times 100 \quad (3.1)$$

Hemoglobin adsorption (Abs) by the samples was investigated using purified red blood cells (RBC). The absorbance of the hemolyzed blood was adjusted to 0.9 - 1 and a final volume of 10.2 mL of blood in PBS was frozen in the fridge at -20 °C overnight and defrosted to obtain lysed RBC. Then the solution was centrifuged at 10,000 g for 10 min. The supernatant solution containing Hb was recovered. The samples were incubated in the solution containing Hb for 60 min at 37 °C. After the incubation, the absorbance of the Hb was measured. The measurements were performed in triplicate.

2.4 Release of reactive oxygen species study

Generation of hydroxyl radical ($\cdot\text{OH}$) was evaluated using the spin trapping technique coupled with electron paramagnetic resonance (EPR) spectroscopy. In this study, we optimized experimental conditions to enhance the detection of surface reactivity in cell-free assays.

The samples were ultrasonically cleaned using acetone followed by 70 % ethanol for 10 min. Ribbon samples (0.4×1 cm) were immersed in 375 μL of 0.13 M H_2O_2 in phosphate buffer 0.33M (PB, Sigma-Aldrich), pH 7. The concentration of H_2O_2 mimics oxidative stress levels found in inflamed cells, exceeding typical concentrations in healthy tissues. The ribbons were incubated in a thermostatic shaker at 37 °C in the dark for 10 min. Following the incubation, an aliquot (180 μL) of the supernatant from each group was separated. The effect of 10 min contact with this oxidizing environment, which mimics what can be found in inflamed tissue, on the ability to generate $\cdot\text{OH}$ radicals was evaluated on both the supernatant and the ribbon samples. Then, 125 μL of 0.17M of 5,5-dimethyl-1-pyrroline-1-oxide (DMPO, Cayman Chemical Company), used as spin trap molecule, was added to the ribbons and the supernatant. The mixtures were again incubated in a thermostatic shaker at 37 °C in the dark. The final concentration of reagents in the solution was DMPO 0.07M, PB 0.2M and H_2O_2 0.06M, pH 7. The pH of 7 was chosen, instead of the more acidic pH usually found in inflamed tissues, to avoid a decrease in signals that can be observed at acidic pH due to the lower stability of DMPO. EPR spectra was recorded by collecting an aliquot of the solution in a capillary at time point (0), 10, 30 and 60 min of incubation. The kinetics of $\cdot\text{OH}$ radical release was studied until 60 min after DMPO addition, due to the rapid degradation of DMPO. Miniscope MS100 (Magnetech) with modulation of 1000 mG, scan range of 120 G, attenuation 7 dB and center of field at 3330 G was used for measuring EPR spectra. A negative control was prepared without the ribbon samples. All the measurements were performed in duplicates. The concentration of released hydroxyl radical was calculated by double integration of the EPR spectra using OriginPro 2023b software.

2.5 Metal ion release study

The ribbons (0.4×0.6 cm) were immersed in DMEM (Dulbecco modified eagle medium, Gibco, ThermoFisher Scientific) cell culture media without cells for 3 days at 37 °C for ion release study. Later aliquots of 1 mL were collected for analyzing ions released in the media using inductively coupled plasma mass spectrometry (ICP-MS) Agilent ICP-MS, model 7900. The study was performed with 3 replicates and compared with blank which was cell culture media without ribbon.

2.6 In vitro cytocompatibility study

The ribbons (0.4×0.6 cm) were sterilized using absolute ethanol for 5 min, and glass coverslips of 1.5 cm diameter were used as control. The experiments were performed in triplicate.

Two different cell lines were used in this study: the human Saos-2 infinite cell line, derived from a human osteosarcoma (ATCC collection), and the finite cell line HOb obtained from healthy human donors. Both cell lines were cultured in DMEM supplemented with 10 % (Saos-2 cells) or 20 % (HOb cells) of FBS (fetal bovine serum, Gibco) and incubated at 37 °C and 5 % CO₂. The ribbons were seeded with 50,000 Saos-2 cells per mL or with 20,000 HOb cells per mL in a 24 well plate.

The cytotoxicity of ribbons was evaluated on day 3 using live/dead kit for mammalian cells (Invitrogen) following manufactures protocol. Calcein was used to stain live cells (green) and ethidium bromide was used to stain dead cells (red). The stained ribbons were observed using an inverted fluorescent microscope (Olympus IX71). The images were processed using ImageJ software and percentage of cell viability was determined.

The morphology of the adhered cells to the ribbons at day 3 of culture was analyzed using FE-SEM (Merlin; Zeiss). The samples were rinsed with PBS and fixed in 4 % paraformaldehyde for 20 min at RT. The samples were later rinsed with PBS and dehydrated using gradient of ethanol ranging from 50, 70, 90 and 100 % for 10 min each. Finally, the samples were dried using hexamethyl-di-silazane (Electron Microscopy Sciences) for 10 min. The samples were sputter coated with gold before imaging.

Cell adhesion and cytoskeleton organization of cells growing on ribbons was investigated after 3 days in culture. The cytoskeleton was visualized by staining actin filaments using phalloidin. After incubation, the cells were fixed with 4 % paraformaldehyde for 20 min, followed by immersion in 0.1 % triton for 15 min and later in 1 % TWIN for 20 min at RT. Samples were then immersed in 1 % PBS-BSA for 20 min at RT. Further, cells were stained by immersing in a mixture of Phalloidin-Alexa 594 (ThermoFisher Scientific), and Hoechst 33258 (Sigma-Aldrich) for 1 h at RT. Finally, cells were washed with PBS and analyzed using confocal laser scanning microscope (CLSM, Leica SP5). The images were processed using Imaris viewer 9.9.1 software.

The alamar blue assay kit (Thermofisher Scientific) was used to investigate proliferation after day 1, 3, 7 of incubation of cells on ribbons. On day 1, ribbons with adhered cells were transferred to new wells. Then, samples were incubated in a mixture of cell media and Alamar blue reagent (10:1 dilution) for 4 h in dark condition at 37 °C and 5 % CO₂. A negative control without sample was prepared as a standard reference. After the incubation period supernatant was collected, and fluorescence was measured at 585 nm with excitation wavelength at 560 nm using a Varian Cary Eclipse Fluorimeter (Agilent Technologies, Santa Clara, CA, USA). The same procedure was performed on day 3 and 7 of cell culture. Media was changed after each time point of study. The data were normalized to day 1.

Cell differentiation was investigated by assessing the ALP (alkaline phosphatase) activity. The cells were incubated on the ribbon and after 7 and 14 days, the incubated cells were lysed in CyQuant cell lysis buffer (Thermo Fisher Scientific) by transferring the samples to eppendorf tubes and subjecting them to 10 min of lysis, followed by 10 sec of vortexing. The resulting cell lysates were then centrifuged at 12,000 rpm for 4 min at 4 °C, and the supernatants were

collected. To measure ALP activity, the hydrolysis of p-nitrophenyl phosphate (pNPP) was employed, leading to the production of p-nitrophenol (pNP). Specifically, 25 μL of 1-step pNPP (Thermo Fisher Scientific) was mixed with 25 μL of the collected supernatant. The absorbance at 405 nm was measured using a Nanodrop Spectrophotometer (Thermofisher Scientific).

2.7 Antimicrobial activity

2.7.1 Measuring biofilm formation

To investigate biofilm formation, gram-negative *Pseudomonas aeruginosa* (PAO1) was utilized. The bacterial inoculum was grown in Lysogeny broth (Sigma-Aldrich, LB media: 1 % tryptone, 0.5 % yeast extract, 0.5 % NaCl) in deionized water (H_2O). Prior to bacterial incubation, the samples (0.4×2 cm) underwent sterilization by immersion in 70 % ethanol, and each study was conducted with three biological replicates and two technical replicates.

Overnight cultures of *Pseudomonas aeruginosa* were grown overnight in 15 mL of LB media at 37 °C. Bacteria were quantified by diluting an aliquot 1:10 in fresh media and the optical density (OD) was measured at 600 nm using a spectrophotometer (Spectramax m384) Cultures were then equalized to 0.1 OD₆₀₀ cultures (10^7 CFU/mL) in preparation for incubation. The samples were then incubated without shaking in 1 mL of the equalized bacterial culture for 24 h at 37 °C in sterile 24-well, flat-bottomed, tissue culture-treated plates.

Following the incubation period, the samples were transferred to a new well-plate containing phosphate-buffered saline (PBS) solution and rinsed gently three times with PBS to remove non-adhered planktonic bacteria. Subsequently, the samples were dried at 37 °C for 30 min. 1 % crystal violet (CV) solution (1 mL) was added to each well and left at room temperature for 15 min. After staining, the ribbons were transferred to a new well-plate and rinsed three times with PBS and dried at 37 °C for 30 min. 1 mL of elution buffer (80 % ethanol and 20 % acetone) was then added to the wells and left at room temperature for 15 min. Afterwards, 1 mL of this elution was transferred to an optically clear plastic cuvette, and the OD of the solution was measured at 595 nm using elution buffer as blank providing a quantitative measurement of biofilm biomass.

2.7.2 Measuring bacterial adhesion

An overnight culture of *Pseudomonas aeruginosa* (PAO1) was grown in LB media. Subsequently, 2 mL of the culture was centrifuged in an Eppendorf tube at a speed of 3000 RPM for 15 min, leading to the formation of a visible pellet. The LB media was carefully discarded, and the pellet was resuspended in a 50/50 mixture of PBS and water to prevent osmotic stress. Soft pipetting was employed for resuspension. The mixture was subjected to another round of centrifugation, and the PBS-water combination was discarded. The pellet was completely resuspended in 1 mL of deionized water using soft pipetting.

The optical density (OD) for each Eppendorf tube was measured at 600 nm using a spectrophotometer, with deionized water as blank. Another Eppendorf tube was prepared for each biological replicate, with the OD equalized to 0.1 in deionized water. The required adjustments were made to ensure the uniformity of the samples.

The samples of amorphous ribbon before and after treatment were sterilized with 70 % ethanol and allowed to dry in a fume hood. After the drying process, 25 μ L of the equalized *Pseudomonas aeruginosa* (OD: 0.1) tube was added to the top of each sample and spread gently over the surface using a pipette. The samples were then left to dry for a period of 2 h in the fume hood. Once completely dried, the samples were fixed using a gradient of ethanol washes from 100-50 % and dried under ambient conditions. Cp-Ti and cp-Cu plates were used as control samples.

Surfaces were imaged before and after incubation with *Pseudomonas aeruginosa* using amplitude modulation atomic force microscopy (MFP-3D, Asylum Research) operated with Si probes (NCH, Nanosensors) having a nominal spring constant of 42 N/m and resonance frequency of 330 kHz. Representative images at 10 x10 μ m are shown from images collected in multiple locations. For presentation, images were flattened to remove sample tilt, horizontal correction was applied if required. All samples are shown with a uniform Z height scale of 400 nm with exception of cp-Cu that has a height of 800 nm due to its complicated topography.

2.8 Statistical analysis

Data are presented as the mean \pm standard error mean (SEM) unless otherwise stated. Normally distributed data were analyzed by one-way ANOVA or two-way ANOVA followed by Dunnett's or Tukey's post hoc test. A 95 % confidence interval was applied, and values with $P < 0.05$ were deemed statistically significant, unless otherwise stated. The GraphPad Prism 8.0.2 software was used for conducting statistical analysis.

3. Results and Discussion

3.1 Investigation and characterization of $\text{Ti}_{42}\text{Cu}_{40}\text{Zr}_{8.5}\text{Fe}_{2.5}\text{Sn}_2\text{Si}_2\text{Ag}_3$ MA1 ribbons treated using nitric acid

Chemical dealloying was applied to $\text{Ti}_{42}\text{Cu}_{40}\text{Zr}_{8.5}\text{Fe}_{2.5}\text{Sn}_2\text{Si}_2\text{Ag}_3$ MA1 partially amorphous ribbons. The treatment involved immersing ribbon samples in a 14.6 M HNO_3 solution at 70 °C for varying durations (24, 48, and 72 hours) and at room temperature (RT) for an extended period of 2 months. The analysis was focused on the airside of the ribbon due to its smooth morphology.

The SEM images revealed the emergence of crystals on the surface of treated ribbon samples after 24, 48, and 72 h, with the latter exhibiting prominent surface patterning (Figure a-c). The crystal dimensions ranged from 2 to 5 μm , and at low magnification, the 72 h sample surface displayed a significant distribution of these crystals (Figure 2.1 d). EDS analysis conducted on the crystals from the 72-hour treated sample indicated an enrichment of Ti, Zr, and Si (Figure 2.1 e).

The FESEM image of the sample treated at RT for 2 months (Figure 2.1 f) demonstrated the presence of nanostructures with crystals on the surface. AES analysis revealed an enrichment of Si and O on the surface, whereas Cu was significantly depleted from the surface and remained low in the subsequent sputter depth. Further, Ti and O showed an evident increase with sputtering into the depth of the sample, while Si decreased in the bulk. This suggests the formation of a mixed oxide of Ti, Si, and Zr. Subsequent sputter layers, especially after 100 sec, highlight the presence of titanium oxides. Consequently, it can be inferred that the crystals on the surface of treated samples are likely titanium silicide.

These findings underscore the challenges associated with employing a silicon-based composition for chemical dealloying treatment, leading to the discontinuation of $\text{Ti}_{42}\text{Cu}_{40}\text{Zr}_{8.5}\text{Fe}_{2.5}\text{Sn}_2\text{Si}_2\text{Ag}_3$ MA1 ribbons in this research work.

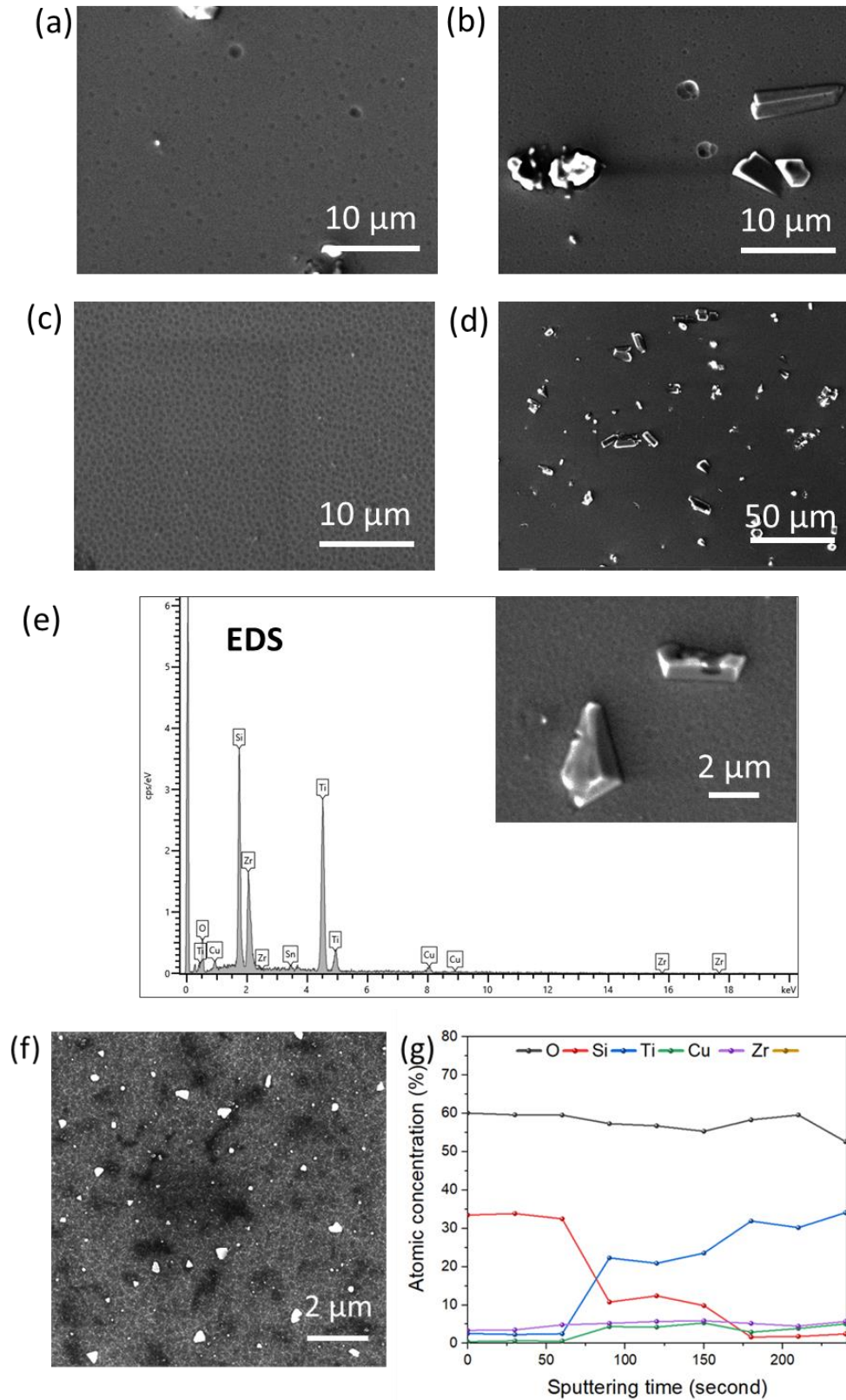


Figure 2.1. $\text{Ti}_{42}\text{Cu}_{40}\text{Zr}_{8.5}\text{Fe}_{2.5}\text{Sn}_2\text{Si}_2\text{Ag}_3$ MA1 partially amorphous ribbon samples treated using 14.7 M nitric acid at 70 °C for (a) 24 h, (b) 48 h, (c) 72 h (d) 72 h at low magnification showing

distribution of crystals on the sample surface, (e) EDS of crystal particles on 72 h rich in Ti/Zr and Si, (f) SEM and (g) AES of samples treated at RT for 2 months.

3.2 Investigation and characterization of $\text{Ti}_{40}\text{Cu}_{40}\text{Zr}_{11}\text{Fe}_3\text{Sn}_3\text{Ag}_3$ MA2 ribbon treated with various electrolytes

Treatment using ferric chloride, acid piranha, ammonium per sulphate, artificial sea water, hydrofluoric acid, sulphuric acid, nitric acid solutions were employed on $\text{Ti}_{40}\text{Cu}_{40}\text{Zr}_{11}\text{Fe}_3\text{Sn}_3\text{Ag}_3$ MA2 amorphous ribbons and the results are described in this section.

In order to create a morphology on the surface of the samples, various selective dissolution strategies were used. In the following the details of the obtained results are reported, with the description of the selective dissolution parameters and respective morphologies. The airside of the ribbon was analyzed throughout in this study due to its smooth morphology. The surface morphology and chemical composition of etched samples were analyzed using SEM and EDS techniques. The results are reported in Figure 3.1 and Table 3.1 respectively. Due to the limitation of EDS with quantification of light elements like C and O [185], the analysis was limited to the quantification of heavy elements detected on the sample surface after the selective dissolution process. While a qualitative analysis using EDS spectra was considered for light elements detected on the sample surface.

In Figure 3.1 (a) the SEM and EDS spectrum of the sample treated with 0.1 M FeCl_3 solution at 70 °C for 30 min is reported. The surface is composed of an oxide layer, confirmed by the presence of a high intensity oxygen peak observed in EDS spectrum. This result can be due to dissociation of ferric chloride in water to Fe^{2+} and Cl^- ions, which can later form CuCl_2 salt. EDS analysis in Table 3.1 showed presence of deposited corrosion products rich in Cl on the surface. Fe^{3+} can reduce to Fe^{2+} as shown in reaction (eq 3.2) [186] which when reacts with Ti can cause oxidation of Ti forming titanium oxide rich surface [187]. It is possible that metallic Ti is inert to ferric chloride while its passivation can hinder the selective dissolution of Cu from the sample surface.



Figure 3.1 (b) shows SEM and EDS of samples treated using 0.1 M ammonium persulfate ($(\text{NH}_4)_2\text{S}_2\text{O}_8$) at RT for 3 days. The surface has a morphology that can be associated with a general corrosion. As shown in reaction (eq 3.3-3.4), Cu reacts with ammonium persulfate to form copper sulphate, further the persulfate in the solution forms sulfate ions and oxidizes metallic copper to cupric ion [188]. The presence of sulphate ions can be detrimental to Ti, as it reacts with Ti leading to corrosion. The surface showed the presence of a pitting corrosion process, which lead to a depletion in Cu in the corroded areas (Table 3.1).



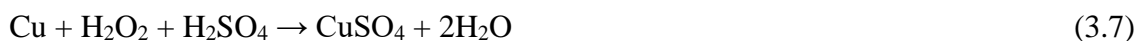
Figure 3.1 (c) shows SEM and EDS of samples treated using artificial sea water at 70 °C for 10 days. The surface of the treated samples shows presence of chloride salts and an oxide layer. Looking at the galvanic series of elements in sea water, Ti is stable in sea water while Cu is prone to corrosion. Therefore, a release of Cu ions can be expected during immersion in this electrolyte [189]. However, the SEM results of the treated surface showed presence of corrosion products which were rich in Cu and O, confirmed using EDS in Table 3.1.

Figure 3.1 (d) shows SEM and EDS of sample treated using a mixture of nitric acid and hydrofluoric acid in deionized water (2HNO₃:3.5H₂O:0.5HF vol ratio) at RT for 6 h. This electrolyte was used to prevent passivation of Ti using hydrofluoric acid [190] and simultaneously promote selective dissolution of Cu with nitric acid [170]. Fluorides show complexing action with Ti and Ti oxides forming soluble compound shown in reaction (eq 3.5-3.6) [191]. On the other side Cu undergoes dissolution with nitric acid. The results obtained after EDS analysis did not show significant reduction of Cu which could be due to insufficient control of the reaction kinetics therefore resulting in occurrence of general corrosion. The SEM images of the sample showed presence of white spots which were enriched in oxygen and slightly increased concentration of silver was detected with EDS in Table 3.1.



Another attempt was made using mixture of sulphuric acid and nitric acid (6HNO₃:1H₂SO₄:3H₂O vol ratio) at 70 °C for 72 h. In Figure 3.1 (e) SEM and EDS results are reported. Sulphuric acid dissolves Ti oxide layer at elevated temperature, thus allowing nitric acid to attack Cu. The reaction kinetics was fast and led to general corrosion. Rounded spots were observed on the sample, EDS analysis in Table 3.1 confirmed the spots were enriched in Cu. In addition, reduction in the sample dimension was observed after the selective dissolution treatment.

Figure 3.1 (f) shows SEM and EDS of sample surface treated using piranha solution (H₂SO₄:H₂O₂ vol ratio) at RT for 75 min. The surface shows homogeneously distributed porosities due to simultaneous dissolution of Ti and Cu indicating general corrosion. Cu reacts with the mixture of hydrogen peroxide and sulphuric acid to form copper sulfate salts which can further react with Ti as shown in reaction (eq 3.7-3.8) [192–194]. The EDS measurement in Table 3.1 showed depletion of Cu from the surface, whereas the white spots showed enrichment in oxygen. The presence of pits on surface of the sample indicates possible corrosion attack of SO₄²⁻ ions. The formation of pit indicates dissolution of Cu from the alloy.



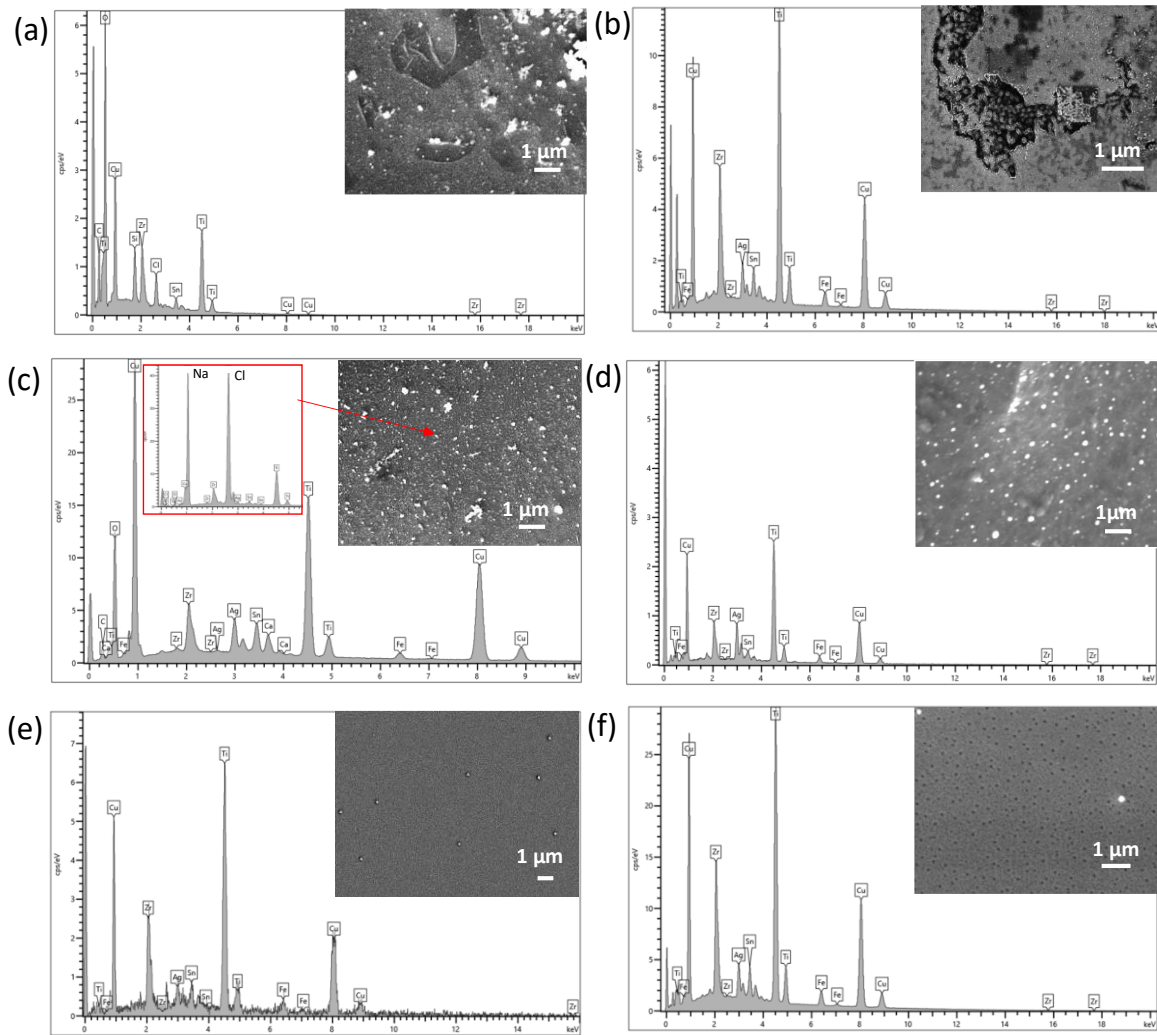


Figure 3.1. SEM micrographs and EDS elemental analysis of chemically etched $\text{Ti}_{40}\text{Cu}_{40}\text{Zr}_{11}\text{Fe}_3\text{Sn}_3\text{Ag}_3$ MA2 amorphous ribbon samples in (a) 0.1 M FeCl_3 at 70 °C for 30 min, (b) 0.1 M $(\text{NH}_4)_2\text{S}_2\text{O}_8$ at RT for 3 days, (c) artificial sea water, 70 °C, 10 days, (d) $2\text{HNO}_3:0.5\text{HF}:3\text{H}_2\text{O}$ vol ratio at 70 °C for 6 h, (e) $6\text{HNO}_3:1\text{H}_2\text{SO}_4:3\text{H}_2\text{O}$ vol ratio, 70 °C, 72 h, (f) $\text{H}_2\text{SO}_4:\text{H}_2\text{O}_2$ at RT for 75 min.

Table 3.1. EDS analysis of treated surfaces of $\text{Ti}_{40}\text{Cu}_{40}\text{Zr}_{11}\text{Fe}_3\text{Sn}_3\text{Ag}_3$ MA2 amorphous ribbon with quantification and error of 1 %.

S. No.	Parameter	Ti	Cu	Zr	Fe	Ag	Sn	O	Na	Cl	Site
1.	0.1 M FeCl_3 , 70 °C, 30 min	50	30	11	0	0	3	Y		7	White artifacts
		40	39	11	3	3	3				Surface
2.	0.1 M $(\text{NH}_4)_2\text{S}_2\text{O}_8$, RT, 3 days	41	38	11	3	3	3	Y			Corroded pits
		41	39	11	3	3	3	Y			Surface
3.	Artificial Sea Water, 70 °C, 10 days	32	51	6	2	4	5	Y	Y	Y	Corrosion products
4.	2 HNO_3 :3.5 H_2O :0.5 HF vol, RT, 6 h	41	38	9	3	6	2	Y			White artifacts
		40	40	10	3	3	3				Surface
5.	6 HNO_3 :1 H_2SO_4 :3 H_2O vol, 70 °C, 72 h	36	46	10	3	3	2				Rounded spots
		39	36	13	4	4	3				Surface
6.	H_2SO_4 : H_2O_2 (1:1), RT, 75 min	41	38	11	3	3	3				Surface

(Note: Y = Yes)

The aforementioned treatment proved ineffective in achieving *pseudo-dealloying*. Consequently, the ribbons underwent nitric acid treatment to explore the impact of temperature, solution concentration, and treatment duration on morphological evolution.

The study involved immersing the samples in a 14.6 M HNO_3 solution at 70 °C for 24, 48, and 72 h, as well as at room temperature (RT) for an extended period of 2 months. FESEM images of these treated ribbons are presented in Figure 3.2 (a-d).

This approach was aimed to enhance the efficacy of the treatment by varying key parameters and conditions to understand the effectiveness of nitric acid treatment compared to the previously attempted method.

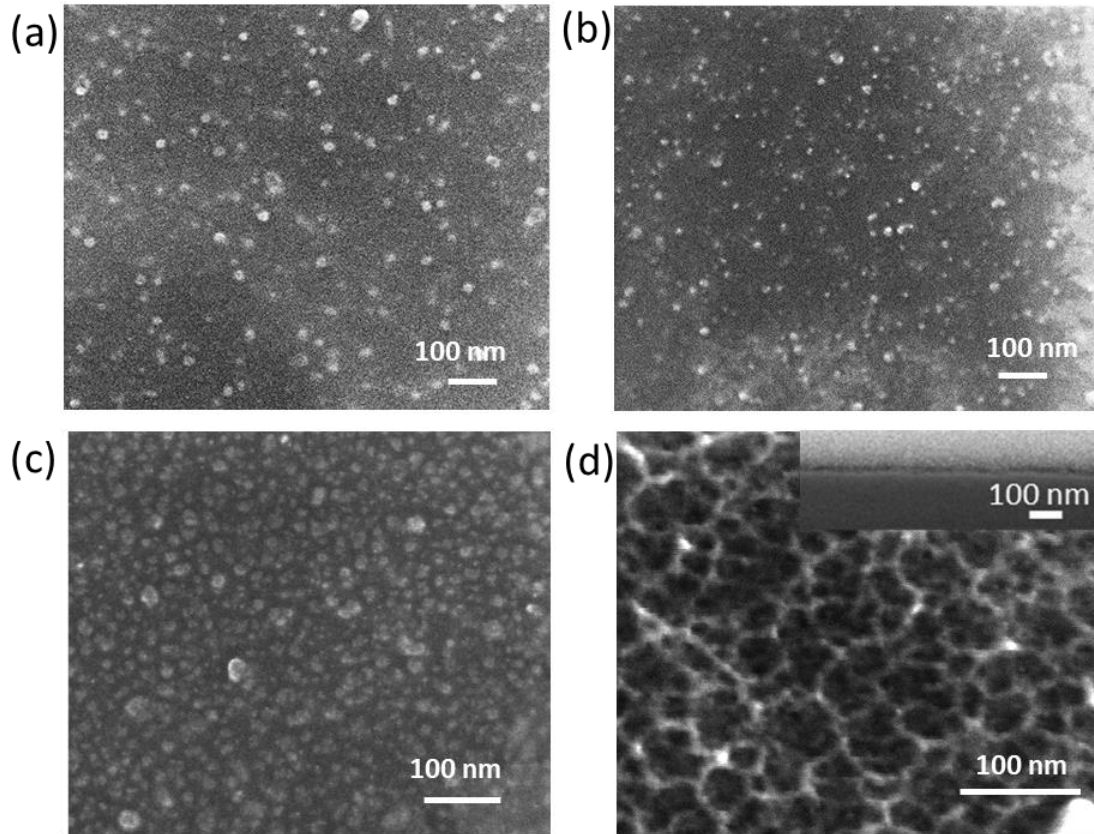


Figure 3.2. FESEM images of *pseudo-dealloyed* ribbon samples in 14.6 M HNO₃ for (a) 24 h, (b) 48 h, (c) 72 h at 70 °C and (d) FESEM and FIB cut (inset) of sample treated for 2 months at RT.

Under the conditions of elevated temperature (70 °C), surface morphology was examined through FESEM. The progression of immersion time correlated with the formation of distinct hilly and globular structures. Upon a 24 h treatment (Figure 3.2 a), small hills became apparent, and these features became more pronounced as the immersion time increased to 48 h (Figure 3.2 b). After 72 h (Figure 3.2 c), the surfaces displayed homogeneous and dense hilly structures, with an average diameter of 18 ± 3 nm and a separation distance of 27 ± 7 nm.

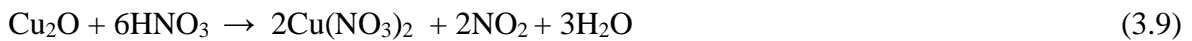
Additionally, the 72 h treated ribbons exhibited more pronounced island-like structures compared to the 24 h and 48 h treated ribbons. Conversely, the ribbon immersed at RT for an extended period of 2 months exhibited different surface morphology when compared to ribbons treated at elevated temperatures (Figure 3.2 d). This morphology was characterized by the presence of porosities with interconnected ligaments, which became evident upon high-magnification observation. Specifically, the 2 month immersed ribbon revealed ligaments with an average thickness of 8 ± 2 nm and pores measuring 22 ± 6 nm in diameter.

The observation suggests a temperature-dependent influence on the removal of Cu atoms from the surface. It was observed in literature, that surface diffusivity increases with increasing the temperature of the solution [195]. Hence it can be inferred that elevated temperature such as

70 °C facilitates the rearrangement of surface atoms through diffusion. This atomic rearrangement process leads to the formation of clusters that exhibit vertical growth, eventually culminating in the development of hilly surface structures. Conversely, when the ribbon is immersed in nitric acid at RT the slower rate of surface diffusion results in the creation of fine pores and interconnected ligaments.

The selective dissolution of Cu, as well as minor species such as iron (Fe) and tin (Sn), initiates from the ribbons surface. As shown in reaction I (eq 3.9-3.10), both copper and cuprous oxide react with nitric acid and oxidizes to Cu^{2+} generating copper nitrate that can be released in the electrolyte. The selective dissolution of Cu atoms from the surface enables the surface diffusion of remaining atoms, mainly Ti, at the surface-electrolyte interface, allowing the atoms to rearrange and modify the surface morphology. This selective dissolution process allows the remaining atoms of Ti and Zr to rearrange via surface diffusion at the surface-electrolyte interface. Notably, these exposed Ti and Zr atoms undergo simultaneous reactions with the surrounding medium, as shown in reaction II (eq 3.11-3.12) forming hydrated titania [196], which further decomposes to form stable titanium dioxide [197,198].

I. Reaction of copper in nitric acid



II. Reaction of titanium in nitric acid



Additionally, formation of brown gas within the sample holder was observed. The presence of this brown gas suggests the evolution of NO_2 gas (Figure 3.3), which is a noteworthy byproduct of the dissolution process [170]. Hereafter the as-quenched ribbon sample is referred to as “untreated ribbon” and ribbon treated for 72 h at 70 °C and 2 months at RT will be named as “Etched 72 h” and “Etched 2 months” respectively.

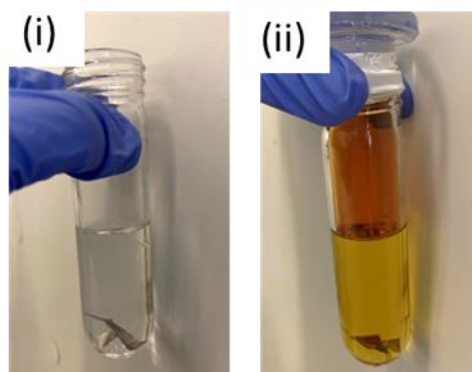


Figure 3.3. Immersed ribbon sample in 14.6 M HNO_3 (i) before and (ii) after treatment, indicating evolution of brown gas (NO_2) is observed for 72 h at 70 °C.

A concentration dependent investigation of 72 h etched sample was performed by using 7 M HNO_3 to understand the effect of solution concentration after 72 h of immersion time at 70 °C. The FESEM of sample treated with 7 M HNO_3 at 70 °C for 72 h shown in Figure 3.4 (a) low magnification, (b) high magnification. It is evident that change in the concentration of HNO_3 at 70 °C did not show significant difference in the surface morphology as compared to etched 72 h sample in 14.6 M HNO_3 (Figure 3.2 c).

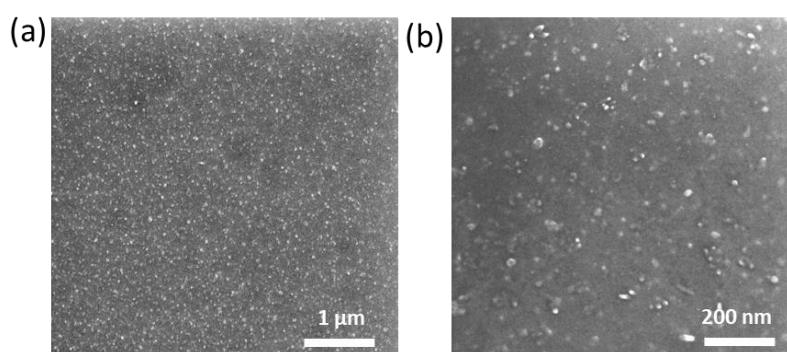


Figure 3.4. FESEM of sample treated with 7 M HNO_3 at 70 °C for 72 h at (a) low magnification, (b) high magnification.

Therefore, further surface analysis was performed on the 72 h treated sample and 2 months treated sample in 14.6 M HNO_3 . The chemical composition of the untreated and treated samples 72 h at 70 °C and 2 months at RT were analyzed using Auger Electron Spectroscopy (AES) to determine the chemical composition on the surface, along with sputter depth profiling using Ar ions (6 nm/min for SiO_2 reference sample).

The as-quenched ribbon sample (Figure 3.5 a) shows evidence of a native oxide layer on the surface of around ~7 nm thick composed of Ti, Cu and Zr. The 72 h treated sample (Figure 3.5 b) shows an enrichment in O, Ti and Zr on the surface, while Cu is significantly depleted with respect to the as-quenched ribbon, indicating the formation of a mixed oxide layer of Ti and

Zr. The content of Cu gradually increases until 125 seconds of sputtering time (i.e., ~12 nm thickness), while the oxygen is reduced till 150 s indicating that the layer formed due to *pseudo-dealloying* is about 15 nm.

A similar behavior is observed for the sample treated for 2 months (Figure 3.5 c) in which the surface shows an enrichment in O, Ti and Zr while Cu concentration is significantly depleted from the surface and gradually increases with the sputtering in depth. The oxygen is reduced in content and arrives to <3% at around 200 s, i.e., the layer formed by *pseudo-dealloying* is about 20 nm thick.

Figure 3.5 (d) shows quantified AES analysis of the sample surfaces. The ratio of Ti-Cu on untreated ribbon was 14:5 while for both treated samples was 8:1 indicating evident removal of Cu from the sample surface after treatment. The FIB cut of 2 months treated sample showed the delayed layer of thickness was approx. 20 nm (Figure 3.2 d) confirming the observations of AES study. Hereafter the as-quenched ribbon sample is referred to as “untreated sample” and samples treated for 72 h at 70 °C and 2 months at RT will be named as “Etched 72h” and “Etched 2 months” respectively.

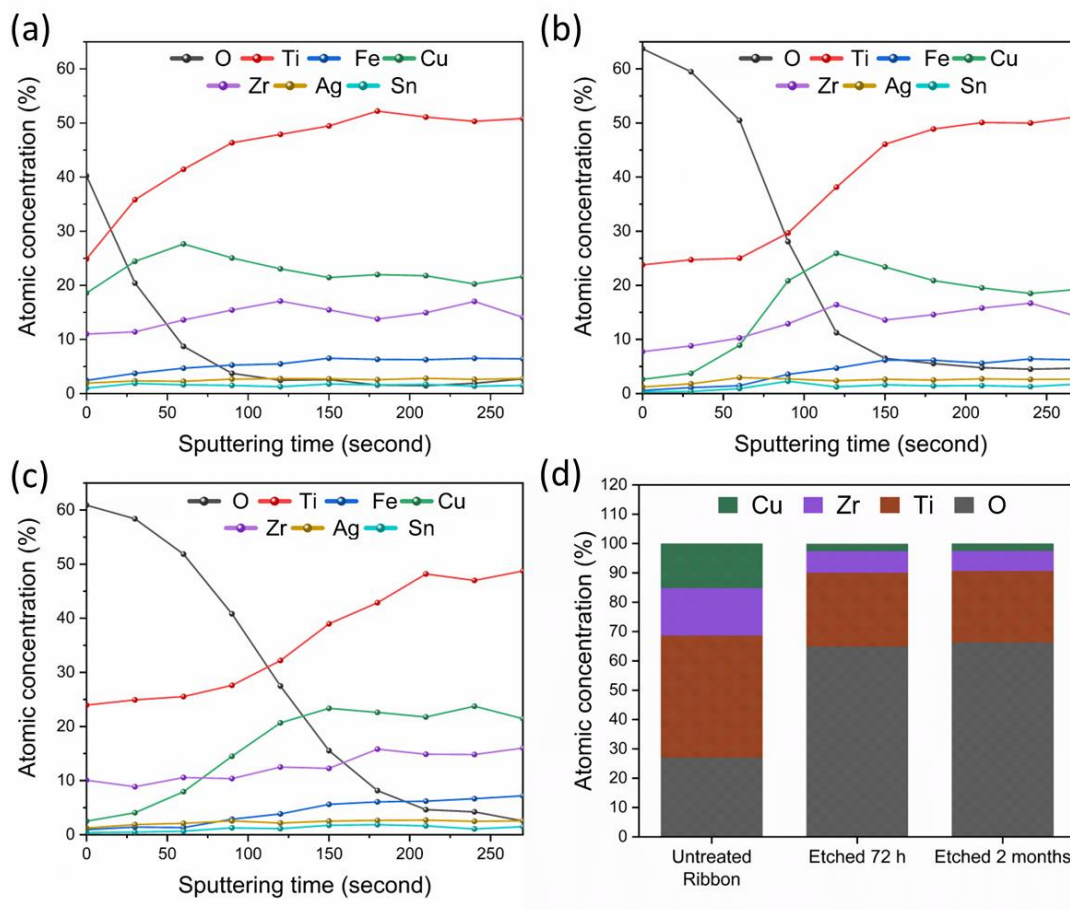


Figure 3.5. Auger electron spectroscopy (AES) measurements (a) depth profiling of untreated ribbon, (b) depth profiling of etched 72 h sample, (c) depth profiling of etched 2 months sample, (d) Quantified surface analysis of untreated, treated 72 h and 2 months sample for Ti, Cu, Zr, O elements (sputter rate 6nm/min).

3.3 Characterization and biocompatibility testing of *pseudo-dealloyed* Ti₄₀Cu₄₀Zr₁₁Fe₃Sn₃Ag₃ MA2 ribbon

3.3.1 Wettability study

The contact angle of untreated ribbon etched 72 h and etched 2 months ribbon was measured using 3 μ L of deionized water. Figure 3.6 shows that the wettability of the ribbons in water increases from hydrophilic for untreated ribbon (contact angle of 75°) towards hydrophobic for etched 72 h ribbon (91°) and etched 2 months in between. All contact angle values are in the range between 75°-91°, thus they follow Wenzel state of wetting which is the complete wetting of the rough surface with the liquid [199].

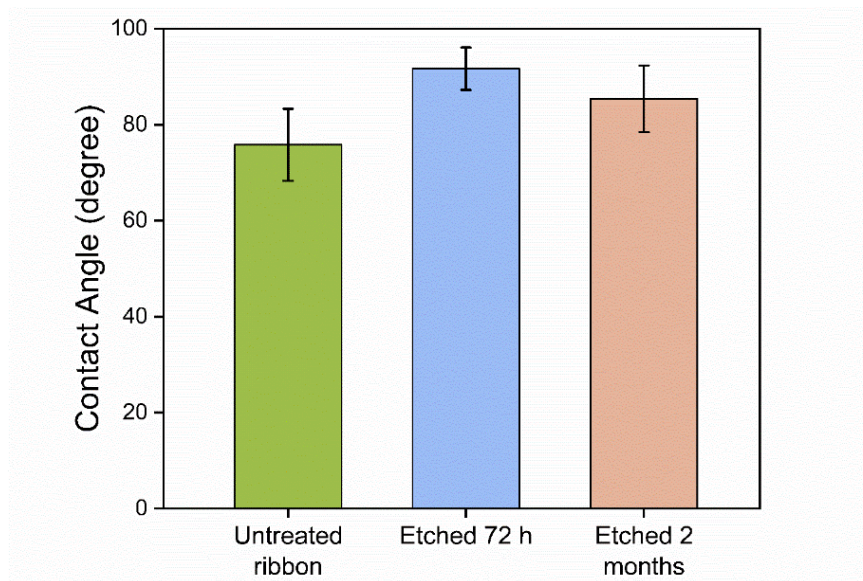


Figure 3.6. Contact angle measurement on untreated and treated ribbons with deionized water.

3.3.2 Hemocompatibility study

Hemocompatibility refers to the ability of an implant to interact with the blood cells without inducing an adverse reaction like hemolysis, which is the rupture of red blood cells [200,201]. The compatibility of the ribbons with blood is studied by evaluating the percentage of hemolysis using defibrinated sheep whole blood. Positive reference materials, i.e., quartz particles [202] and Mg alloy (WE43B) [203,204], and a negative reference material, i.e., cp-Ti [205] were included for comparison. ASTM F0756-17 (2017) considers material with percentage hemolysis less than 2 % as hemocompatible [206].

Untreated and etched 72 h ribbons showed a very low hemolytic activity, not significantly different from the negative control (i.e., only PBS) (Figure 3.7 a). Whereas Mg alloy showed 8 % and quartz particle 24 % of hemolysis indicating their significantly higher hemolytic activity. The ribbon samples before and after chemical *pseudo-dealloying* showed percentage

of hemolysis similar/lower than cp-Ti (i.e., 0.5 % of hemolysis), indicating a safe range of hemolysis for these materials.

Figure 3.7 (b) shows Hb adsorption on the ribbons with PBS as negative control. The ribbons did not show evident Hb adsorption, as the absorbance of all the ribbons was comparable to the negative control. The results point towards the ability of ribbons to exhibit hemocompatibility after the chemical *pseudo-dealloying* treatment and no significant interference due to adsorption of the Hb by the ribbons untreated and etched 72 h.

This result is in line with previous findings on Ti/Zr-based amorphous alloys compositions such as $Zr_{56}Al_{16}Co_{28}$, $Zr_{53}Cu_{33}Al_9Ta_5$, and $Ti_{60}Nb_{15}Zr_{10}Si_{15}$ (at %), which reported no evidence of hemolysis and high hemocompatibility [184,207,208]. Several properties of the alloy may affect hemocompatibility, including surface chemical composition, roughness, hydrophilicity/hydrophobicity [183,209]. In this specific case, the hemocompatibility of the etched 72 h was not affected by the variation of the ribbon surface after the treatment.

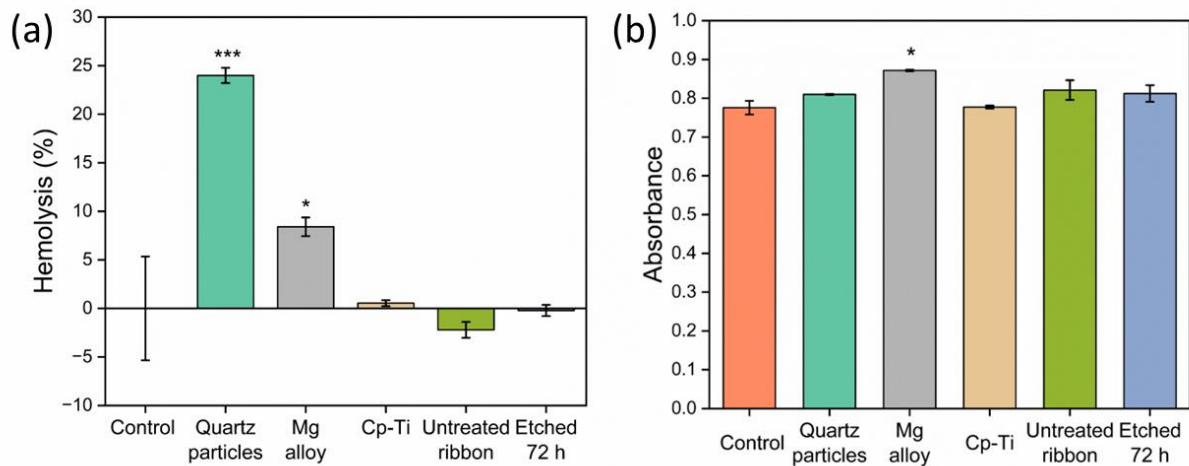


Figure 3.7. (a) Percentage of hemolysis of untreated and etched 72 h ribbon incubated with defibrinated sheep blood, and (b) hemoglobin adsorption on the ribbons. Quartz particles and Mg alloy are used as positive reference materials, while cp-Ti is used as negative reference material. Data are presented with mean \pm SEM of three independent experiments and were analyzed with one-way ANOVA, followed by Dunnett's post-hoc test, sample vs control. * $P < 0.05$, *** $P < 0.001$.

3.3.3 Release of reactive oxygen species study

The production of ROS from the surface of the implanted material can be of great importance because material-induced ROS can boost intracellular oxidative stress with intense membrane lipid peroxidation that may lead to cell death [210]. However, a limited production of ROS by the material can damage bacteria membranes, thus reducing biofilm formation and increasing

the biocompatibility of the alloy [211,212]. Therefore, the production of ROS was studied in a cell free media by mimicking cellular environment [213].

Untreated and etched 72 h ribbons were incubated for 10 min in PBS containing hydrogen peroxide to probe the release of hydroxyl radical when the ribbon samples were contacted in this oxidizing environment, which mimics what can be found in inflamed tissue. To unveil the mechanism of radical release, both the supernatant and the ribbon samples were assessed for hydroxyl radical generation by using the DMPO spin trap molecule.

DMPO is used to trap the released hydroxyl radical to form DMPO-OH adduct, which is measured using EPR spectroscopy as shown in Figure 3.8 (a). The kinetic of DMPO-OH adduct formation was studied over a time of 0, 10, 30, and 60 min after adding DMPO. The test groups for instance in case of untreated sample were named as “Untreated: ribbon” and “Untreated: supernatant” and a similar terminology was used for etched 72 h sample. The results are shown in Figure 3.8 (b).

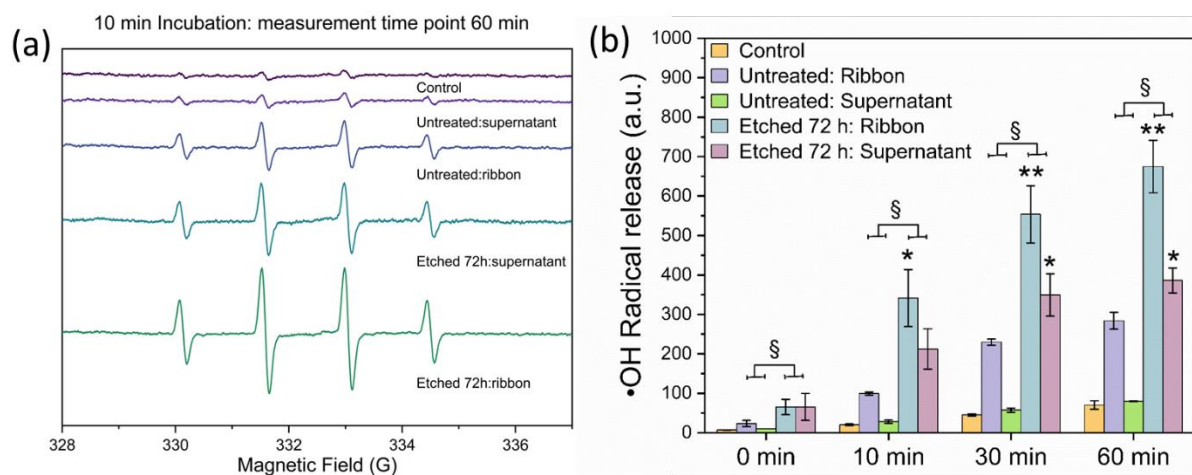


Figure 3.8. (a) EPR spectra of hydroxyl radicals (DMPO-OH) measured in untreated and etched 72 h: supernatant and ribbon sample after 60 min of adding DMPO to samples incubated for 10 min, (b) Hydroxyl radical release after 10 min incubation of untreated and etched 72 h samples. The kinetic of DMPO-OH adduct formation was monitored over a time of 0, 10, 30, 60 min after adding DMPO. Radical release is calculated by double integration of the EPR spectra. Data are presented with mean \pm SEM of two independent experiments and were analyzed with one-way ANOVA followed by Dunnett’s post-hoc test, sample vs control, * $P < 0.05$, ** $P < 0.01$. Two-way ANOVA was applied to compare (i) untreated vs etched 72 h, (ii) ribbon vs supernatant. P value of untreated vs etched 72 h samples: § $P = 0.04$; ribbon vs supernatant: not significant difference.

The results indicate that the production of hydroxyl radical is significantly higher for the etched 72 h than the untreated sample, both for the ribbon and the supernatant. Moreover, for both untreated and etched 72 h, the production of hydroxyl radicals was higher for the ribbon samples than only the supernatant. For the ribbon samples, the kinetic of DMPO-OH formation

increased linearly with the incubation time. These results indicate that both the material surface and the transition metal ions leached from etched 72 h ribbon during 10 min incubation contribute to the production of $\cdot\text{OH}$ radical.

It is worth considering that the generation of free radicals may be attributed to two possible mechanisms:

(i). **The presence of copper:** species could be trapped at the near surface region of the sample due to passivation of Ti/Zr rich sample surface. Similar observation reported for $\text{Au}_{40}\text{Cu}_{28}\text{Ag}_7\text{Pd}_5\text{Si}_{20}$ amorphous alloy wherein elements such as Cu, Ag and Pd were trapped in the ligaments [48,172]. This hypothesis gains support from the observed release of Cu ions from the etched 72 h sample discussed below in section 3.7. Furthermore, it is important to recognize that, although the reactivity of ions is greatly influenced by the nature of the matrix in which they are found [214] and by the environmental pH, isolated transition metal ions are often more chemically reactive than cluster ions. This has been observed for Fe [215] and Cu ions [214,216,217]. In this context, the accessible Cu species present on the sample surface etched for 72 h could potentially be responsible for the observed increase in ROS.

(ii). **The presence of surface layer rich in titanium oxide:** The reactivity of TiO_2 in releasing $\cdot\text{OH}$ radicals under irradiation has been extensively studied and it is well known. In recent years, research on the reactivity of TiO_2 in "dark" conditions has also grown steadily but, to date, only a few studies highlighted the release of $\cdot\text{OH}$ radicals in solution by Ti-based materials [218]. Recently, Liu and colleagues reported that a TiO_2 nanostructured surface similar to an urchin can in situ reduce Ti^{4+} to Ti^{3+} in the presence of H_2O_2 to generate hydroxyl radicals in the dark [219]. Similarly, Sanchez and colleagues (2013) detected hydroxyl radicals and hydroperoxides in a $\text{TiO}_2/\text{H}_2\text{O}_2$ suspension not exposed to light [220]. Besides the presence of Ti(III) ions that can undergo the Fenton reaction [177,178], the $\cdot\text{OH}$ release in absence of light, may be ascribed to complexation of H_2O_2 on surface with Ti(IV) leading to generation of hydroperoxyl radicals ($>\text{Ti III}-\cdot\text{OOH}$), through an inner-sphere electron transfer. The surface generated hydroperoxyl radical can further decompose to produce $\cdot\text{OH}$ radicals (eq 3.13) [221–224].



3.3.4 Metal ion release study

Non biocompatible specimens that shows Cu released from the surface of an implanted material in a limited concentration can contribute to the antibacterial activity of the surface while in high concentration, Cu ions can cause toxicity [225,226]. Examples reported in literature show that 46 $\mu\text{g}/\text{mL}$ Cu ions release resulted in LD50 value (lethal dose which kills 50 % of the test population) for L929 fibroblasts, with nearly complete cell mortality observed at 100 $\mu\text{g}/\text{mL}$ [227] and a LD50 value of 18.4 mg/L Cu ions was observed for peripheral blood mononuclear cells (PBMCs) [228]. Therefore, it is of interest to investigate the ion release of the modified alloy in a cell culture media that mimic the environment of an implanted prosthesis allowing

to detect the release of ions and to connect their concentration to the biocompatibility of the alloy.

Release of metal ions from the untreated and etched 72 h ribbon after 3 days of incubation in the cell culture media was measured using ICP-MS. The Cu ion released from untreated ribbons was 0.15 ± 0.09 mg/L, while 72 h ribbon was 0.06 ± 0.01 mg/L. It can be observed that untreated ribbon showed relatively high release of Cu ions.

It is important to note that the data of Cu release from the surface of the untreated ribbons show high discrepancy among samples indicating the irregularities on the surface contributing to different amount of Cu ion release, while the etched 72 h ribbon show higher consistency in the Cu ion release from the surface. If compared to the literature data, it is possible to note that the amount of Cu ions released from the surface is far below the concentration reported to be lethal for cells. Therefore, it can be inferred that the limited Cu released can be helpful in the antibacterial activity while not detrimental for the cell adhesion to the surface.

3.3.5 In vitro cytocompatibility using Saos-2 and HOb cells

Cytocompatibility investigation was performed on untreated and etched 72 h samples using Saos-2 and HOb cell lines. During cell culture, cells adhere and spread to the sample surface by forming focal contacts. As a general mechanism, in the initial stage they form a passive contact with the substrate or extracellular matrix (ECM) which later changes to complete spreading due to actin polymerization and distribution.

In the first step of cytocompatibility analysis, the ribbons (untreated and etched 72 h), cultured with Saos-2 cells were stained using calcein (green) for live cells and ethidium bromide (red) for dead cells after 3 days of incubation (Figure 3.9 a). Results showed that cell viability of all samples was above 98 %. In addition, the number of adhered live cells was higher on untreated ribbon with 63146 ± 6479 cells/cm², followed by etched 72 h sample with 55880 ± 3433 cells/cm² and then on glass control with 46466 ± 10070 cells/cm². These cytotoxicity results indicated that, despite the 40 at % Cu content in the nominal composition of the amorphous ribbon, no cytotoxic effect was observed for both untreated and etched samples. Copper is generally considered a toxic element and several authors have reported its deleterious effects on cell viability [229]. However, the potential cytotoxicity of copper is reduced when it is alloyed. Several studies have observed that osteoblasts can grow on alloys containing 38 at % of Cu without showing any deleterious effect nor cytotoxicity [230]. Moreover, as described previously, the Cu released from the surface is limited and, therefore, it can be considered as not harmful for cells.

The morphology of the cells growing on samples showed the cell-material interaction and cell spreading. Cell morphology was studied using SEM after 3 days in culture. SEM images (Figure 3.9 a) showed that osteoblasts were adhered to the surface analyzed exhibiting a flat

appearance indicating good attachment. While in the untreated ribbon the presence of few rounded cells was detected, in the etched 72 h samples nearly all the cells were well spread on the surface with filopodia extensions in various directions and several nucleoli in the nucleus of the cells were observed indicating cell activity. The orientation and cytoskeleton distribution of the adhered cells were observed using CLSM (Figure 3.9 a). Phalloidin was used to stain cytoskeletal actin fibers in red and nuclei were counterstained in blue. Well defined actin stress fibers cross linked in the cytoskeleton of the cells were observed for all samples as a sign of good cell adhesion. The adhesion and morphology of cells growing on biomaterials is influenced by surface topography and wettability. Regarding the topography of etched 72 h samples, the topography showed hilly structures with a diameter of 18 ± 3 nm and distance between hills of 27 ± 7 nm. The nano roughness did not have any impact on cell adhesion and morphology. In addition, the contact angle of the treated ribbons was 91° . It is generally considered that the threshold for hydrophobicity is 90° , so although the value is above the threshold to be considered hydrophilic, the results indicated that cells were able to spread on treated ribbons [231].

Figure 3.9 (b) shows results on cell proliferation on the sample surface after 1, 3 and 7 days of incubation. Significant differences were observed between etched 72 h ribbons and untreated ribbons at 3 days incubation; however, no differences were found after 7 days in culture. After analyzing the proliferation of Saos-2 cells, the ability of cells to differentiate on samples was studied. To that end, ALP activity of osteoblast grown on ribbons was quantified after 7 and 14 days in culture (Figure 3.9 c). After 7 days, the ALP activity was high on all samples without significant differences between samples. However, similar values were observed after 14 days in culture, indicating that ALP activity reached its maximum at day 7. The quantitative results for proliferation and ALP activity indicated that Saos-2 cells were able to grow and differentiate on both untreated and etched 72 h samples.

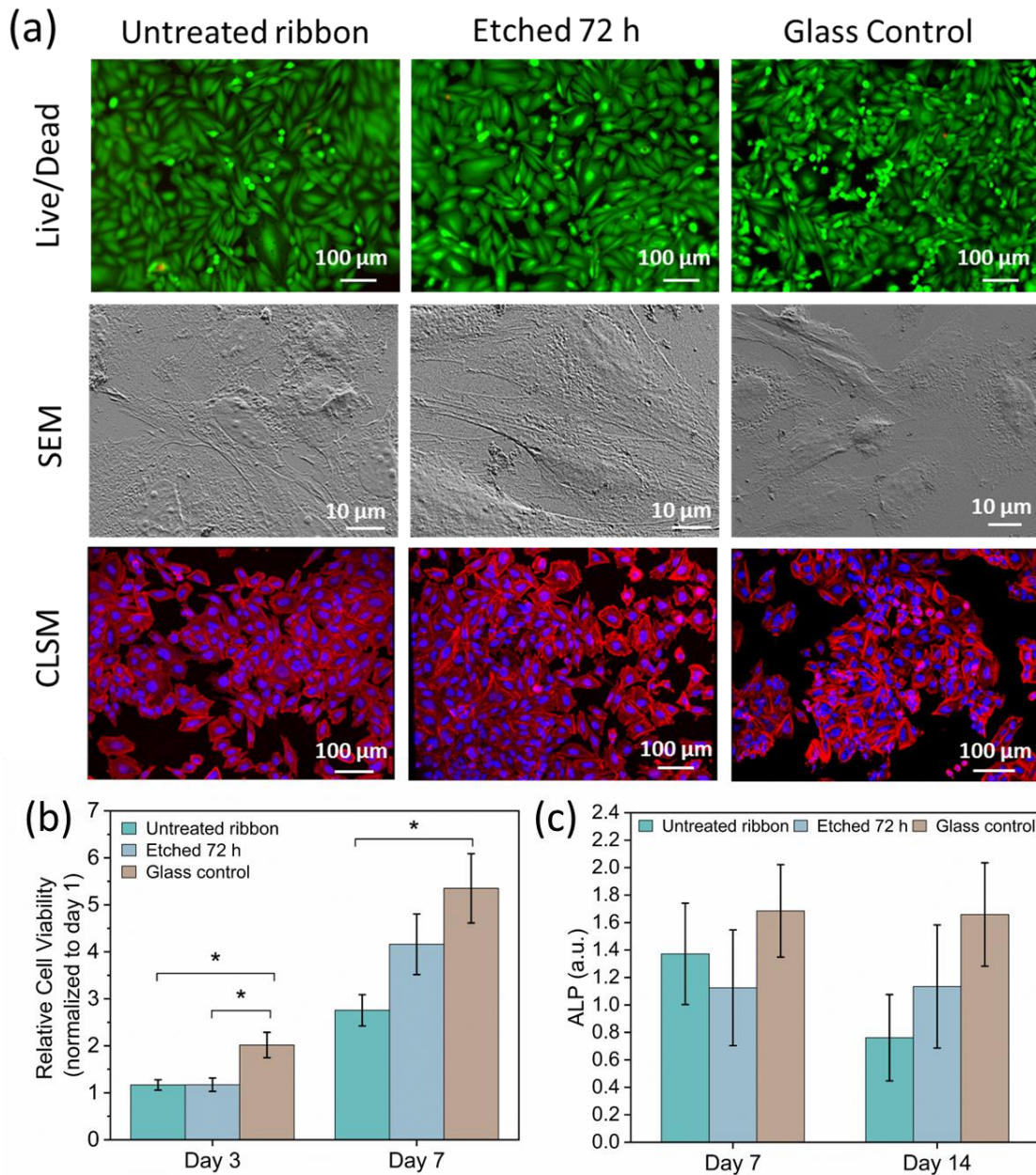


Figure 3.9. (a) Representative images of Saos-2 cells grown on untreated ribbon, etched 72 h, glass control stained using calcein (live/ green) and ethidium di-bromide (dead/ red), SEM images of adhered cells showing the flat morphology, CLSM images of cells showing actin distribution (stress fibers/ red) and nuclei (DNA/ blue), (b) Cell proliferation measured using Alamar Blue after 1, 3, 7 days of culture, (c) ALP activity measured after 7, 14 days of culture. Data are represented with mean \pm SEM of three independent experiments and were analyzed with one-way ANOVA, followed by Tukey's test for multiple comparison. *P < 0.05.

The same experiments previously performed on Saos2 cells were done on HO b cells. In this case, the cells were not derived from a tumor but isolated from healthy donors. The cytotoxicity, cell morphology, and cell adhesion of HO b cells after 3 days of incubation is shown in Figure 3.10 (a). Live and dead cells were evaluated on the samples after 3 days of

culture. The samples showed cell viability above 96 %. The number of live cells were similar on etched 72 h sample with $15,950 \pm 3,859$ cells/cm², glass control with $13,194 \pm 2,244$ cells/cm² and untreated ribbon samples with $10,423 \pm 2170$ cells/cm². SEM images show that cells were well adhered to the sample surface. The filopodia were distributed in all directions indicating good cell spreading on the sample surface. Few dividing cells were observed and cells with several nuclei in the nucleus were also detected. CLSM images show well stained actin stress fibers in multiple directions throughout the cells indicating good cell adhesion on the sample surface. The results for cytotoxicity, morphology and adhesion of HOB were in agreement with the previous results observed for Saos-2 cells. The ribbons allowed cell adhesion, spreading without any cytotoxic effect. Figure 3.10 (b) shows results of cell proliferation on the sample surface after 3 and 7 days of culture. Both samples showed similar cell proliferation and no significant differences were observed between them. Regarding ALP activity quantification, as a cell differentiation parameter, all samples showed ALP activity after 14 days in culture (Figure 3.10 c). No significant differences were observed between untreated and etched 72 h samples, although the ALP values of etched 72 h samples were slightly higher than untreated ones. ALP activity was not quantified in HOB cells after 7 days due to the low values obtained. HOB cells are undifferentiated cells that in order to differentiate need to be cultured under confluent conditions or under differentiated medium.

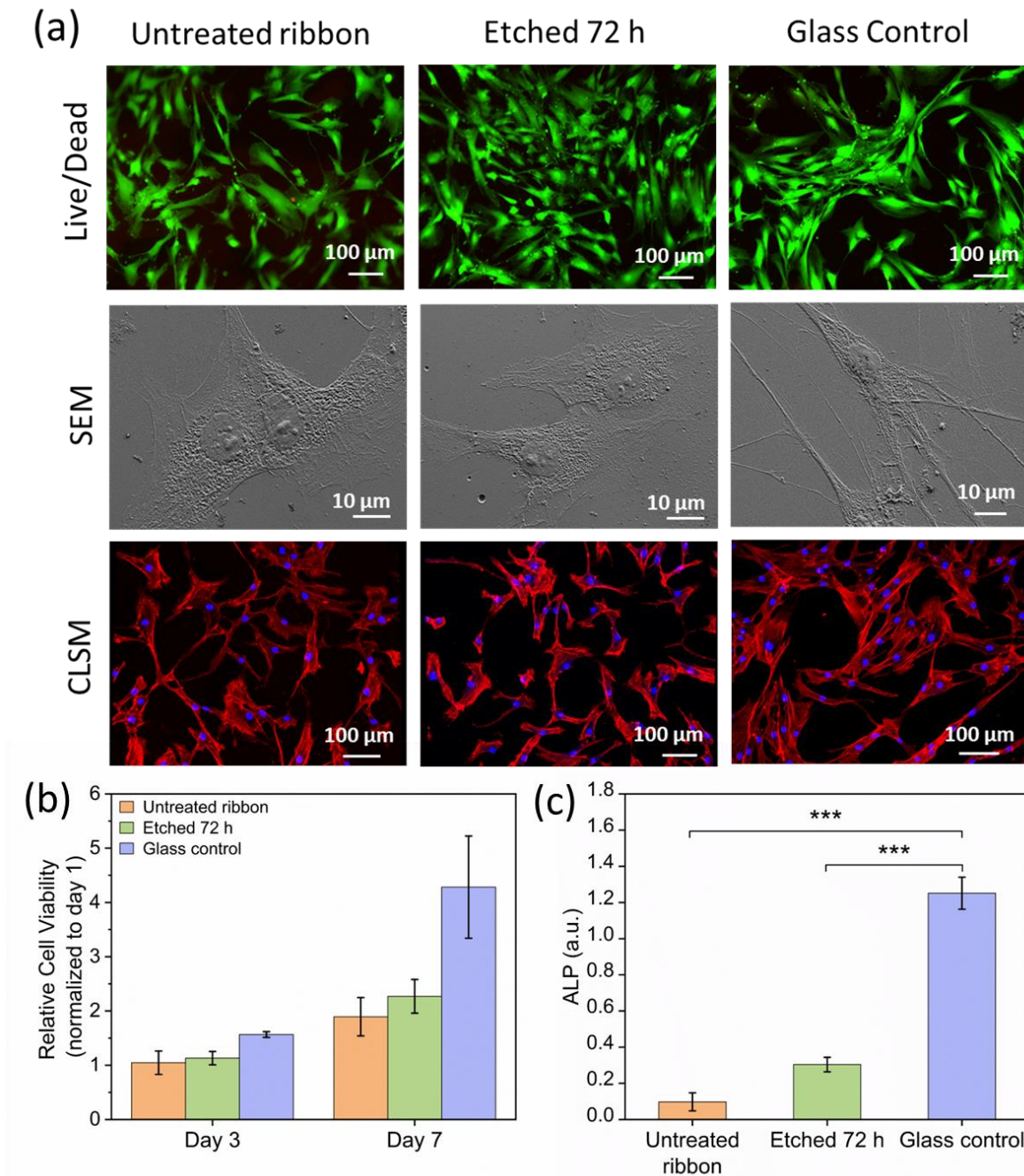


Figure 3.10. (a) Representative images of HO β cells grown on untreated ribbon, etched 72 h, glass control stained using calcein (live/ green) and ethidium di bromide (dead/ red), SEM images of adhered cells showing the flat appearance with long filipodia, CLSM images of cells showing the actin distribution (stress fibers, red) and nuclei (DNA, blue), (b) Cell proliferation measured using Alamar Blue after 1, 3, 7 days of culture, (c) ALP activity measured after 14 days of culture. Data are represented with mean \pm SEM of three independent experiments and were analyzed with unpaired t test or one-way ANOVA, followed by Tukey's test for multiple comparison. ***P < 0.001.

Evaluation of cytocompatibility using two cell lines of Saos-2 and HOb helped in understanding the cellular response of ribbon samples before and after chemical *pseudo-dealloying* treatment. Infinite cell lines like Saos-2 cells are widely used for in vitro studies of materials for evaluation of cytocompatibility. Saos-2 cells is a well characterized cell line that resembled HOb cells in most of the parameters analyzed, including adhesion and differentiation [232]. However, this cell model does not entirely resemble the primary osteoblast cells (HOb cells). The physiological phenotype of HOb is closer to the in vivo osteoblasts than the Saos-2 cells. Thus, a complementary result obtained from both cell lines enhances the knowledge to better understand their interaction with the untreated and etched ribbon samples.

3.3.6 Biofilm growth and bacteria adhesion by *Pseudomonas aeruginosa*

The Biofilm growth study was performed using crystal violet (CV, 1 %) assay to stain the biomass of gram negative bacteria *Pseudomonas aeruginosa* (PAO1) adhered to the surface of the samples. As CV binds non-specifically to cells and extracellular polymeric substances, it allows a quantification of the biofilm biomass. The samples were incubated for 24 h in bacteria media and LB broth at 37°C. Later the samples were washed with PBS 2 times and stained using crystal violet. Later the samples were washed with PBS 2 times and elucidated using UV vis spectroscopy at 595 nm wavelength.

Two different shapes of ribbon samples of MA2 alloy composition were used to understand the influence of shape and texture of the samples on the biofilm growth. Ribbon samples in Figure 3.11 (a-b) were irregular ribbons with 10 x 10 mm, while samples in Figure 11 (c-d) were regular ribbons with 4 x 25 mm. The irregular etched 72 h ribbons showed higher growth of biofilm stained in violet color on the ribbon samples (Figure 3.11 b). While the regular etched 72 h ribbon samples showed fewer violet stains representing lower biofilm growth on ribbon samples (Figure 3.11 d). The site-specific attachment of bacteria on the ribbon samples shows their preference for attachment and proliferation of biofilm. The results indicate the substrate shape greatly influences bacteria attachment and biofilm growth.

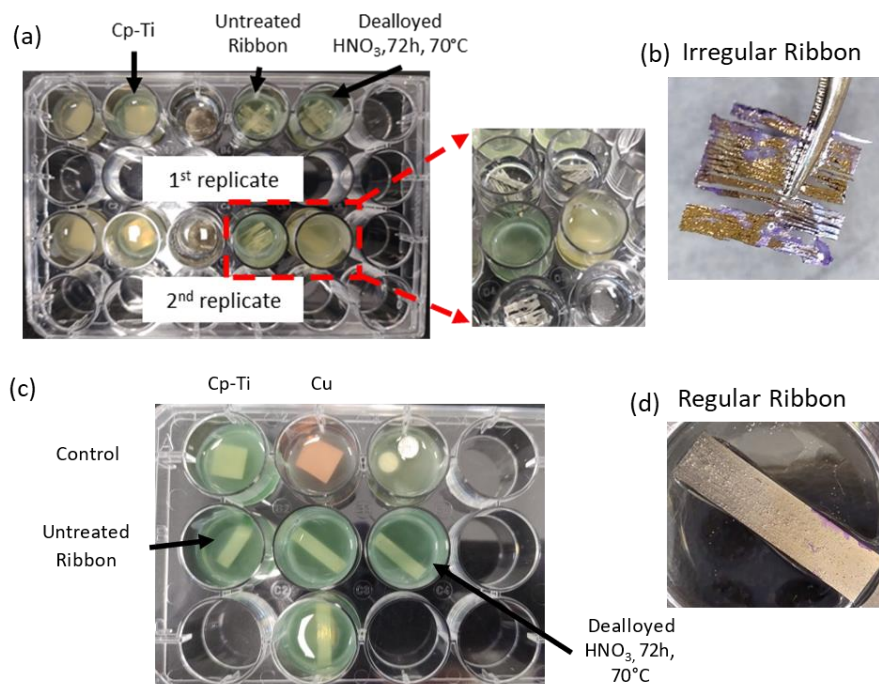


Figure 3.11. Biofilm growth study of amorphous ribbons using *Pseudomonas aeruginosa* in crystal violet assay, (a) Irregular ribbon samples incubated in bacteria media and LB broth at 37°C for 24 h, (b) etched 72 h irregular ribbon showing more stained biofilm using crystal violet staining, (c) regular ribbon samples incubated in bacteria media and LB broth at 37°C for 24 h, (b) dealloyed regular ribbon showing less stained biofilm using crystal violet staining.

The results showed that, when *Pseudomonas aeruginosa* biofilms are grown in contact with the different groups for 24 h, it is possible to observe a difference in the biofilm activity on the irregular and regular ribbons, additionally a significant difference between the cp-Cu and cp-Ti was observed as shown in Figure 3.12 (a). The irregular untreated and etched 72 h ribbon samples showed higher biofilm growth compared to cp-Ti and cp-Cu, while in case of regular ribbons, the biofilm growth on etched 72 h ribbon was lower than cp-Ti and untreated ribbon.

The samples were also analyzed qualitatively by AFM to identify bacteria adherence, coverage, and bacterial surface behavior in contact with these antimicrobial surfaces. It is possible to visualize the samples before incubation (topographical analysis) and after incubation (biological analysis) in 3D view. Decrease adherence and planktonic bacteria prevalence were significantly seen after 2 h when *Pseudomonas aeruginosa* comes in contact with cp-Cu. While on the untreated samples it is possible to observe an agglomeration of bacteria suggesting early-biofilm formation. In case of etched 72 h samples monolayer (in inset with 90 x 90µm) and agglomerated bacteria were observed. This can be likely due to the surface composition of etched 72 h sample which is composed of Ti/Zr rich oxide layer. Allowing bacteria to adhere to surface of Ti/Zr oxide passivated layer in the initial time period of 2 h, which is also observed for cp-Ti. However, it is worth noting that in case of regular ribbon the biofilm growth of etched 72 h ribbon was lower than cp-Ti while untreated ribbon showed

similar behavior as cp-Ti additionally there is a huge deviation observed in untreated ribbon samples which highlights the inhomogeneity and inconsistency in the performance of untreated ribbon.

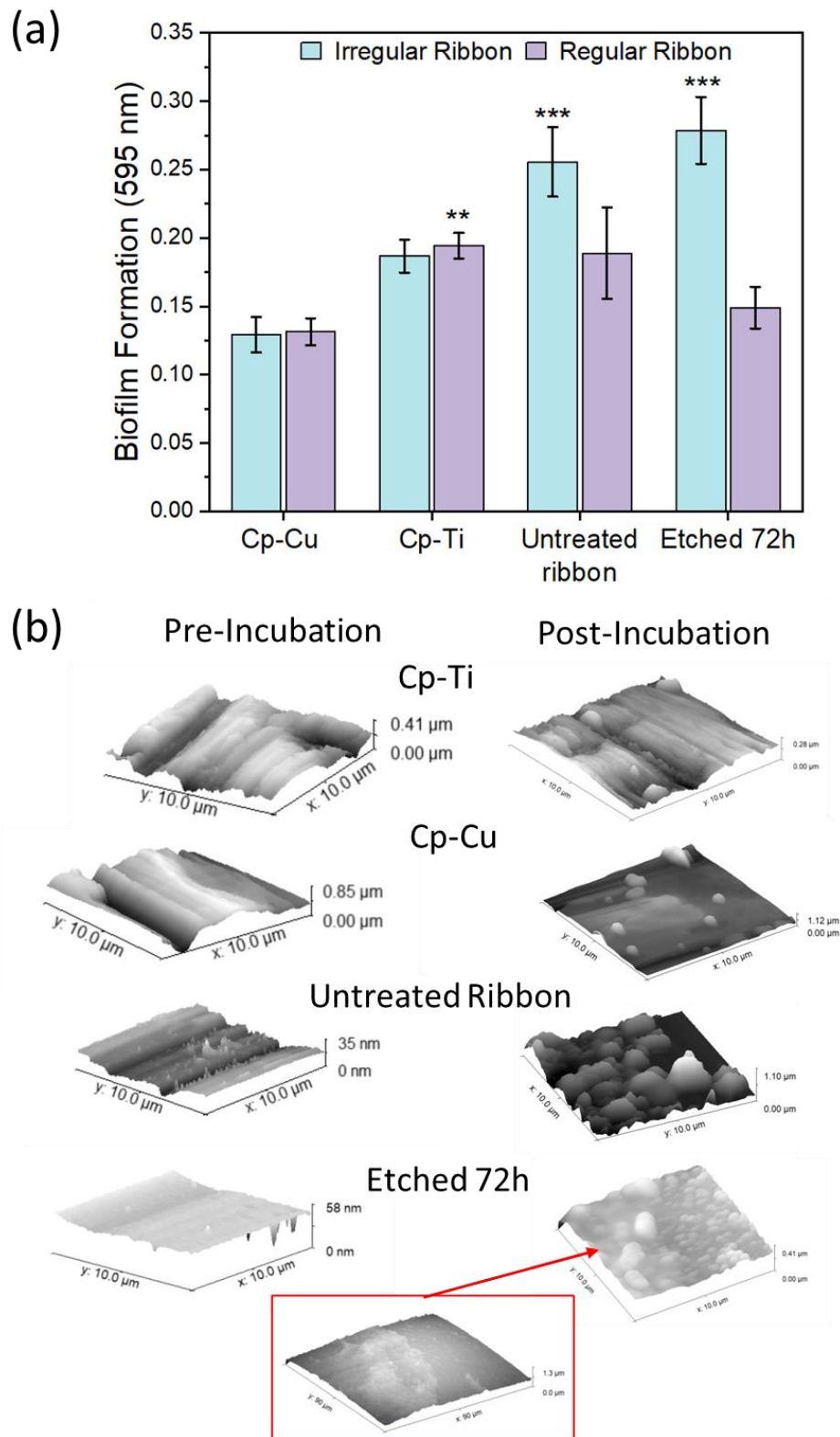


Figure 3.12. (a) Biofilm formation on cp-Ti, cp-Cu, irregular and regular ribbons: untreated, dealloyed 72 h incubated in *Pseudomonas aeruginosa* for 24 h using 1 % crystal violet assay.

Data represented with mean \pm SEM of three independent experiments and analyzed using ordinary one-way ANOVA, followed by Dunnett's test for multiple comparisons of group corresponding to irregular and regular ribbon samples respectively. *P < 0.05, **P < 0.01, ***P < 0.001 (vs cp-Cu), (b) 2D topographical and biological pre-incubation and post incubation, AFM qualitative analysis with *Pseudomonas aeruginosa* (PA01) at 10 x 10 μ m for all the samples (inset showing 90 x 90 μ m for etched 72 h sample). The height data scale was uniform for all samples at 400 nm except for cp-Cu with 800 nm. All samples were analyzed using the software Gwyddion.

The findings from aforementioned investigations on untreated and etched 72 h ribbons are summarized in Table 3.2. It is important to note that treating the material improved the properties of the amorphous ribbon, for instance enhancing the ROS activity of the etched 72 h sample, for possible antimicrobial response as compared to untreated ribbon. The presence of Cu ions released can validate the production of ROS from Cu on the surface after treatment that eventually can be released during incubation.

The overall, cell proliferation and cell differentiation response of the etched 72 h sample with Saos-2 and HOb cells was improved, respectively. Moreover, the amount of Cu released from the surface of untreated and etched 72 h ribbons can be considered limited enough and not harmful for the body. The results from biofilm study showed in-adequate performance by etched 72 h ribbon because of its inability to prevent bacteria adhesion after 2 h of incubation, while after 24 h of incubation the biofilm growth was lower than cp-Ti which could be due to release of metal ions over a longer immersion period causing oxidative stress to bacteria cell wall which can lead to rupture of cell wall and reduction of biofilm formation. However, it is speculation and requires further investigation.

Table 3.2. Condensed overview derived from the comprehensive analysis presented in this work on untreated and etched 72 h ribbons.

Sample	Cu (mg/L)	Hemo-compatibility	<i>Pseudo monas aeruginosa</i> Biofilm and Bacteria adhesion	ROS •OH Radical	Saos-2 Cell		HOB Cell			
					Viability	Proliferation	Viability	Proliferation	Differentiation	
Untreated Ribbon	↑	+++	--	+	+++	+	++	+++	++	+
Etched 72 h	↓	+++	-	+++	+++	++	++	+++	++	++

↑ High ↓ Low (+) Adequate (++) Good (+++) Very good (-) In-adequate (--) Bad

Conclusion

The chemical *pseudo-dealloying* treatment process using HNO₃ as electrolyte resulted in the most promising surface in Ti₄₀Cu₄₀Zr₁₁Fe₃Sn₃Ag₃ (MA 2) ribbon samples. Further these treated samples were optimized in order (i) to maximize the hemocompatibility and biocompatibility of the alloy, (ii) to allow ROS production from the surface that can enable an antibacterial activity of the surface and (iii) tailor the surface composition to enable Cu release from the surface in a limited amount in order to contribute to the antibacterial activity of the surface without having a harmful effect towards cells.

In detail, the investigation shows dependence on parameters such as temperature and time, on evolution of different surface morphologies on Ti₄₀Cu₄₀Zr₁₁Fe₃Sn₃Ag₃ amorphous alloy. Elevated temperature results in faster dissolution and formation of globular structures while lower temperature and longer immersion time results in formation of np morphology with ligaments and pores interconnected. The 72 h etched ribbon sample showed hydrophobic wettability and ability to boost release of hydroxyl radical in a cell free system after 10 min of incubation with H₂O₂. Despite the radical capacity, the rate of hemolysis of the ribbons was comparable to cp-Ti indicating good hemocompatibility. In addition, the results of in vitro studies using Saos-2 and HOB cells showed a good biocompatibility for the 72 h ribbon. The 72 h etched ribbon was non-cytotoxic for Saos-2 and HOB cells, and the etched 72 h showed

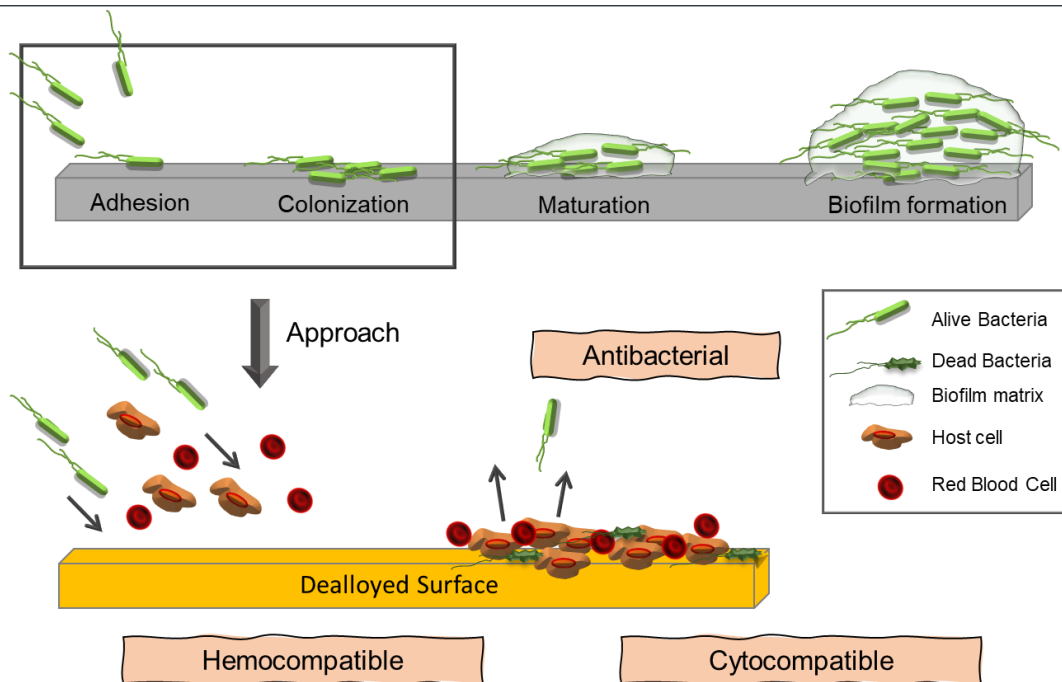
higher cell proliferation after 7 days of incubation. Early stage of osteogenic activity was also observed by the etched 72 h. Thus, overall, the HNO₃ etched Ti₄₀Cu₄₀Zr₁₁Fe₃Sn₃Ag₃ at % amorphous alloy showed promising biocompatible properties. The capacity of this material to induce ROS in a short time could be used for limiting bacteria adhesion and biofilm formation on their surface.

However, the preliminary investigation of biofilm study using *pseudomonas aeruginosa* revealed that sample size and texture plays a major role in biofilm growth in addition to surface morphology and chemistry. In the case of regular etched 72 h sample evident biofilm growth was observed on the sample surface after 2 h of incubation which can be due to presence of TiO₂ surface which is less effective as compared to cp-Cu surface. However, it is worth noting that untreated ribbon shows higher inconsistency due to its inhomogeneous surface properties, hence further investigation is required to fully understand and appreciate the role of etched 72 h sample for implant applications.

Additionally, results from the ROS and biofilm studies cannot be compared because ROS studies were performed in a cell free system mimicking an inflammatory condition while in biofilm study the condition differs. Hence further extensive evaluation is required to correlate the finding of ROS studies and biofilm growth studies by using a combined system such as co-culture mimicking the in vivo conditions.

Chapter IV

CHEMICAL DEALLOYING USING AMMONIA BASED SOLUTION



Specific Aim

- To selectively etch Cu from the surface of the $\text{Ti}_{40}\text{Cu}_{40}\text{Zr}_{11}\text{Fe}_3\text{Sn}_3\text{Ag}_3$ (MA2) at % amorphous ribbons and produce a patterned passivated surface rich in Ti and Zr oxides using chemical dealloying technique employing ammonium hydroxide and hydrogen peroxide solution.
- Investigate the kinetics of selective Cu removal and the influence of electrolyte concentration, immersion time, and stirring velocity on the surface morphology evolution. Utilize atomic force microscopy (AFM), scanning electron microscopy (SEM), and X-ray photoelectron spectroscopy (XPS) to analyze the nanostructured topography of the chemically treated samples.
- Discuss the experimental results to elucidate the mechanism behind dealloying using the ammonia-based solution (NH_4OH and H_2O_2) on the Ti-based amorphous alloy.
- Analyze the biocompatibility of the treated ribbon samples involving hemocompatibility test, antimicrobial test: reactive oxygen species, biofilm growth and bacteria adhesion using *Pseudomonas aeruginosa*, cytocompatibility test using osteoblast cell lines (Saos-2 and HOb).

1. Introduction

Selective dissolution of Cu from Ti-Cu-Zr based multicomponent amorphous materials has not been studied thoroughly for biomedical applications and there have not been so many studies yet [52]. Currently, Ti-based alloys face challenges related to active oxidation of valve metals thereby hindering the percolation of the electrolyte to the bulk that could enable the dealloying of the whole material [167,233,234].

This chapter discusses a new alkaline electrolyte for chemical *pseudo-dealloying* to ensure efficient removal of excessive Cu from the near surface region of multicomponent $\text{Ti}_{40}\text{Cu}_{40}\text{Zr}_{11}\text{Fe}_3\text{Sn}_3\text{Ag}_3$ at % amorphous alloy using ammonia-based solution that has not been completely explored in literature. An electrolyte composed of hydrogen peroxide and ammonium hydroxide was considered to ensure presence of oxygen for oxidation of copper and ammonia to form complex with copper respectively [235].

J. Halpern in 1953, demonstrated that pure copper sample in ammonia solution with a constant supply of oxygen results in the adsorption of oxygen onto copper surface followed by the formation of copper oxide that later forms a complex with ammonia thus, allowing the removal of copper from the sample surface [236,237]. Recently, etching using ammonium hydroxide and hydrogen peroxide has been performed on pure Ti surfaces for obtaining micro/nano structured topography. It was found that the oxidation of the surface was less pronounced due to dissolution of the barrier oxide layer on the surface [238,239]. X. Yuan et al. reported that pure Ti samples treated with ammonium hydroxide and hydrogen peroxide produced topography with 10-30 μm pores and surface roughness between 2-4 μm . The treated surfaces were hydrophilic and showed enhanced cytocompatibility with MG63 cells [240].

While numerous investigations focus on assessing cytocompatibility, there is limited research on the antibacterial activity of amorphous alloys [241]. Addressing biofilm-related infections is crucial, and current research emphasizes surface modification techniques, including both physical and chemical modifications [242]. Tailoring surface properties, including roughness, wettability, and chemical composition, can enhance the biocompatibility and antibacterial response of implants [243].

Alternative approaches for bacterial prevention on implant surfaces involve contact killing, utilizing antimicrobial elements like Zn, Ga, Cu, Ag [244–250]. Notably, biomaterials based on Cu have shown significant advancements, demonstrating both antibacterial and osteogenic properties [251]. In a study by F. Heidenau et al. [252], the authors compared the effects of metal ions such as Al^{3+} , Co^{2+} , Zn^{2+} , Hg^{2+} , Ag^+ and Cu^{2+} by utilizing metal salts. The results showed that Cu^{2+} performed better compared to all metal ions with respect to antibacterial activity and cytocompatibility. The authors further studied the effect of Cu^{2+} by coating Cu- TiO_2 on Ti6Al4V alloy substrate. The response of Cu^{2+} on *Staphylococcus epidermidis* (*S. epidermidis*) and *Staphylococcus aureus* (*S. aureus*) and mouse connective tissue fibroblasts showed good antibacterial activity with LD_{50} (Lethal Dose causing the death of 50 % of population) at 10.58 mg/L and good in-vitro cytocompatibility compared to uncoated Ti6Al4V alloy.

Achieving a delicate balance between effective antibacterial properties and minimal cytotoxicity remains a significant challenge in the development of biocompatible amorphous alloy implants. The need for materials that effectively combat biofilm-associated infections without compromising the safety of the host represents a growing demand in the field of biomedical implants. This chapter focuses on the possibility of attaining an antibacterial response, while ensuring a non-cytotoxic environment for osteoblast cells. Additionally maintaining hemocompatibility for understanding the interaction of blood components with implant materials for successful in vivo applications.

In this chapter, the surface of the $\text{Ti}_{40}\text{Cu}_{40}\text{Zr}_{11}\text{Fe}_3\text{Sn}_3\text{Ag}_3$ (MA2) amorphous alloy was treated with ammonium hydroxide and hydrogen peroxide in different conditions to create unique surface morphologies with modified chemical composition. The goal is to obtain surfaces with tailored composition, roughness, wettability, and surface energy to which hemocompatibility, antimicrobial activity and cytocompatibility can be associated.

Surface characterization utilizing XPS, AFM and FIB was performed at Leibniz-Institute for Solid State and Materials Research Dresden (Leibniz IFW Dresden), Dresden, Germany during my period abroad. The studies related to cytocompatibility were performed in Departament Biologia Cellular, Fisiologia i Immunologia, Universitat Autònoma de Barcelona, Spain during my period abroad. Additionally, the antimicrobial testing was performed in collaboration with School of Biomolecular and Biomedical Science, University College Dublin, Ireland.

2. Experimental Procedure

2.1. Synthesis of samples using ammonia-based solution

The ribbon sample with 2 cm² surface area was cleaned in an ultrasonication bath using acetone and then ethanol for 5 min followed by air drying. The ribbon samples were pseudo-dealloyed in a Pyrex glass beaker with a mixture of ammonium hydroxide (NH₄OH, 25 % Merck), hydrogen peroxide (H₂O₂, 30 % Merck) and deionized water (H₂O, Milli-Q, Merck Millipore) in different concentrations at room temperature (RT) to study the effect of electrolyte concentration on the evolution of porosities. The first solution, composed of equal parts of NH₄OH and H₂O₂ in 1:1 volume ratio, is hereafter referred as concentrated ammonia solution and the second solution, composed of 5:1:4 volume ratio of NH₄OH, H₂O₂, H₂O respectively, here after referred as diluted ammonia solution. Further, treatment was performed in non-stirred and stirred solution, stirring was performed with rotational speed of 1000 rpm. The pH of the solution was recorded using a Knick pH meter 761. After the treatment, samples were rinsed five times with deionized water and dried at RT.

To determine the influence of treatment parameters on the final morphology and composition of the samples, different experiments were performed by varying parameters such as electrolyte concentration, immersion time, stirring and non-stirred solution. In particular, two different concentrations were investigated in the presence of strong oxidizer like H₂O₂, to ensure the presence of sufficient oxygen in the solution [253].

The first solution named as “diluted solution” is composed of 5:1:4 volume ratio of NH₄OH, H₂O₂, H₂O and the second solution named as “concentrated solution” is composed of equal volume parts of NH₄OH and H₂O₂ (1:1). As for the diluted solution, the experiments were performed for different durations of 5, 30, 60, 120, 240 and 360 min, without stirring the solution. For comparison, the diluted solution with immersed ribbon sample was stirred for 60 min. At the same time period of 60 min, a sample was produced using the concentrated solution without stirring the solution.

For clarity, samples will be named in the following using an acronym that identify

- (i) the solution used: CS and DS for concentrated solution and diluted solution, respectively,
- (ii) the time of treatment: 1 min for 1 minute of immersion.
- (iii) the condition of solution: S for solution in stirring (forced convection) and NS for non-stirring (natural convection), respectively.

Therefore, sample named DS-5min-NS is treated for 5 minutes in diluted solution without stirring. Figure 4.1 shows a schematic diagram of the *pseudo-dealloying* conditions used and samples names with respect to characterization performed on the sample.

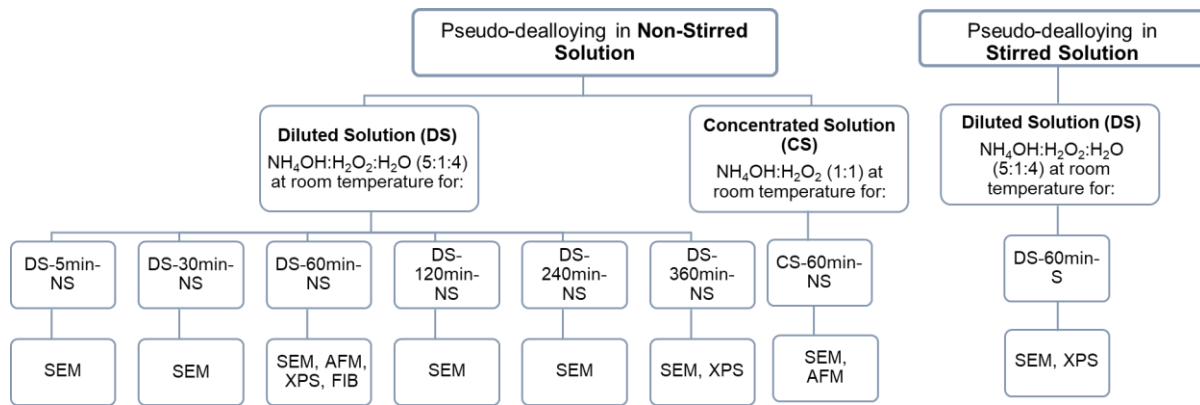


Figure 4.1. Schematic flow chart of chemical *pseudo-dealloying* treatment conditions and samples produced.

2.2. Characterization of treated samples

The surface morphology of the treated samples was characterized using Field Emission Scanning Electron Microscopy (FESEM - Tescan S 9000 G, and LEO Gemini 1530) and the cross section was analyzed by performing an in situ cutting of the sample using a focused ion beam (FIB) inside the FESEM (FIB Helios 5 CX, Thermo Scientific). Average ligament and pore size were calculated using ImageJ software on 40 different spots for each sample. In this study the characterization of both untreated and treated ribbons were performed on the upper air side of the ribbon sample.

The surface composition of the treated sample was analyzed using X-ray Photoelectron Spectroscopy (XPS) on the surface and in-depth profile by sputtering using Argon ions (SPECS ion gun) with 100 mm hemispherical analyzer. Non-monochromatic Mg-K α X-ray source was used at 400 W and 15 kV. SiO₂ on Si wafer sample was used as reference to determine the rate of sputtering during depth profiling. The rate of sputtering was 0.4 nm/min. Satellite subtraction was performed for all measurements with charge correction performed on carbon at 284.8 eV. Pass energy of 15 eV was used for high resolution scans. XPS investigation was performed on the surface of sample and in-depth sputter profiling with 5 sputter steps at time points of 0, 10, 20, 30, 40 min. The recorded elements were quantified in atomic percentage and high-resolution scans were obtained to differentiate between the chemical states of the elements. CASA XPS software was used for plotting the graphs of high-resolution scans [254].

The surface roughness of samples was analyzed using atomic force microscopy (AFM) under ambient conditions using a Bruker Dimension Icon AFM in tapping mode with a scan rate of 0.5 Hz. A TESPA-v2 probe was used with a resonance frequency of 320 kHz. The AFM data was analyzed using WSxM5.0 Develop 10.0 and/or Gwyddion 2.56. AFM images were acquired at $1 \times 1 \mu\text{m}^2$ on three different spots of the samples for calculation of average root mean square (RMS) roughness of the sample surface.

The absorption spectra were acquired employing a UV/vis 900 lite spectrophotometer (Uvikon, Kontron Instruments) to elucidate the formation of metal complexes in an ammonia-based solution. Spectral measurements were conducted in the range of 200-900 nm, utilizing a Quartz Cuvette. To establish a baseline for normalization, a blank solution was prepared using a DS solution without the inclusion of the ribbon sample. This DS solution comprised a mixture of NH_4OH (25 %), H_2O_2 (30 %), and H_2O (5:1:4 vol ratio). The normalization process involved the utilization of this blank solution, ensuring accurate and reliable comparative analyses of the obtained curves.

Reference samples, specifically polished Cu plates and Ti plates (99.99 % pure), were immersed in the DS solution to provide a benchmark for comparison. The test sample consisted of an untreated ribbon immersed in the same DS solution. It is noteworthy that upon initial preparation, the solution exhibited bubbling attributed to the decomposition of hydrogen peroxide into oxygen and water. Consequently, spectral recordings were deferred until 24 hours post-preparation to allow for the stabilization of the solution. This precautionary measure aimed to capture a representative and reliable absorption spectrum reflective of the stable state of the metal complexes formed in the ammonia-based solution.

2.3. Wettability study

The surface wettability measurement of the treated ribbon sample was performed using Theta lite optical tensiometer (Biolin Scientific) in sessile drop. To understand the wettability and surface free energy (SFE) of the sample surface, polar and non-polar solvents were used. The contact angle was measured after 1 s of placing droplet of 3 μL volume of water (polar) and di-iodomethane (non-polar), using oneAttension software. The surface free energy of the treated samples was calculated using Young's equation and Owen, Wendt, Rabel and Fowkes (OWRK) method [255,256]. The measurement was recorded with a minimum of 3 droplets on 3 samples for each group (n=9).

2.4. Hemocompatibility study

Hemocompatibility of the ribbon samples was assessed in accordance with International Organization for Standardization, 2000 (ISO 10993-4) and National Institutes of Health (NIH) guidelines with minor modifications [257,258]. Defibrinated sheep blood (Microbiol Diagnostic) was used to investigate hemolysis with whole blood or red blood cells (RBCs) were purified by washing three times with 0.9 % NaCl (Eurospital). The whole blood and purified RBCs were studied separately and prepared. The whole blood and purified RBCs were studied and prepared separately in 4:5 volume ratio dilution with phosphate buffer saline (PBS, Merck). A positive control was prepared as a calibration by adding 10 mL of ultrapure water (Merck-Millipore) to the diluted blood or purified RBCs (0.2 mL). The absorbance of the

hemoglobin released was measured at 540 nm by a UV/vis 900 lite spectrophotometer (Uvikon, Kontron Instruments) and was adjusted to the range 0.9-1.0 by adding PBS or blood.

Metallic ribbons of 3 cm² surface area were used [258]. Commercially available Mg alloy with composition Mg93/Y4/Nd3 (WE43B, Goodfellow) [259] and quartz particles (Min-U-Sil 5, U.S Silica, 200 cm²/ml, specific surface area of 5 m²/g) [260] were used as positive reference material. The metallic samples were cleaned with 70 % ethanol and washed with ultrapure water and PBS. The metallic samples were pre-incubated in a glass vial with 10 ml of PBS for 30 min at 37 °C in a horizontal thermostatic shaker. Then 0.2 mL of diluted blood or purified RBCs were added to the samples in glass vials and incubated for 60 min at 37 °C in a horizontal thermostatic shaker. The incubated liquid was then centrifuged at 500 g (Centrifuge Rotina 380R) for 5 min to sediment cells and debris, and 5 mL of the supernatant was then collected to measure the absorbance at 540 nm. The percentage of hemolysis of all tested groups was analyzed using eq 4.1, where Abs is the absorbance measured.

$$\% \text{ Hemolysis} = \frac{\text{Abs}(\text{test}) - \text{Abs}(\text{negative control})}{\text{Abs}(\text{positive control}) - \text{Abs}(\text{negative control})} \times 100 \quad (4.1)$$

Hemoglobin adsorption (Abs) by the samples was investigated using purified red blood cells (RBC). The absorbance of the hemolyzed blood was adjusted to 0.9 - 1 and a final volume of 10.2 mL of blood in PBS was frozen in the fridge at -20 °C overnight and defrosted to obtain lysed RBC. Then the solution was centrifuged at 10,000 g for 10 min. The supernatant solution containing Hb was recovered. The samples were incubated in the solution containing Hb for 60 min at 37 °C. After the incubation, the absorbance of the Hb was measured. The measurements were performed in triplicate.

2.5. Metal ion release study

Samples with 0.4 × 0.6 cm size were submerged in cell culture media DMEM (Dulbecco modified eagle medium, Gibco, ThermoFisher scientific) without cells and incubated at a temperature of 37 °C for a period of 3 days to investigate the release of ions. Subsequently, 1 mL aliquots of the media were collected for analysis of the released metal ions using Agilent ICP-MS, model 7900. The study was conducted with three replicates and normalized against a blank control consisting of cell culture media without any samples.

2.6. Release of reactive oxygen species study

To assess the generation of hydroxyl radical (•OH), the spin trapping technique coupled with electron paramagnetic resonance spectroscopy (EPR) was employed. Cleaned metallic samples with 0.4 × 1 cm size were immersed in 1 mL of phosphate buffer (PB, 0.5M, pH 7.4, Sigma-Aldrich, Milan, Italy) containing 0.04 M DMPO (5,5-dimethyl-1-pyrroline-1-oxide, Cayman Chemical Company, Ann Arbor, Michigan) as spin trap molecule, and freshly prepared 0.2 M

H₂O₂ as target molecule. The samples were incubated in the solution at 37 °C, while being continuously stirred using a thermostatic shaker in darkness. After 10, 30, and 60 min, 50 µL of the supernatant were collected in a capillary, and EPR spectra were recorded utilizing a Miniscope MS100 spectrometer (Magnettech, Berlin, Germany) at a microwave power level of 10 mW, a modulation of 1 G, scan range of 120 G, and a center field at 3355 G. A blank control without samples was prepared. The number of radicals released is proportional to the intensity of the EPR signal. To compare the amount of hydroxyl radicals produced by the samples, the signals were double integrated using Origin 2023 software and results were reported as arbitrary units. The measurements were conducted in duplicate.

2.7. Antibacterial activity

2.7.1. Measuring biofilm formation

To investigate biofilm formation, gram-negative *Pseudomonas aeruginosa* (strain PAO1, *P. aeruginosa*) was utilized. The bacterial inoculum was grown in Lysogeny broth (Sigma-Aldrich, LB media: 1 % tryptone, 0.5 % yeast extract, 0.5 % NaCl) in deionized H₂O. Prior to bacterial inoculation, the samples (0.4 × 2 cm) underwent sterilization by immersion in 70 % ethanol, and each study was conducted with three biological replicates and two technical replicates.

Overnight cultures of *P. aeruginosa* were grown in 15 mL of LB media at 37 °C. Bacteria were quantified by diluting an aliquot 1:10 in fresh media and the optical density (OD) was measured at 600 nm using a spectrophotometer (Spectramax m384). Cultures were then equalized to 0.1 OD₆₀₀ cultures (10⁷ CFU/mL) in preparation for inoculation. The samples were then incubated without shaking in 1 mL of the equalized bacterial culture for 24 hours at 37 °C in sterile 24-well, flat-bottomed, tissue culture-treated plates.

Following the incubation period, the samples were transferred to a new well-plate containing phosphate-buffered saline (PBS) solution and rinsed gently three times with PBS to remove non-adhered planktonic bacteria. Subsequently, the samples were dried at 37 °C for 30 min. 1 % crystal violet (CV) solution (1 mL) was added to each well and left at room temperature for 15 min. After staining, the ribbons were transferred to a new well-plate and rinsed three times with PBS and dried at 37 °C for 30 min. 1 mL of elution buffer (80 % ethanol and 20 % acetone) was then added to the wells and left at room temperature for 15 min. Afterwards, 1 mL of this elution was transferred to an optically clear plastic cuvette, and the OD of the solution was measured at 595 nm using elution buffer as blank providing a quantitative measurement of biofilm biomass.

2.7.2. Measuring bacteria adhesion

The overnight culture of *P. aeruginosa* was grown in LB media. Subsequently, 2 mL of the culture was centrifuged in an Eppendorf tube at a speed of 3000 RPM for 15 min, leading to the formation of a visible pellet. The LB media was carefully discarded, and the pellet was resuspended in a 50/50 mixture of PBS and H₂O to prevent osmotic stress. Soft pipetting was employed for resuspension. The mixture was subjected to another round of centrifugation, and the PBS - H₂O combination was discarded. The pellet was completely resuspended in 1 mL of deionized H₂O using soft pipetting.

The optical density (OD) for each Eppendorf tube was measured at 600 nm using a spectrophotometer, with deionized H₂O as blank. Another Eppendorf tube was prepared for each biological replicate, with the OD equalized to 0.1 in deionized H₂O. The required adjustments were made to ensure the uniformity of the samples.

The samples of amorphous ribbon before and after treatment were sterilized with 70 % ethanol and allowed to dry in a fume hood. After the drying process, 25 µL of the equalized *P. aeruginosa* (OD: 0.1) culture was added to the top of each sample and spread gently over the surface using a pipette. The samples were then left to dry for a period of 2-3 hours in the fume hood. Once completely dried, the samples were fixed using a gradient of ethanol washes from 100-50 % and dried under ambient conditions. Cp-Ti and cp-Cu plates were used as control samples.

Surfaces were imaged before and after inoculation with *P. aeruginosa* using amplitude modulation atomic force microscopy (AFM) (MFP-3D, Asylum Research) operated with Si probes (NCH, Nanosensors) having a nominal spring constant of 42 N/m and resonance frequency of 330 kHz. Representative images at 90 x 90 µm, 50 x 50 µm and 10 x 10 µm are shown from images collected in multiple locations. For presentation, images were flattened to remove sample tilt, horizontal correction was applied if required. All samples are shown with a uniform Z height scale of 400 nm with exception of cp-Cu that has a height of 800 nm due to its complicated topography.

2.8. In vitro cytocompatibility study

The samples, measuring 0.4 × 0.6 cm, were subjected to sterilization using absolute ethanol for a duration of 5 min. The experiments were conducted in triplicate, employing a 1.5 cm diameter glass coverslip as a control, from now on “glass control”. Two distinct cell lines were used in this study.

The first cell line, Saos-2 (ATCC), was a transformed cell line of human osteosarcoma tumor cells. These cells were cultured in Dulbecco modified eagle medium (DMEM, Gibco, Thermofisher Scientific) supplemented with 10 % fetal bovine serum (FBS, Gibco,

ThermoFisher Scientific). Cells were cultured at 37 °C and 5 % CO₂. The samples were seeded with a density of 50,000 Saos-2 cells per mL in a 24-well plate.

The second cell line, HO_b, was a finite cell line derived from human osteoblasts obtained from a human donor. These cells were cultured in DMEM supplemented with 20 % FBS and maintained at 37 °C with 5 % CO₂. The samples were seeded with 20,000 HO_b cells per mL in a 24-well plate.

Cellular cytotoxicity of the samples was assessed on day 3 after seeding using a live/dead kit specifically designed for mammalian cells (Invitrogen). The manufacturer's protocol was followed for staining live cells (green) with calcein and dead cells (red) with ethidium bromide. The stained samples were observed under an inverted fluorescent microscope (Olympus IX71). ImageJ software was utilized for image processing, and the percentage of cell viability was determined by quantifying live and dead cells from four different areas for each sample and replica.

The morphology of adhered cells on day 3 was analyzed using scanning electron microscopy (SEM; Zeiss Merlin, Jena, Germany). The samples were rinsed with PBS, fixed in 4 % paraformaldehyde for 20 min at room temperature, and subsequently rinsed with PBS. Dehydration of the samples was accomplished using an ethanol gradient (50 %, 70 %, 90 %, and 100 %), with each concentration step lasting 10 min. The samples were then dried using hexamethyl-di-silazane for 10 min. Prior to imaging, the samples were sputter-coated with gold.

Cell adhesion on the sample surface was evaluated after 3 days in culture. The actin filaments, representing the cytoskeleton of the cells, were stained using phalloidin. The cells were fixed with 4 % paraformaldehyde for 20 min and washed with PBS, then the samples were immersed in 0.1 % Triton for 15 min and 1 % Tween 20 (Sigma) for 20 min at room temperature. Subsequently, the samples were immersed in 1 % PBS-BSA for 20 min at room temperature. A mixture of phalloidin and a nuclei stain consisting of Alexa fluor 594-conjugated phalloidin (Invitrogen), and Hoechst 33258 (Sigma) was used for staining the samples, with an incubation time of 60 min at room temperature. Finally, the samples were washed with PBS and analyzed using a confocal laser scanning microscope (CLSM, Leica SP5). The acquired images were processed using Imaris viewer 9.9.1 software (Oxford Instruments).

The metabolic activity of cells growing on the samples was assessed at days 1, 3, and 7 using the Alamar Blue reagent (Thermo Fisher Scientific). On day 1, the samples were transferred to new wells to eliminate background interference from the cells growing at the bottom of the well plate. Subsequently, the samples were incubated in a mixture of cell media and Alamar Blue reagent (dilution of 10:1) for 4 h in the dark at 37 °C with 5 % CO₂. A negative control of Alamar Blue without any sample was prepared as a standard reference. Following the incubation period, the supernatant was collected, and the fluorescence intensity was measured at an excitation wavelength of 560 nm and an emission wavelength of 585 nm using a spark multimode microplate reader (Tecan, Männedorf, Switzerland). Fresh cell culture medium was added after the assay and the experiment was repeated on day 3 and 7.

The differentiation of cells was investigated by assessing alkaline phosphatase (ALP) activity at 7 and 14 days of incubation. The cells incubated on the samples for the specified durations were lysed in CyQuant cell lysis buffer (Thermo Fisher Scientific). Lysis was achieved by transferring the samples to eppendorf tubes and subjecting them to 10 min of lysis, followed by 10 sec of vortexing. Subsequently, the cell lysates were centrifuged at 12,000 rpm for 4 min at 4 °C, and the resulting supernatants were collected. ALP activity was measured by employing the hydrolysis of p-nitrophenyl phosphate (pNPP), resulting in the production of p-nitrophenol (pNP). Specifically, 25 µL of 1-step pNPP (Thermo Fisher Scientific) was mixed with 25 µL of the collected supernatant. The absorbance at 405 nm was measured using a Nanodrop Spectrophotometer (Thermo Fisher Scientific).

2.9. Statistical analysis

The data are presented using mean \pm standard error of the mean (SEM). In case of normally distributed data, ordinary one-way ANOVA followed by Dunnett's or Tukey's post hoc test was used. A 95 % confidence interval was applied, and values with $P < 0.05$ were considered statistically significant, unless otherwise stated. GraphPad Prism 8.0.2 software was used for conducting statistical analysis.

3. Results and Discussion

3.1. Surface modification by chemical *pseudo-dealloying*

3.1.1. Ammonia based diluted solution

Investigation was performed using diluted solution composed of 5:1:4 volume ratio of NH_4OH , H_2O_2 , H_2O to understand the different effects of immersion time and immersion in non-stirred or stirred solution. The morphology of samples immersed in the electrolyte, without stirring the solution, for different times (5, 30, 60, 120, 240 and 360 min) was studied by FESEM and the images are reported in Figure 4.2 (a-h).

The samples show the formation of ligaments and porosities on the surface at an immersion time of 5 min (Figure 4.2 a). An evident increase in surface roughness with the evolution of a bimodal distribution in the pore dimension is observed on the surface of sample treated for 30 min (Figure 4.2 b), while a treatment time of 60 min (DS-60min-NS sample) allows the formation of a homogeneous distribution of pores of the same size and fine ligaments (Figure 4.2 c). The thickness of the treated layer for sample DS-60min-NS is roughly 30 nm observed using a FIB cut shown in the inset of Figure 4.2 (c). AFM investigation performed to determine the roughness of the surface shows an average root mean square (RMS) roughness of 3.6 ± 0.3 nm (Figure 4.2 d) and the identified morphology is in good agreement with FESEM data. Further investigation was performed by stirring the electrolyte at 1000 rpm for 60 min to distinguish between the morphology of sample between stirred and non-stirred electrolyte. The ribbon treated in stirred solution for 60 min (DS-60min-S) (Figure 4.2 e) showed different surface morphology with respect to the non-stirred sample (DS-60min-NS). In particular, DS-60min-S shows a bimodal distribution of pores and ligaments size arranged in two superimposed layers. The inner layer is composed of fine pores, compared to the outer top layer that is composed of densely interconnected ligaments distributed on the surface. The average thickness of inner layer ligaments is 4.9 ± 1.0 nm, and the average pore diameter is 14.0 ± 4.0 nm indicating formation of finer and homogenous morphology whereas the outer layer is composed of an average ligament thickness of 13.3 ± 3.5 nm and an average pore diameter of 46.0 ± 6.5 nm.

Further investigation was performed by increasing the immersion time in DS in non-stirred condition. The surface morphology of samples treated for 120, 240 and 360 min (Figure. 4.2 f, g, h) do not show notable changes, the ligaments and pores are homogeneously distributed with dimensions almost unchanged. It is worth noting that at lower treatment time, such as 5 min and 30 min, the pore size is larger while increasing the immersion time to 60 min led to formation of smaller pores on DS-60min-NS (Figure 4.2 i). Conversely the ligament size became thicker with increasing immersion time to 60 min. At higher treatment time such as, 120 min and 240 min, finer ligaments are produced with pore size higher than that of the DS-60min-NS sample. A change in pore size is observed on the sample treated for 360 min, where the ligaments were finer while the pore size was larger.

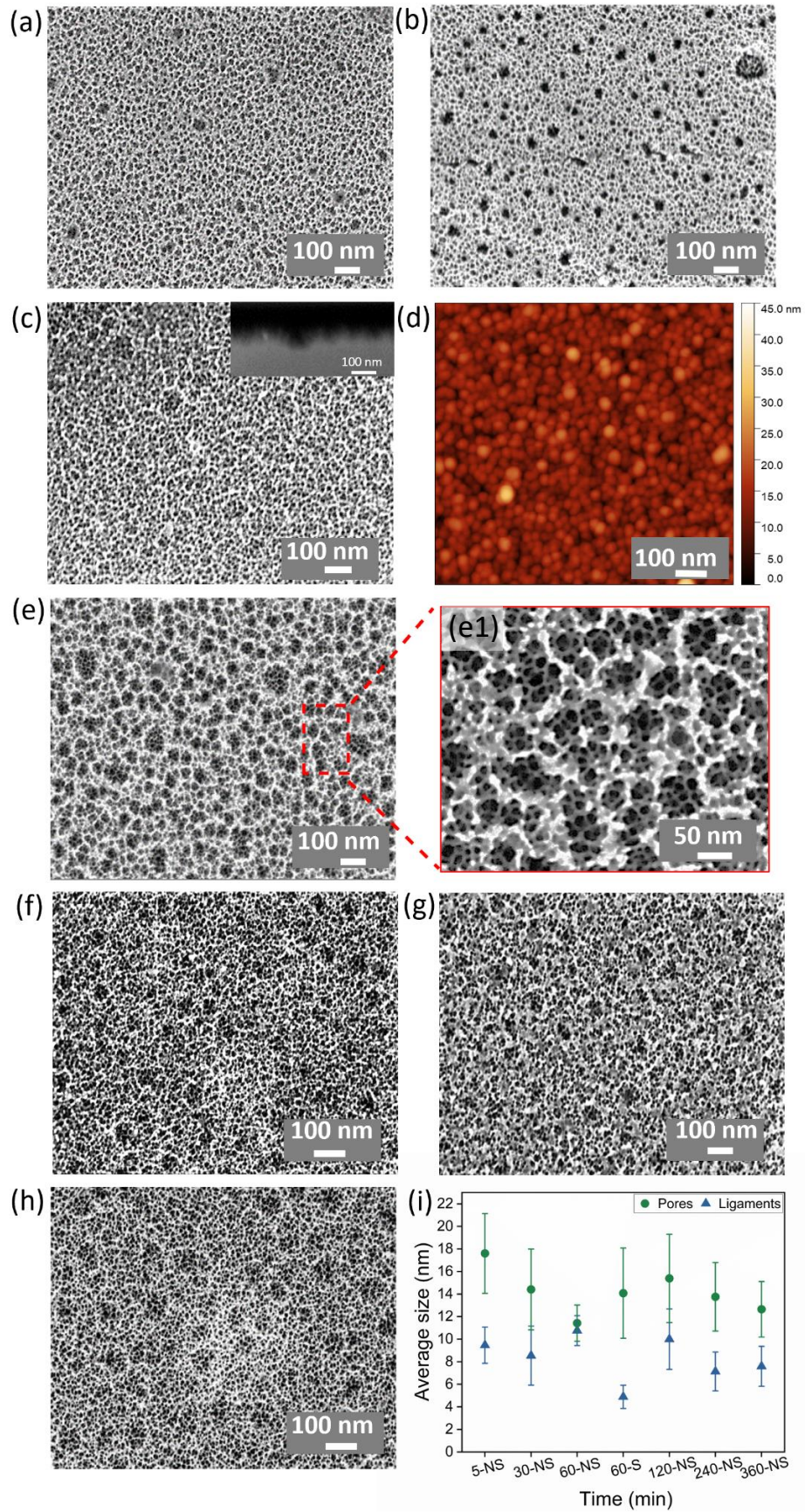


Figure 4.2. Surface morphology and topography of *pseudo-dealloyed* ribbon samples in diluted solution composed of 5:1:4 volume ratio of NH_4OH , H_2O_2 , H_2O , i.e., FESEM images (a-c, e-

h), and AFM image (d). The surface features at different conditions i.e., (a) DS-5min-NS, (b) DS-30min-NS, (c) DS-60min-NS, (inset shows cross section using a FIB cut), (d) DS-60min-NS, (e) DS-60min-S ((e.1), magnified image), (f) DS-120min-NS, SEM, (g) DS-240min-NS, (h) DS-360min-NS, (i) distribution of the average ligament and pore sizes of *pseudo-dealloyed* samples (n=40).

3.1.1.1. XPS analysis of sample treated using diluted solution

In order to investigate the composition of the modified surface state produced onto the $\text{Ti}_{40}\text{Cu}_{40}\text{Zr}_{11}\text{Fe}_3\text{Sn}_3\text{Ag}_3$ ribbon samples by the chemical *pseudo-dealloying* process, XPS was utilized. A chemical depth profile depth analysis was performed by sputtering with argon from 0 min to 40 min with an interval time of 10 min. A standard rate of sputtering of 0.4 nm/min (SiO_2 on Si wafer was used as a reference) was used to estimate the depth of surface investigated. An air side of untreated ribbon sample, and *pseudo-dealloyed* samples in diluted solution (DS, 5:1:4 volume ratio of NH_4OH , H_2O_2 , H_2O) with stirring and non-stirring i.e., DS-60min-NS, DS-60min-S, DS-360min-NS were selected for XPS investigation being the samples characterized by an evident change in morphology during the treatment. Detailed XPS sputter depth profile is shown in Figure 4.5. It is necessary to mention that prominent elements such as Ti, Zr, Cu and O were considered while the other elements such as Fe, Sn and Ag were detected to be below 2 at % and therefore discarded for the sake of clarity.

From the chemical depth profiles shown in Figure 4.3 (a) for the as-spun and air-aged (untreated) alloy state, an overall thickness of the native oxide layer of more than 16 nm can be estimated, according to the decaying oxygen profile. Remarkably, without sputtering (0 nm) the Cu concentration is high compared to that of Ti and Zr species, but it is strongly reduced after the first sputter step corresponding to the 4 nm depth. This implies that the outermost passive layer comprises mainly Cu-oxide species, while the inner layer region is richer in Ti- and Zr-oxides. This is opposite to the typical passive layer composition of most Zr-Cu- and Ti-Cu-based glasses and can be attributed to the relatively high Cu content of the alloy (40 at %) which can cause Cu surface segregation.

In Figure 4.3 (b), after treatment in diluted solution for 60 min without stirring (DS-60min-NS sample), the oxide layer on the amorphous alloy surface appears to be of similar thickness to the untreated surface. The change of the oxygen profile within the first sputter points may be attributed to the change in the surface roughness (Figure 4.3 c). Cu still dominates in the outermost oxide layer regions, Ti and Zr species the inner oxide layer regions. This is similarly observed when stirring the diluted solution during sample exposure for 60 min, DS-60min-S in Figure 4.3 (c). After prolonged exposure to this solution without stirring, i.e., up 360 min, DS-360min-NS sample, a substantial thickening of the porous (Figure 4.3 d) oxide layer can be derived. At all 4 sputter steps the oxygen concentration was high indicating that only the outer part of the formed oxide layer region was analyzed. This is related to a depletion of the Cu concentration already from the initial non-sputtered surface (0 nm) throughout all sputter

steps. This hints to a removal of the Cu species from the formed np surface region which are now mainly composed of Ti- and Zr-oxide species.

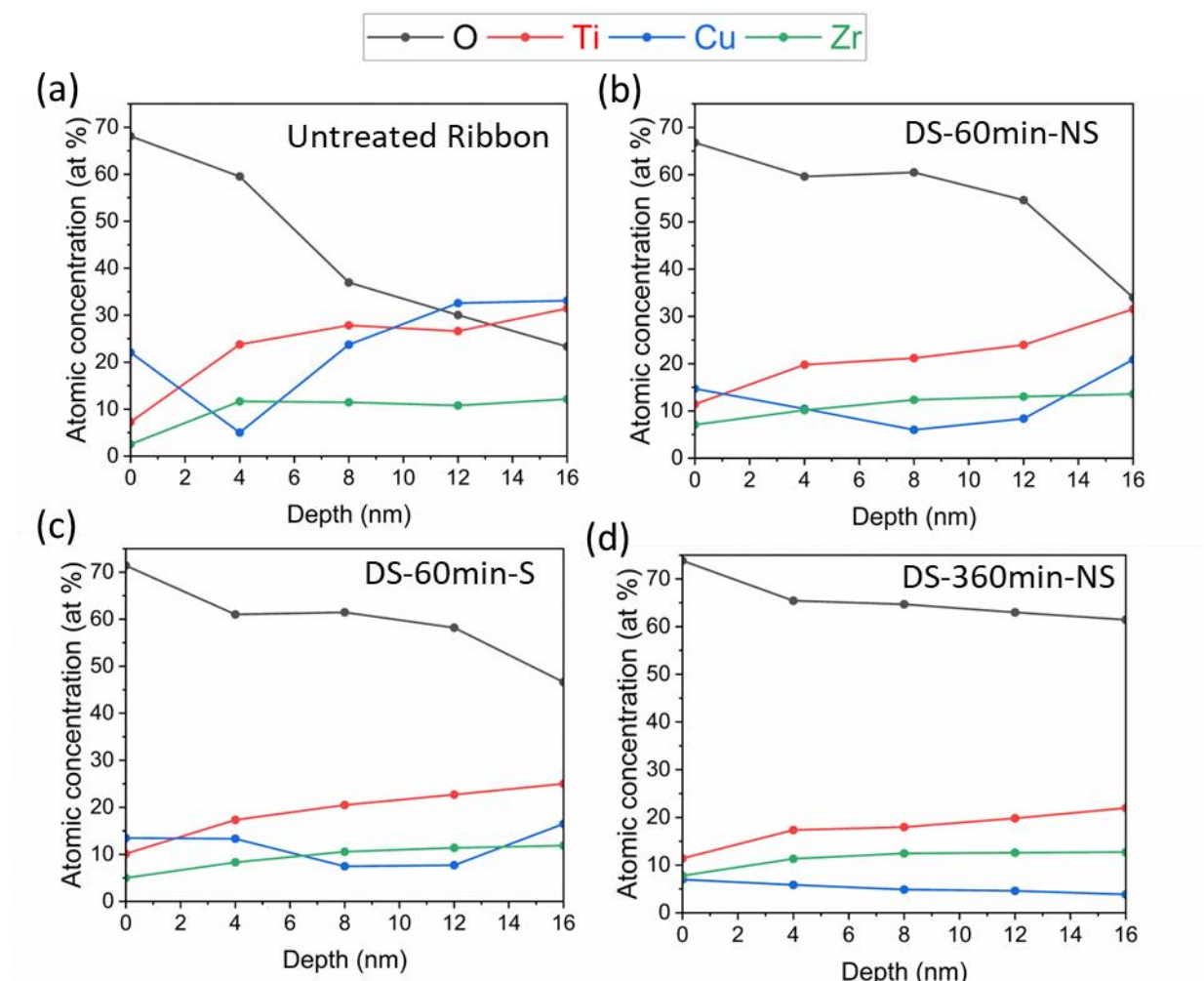


Figure 4.3. XPS sputter depth profile of $\text{Ti}_{40}\text{Cu}_{40}\text{Zr}_{11}\text{Fe}_3\text{Sn}_3\text{Ag}_3$ ribbon samples with O, Ti, Cu, Zr (a) untreated (air side), and *pseudo-dealloyed* samples in diluted ammonia solution (b) DS-60min-NS, (c) DS-60min-S, (d) DS-360min-NS. The reference rate of sputtering is 0.4 nm/min.

All the elements in the composition were detected using high resolution XPS spectra but only relevant elements such as O 1s, Ti 2p, Cu 2p were selected to be shown in Figure 4.4 (a-l). Additionally, the high resolution XPS spectra of Zr 3d is shown in Figure 4.6. Zr has specific binding energy for metallic Zr(0) at 178.9 eV and Zirconium oxide (ZrO_2) at 182.8 eV.

Characteristic XPS peaks reveal information on the chemical state of the elements based on their binding energy (BE) values. For instance, $\text{Ti}2p_{3/2}$ for the chemical states Ti(0), Ti(II), Ti(III), and Ti(IV) have a corresponding peak at 453.3 eV, 455.7 eV, 457.3 eV, and 458.5 eV, respectively. Cu metal (Cu(0)) has Cu $2p_{1/2}$ at 952.6 eV and Cu $2p_{3/2}$ at 932.6 eV. For the oxides of Cu, Cu_2O and CuO, the Cu $2p_{3/2}$ peak is at 932.4 eV (Cu(I)) and 933.6 eV (Cu(II)), respectively. Their O1s is comprised of the main peak corresponding to a structural oxygen

i.e., O^{2-} chemical state (BE at 530.5 eV) and adsorbed H_2O (BE at 533 eV) [261]. This information was used to identify the chemical state of the samples [262,263].

For the untreated sample (Figure 4.4 (a-c)), the spectra of O1s acquired at the surface (0 nm) show main peak corresponding to adsorbed water. While the presence of structural oxygen can be seen evidently in the spectra obtained from depth profile (0 nm-16 nm). Titanium on the surface appears to be in a stable Ti(IV) state likely related to TiO_2 . At 4 nm depth, Ti(II) can be seen in the spectra which is a short lived and unstable state, formed due to decomposition of TiO_x during the sputtering process [263]. Further increase in sputtering time reveals the presence of metallic titanium (Ti(0)). No apparent shifts can be seen with Cu peaks, ruling out the presence of Cu(II) species. Instead, Cu is present in either the Cu(I) or Cu(0) state as these two species only differ slightly in their binding energies [264], and cannot be distinguished unambiguously based on the given resolution. The spectra of Zr shows presence of zirconium oxide (ZrO_2) at 182.8 eV on the surface (0 nm) while during the depth profiling the spectra shifted to metallic Zr(0) at 178.9 eV (Figure 4.5 a). The spectra of Zr 3d presents similar trend as Ti 2p. Therefore, the presence of a mixed Ti/Zr oxide layer is observed on the surface, while at about 8 nm depth a metallic structure starts to appear in the as quenched ribbons beside the oxides that are gradually reducing in quantity.

Figure 4.4 (d-f) and (g-i) show the XPS spectra of DS-60min-NS and DS-60min-S samples, respectively. Here, the dominant O 1s peak corresponds to the structural oxygen while small peak of adsorbed water can be seen. The Ti peaks show the presence of TiO_2 (i.e., Ti(IV) is detected) on the surface, further sputtering from ~8nm showed a gradual peak shift from a mainly (Ti(IV)) state towards Ti(II) and later on to Ti(0) at ~16 nm, indicating that the bulk is solely in its metallic state. No apparent shifts can be seen with Cu peaks, ruling out the presence of Cu(II) species. Most likely Cu is present in either the Cu(I) or Cu(0) state. The spectra of Zr 3d shows presence of Zr(IV) i.e., ZrO_2 on the surface while during the depth profiling at ~16 nm, the spectra slightly shift to metallic state Zr(0) (Figure 4.5 b, c). For the DS-360min-NS sample in Figure 4.4 (j-l), the dominant O 1s peak corresponds to the structural oxygen. The chemical state of Ti on the surface is Ti(IV). Unlike in the previous samples, a sputtering of up to 16 nm depth did not result in the disappearance of higher oxidation states of Ti. Instead, the spectrum shows a broad peak comprised of Ti 2p_{3/2} peaks of different oxidation states, indicative of the presence of not only the Ti(0), but also the oxides at this depth. This points to a likely thicker titanium oxide layer indicating a larger *pseudo-dealloyed* layer. Cu 2p peaks do not show apparent shifts indicating presence of Cu(I) or Cu(0) state. The spectra of Zr 3d shows presence of Zr(IV) i.e., ZrO_2 on the surface but during the depth profiling at about 16 nm, the spectra show minor peak corresponding to metallic state Zr(0) while dominant peak still corresponds to Zr(IV), shown in Figure 4.5 d.

Summarizing, the results obtained from the XPS depth analysis of treated samples indicate a general depletion in concentration of Cu species from the surface of all the samples examined. For instance, in DS-360min-NS sample, the concentration of Cu measured on the surface is substantially lower than the concentration of Cu species on the DS-60min-NS and DS-60min-S samples. The treated surfaces are mostly composed of a layer of oxides likely from Ti and Zr.

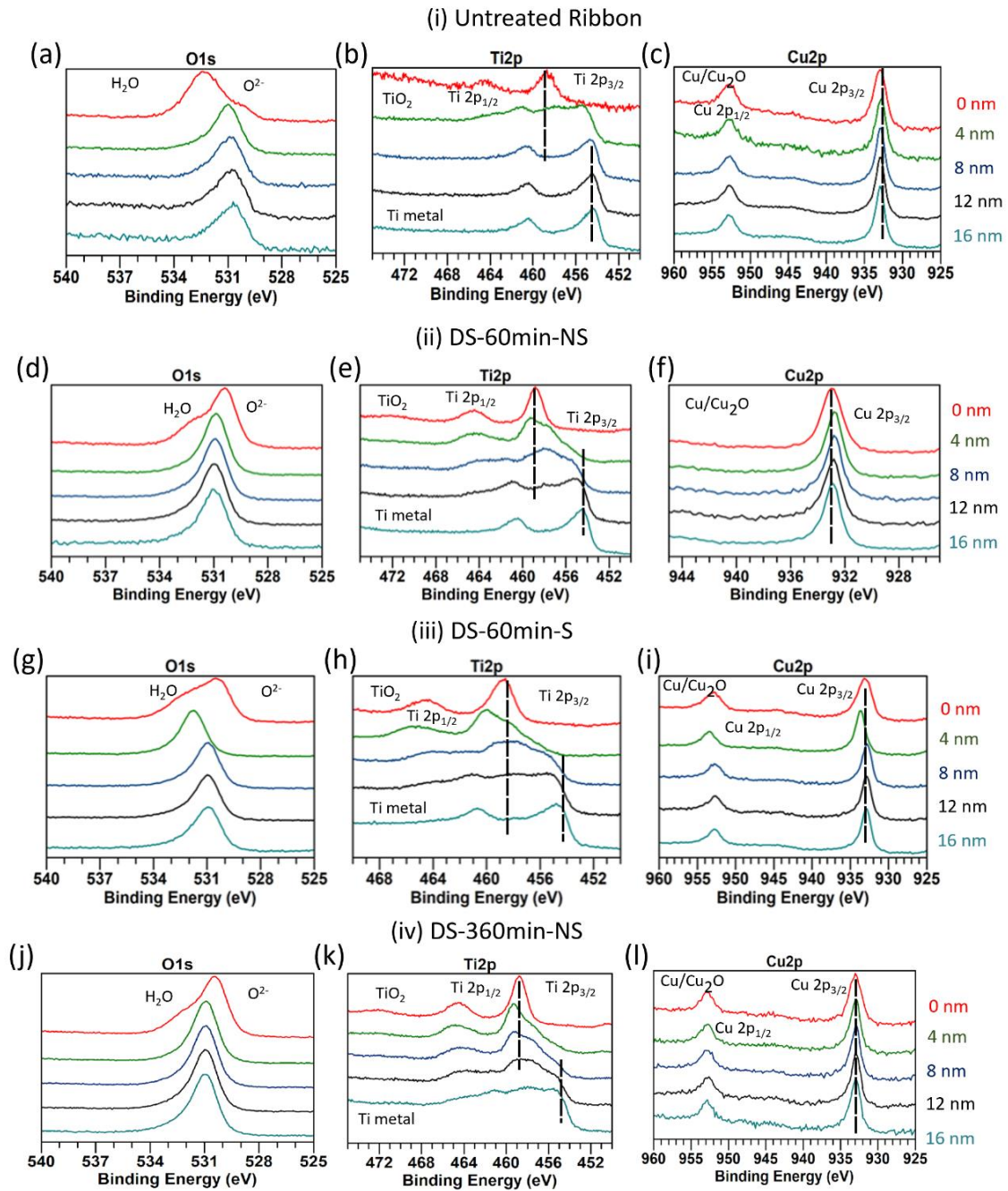


Figure 4.4. High resolution XPS spectra of O1s, Ti2p, Cu2p elements of (a-c) untreated, and *pseudo-dealloyed* samples in diluted ammonia solution (d-f) DS-60min-NS, (g-i) DS-60min-S, (j-l) DS-360min-NS.

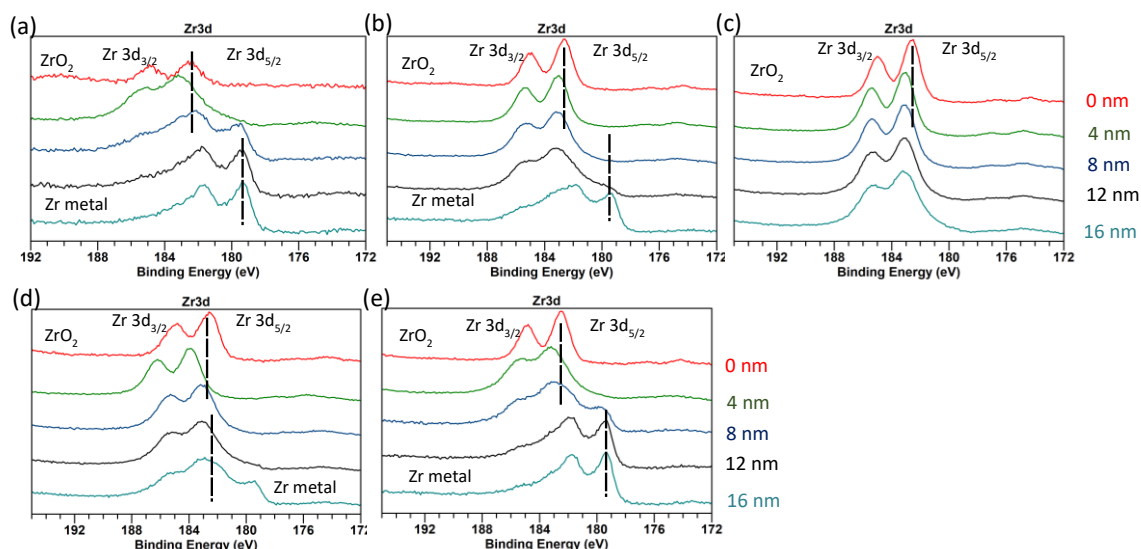


Figure 4.5. High resolution XPS scan of Zr 3d element on (a) untreated ribbon, (b) DS-60min-NS, (c) DS-360min-NS, (d) DS-60min-S, (e) H₂O₂-180min.

3.1.2. Ammonia-based concentrated solution

Further investigation was performed by changing the concentration of the electrolyte to understand the influence of solution concentration on the sample morphology. Concentrated solution composed of equal volume parts of NH₄OH and H₂O₂ (1:1) in non-stirred solution with immersion time of 60 min was selected to establish a comparison with DS-60min-NS, (DS-5:1:4 volume ratio of NH₄OH, H₂O₂, H₂O), because the sample showed a homogeneous morphology with similar pore and ligament size. The CS-60min-NS sample analyzed by FESEM (Figure 4.6 a-b) shows formation of np topography with an average ligament size of 12.4 ± 3.1 nm. The pore formation on the sample is hierarchically bimodal with smaller pores found within larger networks showing depressed (darker) regions within raised features (lighter regions). The average size of larger pore networks is 178.6 ± 44.6 nm (Figure 4.6 a). Whereas the average pore diameter of small pores is 15.3 ± 4.6 nm (Figure 4.6 b). The RMS roughness calculated by AFM is 4.7 ± 0.7 nm (Figure 4.6 c).

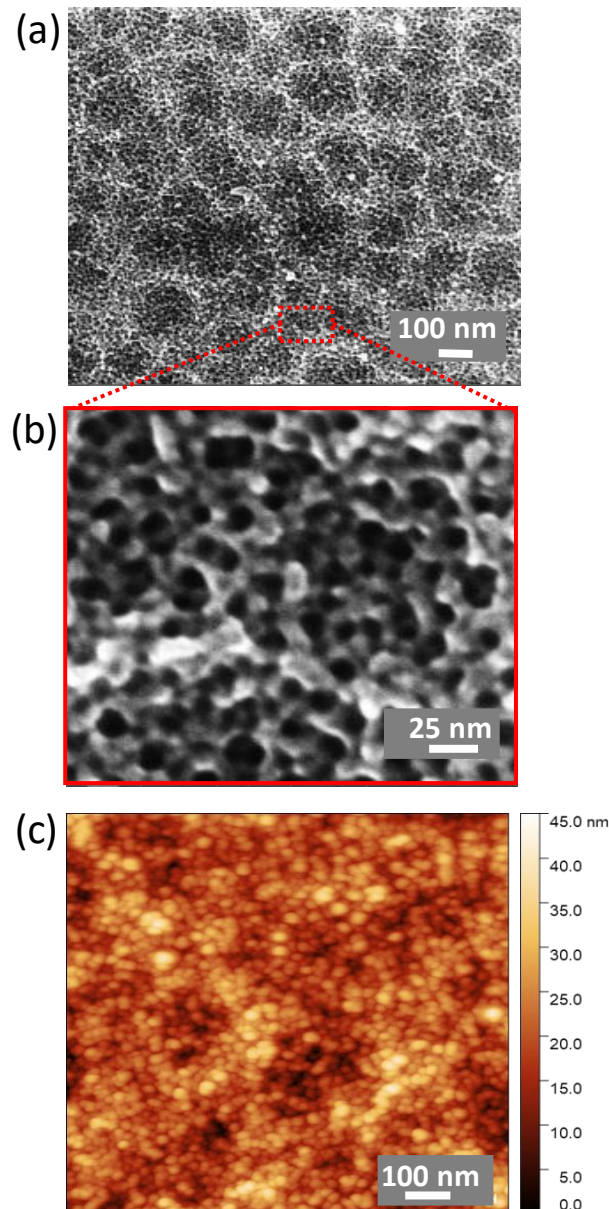


Figure 4.6. SEM image of CS-60min-NS (a) at low magnification (indicating the big pores), (b) at high magnification (indicating the small pores), (c) AFM image.

The results obtained from the samples treated for 60 min with concentrated solution and diluted solution in non-stirred condition (CS-60min-NS and DS-60min-NS) shows that a change in concentration of the electrolyte promotes a change in the morphology of the samples. The presence of a bimodal hierarchical distribution of pores, with larger size (150 nm) in CS-60min-NS, could be due to the presence of hydrogen peroxide in higher concentration, which is a strong oxidizer and can possibly facilitate faster surface diffusion of atoms.

3.2. Investigating the role of ammonium hydroxide and hydrogen peroxide

To better understand the role of ammonium hydroxide and hydrogen peroxide on selective removal of Cu, separate investigations were conducted by (i) immersing the as-quenched ribbon in ammonium hydroxide (NH_4OH , 25 %) at room temperature for 60 min and (ii) immersing the as-quenched ribbon in hydrogen peroxide (H_2O_2 , 30 %) at room temperature for 180 min. Figure 4.7 (a) shows FESEM micrographs of sample immersed in ammonium hydroxide at room temperature for 60 min. The result indicates that the morphology of the sample surface was not altered effectively as compared to DS-60min-NS sample. The surface shows the presence of corrosion products (white artefacts) and evolution of irregular porosities, indicating the slow rate of etching in the absence of an oxidizer like hydrogen peroxide.

Figure 4.7 (b) shows an XPS chemical depth profile analysis of the sample immersed in hydrogen peroxide for 180 min. It is observed that an oxide layer with more than 16 nm thickness is formed on the surface. The main inner oxide region is mainly composed of Ti and Zr species in equi-atomic percentage, while the outermost oxide region (0 nm) is enriched in Cu species.

Furthermore, high resolution XPS spectra in Figure 4.7 (c-e) shows the dominant O1s peak corresponding to the structural oxygen while small peak of adsorbed water can be seen. The Ti peaks show the presence of TiO_2 (i.e., Ti(IV) is detected) on the surface, further sputtering from 12 nm showed a gradual peak shift from a mainly (Ti(IV)) state to Ti(0) at 16 nm. No apparent shifts can be seen with Cu peaks, indicating presence of Cu(I) or Cu(0) state. The spectra of Zr3d shows presence of Zr (IV) i.e., ZrO_2 on the surface while during the depth profiling at 12 nm, the spectra slightly shift to metallic state Zr(0) (Figure 4.5 e). It is possible that the presence of hydrogen peroxide resulted in the growth of an oxide layer on the sample surface [265]. This phenomenon is observed on Ti rich sample surfaces, during the initial contact of hydrogen peroxide with a consequent Ti surfaces partial dissolution of native oxide layer. While with longer immersion time, the surface tends to show regrowth of the oxide layer which eventually grows denser [266].

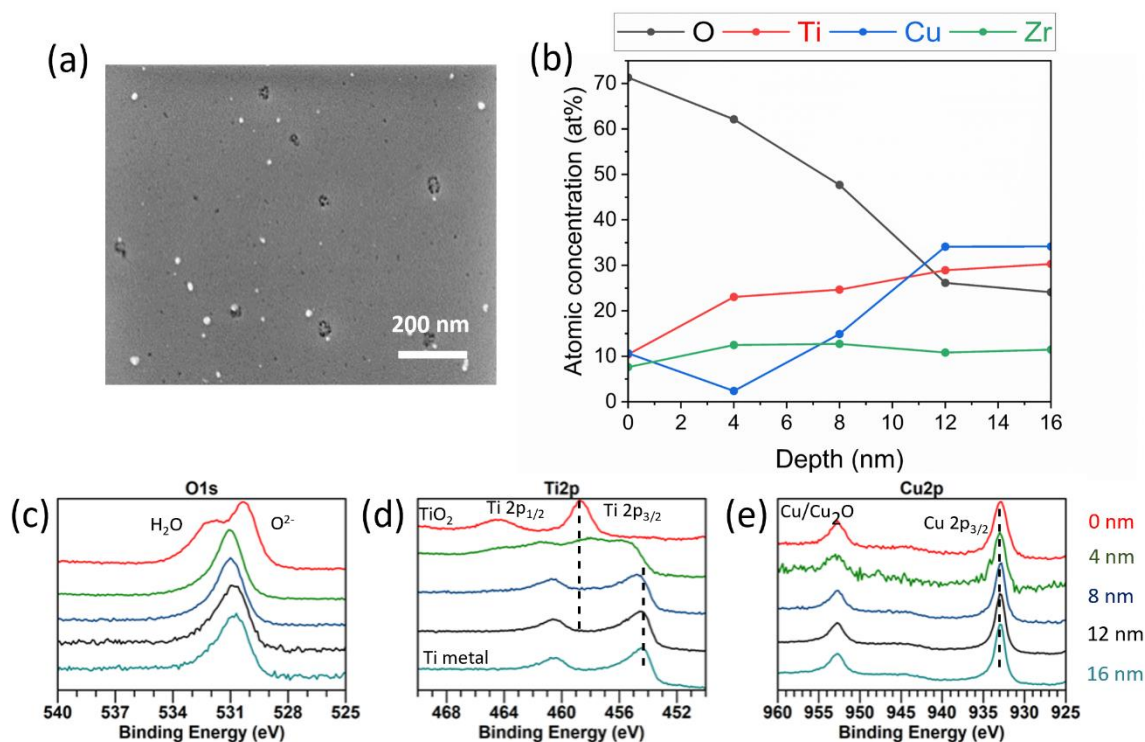


Figure 4.7. (a) SEM images of sample immersed in NH_4OH (25 %) at room temperature for 60 min, (b) XPS depth profile analysis of sample immersed in H_2O_2 (30 %) for 180 min at room temperature, (c-e) XPS high resolution spectra of O1s, Ti2p, Cu2p elements of sample immersed in H_2O_2 (30 %) for 180 min at room temperature.

The absorption spectra were obtained for a diluted ammonia solution (DS) serving as the blank solution, as well as for copper and titanium plates, and an amorphous ribbon sample immersed in DS (with a volume ratio of NH_4OH , H_2O_2 , and H_2O in 5:1:4). In Figure 4.8 (a), distinct color changes are observable upon immersion of samples in DS. Specifically, the copper plate induces a dark blue color representative of copper tetraamine complex [267], while the titanium plate does not alter the solution color. Notably, the amorphous ribbons in DS exhibit a light blue color.

To ensure minimal interference from solution bubbling, attributed to the gradual decomposition of hydrogen peroxide into water and oxygen, spectra were recorded after a 24-hour stabilization period. Figure 4.8 (b) highlights a prominent absorption peak at a wavelength of 655 nm for both the copper plate and ribbon samples immersed in DS. This peak corresponds to the formation of a copper tetraamine complex [268]. The observed disparity in absorption intensity between the copper plate and ribbon sample solutions can be attributed to variations in copper concentration within the respective samples.

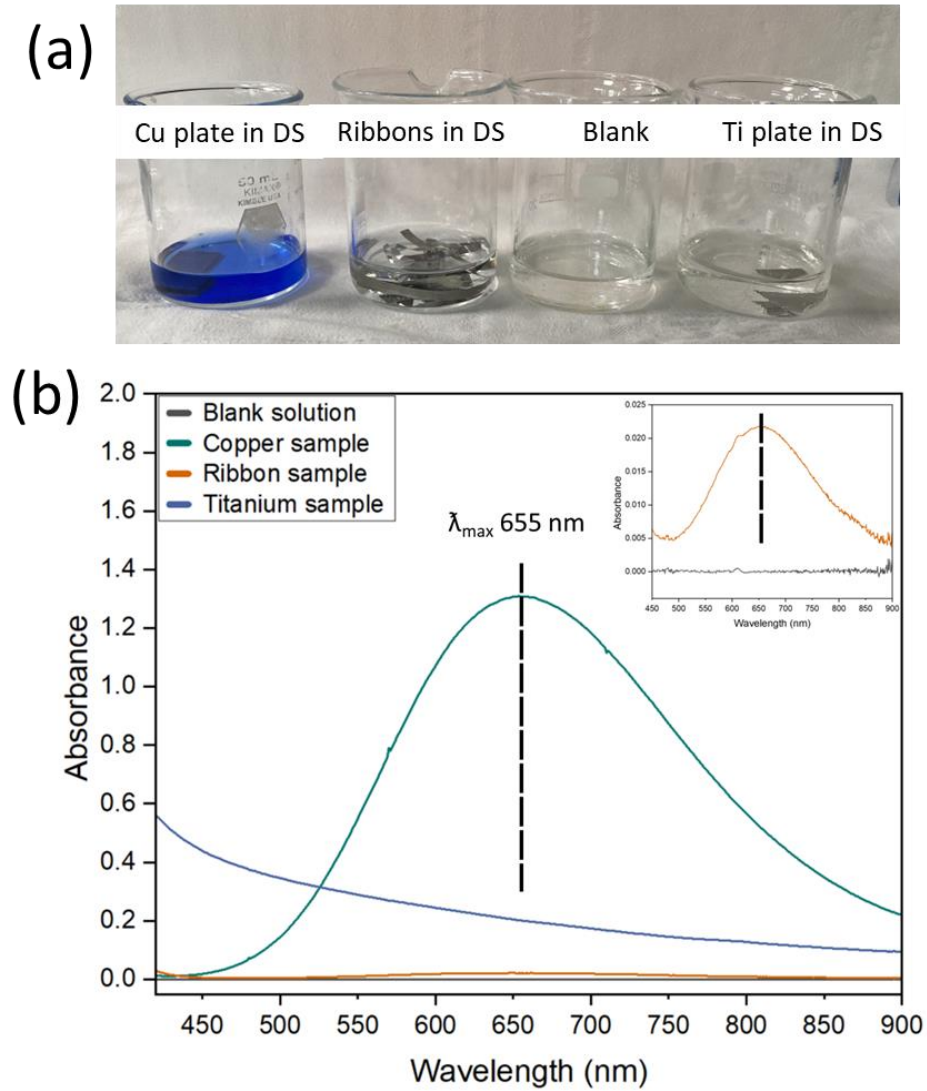


Figure 4.8. Absorption spectra of diluted ammonia solution (DS) as blank and copper plate, titanium plate, amorphous ribbon sample immersed in DS (5:1:4 volume ratio of NH_4OH , H_2O_2 , H_2O).

3.3. Pseudo-dealloying mechanism with ammonia-based solution

In this study, we have created a simplified schematic illustration (Figure 4.9) to depict the dissolution of Cu and the formation of a porous Ti/Zr oxide-rich layer. It is important to note that this model does not consider the atomistic scale for chemical *pseudo-dealloying* influenced by the experimental conditions in this research.

Additionally, a mechanism is proposed in this work for chemical *pseudo-dealloying* of $\text{Ti}_{40}\text{Cu}_{40}\text{Zr}_{11}\text{Fe}_3\text{Sn}_3\text{Ag}_3$ using an ammonia-based solution containing hydrogen peroxide, ammonium hydroxide and water with $\text{pH} = 10\text{--}12$. The hydrogen peroxide at this pH and room temperature decomposes over time into oxygen and water and it has been described as a base-catalyzed reaction [269–271]. Therefore, in the electrolyte the presence of O_2 and NH_4^+ is expected. The O_2 in free corrosion condition and in alkaline solution can be further reduced to form stable reaction product of OH^- [272]. When the untreated ribbon samples are immersed in the electrolyte, the mixed oxide layer of Ti, Zr and Cu present on the surface (Figure 4.6 a-c) is interacting with the solution. At this stage, ammonium ion reacts with copper oxide at the sample surface, generating water-soluble copper-ammonia complexes like $\text{Cu}(\text{NH}_3)_4^{2+}$ and $\text{Cu}(\text{NH}_3)_2^+$, facilitating its dissolution [237,273,274].

As soon as the oxide layer is removed, in the presence of oxygen and water, metallic copper, present underneath, undergoes oxidation resulting in the formation of copper oxides [275]. Subsequently, ammonium ions react with copper oxides as described before, resulting in the removal of copper atoms from the surface. Copper can also react with aqueous ammonia to form $\text{Cu}(\text{OH})_2$ which can later dissolve in excess ammonia to form a complex ion.

The phenomenon for the formation of copper-ammonia complexes has been widely reported, where in copper is etched using ammonia during oxidation of copper from dissolved oxygen in the solution [276–278]. The specific outcomes of these reactions depend on various conditions, including concentration, temperature, pH, and the unique characteristics of the copper surface. The intricate interplay between ammonia and copper is influenced by the oxidation state of copper and the presence of chemical species in the environment. Pourbaix stability diagram of the $\text{Cu-NH}_4\text{OH-H}_2\text{O}$ system at temperature 293 K has shown that solution pH is responsible for obtaining the copper tetra-amine complex in solution at pH ranging from 7 to 14 for the entire potential range [279].

The diluted solution (DS) used for chemical *pseudo-dealloying* includes a mixture of ammonium hydroxide, hydrogen peroxide, and water in 5:1:4 vol ratio, resulting in a basic $\text{pH} = 10.82$ (without any sample immersed). On the other hand, ammonium hydroxide (25 %) has a $\text{pH} = 11.7$. It was observed that after treatment for 1 h the pH shifts to 10.92 pH and after 6 h the pH shifts to 11.17. A similar change was observed for concentrated solution (CS) ammonium hydroxide, hydrogen peroxide (1:1), (Table 4.1). The slight changes in the pH of the solution with respect to immersion time can be due to the production of hydroxyl ion in the DS and CS [280,281].

Table 4.1. pH measurement of etching solution at different time points with (w) and without (wo) immersed sample, (t= 0h, 1h, 6h).

	pH at t=0 h	pH at t=1h	pH at t=6h	pH at t=24 h
NH₄OH (25 %)	11.7	-	-	-
Diluted Solution (wo) sample	10.82	10.92	11.17	9.62
Concentrated Solution (wo) sample	10.44	10.44	11.12	-
Diluted Solution (w) sample	-	11.35	11.76	9.60
Concentrated Solution (w) sample	-	11.26	11.22	-
Cu plate in DS				9.88
Ti plate in DS				10.56

It is also important to consider the surface reaction of Ti, Zr, Fe, Sn and Ag in the presence of mixture of hydrogen peroxide, water, and ammonium hydroxide. However, for the sake of simplicity, minor species such as Fe, Sn and Ag are not considered for the discussion.

It is likely when Cu begins to selectively remove from the surface, vacancies are created, wherein Ti and Zr ad-atoms can move by surface diffusion, creating ligaments. It is possible that Ti and Zr undergo immediate passivation in presence of hydrogen peroxide (water and O₂). Ti can react with H₂O₂ to form TiO₂ with subsequent evolution of H₂ gas, further TiO₂ hydrolyze with water to form titanium hydroxide [282]. Hence, an increased amount of oxidized Ti (and Zr) can be detected closer to the surface of the treated ribbon samples in the XPS spectra. Rapid oxidation of Ti and Zr atoms, which are generated during the chemical surface etching process can significantly hinder surface diffusion resulting in a surface limited dealloying of few nanometers in depth.

It is also possible that the subsequent dissolution of Cu from bulk allows formation of ligaments and pores of varying dimension influenced by changing immersion time. The atoms of Cu can diffuse from the bulk to the surface forming copper ammonia complexes in the solution. Although due to active passivation of Ti/Zr, it is possible that Cu atoms are trapped in metallic state. This phenomenon is widely observed in Au based alloys where small fraction of less noble elements remains in the np structure of Au after dealloying [283,284].

The findings described in Figure 4.3 (b-c), i.e., after exposure of samples to diluted solution for 60 min in non-stirred and stirred convection (DS-60min-NS, DS-60min-S) indicates that Cu species can be detected on the outermost region of the oxide layer of the sample, whereas

after 360 min immersion, the presence of Cu species is drastically reduced from the surface as compared to the untreated ribbon. It is likely that after 60 min of immersion excessive Cu species can precipitate on the sample surface while after longer immersion time such as 360 min the precipitate of Cu species reacts with ammonium ions forming copper-ammonia complex in the solution.

The change in the surface morphology in the diluted solution (5:1:4 vol ratio of NH_4OH , H_2O_2 , H_2O) and concentrated solution (1:1 vol ratio of NH_4OH , H_2O_2) can be correlated to elevated concentration of hydrogen peroxide (H_2O_2) which can enhance the surface reactivity, in turn, accelerating the formation of np oxide structures. Numerous scientific studies have documented notable changes in the surface morphology of Ti following exposure to hydrogen peroxide solutions with varying concentrations, although these findings are not directly related to atomic diffusion [285–287].

While our research has explored the complexities of copper dissolution in ammonia-based solution, the specific details regarding the process involving formation of a nano-porous Ti/Zr oxide layer and the simultaneous dissolution of copper from the sample surface remains unclear with ammonia-based dealloying. The current study highlights the need for further research to unravel the reaction kinetics and *pseudo-dealloying* process. This step is crucial in advancing our understanding of the chemical behavior of the solution and sets the stage for future investigations into the mechanisms behind surface diffusion, oxide layer formation, and copper dissolution.

Modified surfaces with enriched titanium oxide layer have shown enhanced biocompatibility and corrosion resistance, thereby making it suitable for implant application [288–290]. Therefore, the *pseudo-dealloyed* samples can be interesting for further evaluation of biocompatibility.

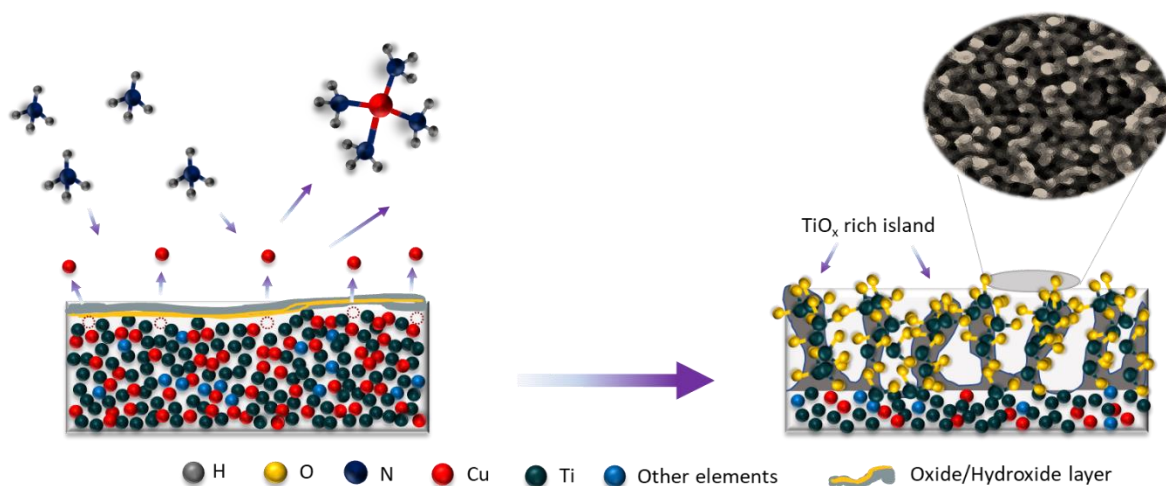


Figure 4.9. Schematic illustration of *pseudo-dealloying* of copper from Ti-Cu based amorphous alloy (in cross section) while immersion in ammonia-based solution.

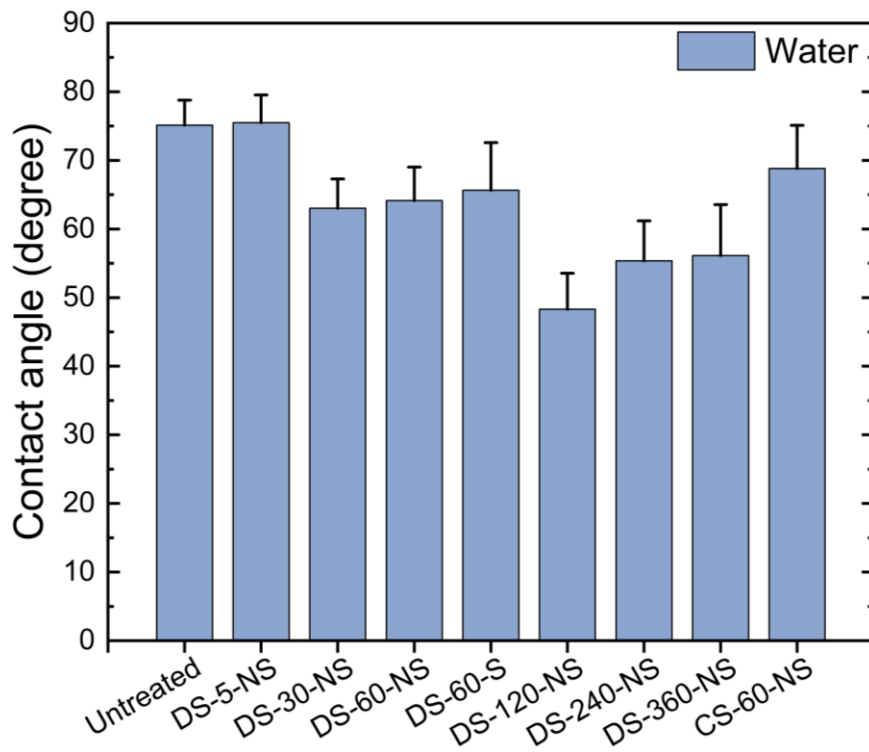
3.4. Wettability study

Wetting phenomena explains interaction of biomaterials with physiological environment when implanted in the body. This can also influence the adhesion and proliferation of cells, interaction/coagulation of blood, protein activation/adsorption and adhesion of bacteria [199,291–293]. Surface free energy is another parameter that can influence the wettability and adhesion strength of materials [294]. Therefore, contact angle and surface free energy of *pseudo-dealloyed* sample surfaces were analyzed. The wettability is measured by performing contact angle (CA) tests, which can be categorized as hydrophilic ($CA < 90^\circ$), hydrophobic ($CA > 90^\circ$), superhydrophilic ($CA < 10^\circ$), and superhydrophobic ($CA > 150^\circ$) [295]. Young's model is used for describing wetting on ideally smooth surfaces, while for describing wetting on rough surfaces, the Wenzel and Cassie-Baxter model is used [296]. Figure 4.10 shows the contact angle of the untreated and *pseudo-dealloyed* samples using a polar solvent i.e., water. In the polar solvent, the contact angle of all the samples showed hydrophilic wetting behavior, which follows the Wenzel model of wetting. The change in the wettability of the samples is mainly affected by the changes in the morphology and roughness of the samples as observed with SEM. The samples treated for 60 mins in concentrated solution (1:1 vol ratio of NH_4OH , H_2O_2) showed contact angle higher than samples treated with diluted solution (5:1:4 vol ratio of NH_4OH , H_2O_2 , H_2O) for 60 min in non-stirring and stirring condition which can be due to the difference in the surface morphology, that CS-60min-NS sample had bimodal porosity resulting in higher surface area.

The contact angle in water and diiodomethane is used to calculate the surface free energy (Table 4.2) using Owen-Wendt equation [297]. The trend in surface free energy (highest to lowest) for the sample is: DS-120min-NS (59.3 mN/m) > DS-240min-NS (55.8 mN/m) > DS-360min-NS (53.2 mN/m) > DS-60min-NS (50.2 mN/m), DS-60min-S (50.2 mN/m), DS-30min-NS (50.3 mN/m) > CS-60min-NS (46.9 mN/m) > DS-5min-NS (41.0 mN/m) > Untreated sample (40.9 mN/m). Surface free energy, being correlated to contact angle, is influenced by the change in morphology so that with increasing the treatment time the surface free energy is higher, while lowering the treatment time results in lower surface free energy.

Table 4.2. Contact angle and surface free energy measurement of untreated and *pseudo-dealloyed* samples (n=9).

Sample	Contact angle (°) (deionized water)	Contact angle (°) (Di-iodomethane)	Surface free energy (mN/m)
Untreated	75.1 ± 3.6	50.2 ± 5.4	40.9
DS-5min-NS	75.5 ± 4.0	49.5 ± 2.9	41.0
DS-30min-NS	63.0 ± 4.2	40.5 ± 3.0	50.3
DS-60min-NS	64.1 ± 4.8	39.2 ± 4.5	50.2
DS-60min-S	65.6 ± 6.9	36.9 ± 2.6	50.2
DS-120min-NS	48.3 ± 5.2	37.9 ± 3.0	59.3
DS-240min-NS	55.4 ± 5.8	36.4 ± 4.1	55.8
DS-360min-NS	56.1 ± 7.4	43.8 ± 1.9	53.2
CS-60min-NS	68.8 ± 6.3	42.1 ± 2.3	46.9

Figure 4.10. Wettability measurement using polar (i.e., deionized water) solvent on untreated and *pseudo-dealloyed* samples.

3.5. Hemocompatibility study

The hemocompatibility of the samples was evaluated using Mg alloy and quartz particles as positive reference material. The untreated and two *pseudo-dealloyed* samples for 60 min in non-stirred conditions DS-60min-NS (NH₄OH, H₂O₂, and H₂O in 5:1:4 vol ratio) and CS-60min-NS (NH₄OH, H₂O₂, in 1:1 vol ratio) were selected for hemocompatibility analysis. The DS-60min-NS sample was selected due to its homogeneous morphology and chemical composition which showed dominance of Cu species on the outermost oxide layer region, Ti and Zr species in the inner oxide layer. While CS-60min-NS sample is selected due to its bimodal morphology.

The hemolytic activity was assessed using defibrinated sheep whole blood and purified RBCs and is reported in Figure 4.11 (a) and (b) respectively. The hemolytic activity was calculated by measuring the absorbance of released hemoglobin during the rupture of RBCs when in contact with the ribbons. After 60 min of incubation, all the ribbon samples showed no evidence of hemolysis both in contact with whole blood (also containing the plasmatic fraction, white cells, and platelets) and with purified RBCs (containing only the cellular fraction). The inactivity of samples in blood could be due to the passivation of the surface after treatment, which enhances its resistance to release of toxic ions that may perturb the RBC membrane. It is important to carefully study the interaction of implants with blood to mitigate destruction or activation of blood components [298]. The hemolysis percentage of the ribbon samples was below 1.5 %, which is non hemolytic according to ASTM F756-17 standard. The study of hemoglobin adsorption on unetched and etched samples showed no significant adsorption of hemoglobin by the samples (Figure 4.11 c).

Notably, the samples did not induce RBC rupture even when the plasma was removed. It is known that plasma can boost up the hemocompatibility of materials because of the proteins and other biomolecules that may coat the material surface preventing interaction with RBC's [299]. As quenched ribbons were also inactive towards RBCs, and ribbon samples could be compatible with biological membranes in general. Therefore, they can be suitable for blood contacting device application such as stents [300,301].

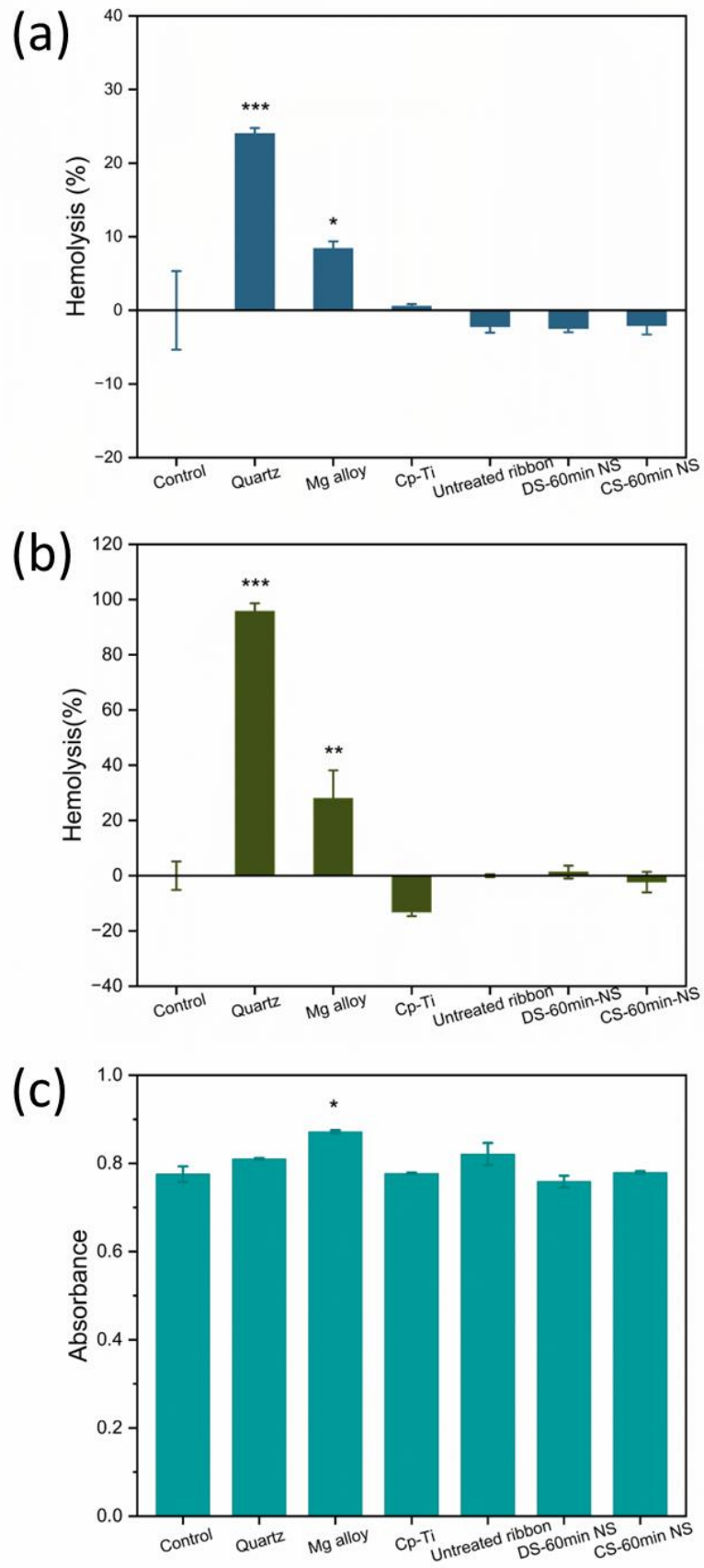


Figure 4.11. Hemocompatibility of ribbon before and after *pseudo-dealloying* treatment. Ribbons were incubated for 60 minutes with (a) defibrinated whole blood of sheep, (b) purified

RBCs, (c) Hemoglobin adsorption by the samples. Mg alloy and quartz particles were used as positive reference, cp-Ti was used as negative reference in each set of data, respectively. Values reflect the fraction of the total hemoglobin content released and are reported as mean \pm SEM of three independent experiments. Data were analyzed with one-way ANOVA, followed by Dunnett's post-hoc test. *P < 0.05, **P < 0.01, ***P < 0.001 vs. control (i.e., only PBS).

3.6. Metal ion release and release of reactive oxygen species study

Metal ion release: Assessed using ICP-MS to explore potential leaching from the sample surface in order to determine the possible cytotoxic effect arising for the samples. The samples were immersed in DMEM cell culture media for 3 days at 37 °C, and the measured ions released in the cell culture media are depicted in Figure 4.12 (a). A notable difference is evident, with DS-60min-NS exhibiting the highest release of Cu ions, followed by CS-60min-NS and the untreated ribbon sample, which displays limited release. The release of Cu in the DMEM media may be attributed to the presence of Cu in the outer region of the np layer of DS-60min-NS (NH₄OH, H₂O₂, and H₂O in 5:1:4 vol ratio) and CS-60min-NS (NH₄OH, H₂O₂, in 1:1 vol ratio) samples. The release of Cu ions in the DMEM media can be ascribed to the existence of Cu species predominantly present in the outer region of the np layer on the treated samples. The XPS sputter depth profile data supports this observation, revealing that Cu species remains detectable in the outermost oxide layer regions subsequently impacting the release of Cu ions into the surrounding media.

Reactive oxygen species: Hydroxyl radical release was quantified in a cell-free system simulating the inflammatory environment within the human body to determine possible antimicrobial activity of the sample. DS-60min-NS exhibited greater reactivity in hydroxyl radical release after 10 minutes of incubation compared to the other samples (Figure 4.12 b). Reactivity further increased at 30 and 60 minutes of incubation. Similarly, the CS-60min-NS sample demonstrated the ability to release hydroxyl radicals, significantly surpassing the untreated ribbon sample. The observed trend in hydroxyl radical generation by the samples corresponded to the release of Cu ions from the sample surface, suggesting the involvement of Cu ions in the mechanism of hydroxyl radical generation. Notably, Cu is recognized for generating reactive hydroxyl species in a Fenton-type reaction, as depicted in the reaction 4.1 [302,303]. The process of Cu killing bacteria involves several key steps. Firstly, Cu damages both the outer and inner membranes of bacterial cells. This membrane damage is considered a crucial initial event in contact killing [304,305], which leads to protein oxidation and degradation of DNA [306]. Secondly, the toxicity of Cu ions is associated with their ability to catalyze Fenton chemistry, leading to the generation of reactive oxygen species (ROS). ROS can cause irreversible damage to cellular components and disrupt the normal functioning of the bacterial cells. This oxidative damage can inhibit the respiratory chain, divert electrons, and further enhance ROS production, resulting in a cascade of detrimental effects on the bacteria [307,308]. It is observed in the XPS sputter depth profiling, the concentration of Cu species is

evident on the surface and drastically diminishes, with Ti and Zr species becoming dominant in the inner oxide layer regions. This transition in composition could influence the release of Cu species which produce ROS and presence of Ti oxide species can additionally contribute to the generation of hydroxyl radical species. The emission of $\cdot\text{OH}$ in the absence of light may be attributed to the binding of H_2O_2 on the Ti(IV) surface, resulting in the formation of hydroperoxyl radicals ($>\text{Ti III}-\cdot\text{OOH}$) through an inner-sphere electron transfer mechanism. The hydroperoxyl radicals generated on the surface can undergo additional decomposition to generate $\cdot\text{OH}$ radicals (discussed in detail in chapter 3 section 3.4).

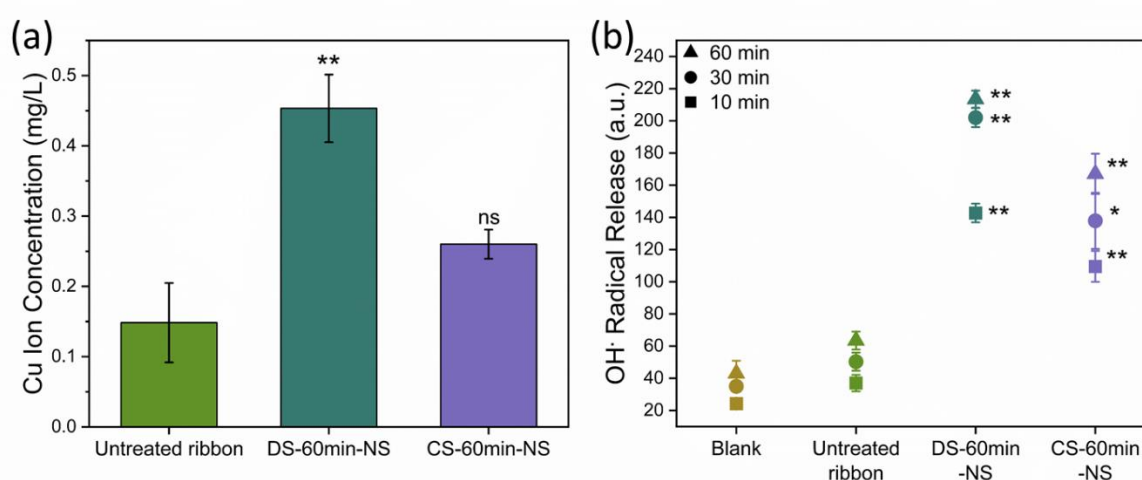


Figure 4.12. (a) ICP-MS measurement of Cu ions release in cell culture media without cells after 3 days of incubation, (b) DMPO- OH adduct concentration measured by double integration of EPR spectra of samples after 10, 30, 60 min of incubation. Data represented with mean \pm SEM of three independent experiments and analyzed using ordinary one-way ANOVA, followed by Dunnett's post-hoc test. * $P < 0.05$, ** $P < 0.01$ (treated vs untreated ribbons)

3.7. Biofilm formation and bacterial adhesion study with *Pseudomonas aeruginosa* (PAO1)

To measure biofilm formation, Crystal violet (1 %) was used to stain the biomass adhered to the surface of the samples. As CV binds non-specifically to cells and extracellular polymeric substances, it allows us to conduct a quantification of the biofilm biomass. The results showed that, when *P. aeruginosa* biofilms are grown in contact with the different groups for 24 h, it is possible to observe a significant difference between the untreated ribbons, DS-60min-NS (NH_4OH , H_2O_2 , and H_2O in 5:1:4 vol ratio) and CS-60min-NS (NH_4OH , H_2O_2 , in 1:1 vol ratio) samples in comparison to cp-Ti, which suggests that the ribbons possess an antimicrobial effect

as shown on Figure 4.13. The sample DS-60min-NS proved to be as effective as cp-Cu, followed by CS-60min-NS and the untreated ribbon.

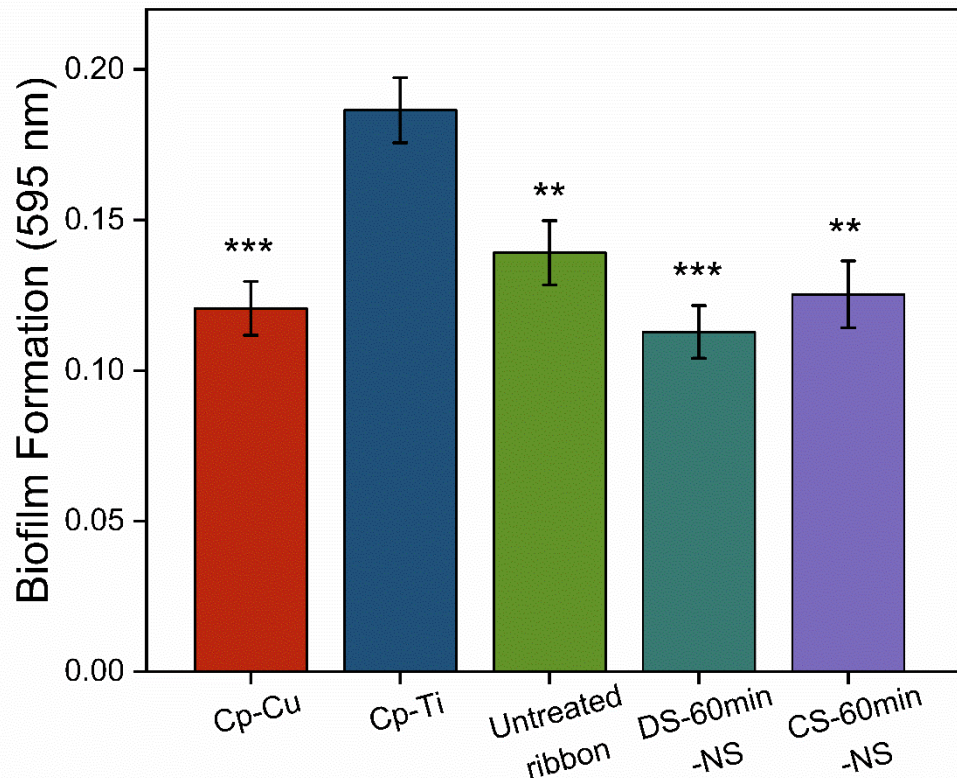


Figure 4.13. Biofilm formation study by *P. aeruginosa* analyzed using 1 % crystal violet assay after 24 h incubation. Data represented with mean \pm SEM of three independent experiments and analyzed using ordinary one-way ANOVA, followed by Dunnett's post hoc test. **P < 0.01, ***P < 0.001 (vs cp-Ti).

The samples were also analyzed qualitatively by AFM to identify bacterial adherence, coverage, and bacterial surface behavior in contact with these antimicrobial surfaces. On Figure 4.14, it is possible to visualize the samples before incubation (topographical analysis) and after incubation (biological analysis) in 3D and 2D top view.

The average roughness (Ra) and root mean square roughness (Rq) was calculated for each sample and presented below each image for comparison between analyses. Decrease adherent and planktonic bacteria prevalence were significantly seen after 2 hours when *P. aeruginosa* came into contact with cp-Cu and DS-60min-NS as confirmed by the decrease of roughness in the surface. While on the untreated and CS-60min-NS samples, it was possible to appreciate an agglomeration of bacteria suggesting early-biofilm formation. On CS-60min-NS, it was possible to differentiate each cell from the cluster alongside an increase of the roughness confirming bacterial presence. Simultaneously on the untreated ribbon there is a slight increase in roughness, alongside agglomerated bacteria that are not easily visualized individually after 2 hours.

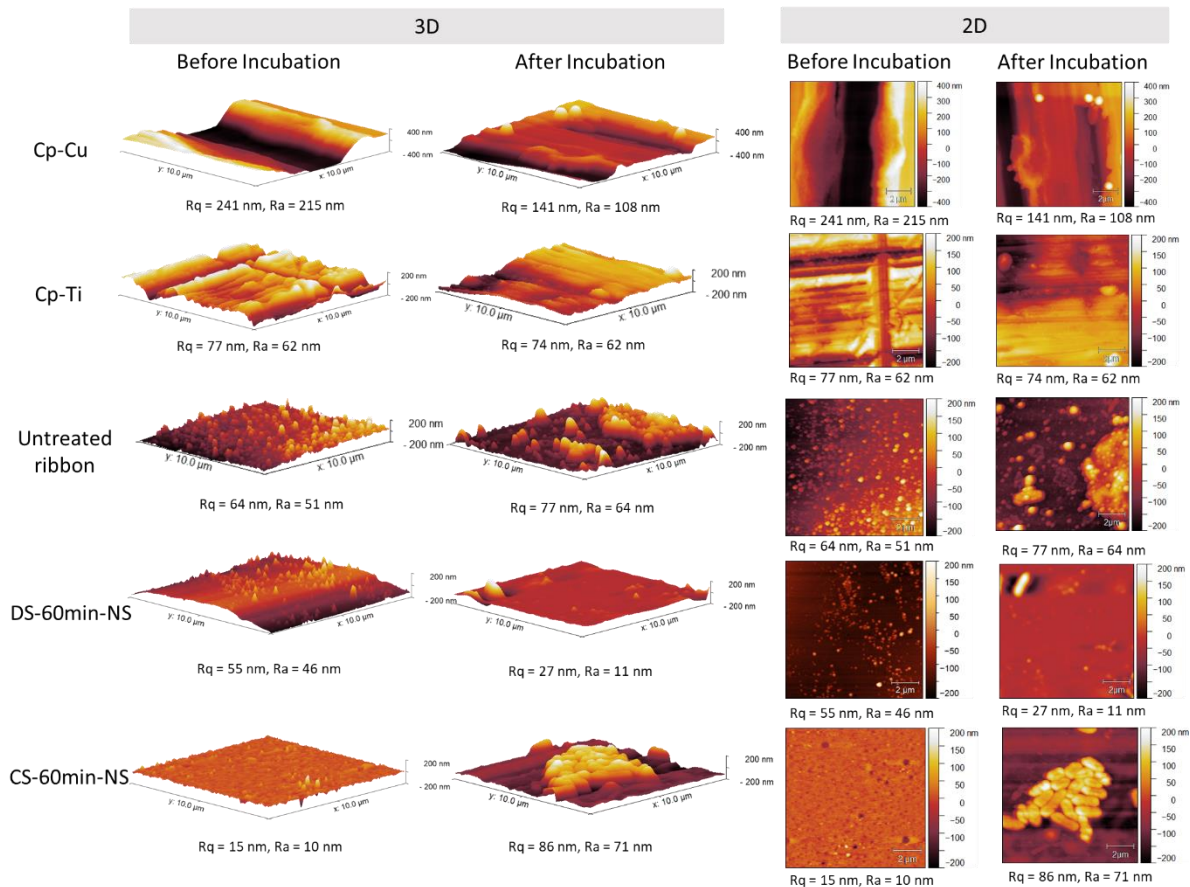


Figure 4.14. 3D and 2D topographical and biological AFM qualitative analysis before and after incubation with *Pseudomonas aeruginosa* (PAO1) at 10 x 10 μm for 2 hours. The height data scale was uniform for all samples at 400 nm except for cp-Cu with 800 nm. All samples were analyzed using the software Gwyddion.

3.8. In vitro cytocompatibility assessment with Saos-2 and HOB cells

In the case of the treated sample DS-60min-NS (NH₄OH, H₂O₂, and H₂O in 5:1:4 vol ratio) and CS-60min-NS (NH₄OH, H₂O₂, in 1:1 vol ratio), it is observed that the surfaces showed significantly high concentration of Cu ions released in the cell culture media. Therefore, it is important to determine the tolerance limit of the treated surfaces by investigating the cytocompatibility of the sample to obtain a balanced activity as an implant material.

The cytocompatibility of the sample were investigated using two cell lines i.e., Saos-2 and HOB. The cytocompatibility studies included cell viability test using live/dead kit after 3 days in culture, cell proliferation after 1, 3, and 7 days, and cell differentiation studies involving ALP activity after 7 and 14 days.

On day 3 after cell seeding, the cytotoxicity of the samples was analyzed using live/dead kit. Live cells were stained green and dead cells were stained red via calcein and ethidium bromide staining, respectively. The result showed abundance of live cells, while only a few dead cells were observed on the surface of DS-60min-NS and CS-60min-NS sample (Figure 4.15). For Saos-2 cells, rounded cells were observed on the DS-60min-NS and CS-60min-NS sample. However, for HOB cells, the samples showed well spread cells on the surface after 3 days in culture. The cell viability of samples was above 98 % and 96 % for Saos-2 and HOB cells, respectively. In addition, the number of adhered live cells on the sample surface were quantified (Table 4.3). We observed that the untreated ribbon presented the highest number of Saos-2 cells, followed by the DS-60min-NS, glass control and the CS-60min-NS samples. For instance, the number of HOB cells was higher on DS-60min-NS than on CS-60min-NS and glass control, being the untreated ribbon the sample with less cells. It is noteworthy to acknowledge that HOB cells, being larger in size than Saos-2 cells, resulted in comparatively lower cell counts across all tested samples.

Table 4.3. The number of adhered Saos-2 and HOB cells on the samples.

Samples	Saos-2 cells/cm ²	HOB cells/cm ²
untreated ribbon	63146 ± 6479	10423 ± 2170
DS-60min-NS	53913 ± 5690	14190 ± 3678
CS-60min-NS	39550 ± 4498	13660 ± 6256
glass control	46466 ± 10070	13194 ± 2244

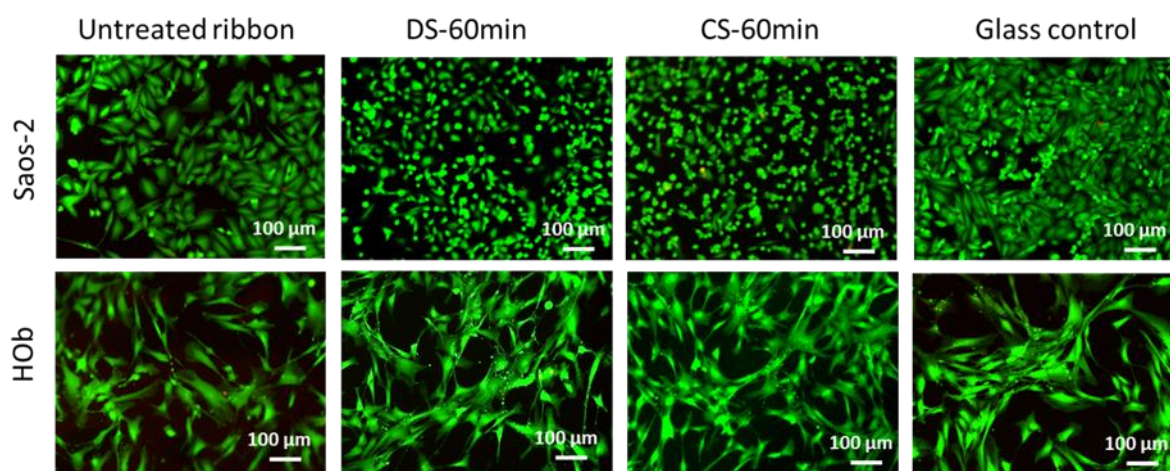


Figure 4.15. Cytotoxicity measurements using live/dead kit measured on Saos-2 and HOB cells after 3 days of incubation. Live cells represented in green and dead cells in red.

As stated, the morphology of the adhered cells on the samples was analyzed using SEM (figure 4.16). Saos-2 cells grown over the untreated ribbon samples showed flat cells after 3 days in culture. However, over DS-60min-NS sample some cells presented a more rounded morphology, along with some flat well adhered cells (shown in the inset) with polygonal morphologies and filipodia spread on the surface. In CS-60min-NS sample, flat cells were observed with polygonal morphology with contacts between cells, although few rounded cells were also observed in the vicinity of the flat cells (shown in the inset). The presence of rounded cells could indicate some degree of cell death. In few cases, the morphology was compatible with apoptosis, a type of regulated cell death [309–311]. These results could be due to surface chemistry of the DS-60min-NS and CS-60min-NS samples which show presence of Cu species on the near surface region of the *pseudo-dealloyed* sample. On the other hand, HOb cells cultured on all samples were flat and well spread on the surface of all samples. Prolonged filopodia extensions were observed on all the samples which indicate presence of healthy cells with visible nucleus and nucleoli within the nucleus. Interestingly, the presence of rounded Saos-2 cells previously observed on DS-60min-NS and CS-60min-NS samples was not observed for HOb cells. Both cell lines are osteoblasts, but from different origins. Saos-2 cells are tumoral cells, whereas HOb are cells isolated from healthy patients. In this regard, the results showed a different behavior when cultured on the same surface type.

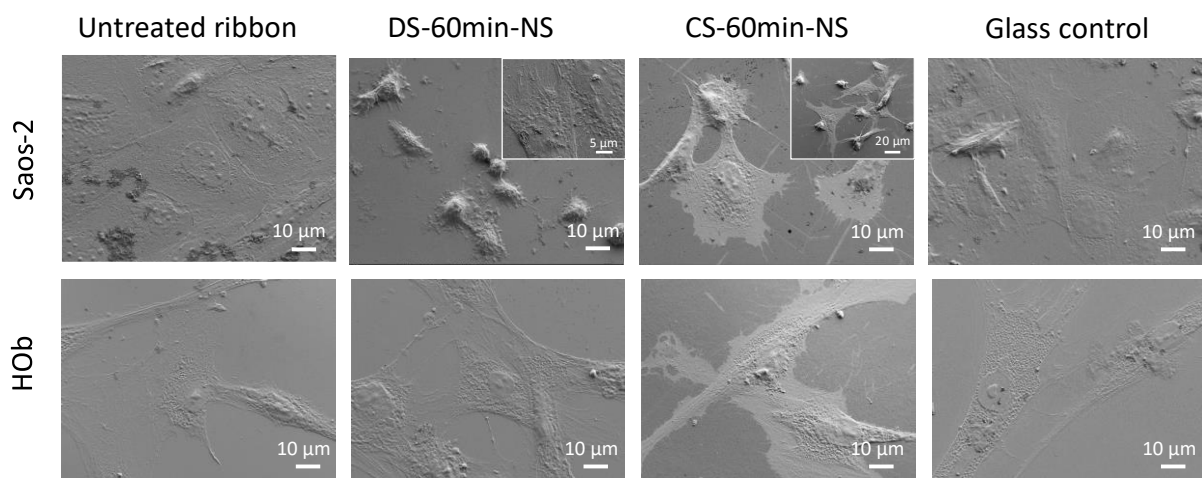


Figure 4.16. SEM micrographs of Saos-2 and HOb cells on sample surfaces after 3 days of incubation.

Adhesion was studied through the analysis of stress fibers via the actin filaments staining of Saos-2 and HOb cells (figure 4.17). The cells grown on all sample surfaces showed well defined actin stress fibers after 3 days of incubation. This indicates that cells were able to adhere and spread to the surface of the samples. The multidirectional distribution of the actin filaments could be due to surface topography of the sample. The actin filaments can be seen aligning at one end forming contact points between cells to cells or cells to substrate. For Saos-

2 cells, few cells showed short and disrupted actin bundles which corresponds to less spread cells or rounded cells growing on DS-60min-NS and CS-60min-NS samples. These results are in agreement with the ones observed for morphology using SEM.

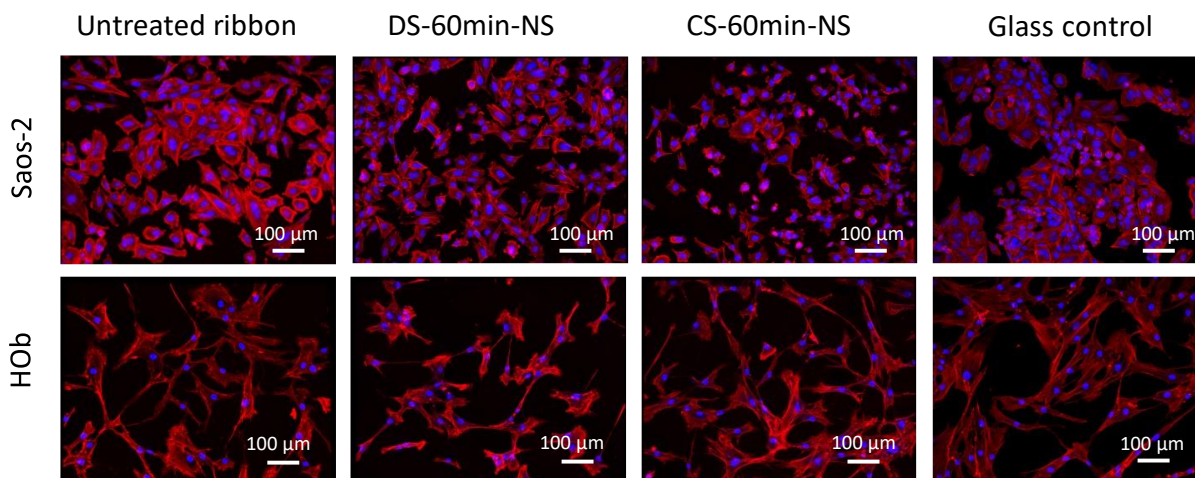


Figure 4.17. CLSM images of samples with Saos-2 and HOb cells after 3 days of incubation. Stress fibers (actin; red) and nuclei (DNA; blue).

Furthermore, Saos-2 and HOb cell proliferation was analyzed after 1, 3, 7 days in culture (figure 4.18 a, b). The results showed no significant differences on Saos-2 neither on HOb cell proliferation among untreated ribbon, DS-60min and CS-60min samples over time. The gradual increase in the cell proliferation between 3 and 7 days indicates that both cell lines were able to adhere to the sample surface and to proliferate. By contrast, significant differences were found in cell proliferation between the three samples (untreated ribbon, DS-60min and CS-60min samples) and the glass control samples. Denoting that, at least, during the first days on culture, the metabolic activity is higher for both type of cells growing on glass control surfaces, even though no cytotoxicity was detected.

Finally, the samples were investigated for cell differentiation by measuring ALP enzyme activity of Saos-2 cells after 7 and 14 days in culture (figure 4.18 c) and HOb cells after 14 days (figure 4.18 d). The ALP activity of Saos-2 cells growing on samples was already detected after 7 days in culture, and the activity was maintained after 14 days in culture. No significant difference between the samples and glass coverslips was observed for both time points evaluated. For HOb cells, ALP activity of cells growing on the three samples was detected, although the activity was lower compared to Saos-2 cells. Similar ALP activity was observed among the samples and significant differences were observed when comparing the samples with glass control.

Saos-2 and HOb cells showed different behavior when cultured on the same samples. Saos-2 cells proliferated faster than HOb cells, although for each cell line no significant differences were observed among samples. Similarly, Saos-2 cells showed higher ALP activity compared to HOb cells. It is known that tumor cells have rapid proliferation, and the contact inhibition is

disrupted [6]. In this sense, several authors have considered that HOB cells from healthy donors are cells that mimic better the *in vivo* cellular processes [312]. Regarding osteoblasts differentiation, a comparison between Saos-2 and HOB cells was previously performed by other authors, and the results demonstrated that both cell lines had similar differentiation pattern [312]. However, HOB cells are usually cultured using a differentiation cell culture medium that contains differentiation supplements. In the present paper, the use of differentiation supplements was avoided to evaluate the effect of the samples and the sample surfaces topography on osteoblasts differentiation. Thus, the ALP activity of HOB cells was due to the spontaneous differentiation that occurred over time. For Saos-2 cells, their more mature phenotype due to tumoral origin was responsible for the higher initial levels of ALP activity.

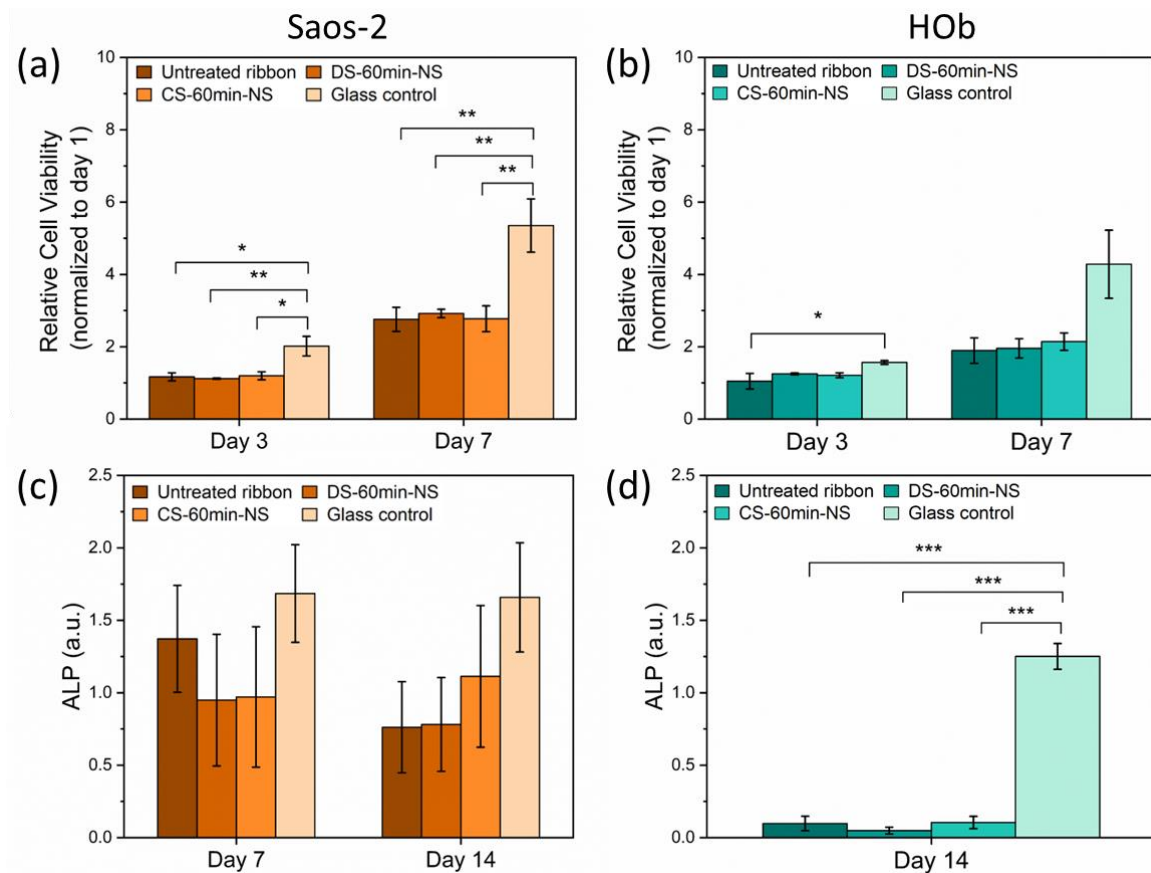


Figure 4.18. Cell proliferation was measured using Alamar Blue assay for 3 days of incubation of (a) Saos-2 cells and (b) HOB cells. ALP activity measured after 7 and 14 days of incubation for (c) Saos-2 cells and after 14 days of incubation for (b) HOB cells. Data represented with mean \pm SEM of three independent experiments and analyzed using ordinary one ANOVA, followed by Tukey's post hoc test for multiple comparisons. * $P < 0.05$, ** $P < 0.01$, *** $P < 0.001$.

3.9. Converging insights from the studies to illuminate common ground

The goal of the present work is to design the surface morphology and composition of the Ti based alloy in order to obtain a material with enhanced biocompatibility and antibacterial activity. To tackle this challenge, an advanced and facile chemical process was proposed to perform *pseudo-dealloying* on a Ti-based amorphous alloy obtaining a patterned Ti/Zr mixed oxides surface. Two samples, DS-60min-NS and CS-60min-NS (Diluted solution: NH₄OH, H₂O₂, and H₂O in a 5:1:4 volume ratio and concentrated solution: NH₄OH, H₂O₂, in a 1:1 volume ratio) were produced with unique chemical and morphological characteristics. The results obtained from cytocompatibility study performed with Saos-2 and HOB cells, Cu ion release, ROS production and antimicrobial effects of ribbons against gram-negative *P. aeruginosa* can be summarized and taken into account in a comprehensive way to understand in a whole the behavior of the DS-60min-NS and CS-60min-NS samples. The peculiarities of the DS-60min-NS sample are: np topography with average ligaments thickness 10.7 ± 1.3 nm and pore diameter 11.4 ± 1.6 nm; wettability of 64° ; release of Cu species of 0.45 ± 0.04 mg/L. CS-60min-NS sample characteristics are: bimodal np porosity with diameter of small pores 15.3 ± 4.6 nm and of bigger pores 178.6 ± 44.6 nm; ligament size of 12.4 ± 3.1 nm; wettability of 68.8° ; Cu species release of 0.26 ± 0.02 mg/L.

The different chemistry and morphology affect both cytocompatibility and antibacterial activity via different possible actions. (i) Cu release: Cu can be a cytotoxic element but when released in a limited amount can kill bacteria by ROS production via Fenton reaction. (ii) Morphology: cells and bacteria participate in the race for the surface to adhere on the implanted materials, roughness and wettability of the surface can play a major role to favor cell with respect to bacteria.

Several studies have reported Cu as a cytotoxic element [313–315]. However, when Cu is alloyed with biocompatible elements such as Ti and Zr it does not show cytotoxic behavior [316]. Pd based dental alloys with composition Pd₈₀Cu₁₀Ga₁₀ wt % showed a Cu release in cell cultured media between 0.1 mg/L and 1 mg/L and the cell viability with mouse fibroblast cells was 81 ± 8 % and 75 ± 13 %, respectively. However, when the Cu ion release increased at 10 mg/L the cell viability was reduced to 54 ± 16 % [317]. Chai et al. [318] reported an in vitro response of bacteria (*S. aureus* and *E. coli*) and cells (MG63 osteoblast-like cells) on bone screws made from austenitic stainless steel with 4.5 wt % Cu (317L–Cu). The reported Cu ion concentration in the rabbit blood after 72 h of incubation was approximately 1 mg/L and the 317L–Cu sample shows good biocompatibility, no evident toxicity with MG63 osteoblast-like cells and good antimicrobial activity as compared with Ti6Al4V control alloy. The in vivo study indicated that 317L–Cu can stimulate osteoblast like cell growth and significantly reduce infection and inflammation in rabbits. Moreover, Cu is known for killing bacteria by various routes, one possible is by ROS via Fenton reaction which induces cellular stress and impact bacterial membrane integrity of bacteria [139,319].

In the present work, the release of Cu ion reached a maximum of 0.45 ± 0.04 mg/L for DS-60min, in the range that was shown in literature as associated with both good antibacterial activity and high cell viability. Therefore, literature observations are in line with what was observed in this work, where the Cu release from the surface of the DS-60min-NS (0.45 ± 0.04 mg/L) and CS-60min-NS (0.26 ± 0.02 mg/L) is within the safe limit for cytocompatibility. In fact, the overall results from cytocompatibility study performed with Saos-2 and HOB cells indicated that the untreated and treated samples (DS-60min-NS and CS-60min-NS) did not induce cell toxicity up to 3 days of cell culture and the samples allowed cell proliferation up to 7 days and early signs of osteogenic cell differentiation.

Substantial antimicrobial effect was observed in the case of DS-60min-NS sample, comparable with cp-Cu, in 1 % crystal violet study. The AFM analysis further substantiated these findings, illustrating reduced bacterial adherence and planktonic bacteria after 2 h on cp-Cu and DS-60min. Whereas, CS-60min-NS samples exhibited agglomerated bacteria, indicating early biofilm formation. The distinct anti-bacterial properties observed between DS-60min-NS and CS-60min-NS can be attributed to a combined effect due to variations in their surface topography, wettability, and ability to release Cu species. According to force-distance curve proposed by Cheng et al. [320] textured surfaces with small pore sizes significantly reduce bacterial attachment due to weaker interactions and higher energy barriers preventing adhesion as in the case of DS-60min-NS sample. Moreover, the hydrophilicity associated with DS-60min-NS sample inhibits bacterial adhesion through hydrogen bonding and ionic interactions with surrounding liquid where “conditioning film” with adsorbed molecules are formed. In literature it was reported that effective bactericidal response was observed on nanostructured Ti surfaces with hydrophilicity 71° , due to cell membrane deformation of *P. aeruginosa* at the initial attachment on to the surface [321]. In contrast, CS-60min-NS has bimodal porosity in which the larger pores (178.6 ± 44.6 nm) can reduce energy barriers for bacteria, enhancing adhesion, while the smaller nanostructures on the surface contribute to a certain level of anti-adhesion and could reduce bacterial attachment [322]. The combination of these factors makes CS-60min-NS less effective in preventing *P. aeruginosa* adhesion and biofilm formation compared to DS-60min-NS. Moreover, the ROS production and Cu ion release for CS-60min-NS sample is reduced with respect to DS-60min-NS.

Summarizing, DS-60min-NS sample is characterized by a relatively higher Cu release and ROS production, hydrophilicity of the surface and small homogeneous pores that allow its antibacterial activity while maintaining a good cytocompatibility. Conversely, CS-60min-NS sample shows a lower Cu and ROS production correlated with a bimodal morphology that is more in favor of bacterial adhesion. These observations underline the potential of DS-60min-NS sample in combating *P. aeruginosa* biofilms. The investigation is focused on assessing the antimicrobial effects of ribbons against gram-negative *P. aeruginosa*. However, it is crucial to acknowledge that medical devices and biofilms often encompass various strains/species, and the interplay among them in multi-strain biofilms remains significant. While the study highlights promising antimicrobial properties, it primarily pertains to *P. aeruginosa*, necessitating further exploration encompassing gram-positive and drug-resistant bacteria to ascertain broader antibacterial efficacy. DS-60min-NS sample with hierarchically structured

surfaces with presence of residual Cu on the surface can potentially provide a balanced activity between biofilm resistance against *P. aeruginosa* and cytocompatibility with Saos-2 and HOB cells. This scheme illustrates the possibility for preventing bacteria adhesion and colonization, simultaneously maintaining balanced cytocompatibility to human bone cells in the so called “race for the surface” [323].

Table 4.4. Condensed overview derived from the comprehensive analysis presented in this work on untreated, DS-60min-NS (NH₄OH, H₂O₂, and H₂O in 5:1:4 vol ratio) and CS-60min-NS (NH₄OH, H₂O₂, in 1:1 vol ratio) ribbons.

Sample	Cu (mg/L)	Hemo-compatibility	<i>Pseudo</i>	ROS	Saos-2 Cell			HOB Cell		
			<i>monas</i>	•O	Viability	Proliferation	Differentiation	Viability	Proliferation	Differentiation
			<i>aeruginosa</i>	H Radical						
			Biofilm and Bacteria adhesion							
Untreated Ribbon	↓	+++	-	+	+++	++	+	+++	++	+
DS-60min-NS	↑	+++	+++	+++	+++	++	+	+++	++	+
CS-60min-NS	↑	+++	+	++	+++	++	+	+++	++	+
↑ High ↓ Low (+) Adequate (++) Good (+++) Very good (-) In-adequate										

Conclusion

The $\text{Ti}_{40}\text{Cu}_{40}\text{Zr}_{11}\text{Fe}_3\text{Sn}_3\text{Ag}_3$ at % amorphous ribbons were evaluated for both glass-forming ability and thermal stability, showing promising properties. In order to enhance the biocompatibility and antibacterial activity of the amorphous alloy, chemical *pseudo-dealloying* experiments were performed with the goal of modifying both the surface morphology and chemistry to exploit both strategies to enhance the effectiveness of the process. Treatment was performed by employing solutions containing different concentrations of NH_4OH , H_2O_2 , H_2O for different immersion time and in both stirring and non-stirring conditions, in order to evaluate the evolution of morphology, roughness and composition and identify the more promising conditions for implant applications.

In detail, the employ of diluted solution (DS, 5:1:4 vol ratio of NH_4OH , H_2O_2 , H_2O) over a range of immersion time (5, 30, 60, 120, 240, 360 min) demonstrated that the increasing of the immersion time from 5 min to 60 min led to formation of finer porosities and thicker ligaments. Further increase in processing time from 120 min to 360 min resulted in formation of larger pores and finer ligaments with respect to 60 min treated sample. The most homogeneous aspect of pore and ligament size was observed in sample treated for 60 min in non-stirred condition (DS-60 min-NS) with mean pore size of 11.4 ± 1.6 nm and ligament size of 10.7 ± 1.3 nm. However, the sample produced in stirred electrolyte condition for 60 min resulted in two distinct layers with fine pores and ligaments in the inner layer (pore diameter 14.0 ± 4.0 nm, ligaments size 4.9 ± 1.0 nm) while larger pores and ligaments on the outer layer (pore diameter 46.0 ± 6.5 nm, ligament size 13.3 ± 3.5 nm), demonstrating the modulatory effects of solution conditions.

The XPS analysis revealed the trend in depletion of Cu, along with the emergence of Ti and Zr oxide-rich layers with increase in the immersion time. For instance, sample after 360 min treatment compared to 60 min treatment revealed substantial removal of the Cu species from the np surface region which are composed of Ti- and Zr-oxide species. When the treatment was performed using concentrated solution for 60 min (CS, 1:1 vol ratio of NH_4OH , H_2O_2) in non-stirred condition a distinct surface morphology was obtained with bi-modal pores, underscoring the pivotal role of hydrogen peroxide in shaping the surface characteristics.

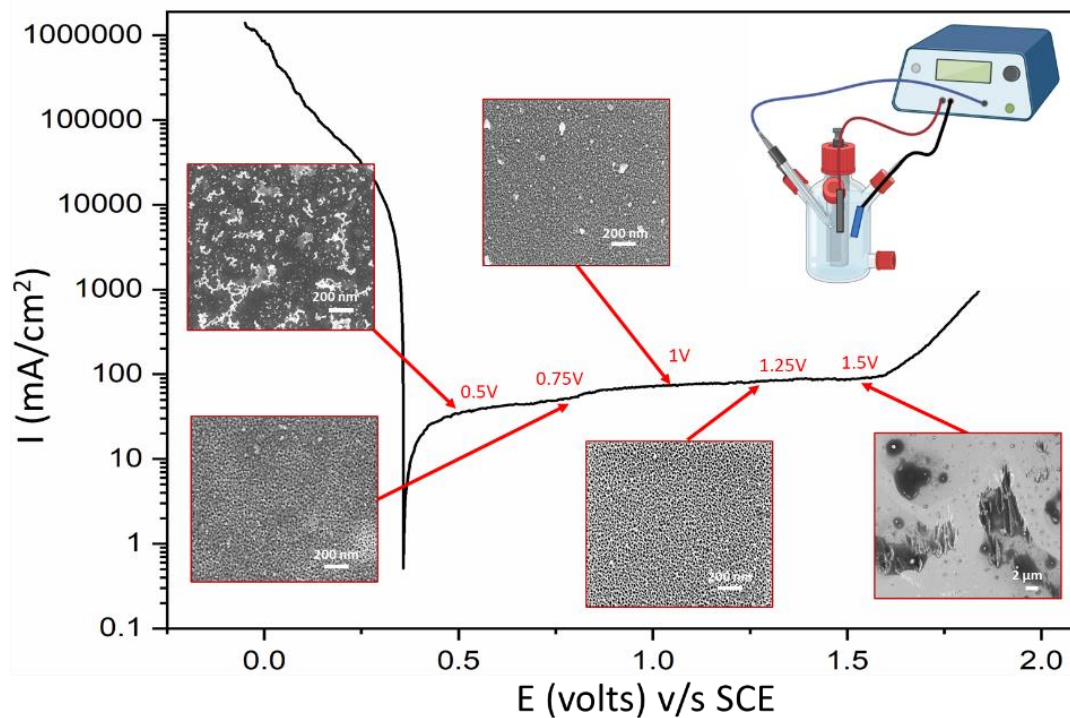
The mechanism of chemical *pseudo-dealloying* using ammonia involves: (i) formation of reactants (NH_4^+ , O_2 , OH^- , H_2O) in the solution and simultaneous mass transfer to metal surface; (ii) reaction at the interface of metal surface and solution leading to formation of copper-ammonia complexes; (iii) rapid oxidation of Ti and Zr surface atoms during the etching process, thus impeding the surface diffusion of metal atoms, resulting in surface-limited dealloying of few nanometer-scale depth (approx. 30 nm in DS-60min-NS). Nevertheless, careful control of immersion time allowed controlled removal of Cu, and variations in morphologies were achieved by adjusting the concentration of hydrogen peroxide.

Notably, the *pseudo-dealloyed* samples DS-60min-NS and CS-60min-NS exhibited hydrophilic interactions and demonstrated hemocompatibility, making them promising candidates for blood-contacting medical devices. Overall, DS-60min-NS sample exhibited

significant potential in combating bacteria adhesion and biofilm formation by *Pseudomonas aeruginosa*, as well as increased generation of reactive oxygen species (ROS) compared to CS-60min-NS and untreated ribbon samples. The DS-60min-NS and CS-60min-NS modified surfaces exhibited no cytotoxic effects on osteoblast cells (Saos-2 and HOb). In summary, this study highlights the potential of *pseudo-dealloyed* surfaces to promote an effective antimicrobial response without compromising the cytocompatibility, offering promising prospects for effective antimicrobial biomaterial.

Chapter V

ELECTROCHEMICAL DEALLOYING USING NITRIC ACID



Specific Aim

- To selectively etch copper from the near surface region of $\text{Ti}_{40}\text{Cu}_{40}\text{Zr}_{11}\text{Fe}_3\text{Sn}_3\text{Ag}_3$ multicomponent amorphous alloy using electrochemical treatment.
- To assess the impact of applied potential on the topography and chemical composition of the alloy, analyze the surface with the goal of understanding the changes in nanostructure and chemical composition.

1. Introduction

To achieve tailored np structures and reduce Cu species in the near-surface region of Ti-Cu based amorphous alloys, techniques adapted from the concept of electrochemical dealloying have emerged as a promising avenue [324–326]. Jayaraj et al. [107] focused on phase-separated Ti-based metallic glass ribbons $Y_{56}Al_{24}Co_{20}$, $Ti_{56}Al_{24}Co_{20}$, and $Y_{20}Ti_{36}Al_{24}Co_{20}$, employing electrochemical dealloying to selectively dissolve the Y-rich phase, leaving behind a well-defined Ti-rich phase. The study revealed a successful homogeneous dealloying process, resulting in interconnected porous structures, with distinct Y and Ti-rich phases. The dealloying conditions involved treatment in 0.1 M HNO_3 solution at 1.9 V for 30 min, wherein a porous morphology was obtained.

Dongmian Zang et al. [112] utilized electrochemical dealloying at 1.82 V in 2 M HNO_3 for 3 hours to create a bicontinuous porous layer on NiTi alloy by dissolution of Ni and oxidation of Ti-oxide rich layer. Subsequent hydrogel coating of the dealloyed samples produced superoleophobic NiTi/hydrogel nanocomposites with enhanced hemocompatibility. The samples showed successful inhibition of platelet adhesion and protein adsorption, additionally the sample showed lower modulus compared to the untreated NiTi alloy indicating the potential application of these nanocomposites in endovascular stents.

In the study conducted by S. L. Zhu, [327] explored electrochemical dealloying of amorphous alloys ($Ti_{40}Cu_{60}$ and $Ti_{50}Cu_{50}$ at %), using HNO_3 solution. Varied parameters included HNO_3 concentration (3.38–7.55 mol/L), temperature (60–80 °C), and applied potential (0.6–1.4 V). Lower HNO_3 concentrations reduced corrosion and oxide formation, revealing fine pores (15–20 nm). Higher potential led to excessive passivation, impeding Cu removal. Pore depth and diameter correlated with applied voltage, emphasizing its importance. Increasing temperature enhanced pore formation due to heightened system energy, accelerating atom migration. Np-Ti and Cu oxides were synthesized on a $Ti_{30}Cu_{70}$ amorphous ribbon employing conditions of 5.36 M HNO_3 , 1.0 V, 3 hours, and 70 °C resulted in the formation of np structures. The obtained structures exhibited an average pore size of 50 nm, average thickness of the pore walls was 100 nm. However, the depth of the np-structure was limited to 500 nm.

Dealloying is not without its challenges, particularly for valve-metal-based alloys. Surface processes are hindered by immediate oxidation, limiting the penetration depth of the dealloying process. Thus, the term "*pseudo-dealloying*" was introduced to describe the surface nanostructuring process specific to Ti-Cu based amorphous alloys. We performed electrochemical *pseudo-dealloying* of $Ti_{47}Cu_{38}Fe_{2.5}Zr_{7.5}Sn_2Si_1Ag_2$ amorphous alloy using 5 M HNO_3 solution at 60 °C applying an anodic potential of 1 V vs. SCE which led to formation of homogenous and defined np structure with the largest pores (18 ± 3 nm) and finest ligaments (6 ± 1 nm). Additionally, increasing the potential led to the formation of wider ligaments and smaller pores in addition to a thicker oxide layer (33.6 ± 0.1 nm at 1.4 V vs. SCE after 3600 s). The produced np-oxide layers showed improved corrosion resistance of the treated surface in a synthetic body fluid compared to untreated surfaces [173].

In this work, we attempted to effectively remove Cu from the near-surface regions of the $\text{Ti}_{40}\text{Cu}_{40}\text{Zr}_{11}\text{Fe}_3\text{Sn}_3\text{Ag}_3$ (at %) amorphous alloy. An electro-chemical process was conducted under specific pH and potential regimes that allow the formation of soluble Cu species, typically involving strong acid solutions within the water stability range. In this chapter, we report our initial successful efforts to develop an approach for the creation of a np Ti-oxide based layer on amorphous $\text{Ti}_{40}\text{Cu}_{40}\text{Zr}_{11}\text{Fe}_3\text{Sn}_3\text{Ag}_3$ (at %) ribbon samples through electrochemical *pseudo-dealloying* in a nitric acid solution at elevated temperatures. This study demonstrates how the applied anodic potential governs the surface reactions leading to formation of porous surface layers with ligament and pore sizes in the nanometer range.

This work was carried out in Leibniz-Institute for Solid State and Materials Research Dresden (Leibniz IFW Dresden), Dresden, Germany during my period abroad.

2. Experimental Procedure

Electrochemical treatment was performed using a Solartron SI 1287 electrochemical interface connected to a three-electrode cell with a double-wall jacket for temperature control (BioLogic). A saturated calomel electrode (SCE) (SHE = 0.241 V) was used as the external reference electrode with a luggin capillary. A Pt sheet served as a counter electrode. As a working electrode, 3-4 cm long ribbon pieces were cut, electrically connected at one end and partially isolated with Teflon tape exposing an area of 1 cm².

The potentiodynamic Tafel plot was recorded after pre-exposure of the ribbon sample for 30 min under open circuit potential (OCP) conditions using 5M nitric acid (HNO₃, 65 % p.a., CHEMSOLUTE®, pH = -0.7) at 60 °C from -0.5V to 2V at scan rate of 1mV/s.

These electrolyte conditions (pH value and concentration) for the surface modification were selected considering the Pourbaix diagrams of Ti (hydrous and anhydrous) and Cu at 25 °C.

Further potentiostatic measurements were performed using 5 M HNO₃ at 60 °C for a duration of 1 and 2 hours. The treated sample was rinsed five times with deionized water and then air dried. The samples were stored in vacuum condition until surface characterization.

The surface morphology of the non-treated and treated samples was investigated by FESEM LEO Gemini 1530, Field Emission Scanning Electron Microscope (FESEM) with an energy of 20 keV. The chemical composition of the sample was analyzed using X-ray photoelectron spectroscopy. The spectrometer (Physical Electronics PHI 5600) is equipped with a 150 mm hemispherical analyzer and a monochromatic Al-K α Xray source. High resolution spectra were obtained with a 29 eV pass energy and a 0.8 mm spot size. A low energy electron gun (5 V) is used as a neutralizer to prevent surface change during the measurement. All spectra were energy corrected using graphitic carbon at 284.4 eV as a reference.

The calculation of dimension of surface topography was carried out using Image J software with a minimum of 40 points.

3. Results and Discussion

3.1 Electrochemical surface treatment using nitric acid

Superimposed Pourbaix diagrams of Cu and Ti were designed to understand the thermodynamics of corrosion of Ti (hydrous and anhydrous) and Cu at 25 °C, with regions of immunity, passivation, and corrosion at different pH and potential. The electrolyte conditions (pH value and concentration) for the surface modification parameters were selected considering the Pourbaix diagrams (Figure 5.1 (a-b)). The solid lines in Figure 5.1 (a-b) represent concentration of dissolved species in 10^0 M and dash-dot lines represent 10^{-6} M.

Limited species of titanium and copper (CuO , Cu_2O , $\text{Cu}(\text{OH})_2$, TiO , Ti_2O_3 , TiO_2 and $\text{Ti}(\text{OH})_3$) were considered in the Pourbaix diagram [328,329]. The dashed blue lines (1) and (2) represent the thermodynamic stability of water at a given temperature and pH. In Figure 5.1 (a) in acidic region for pH below 3.5 and applied potential between 0.5 V to 2 V copper undergoes corrosion while Ti remains passivated in the whole range. Whereas, in the same pH and V range, in Figure 5.1 (b) Ti and Cu likely undergo corrosion.

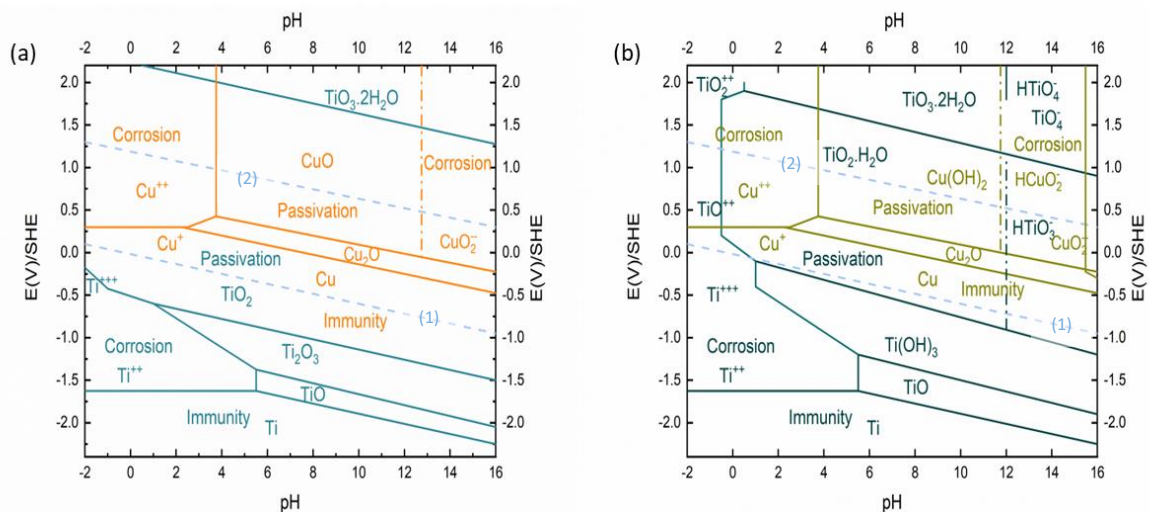


Figure 5.1. Superimposed Pourbaix diagrams of Cu and Ti (a) anhydrous, (b) hydrous at 25 °C.

Potentiodynamic polarization curves of the ribbon samples in 5M HNO_3 solution at 60 °C are shown in Figure 5.2, recorded after 1 hour of OCP stabilization (inset). The corrosion current density (i_{corr}) is 1×10^{-8} A/cm² and the corresponding corrosion potential (E_{corr}) 0.357 V.

Upon anodic polarization, a direct transition into a current density plateau in pseudo-passive region is observed. In the plateau regime, the current density increases gradually at 1.5 V vs. SCE. At potentials higher than 1.5 V vs. SCE, a steep current density increase occurs, which indicates a trans-passive regime where alloy surface oxidation is due to water decomposition. The polarization curves were used to identify the appropriate conditions for further studying

potentiostatic *pseudo-dealloying*. Different potentials, indicated by arrows, were selected within the pseudo-passive regime at 60 °C to analyze their effect on the morphology and composition of the sample surface after 1 hour of treatment in 5 M HNO₃ solution.

It is observed that at applied potential of 0.5 V, which is in the active region resulting in breakdown of oxide layer [330], the surface of the sample is covered with white artifacts (Figure 5.2 a). Further, at elevated potentials such as, 0.75 V, 1 V, 1.25 V, a np and homogenous surface is observed (Figure 5.2 b-d). At a potential of 1.5 V in the vicinity of the transpassive regime, the processes of alloy surface oxide formation and dissolution are concurrently influenced by the water decomposition reaction leading to oxygen evolution (Figure 5.2 e).

This observation elucidates the surface morphology, resembling an occurrence associated with corrosion events. This phenomenon is likely attributed to the ability of oxygen to not only enhance the alloy surface oxidation through chemical side reactions but also induce localized acidification in electrolyte regions near the surface. Consequently, this localized acidification contributes to the corrosion of the surface. In summary, the feasibility of the electrochemical *pseudo-dealloying* process for the Ti-Cu based amorphous alloy is constrained to a potential range corresponding to the pseudo-passive and early transpassive state due to these observed effects.

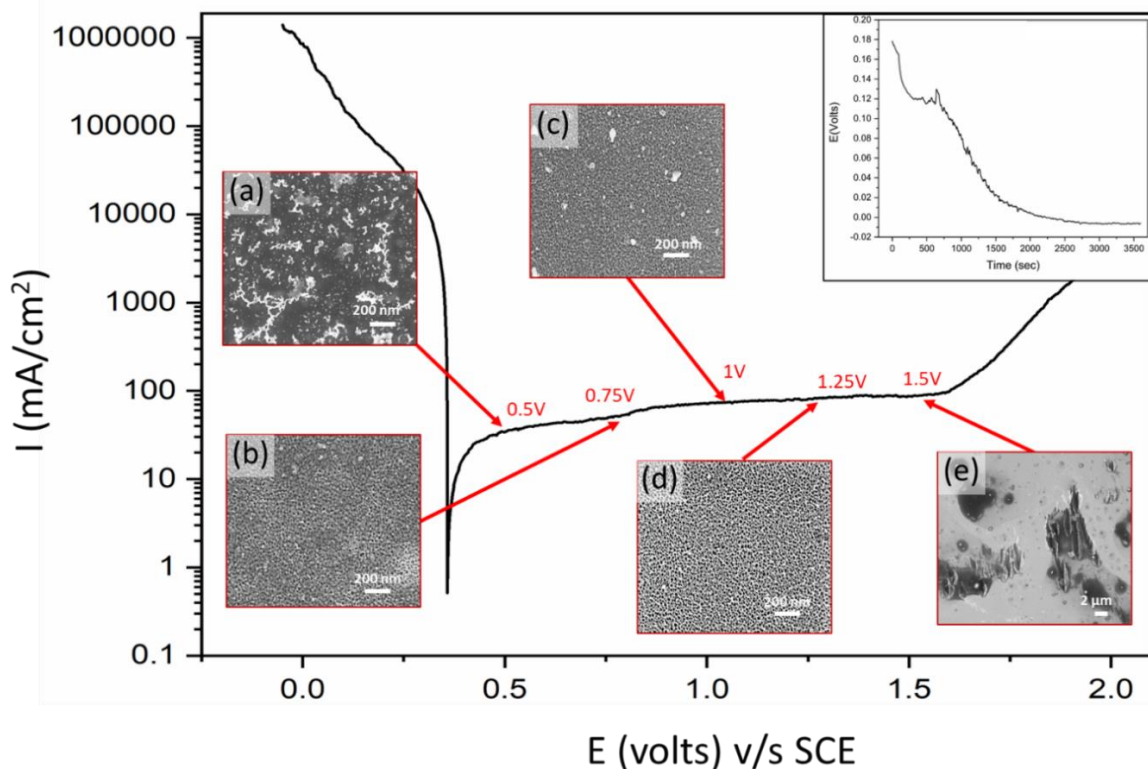


Figure 5.2. Potentiodynamic polarization curves of ribbon samples in 5 M HNO₃ solution at 60 °C, measured with a potential scan rate of 1 mV/s. The arrows indicate anodic potentials which were selected for further potentiostatic studies; inset: OCP stabilization at 60 °C after 1 hour.

After subjecting the ribbon surfaces to potential-dependent treatments in a 5 M HNO₃ solution at 60 °C for 1 hour, we selected surfaces treated at 0.75 V, 1 V, and 1.25 V for further comparative analyses using FESEM and XPS. To explore the impact of longer treatment times, such as 2 hours, we investigated the surface transformation in the same solution.

The potentiostatic polarization curve in Figure 5.3 (a-b) for 1 hour and 2 hours of treatment time at potentials of 0.75 V, 1 V, and 1.25 V vs. SCE potentials showed striking similarities. However, the curve at 1.2 V vs. SCE for 2 hours displayed a higher current density, likely due to contact issues with the sample during treatment.

Analyzing the surfaces of the samples treated under the selected potentials for 1 hour and 2 hours revealed a very uniform np morphology with distinct pores and ligaments (Figure 5.3 c-h). For treatment at 0.75 V vs. SCE, a nanostructure was formed with a mean pore size of 17 ± 3 nm and a ligament size of 14 ± 2 nm after 1 hour. At 2 hours, the mean pore size was 13 ± 2 nm, with a ligament size of 8 ± 1 nm (Figure 5.3 c-d).

Similarly, treatment at 1 V vs. SCE resulted in a finer structure with an average pore size of 12 ± 2 nm and a ligament size of 9 ± 1 nm after 1 hour. After 2 hours, the mean pore size and ligament size remained the same (Figure 5.3 e-f).

At a higher applied potential of 1.25 V vs. SCE, the np structure showed minimal changes, with a pore size of 15 ± 2 nm and a ligament size of 9 ± 2 nm after 1 hour. After 2 hours, the mean pore size was 17 ± 3 nm, while ligament size was 18 ± 4 nm (Figure 5.3 g-h).

Analyzing the trends in pore size and ligaments at 1 hour showed that at a low applied potential (0.75 V vs SCE), the pore and ligament size were high. As the applied potential increased to 1 V, the pore and ligament size slightly decreased and remained almost unchanged, within the experimental error, at 1.25 V (Figure 5.3 i). For 2 hours, a slight gradual increase in pore and ligament size was observed with an increase in applied potential (Figure 5.3 j).

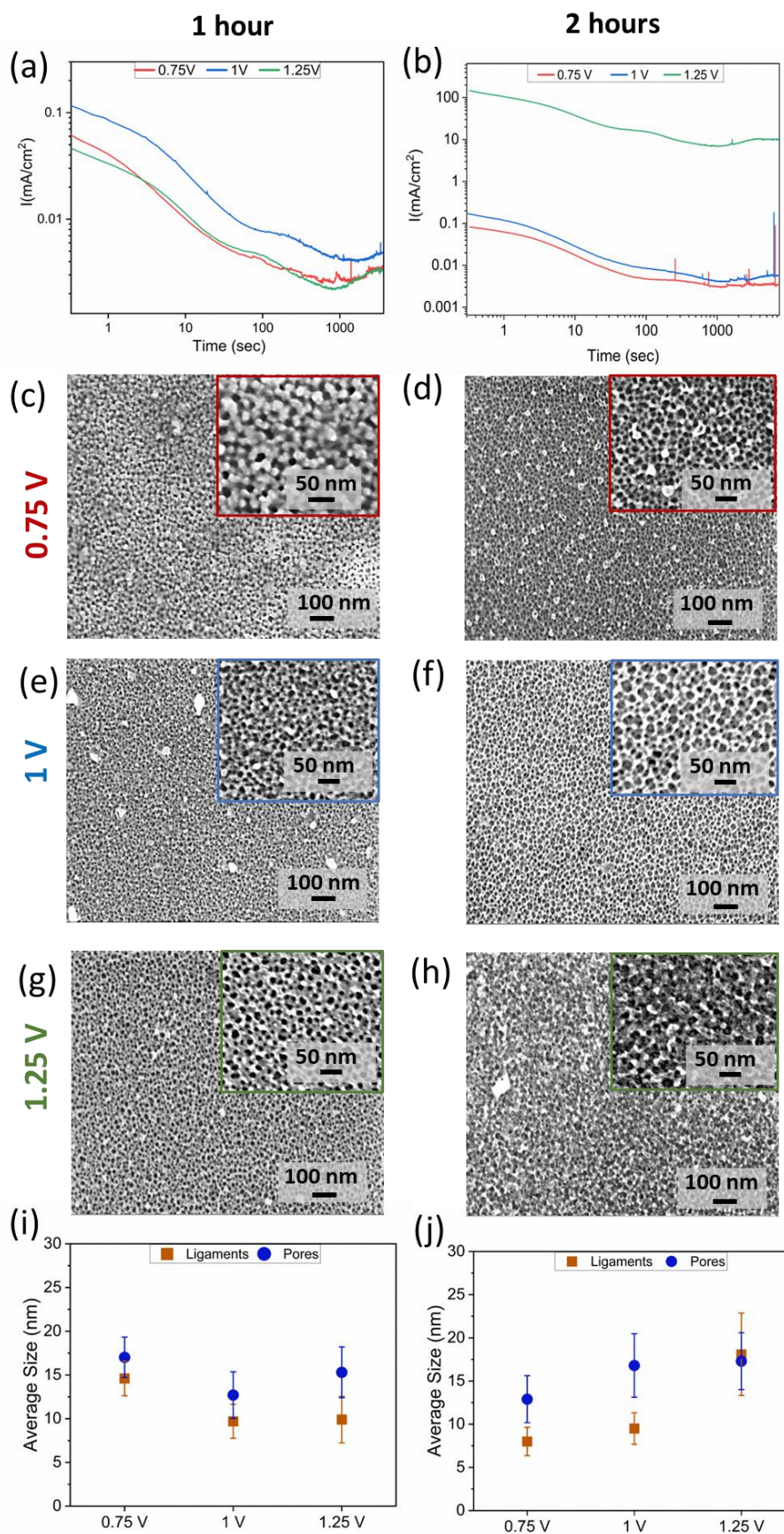


Figure 5.3. Current density transient of a ribbon sample recorded during potentiostatic polarization (a) 1 hour and (b) 2 hours. FESEM images of the potentiostatic treated surfaces at

different potentials in 5 M HNO₃ solution at 60 °C for 1 hour at (c) 0.75 V, (d) 1 V, (e) 1.25 V and for 2 hours at (f) 0.75 V, (g) 1 V, (h) 1.25 V, pore, and ligament size graph for (i) 1 hour and (j) 2 hours.

3.2 Surface characterization using XPS

The untreated ribbon samples and the treated for 1 hour at 0.75 V, 1 V, 1.25 V were further analyzed to investigate the chemical composition using XPS (Figure 5.4). Only the main constituents Ti, Zr and Cu as well as oxygen O were considered, while the other minor constituents remained below a reliable analysis detection limit. It is worth mentioning that all the components were detected but only the relevant ones for this study (Cu, Ti, Zr and O) are elaborated further.

In Figure 5.4 (a), the XPS analysis reveals the presence of carbon on the sample surface. It is important to note that this carbon signal primarily originates from atmospheric exposure of the ribbon samples and the subsequent cleaning process involving organic solvents. As such, it is considered a contamination rather than an inherent characteristic of the samples under investigation. The discussion will focus on the elemental composition and characteristics relevant to the research objectives, while acknowledging and excluding the carbon contamination observed in Figure 5.4 (a). In treated samples the concentration of Cu was significantly reduced from the surface of the samples as compared to untreated ribbon samples (Figure 5.4 b). The ratio of Cu/(Ti+Zr) for each sample is mentioned in Table 5.1. It is evident that the ribbon sample treated at 1V vs SCE showed the lowest concentration of Cu vs (Ti+Zr). It is also important to note that the concentration of O increases with increasing the applied potential.

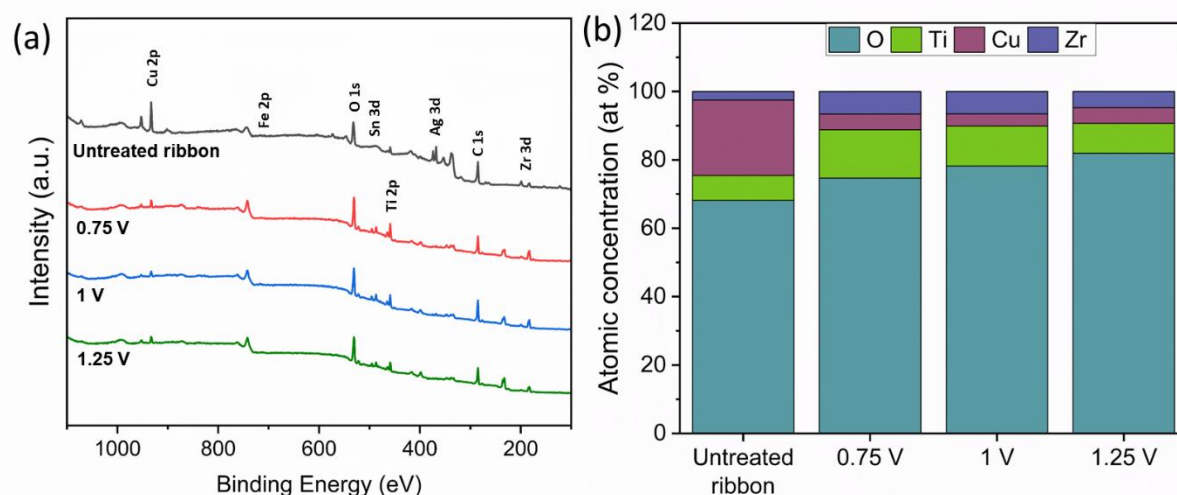


Figure 5.4. XPS analyses (a) surface survey scan and (b) stacked elemental scan of samples treated in 5 M HNO₃ 60 °C at 0.75 V, 1 V, 1.25 V vs. SCE for 1 hour and of the untreated ribbon.

Table 5.1. The ratio of Cu/(Ti+Zr) for untreated and treated samples.

Samples	Cu	Ti	Zr	Cu/Ti+Zr
Untreated ribbon	69.24	22.82	7.93	2.25
0.75 V	18.10	55.78	26.11	0.22
1 V	16.18	53.83	29.99	0.19
1.25 V	25.63	48.41	25.96	0.34

The survey spectra illustrating the Cu2p, Ti2p, Zr3d, and O1s states are presented in Figure 5.5. For the discussion, the focus is directed solely towards the spin-orbit peaks with the highest area ratio: Ti2p_{3/2}, Zr3d_{5/2}, and Cu2p_{3/2}. Overlapping peaks in Ti2p_{1/2}, Zr3d_{3/2}, and Cu2p_{1/2} complicate the interpretation of their oxidation states. Nevertheless, due to the nature of the splitting, any assumption drawn from the initial peaks extends to the subsequent ones.

Examining the Ti2p spectrum (Figure 5.5 a), the untreated ribbon sample exhibits a distinctive peak at 458.8 eV, primarily corresponding to the oxidation state Ti(IV). In contrast, the treated sample shows the same peaks shifted to a higher binding energy (BE) of 459.2 eV. This shift is attributed to the reduction of the work function of Ti resulting from Cu dissolution in the near-surface regions due to electrochemical treatment, thereby altering the Ti environment.

Considering the Zr3d spectra (Figure 5.5 b), the untreated ribbon sample displays a characteristic peak at 182.3 eV, corresponding to the oxidation state Zr(IV). Similar to Ti2p, the treated sample presents the same peak shifted to a slightly higher BE of 182.9 eV due to the same reason.

In the O1s spectra (Figure 5.5 c), two main peaks are visible: structural oxygen at 530 eV corresponding to coordination with Ti(IV) and Zr(IV) (non-hydrous oxides), and another at 532-533 eV associated with hydroxides (coordinated to Cu(II) or Ti and Zr) [331,332]. Notably, in the treated sample, the dominance of the structural oxygen peak is observed. This is explained by the thicker oxide layer formed after electrochemical treatment, the absence of Cu(II) in the oxide film, and the consequent increased availability of O atoms for coordination with Ti and Zr.

In the case of Cu2p (Figure 5.5 d), two oxidation states are identified. In the untreated ribbon sample, the main peak appears at 933.1 eV, corresponding to the oxidation state Cu(0). The defined peak at 932.7 eV may correspond to Cu(0) or Cu(I). Additionally, a thin oxide film formed by air-aging with a predominant presence of Ti/Zr(IV) non-hydrous oxides is observed. In contrast, the treated sample shows a np thicker oxide film resulting from selective Cu(0) oxidation and subsequent dissolution. It also demonstrates a significant contribution of Ti/Zr(IV) non-hydrous oxides due to film growth and a minor presence of Ti/Zr(0) and Ti/Zr hydrous oxides due to spontaneous reactions with HNO₃.

Notably, the presence of Cu in its metallic state within the oxide film of treated ribbon samples can be inferred. This suggests Cu may be in an alloyed form, coordinated to other metallic species such as Ti, Zr, and/or another Cu. Given the structural rearrangement required for oxide film growth and np formation, it is plausible that at some point, Ti and/or Zr oxides are coordinated to Cu (and other metallic species), confining Cu within the alloy system, and preventing its further oxidation and dissolution.

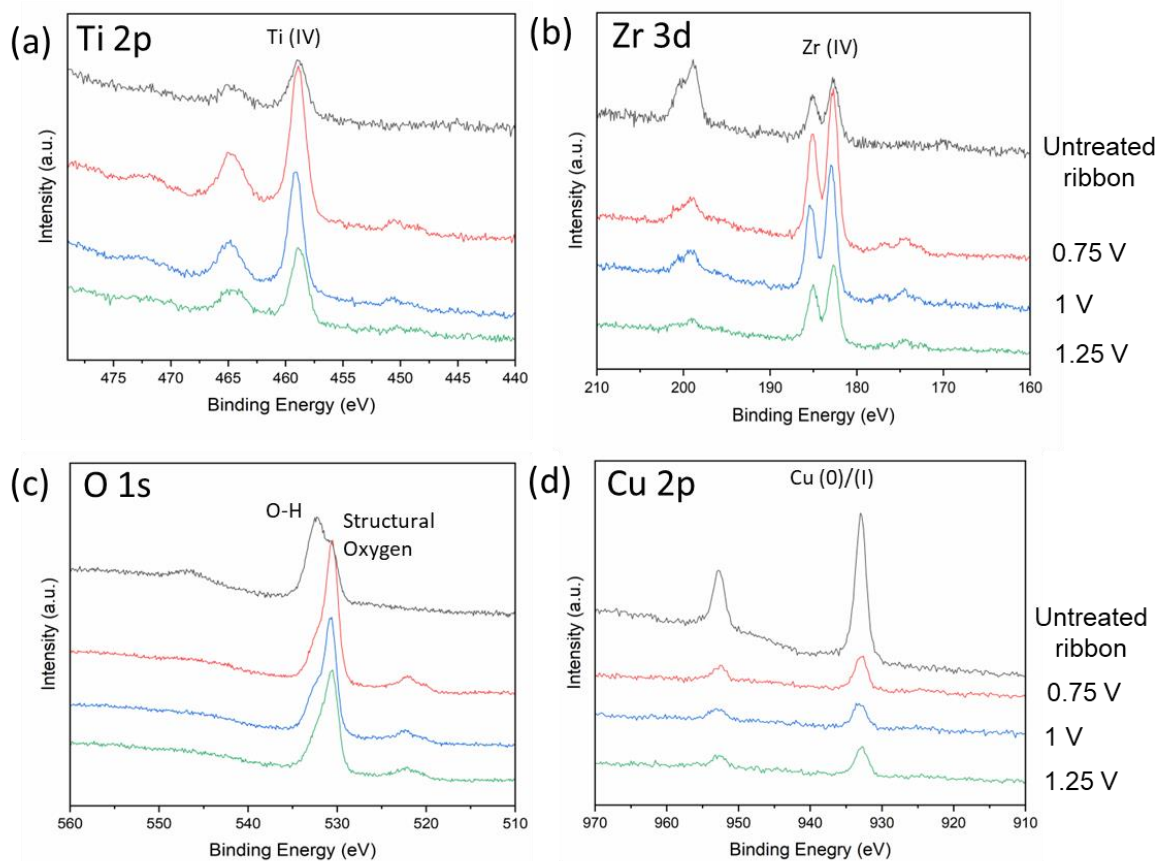


Figure 5.5. High resolution XPS analyses considering (a) O1s, (b) Cu2p, (c) Ti2p, (d) Zr3d, surface states of the ribbon sample after an electrochemical treatment in 5 M HNO₃ 60 °C at 0.75 V, 1 V, 1.25 V vs. SCE for 1 hour and of the untreated ribbon.

A mechanistic elucidation of electrochemical *pseudo-dealloying* process under applied pseudo-passive potentials (0.75, 1, 1.25 V) for 1 hour and 2 hours can be outlined as follows:

- i. Initial passive film on the surface of the untreated ribbons is observed (using XPS).
- ii. Passivity Breakdown and Cu Dissolution: breakdown of passivity follows, leading to temporary Cu dissolution from the near-surface regions and beyond. Local film breakdown permits the dissolution of Cu (and minor species) in the near-surface regions (as represented by eq. 5.1). Simultaneously, the oxide layer undergoes growth as detected in XPS. Nitric

acid influences this process, resulting in porous morphology and topography as observed with FESEM.



The surface transformation involves the gradual growth of a np oxide with a mixed composition of hydrous and non-hydrous Ti- and Zr-oxides. According to XPS findings, Cu is either in the oxide state (CuI) or metallic state (Cu0). The coordination of Cu with oxidized Ti and Zr atoms hinders its diffusion, oxidation, and dissolution. This inhibition prevents further pore formation that would expose Ti/Zr(0) to the electrolyte for additional oxide formation.

The surface processes on the amorphous Ti-Cu based alloy, characterized by no excess concentration of Cu relative to valve metal components, exhibit self-restrictive behavior. Consequently, the progression of the surface transformation front remains confined.

Conclusion

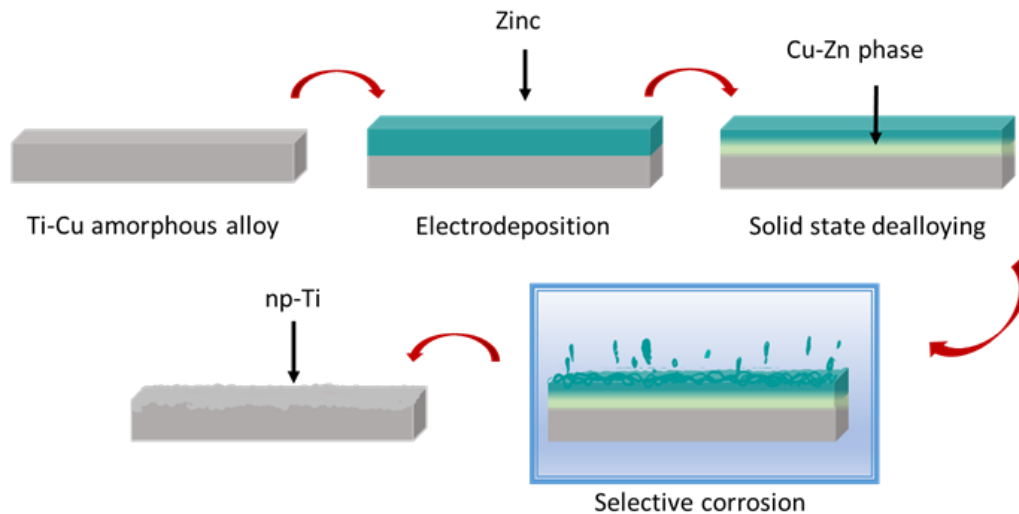
This research introduces an innovative electrochemical surface treatment strategy for the $\text{Ti}_{40}\text{Cu}_{40}\text{Zr}_{11}\text{Fe}_3\text{Sn}_3\text{Ag}_3$ (at %) alloy. This method involves anodic polarization within the pseudo-passive potential range in a 5 M HNO_3 solution at 60 °C. Under these conditions, the generation of Cu-depleted nanostructured Ti/Zr oxides was successfully demonstrated.

It is noteworthy that, while the occurrence of such a process was observed across all pseudo-passive potentials, the application of an anodic potential of 1 V vs. SCE for 1 hour resulted in the highest depletion of Cu concentration. This specific condition yielded a remarkably homogeneous and well-defined np structure characterized by the largest pores (12 ± 2 nm) and finest ligaments (9 ± 1 nm). Notably, extending the polarization time to 2 hours did not substantially alter the surface morphology and chemical composition.

Furthermore, it is crucial to highlight that the formation of the np structure was confined to the pseudo-passive regime. Transitioning into transpassive conditions led to surface dissolution and degradation, emphasizing the critical role of maintaining the pseudo-passive potential for the controlled and optimal development of the desired np structure. This research not only provides insights into the electrochemical treatment of Ti-based alloys but also offers a strategic approach for tailoring surface characteristics with potential applications in diverse fields.

Chapter VI

SOLID STATE DEALLOYING



Specific Aim

- Attempt solid-state selective Cu dissolution using Zn to produce np-Ti on $\text{Ti}_{40}\text{Cu}_{40}\text{Zr}_{11}\text{Fe}_3\text{Sn}_3\text{Ag}_3$ amorphous alloy.
- Investigate the parameters involved in the heat treatment process for the efficient diffusion of Zn into the Ti-Cu amorphous alloy.
- Develop and refine the selective etching process using a mixture of ammonium hydroxide and hydrogen peroxide to achieve optimal removal of Cu/Zn-rich phases, ensuring the creation of a well-defined np-Ti layer.
- Utilize scanning electron microscopy (SEM), energy-dispersive X-ray spectroscopy (EDS), and X-ray diffraction (XRD) to comprehensively characterize the microstructure, composition, and crystallographic properties of the synthesized np-Ti.

1. Introduction

Selective element dissolution is a promising method for the fabrication of np structures that have been extensively applied in different areas such as catalysts, fuel cells, batteries, sensors and biomedical [17]. This process selectively removes one or more components from a parent alloy, while the remaining component(s) form a bi-continuous structure [333]. Selective element dissolution techniques such as chemical etching or electrochemical etching have limitations when it comes to Ti alloys. Ti and Ti alloys face challenges in generating np structures by chemical and electrochemical route due to their low standard electrode potential and their tendency to passivate quickly [79,334].

A new selective element dissolution method using magnesium (Mg) melt was reported by Wada et al. to produce np-Ti, using immersion of the Ti₃₀Cu₇₀ alloy [334]. This method is based on the solubility of liquid melt with the precursor alloy. For instance, the authors used Mg melt to selectively dissolve Cu atoms into the melt, while Ti atoms reorganize resulting in formation of Ti/Mg nanocomposites. Which are chemically etched using nitric acid solution to obtain np-Ti structure [97]. However, this technique has drawbacks such as, requirement for high temperature for magnesium melt, coarsening of nanopores structures due to selective element dissolution at high temperature, handling of magnesium melt as it poses hazards such as inflammable and explosive [52,79,82].

Therefore, a new method for selective element dissolution using Mg powder was proposed by Wada et al. via solid state diffusion for selective element dissolution [77]. This process involves the selective dissolution of one or more elements from a metallic alloy using solid state diffusion which forms np structure [79]. This technique has garnered significant attention in recent years due to its potential applications in fields such as catalysis, energy storage, and sensing [335]. In recent years, solid state selective element dissolution has emerged as an effective method for producing np materials with unique properties on alloys such as, Ti-Cu [79], Fe-Ni [336], Ta-Ti [75], Fe-Cr-Ni [77].

F Zhang et al. produced alpha Ti foams by heat-treating Ti₃₀Cu₇₀ at % master alloy in Mg powders. A densified Ti₃₀Cu₇₀ master alloys with Cu₃Ti₂ and Cu₄Ti₃ phases react with Mg powders during heat treatment, forming Cu₂Mg phase and Ti/Mg nanocomposites. Through subsequent etching in nitric acid solution alpha Ti foams were produced with Brunauer Emmett and Teller BET surface area of 34.4 6 0.8 m²/g and pore size in the range of 2–50 nm [337].

I. McCue et al. reported that specific design criteria are required to fabricate damage-free fully dense composites via selective metal dissolution. Two identified criteria reported by author's were that the alloy systems should not undergo significant volume changes or phase transformations during dealloying. Solid solution of the parent alloy is most important, and interdiffusion between the solvent and dissolving component should be comparable in magnitude which requires consideration of enthalpy of mixing. The authors studied three alloy systems with Ti₆₅Ta₃₅ at % alloy deposited on Cu substrate, Ni₅₅Fe₄₅ deposited on Cu substrate, and Ti₆₅Ta₃₅ deposited on a Zr substrate. The study proposed a "kinetic" selective dissolution

criterion for dealloying. This criterion suggests that the solvent should have negative enthalpy of mixing with all components in the parent alloy but should have significantly slower inter-diffusivity with the remaining component compared to the dissolving component. The Ti-Ta/Zr alloy system was identified as a suitable model for further investigation of selective metal dissolution by authors [75,338].

Y Shi et al. np-Ti was successfully fabricated by dealloying Ti-Cu precursor alloy powders in Mg solids. The dealloying process occurred at a lower temperature compared to traditional liquid metal dealloying, and the mass transport conversion shifted from liquid-solid to solid-solid when the temperature was below the eutectic temperature. The resulting np-Ti had a ligament size ranging from 150 to 500 nm, which could be controlled by adjusting dealloying parameters. The coarsening behavior of the ligament was attributed to surface diffusion and could be predicted using a diffusion-based growth kinetic model. The calculated specific capacitance values for np-Ti were significantly higher (7-60 times) than those for raw Ti powders, and np-Ti with smaller ligament sizes exhibited improved electrochemical active surface area and electrochemical capacitance [79].

C Zhao et al. demonstrated a new method called thin-film solid-state interfacial dealloying for fabricating a 3D bi-continuous porous structure using Ti adhesion layer, Ta barrier layer, Ti₃₀Cu₇₀ (at %) parent alloy layer, and Mg dealloying agent. The pore and ligament sizes achieved through thin-film solid-state interfacial dealloying were in the range of 5-15 nm, similar to the smallest sizes obtained with aqueous solution dealloying and liquid metal dealloying methods. The use of barrier and adhesion layers prevented morphological changes and substrate interactions. Multimodal microscopy techniques were employed to analyze the 3D morphology of the dealloyed film. The presence of Ti oxides in the thin films offered dual-functionality as chemical reactive materials and diffusion barriers. The formation of np bcc-Ti at relatively low temperatures was reported. Design criteria for thin-film solid-state interfacial dealloying were explored, suggesting the inclusion of entropy considerations in addition to enthalpy criteria. The study demonstrates a novel approach for fabricating np metal thin films and provides insights for future applications [339].

Despite the promising results obtained using Mg powder for solid-state selective element dissolution of Ti-Cu alloy, there are still challenges to be addressed. One of the major challenges is the use of magnesium powders, which can be difficult to handle and pose a safety hazard [337]. Finding alternatives to magnesium powders could lead to safe and efficient way for solid-state selective element dissolution technique. Zn is known to form phases with Cu via diffusion, while Ti is less likely to form phase with Zn [340,341].

The other factor involved in choice of Zn was due to its surface diffusion with Cu is faster compared to Ti. For instance, Zn has shown a higher diffusion coefficient as compared to Ti. In a study performed by Ke Liu et al. the author studied the growth behavior and diffusion kinetics of Cu - Zn based intermetallic compounds. In the diffusion zones between 289 - 379 °C the integrated interdiffusion coefficients of the Cu - Zn intermetallic compounds were $1 \times 10^{(-10)-(-14)}$ m²/s [342]. While in Ti - Zn IMCs, Younjang Tan et al. reported the integrated

interdiffusion coefficients are in the range of 1×10^{-16} m²/s for temperature ranges between 300 °C to 374 °C [340].

Therefore, in this study we use metallic Zn to attempt to remove Cu from surface of Ti₄₀Cu₄₀Zr₁₁Fe₃Sn₃Ag₃ amorphous alloys. Zn is electrodeposited onto the surface of the amorphous alloy, forming a layer that is a few micrometers thick. Zn is selected considering its difference in diffusivity with Cu and Ti. Electrodeposition is a commonly used method for synthesizing metallic materials due to its simplicity, cost-effectiveness, and ability to control the deposition parameters. The Zn layer is further subjected to a heat treatment, which causes the formation of Cu-Zn based phases. The heat treated sample was further selectively etched to remove Zn and Cu-Zn based phases using a mixture of ammonium hydroxide and hydrogen peroxide [343].

Overall, solid-state selective element dissolution using electrodeposited Zn on Ti-Cu based amorphous alloys can be a promising method for producing np structures with unique properties. The resulting materials have potential applications in a variety of fields and could pave the way for the development of new and innovative technologies for solid state selective element dissolution of less noble metals like Ti, Zr. In this chapter the electrodeposition of Zn, and the solid-state selective element dissolution process is discussed.

2. Experimental Procedure

2.1 Sample preparation

2.1.1 Electrodeposition of Zn

The electrodeposition was performed using autolab potentiostat instrument (Metrohm, Netherlands) and data collection using NOVA 2.1.4 software. Three electrode cells with platinum as counter electrode, Ag/AgCl double bridge as reference electrode and amorphous ribbon as working electrode was used. Zinc sulphate heptahydrate ($\text{ZnSO}_4 \cdot 7\text{H}_2\text{O}$) ($\geq 99.5\%$, Sigma-Aldrich) solution with 1.0M, 0.5M and 0.1M was used for conducting linear sweep voltammetry with open circuit potential for 300 sec voltage range from 5 mV to -2 V and scan rate 0.010 V/s. The ribbon sample was placed at a fixed distance of 2 cm with platinum counter electrode. Potentiostatic deposition of Zn was performed at -1.2V, -1.3V, -1.4V, -1.6V with 1.0M, 0.5M and 0.1M zinc sulphate solution to optimize the thickness of Zn deposit between 2-3 μm . After electrodeposition the ribbons samples were rinsed with deionized water and isopropanol two times.

2.1.2 Heat treatment

The electrodeposited ribbon samples were sealed in a quartz crucible with argon gas to prevent oxidation of Zn. The heat treatment of the sample was performed in an isothermal condition for diffusion of Zn with Cu. The sample was heated starting at room temperature till 300 °C at a rate of 3°C/min. Isothermal temperature at 300°C was maintained for 24 h then the samples were cooled to room temperature at 3°C/min.

2.1.3 Selective corrosion

The samples were immersed in a solution with NH_4OH (30 %, Sigma Aldrich) and H_2O_2 (35 %, Merck) in 1:1 vol ratio for 5 and 10 min to ensure selective etching of Zn, Cu-Zn based phases. The samples were washed with deionized water and dried in oven at 50 °C for 1 h.

2.2 Sample characterization

The surface morphology of the sample was analyzed with Tescan Vega 4, scanning electron microscopy (SEM), Tescan S 9000G, Field emission scanning electron microscopy (FESEM). The chemical composition of the sample was analyzed using energy dispersive X-Ray spectroscopy (EDS) Ultim max 40mm² Oxford instruments. The structure of the deposited Zn surface was analyzed using X-Ray diffractometer (X'Pert Panalytical), with Cu K α radiation ($\lambda = 1.5418 \text{ \AA}$) in Bragg Brentano geometry at tension 40 kV and current 30 mA. The slit size was 1/2 degree and 5 mm. XRD indexing was performed using X'pert highscore software (version 2.2c (2.2.3)). ImageJ software was utilized to calculate the average thickness of the ligaments with 30 data points.

3. Results and Discussion

3.1. Electrodeposition of pure zinc on the substrate

The electrodeposition of Zn depends on the parameters like applied voltage and electrolyte concentration. Figure 6.1 (a) shows linear sweep voltammogram curve for I vs E, at sweep rate of 0.010 V/s with three different concentrations of zinc sulphate solution. The deposition of Zn occurs at the cathodic part with an increase in current density -0.8V to -1.2V.

Further the different regions of Zn deposition were studied, region I (RI) represents the zone before deposition starts, region II (RII) is potential at which nucleation of Zn occurs on the substrate, while region III (RIII) involves hydrogen evolution.

The curves for the 0.1 M solution indicate a lower current density, suggesting an uneven deposition of Zn. Conversely, an increase in molarity corresponds to a rise in current density. Figure 6.1 (b) illustrates that the surface of the sample electrodeposited with the 0.1M solution is sparsely covered, revealing a visible ribbon sample.

In contrast, Figure 6.1 (c) displays a sample electrodeposited with the 0.5M solution, showcasing a flower-like morphology and a densely covered Zn layer on the surface. Nevertheless, traces of sulfur were detected in the EDS scan, indicating its presence from the electrolyte.

For the sample deposited with a 1M solution, Figure 6.1 (d) reveals a homogeneously deposited and thick Zn layer on the sample surface. This suggests that the higher molarity solution leads to a more uniform and substantial deposition of Zn.

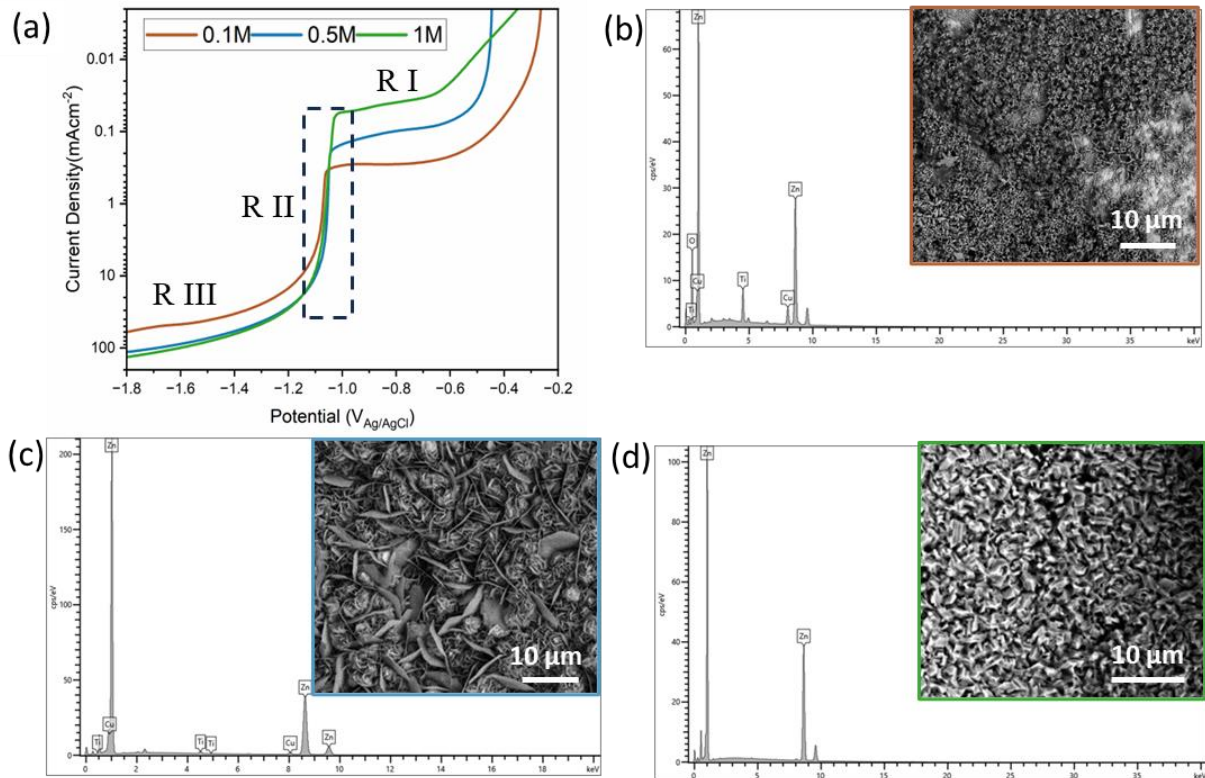


Figure 6.1. (a) LSV of Zn deposited sample with 0.1M, 0.5M and 1M ZnSO₄·7H₂O solution. EDS measurement and SEM micrographs of deposited samples after LSV scans of (b) 0.1M solution, (c) 0.5M solution and (d) 1M solution.

Further investigation was performed to understand the influence of potentiostatic deposition with changing the molarity of the solution. Different potentials -1.2V, -1.3V, -1.4V, -1.6V were selected to optimize electrodeposition thickness and homogeneity of Zn on the surface of ribbon sample. Figure 6.2 shows SEM images of Zn electrodeposited samples for 60 sec with different concentration of ZnSO₄·7H₂O and different potentials. The potentials were selected from the LSV curves and considering the potential zone for nucleation and deposition of Zn on the substrate [344].

The images in Figure 6.2 (a-d) show electrodeposited samples with 0.1M solution. The Zn deposition was sparse and inhomogeneous on the surface (Figure 6.2 a-c), additionally with increasing the voltage the Zn layer became irregular and showed cracks in the electrodeposited layer (Figure 6.2 d). EDS scan of the samples showed traces of sulfur and oxygen on the coating. In Figure 6.2 (e-h) samples electrodeposited using 0.5M solution showed thin Zn deposition on the sample surface (Figure 6.2 e-f). Increasing voltage, the deposited layer showed traces of sulfur and higher oxygen content. The Zn coating was cracked and inhomogeneously deposited (Figure 6.2 g-h). The samples treated with 1M solution as shown in Figure 6.2 (i-l) consists of homogenous and evenly deposited Zn layer on the sample surface, moreover hexagonal shaped Zn crystals were observed [345].

Increasing the applied voltage led to the formation of thicker Zn layer. For instance, the Zn coating at -1.2V was about 1 μm thick, while increasing the voltage to -1.3 V showed a Zn deposition around 2.5-3 μm thickness. In case of higher voltage -1.4V and -1.6V the deposited layer thickness increased to 5-6 μm . The EDS analysis (Figure 6.5 d) showed presence of Zn in high concentration with no traces of sulfur and oxygen on the deposited layer. The results from potentiostatic electrodeposition of Zn indicated the influence of voltage on the thickness of the Zn deposition and influence of solution concentration on the coverage of the Zn on the sample surface. The samples electrodeposited with 1M of $\text{ZnSO}_4 \cdot 7\text{H}_2\text{O}$ showed homogeneous sample coverage and thick Zn layer due to higher concentration of Zn in the solution. As the solution concentration reduces to 0.5M - 0.1M the deposition of Zn layer on the sample surface reduces. In the case of 1M of $\text{ZnSO}_4 \cdot 7\text{H}_2\text{O}$ solution, at applied potential of -1.2V, the formation of Zn grains is observed exhibiting presence of small crystals on the surface. While at -1.3V the layer consists of bigger Zn crystals due to higher Zn diffusion in this region of voltage. Increasing the voltage further shifts the deposition to region with hydrogen evolution (due to splitting of water). Thus, Zn layer was observed to be irregular and with traces of oxygen. The results from the electrodeposition studies show ideal electrodeposition parameters with 1M $\text{ZnSO}_4 \cdot 7\text{H}_2\text{O}$ solution at -1.3V for 60 sec.

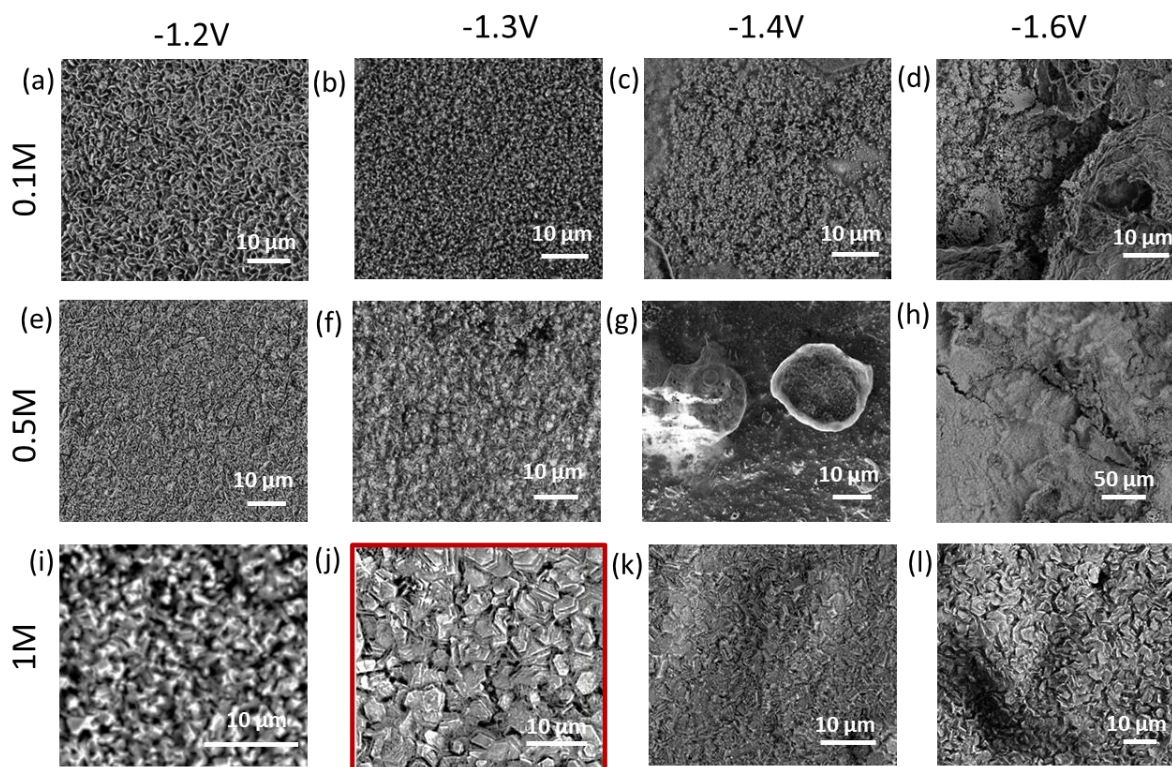


Figure 6.2. SEM images of Zn electrodeposited samples for 60 sec with varying $\text{ZnSO}_4 \cdot 7\text{H}_2\text{O}$ solution concentration and potential.

Further investigation was performed using -1.3 V and 1 M $\text{ZnSO}_4 \cdot 7\text{H}_2\text{O}$ solution to underline influence of deposition time on the thickness and coverage of the deposited Zn layer. As shown in Figure 6.3 (a-e), increasing the deposition time from 7 sec to 30 sec resulted in full coverage

of Zn layer on the surface with about 1.5 μm layer thickness. Whereas, at 60 sec the layer thickness increased to about 3 μm in Figure 6.3 (f), with further increase in deposition time the layer thickness increased to about 5 μm which was relatively bulky and difficult to adhere to the substrate. Hence, after careful investigation of deposition parameter, the selected electrodeposition parameter was -1.3V for 60 sec using 1 M of $\text{ZnSO}_4 \cdot 7\text{H}_2\text{O}$ solution, hereafter names as Zn-ED.

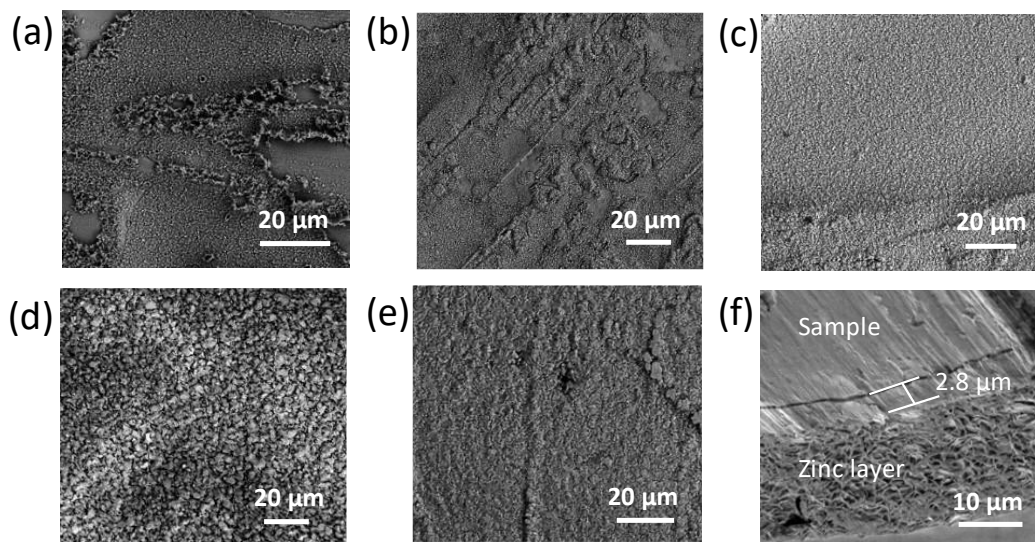


Figure 6.3. SEM images of Zn electrodeposited samples at -1.3 V for (a) 7 sec, (b) 15 sec, (c) 30 sec, (d) 60 sec, (e) 120 sec, (f) cross section of 60 sec. deposited samples.

3.2. Heat treatment of electrodeposited zinc

The Zn coated samples were subjected to a heat treatment procedure at 300 $^{\circ}\text{C}$ for 24 h in an inert atmosphere to initiate the diffusion of Zn with Cu. The electrodeposited Zn samples and heat treated Zn samples were analyzed using XRD technique. Hereafter the heat treated sample will be named as Zn-ED-HT. Figure 6.4 shows the XRD pattern on Zn electrodeposited sample and heat treated sample. The XRD peak of Zn-ED sample indicates presence of pure Zn (004-0831) on the samples while after heat treatment phases corresponding to CuZn_5 (035-1152), CuZn_2 (039-0400) and TiZr (03-065-9625) along with pure Zn (004-0831) were confirmed [346,347].

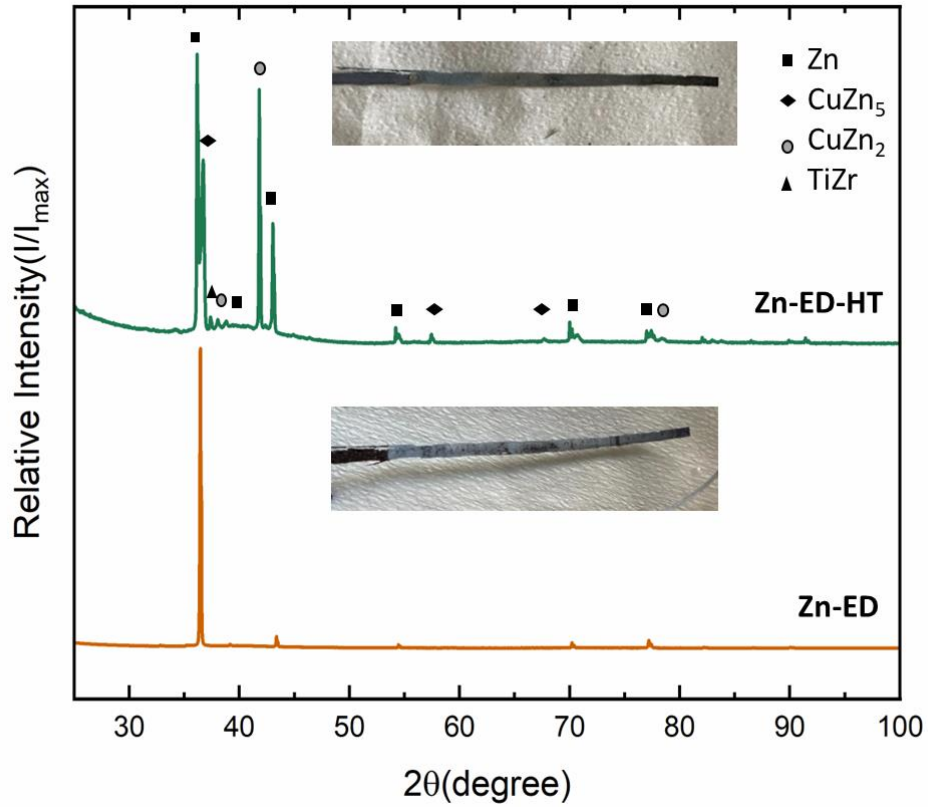


Figure 6.4. XRD of Zn electrodeposited samples and heat-treated samples.

Further analysis of the samples using SEM and EDS (Figure 6.5 a-d) revealed that after the heat treatment the morphology of the samples were altered whereas the chemical composition of the Zn electrodeposited surface was similar in EDS surface analysis. Additionally, no evident oxygen contamination was observed on Zn-ED-HT sample.

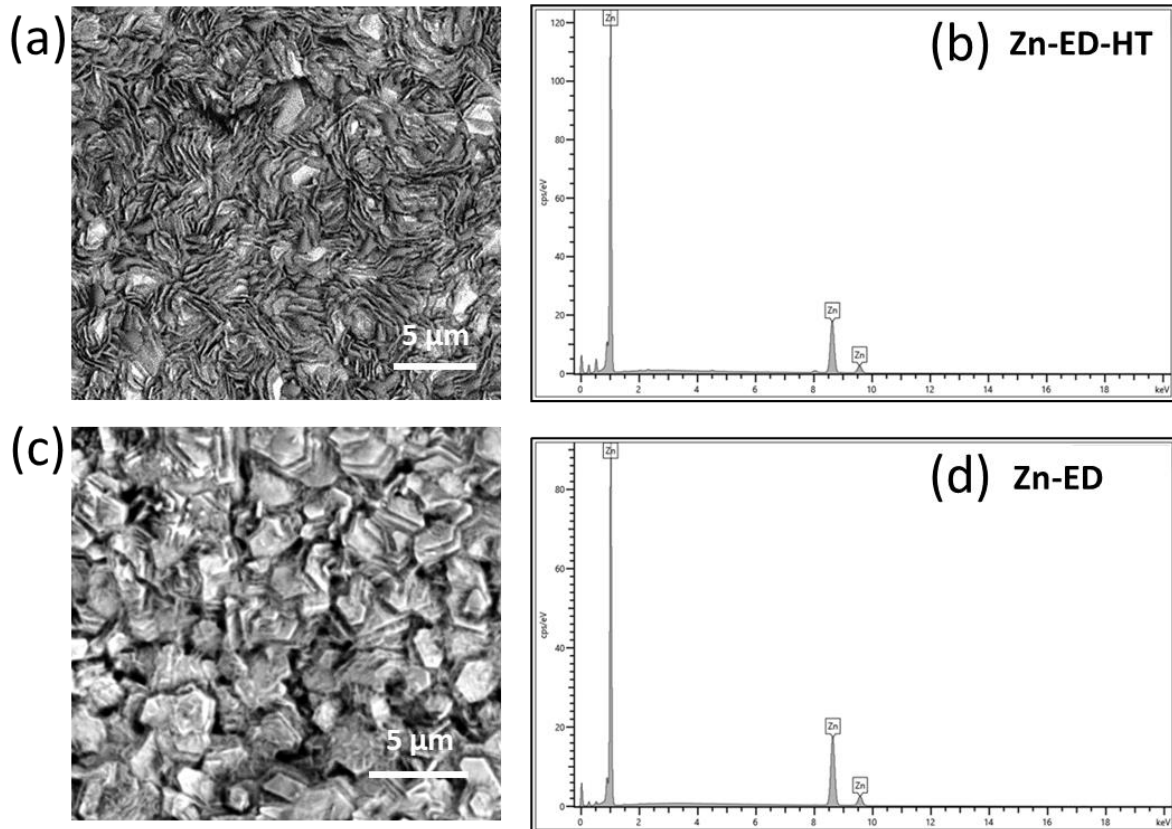


Figure 6.5. (a) SEM and (b) EDS of Zn heat treated Zn-ED-HT samples, (c) and (d) SEM and EDS of Zn electrodeposited Zn-ED samples.

EDS color map was recorded on the cross section of Zn-ED-HT sample, it is worth mentioning that all the elements in the alloy were detected but only prominent elements such as Ti, Zn and Cu is shown in here (Figure 6.6 a). It is possible to appreciate the enrichment of Cu in the Zn layer which is about 1.4 μm . It is also possible to see presence of Ti in the Zn layer which hints towards formation of a surface rich in Ti due to diffusion of Cu with Zn layer. The EDS analysis was performed using a line scan on the sample (ribbon to Zn layer) (Figure 6.6 b).

The EDS profile from ribbon sample to Zn layer shows evident signals corresponding to Ti (red), Cu (pink) and Zn (gold). There is a plateau of Ti and Cu on the left side (ribbon sample) similarly a Zn plateau is seen on the right side. The signals show a gradual reduction such as Zn peak, which reduces near the left side similarly Ti and Cu signal reduces in the right side. This confirms the presence of a diffusion layer resulting from the heat treatment process.

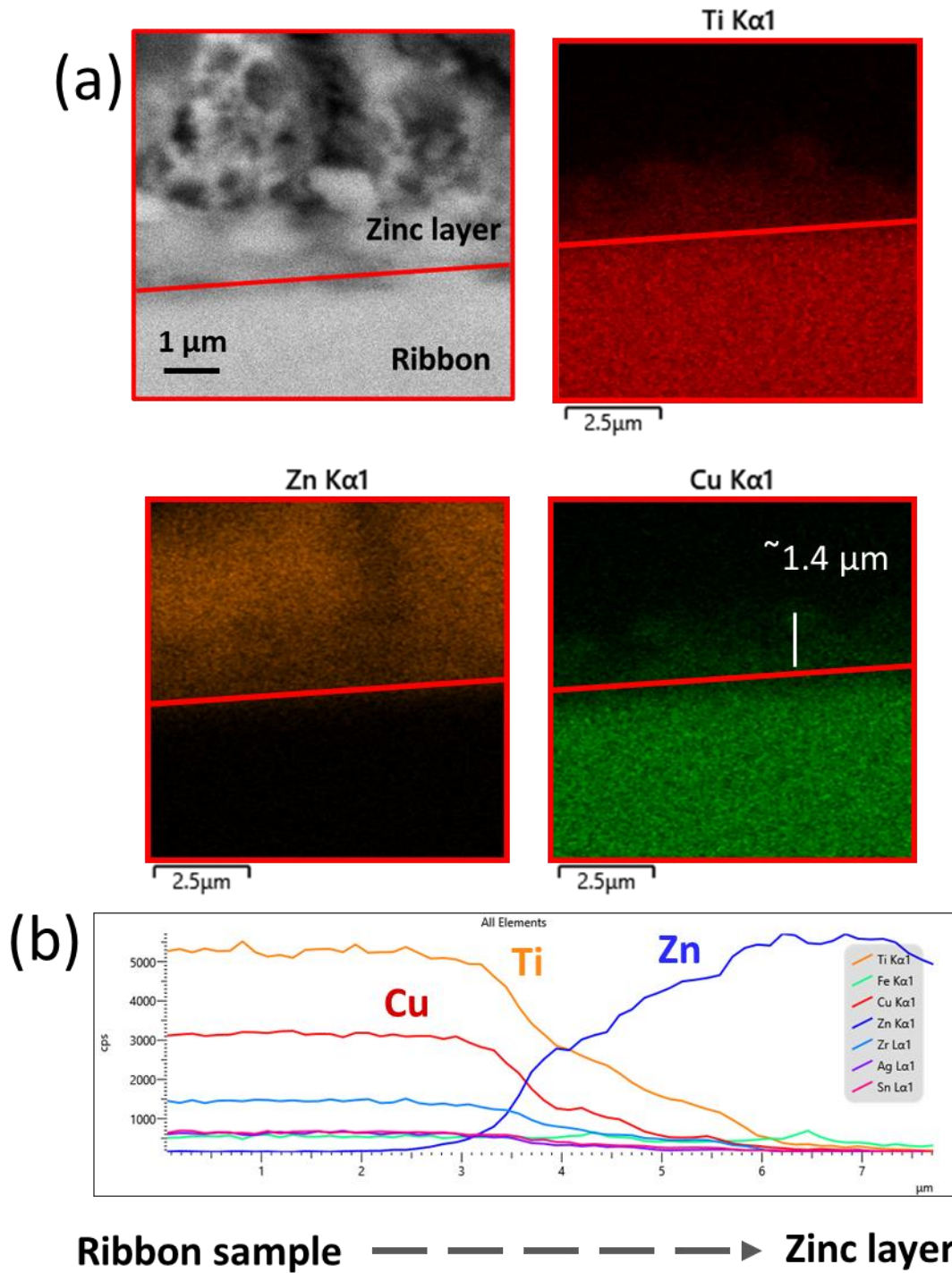


Figure 6.6. (a) EDS cross-sectional color map and (b) EDS line scan of Zn-ED-HT sample.

3.3. Selective etching

The Zn-ED-HT samples were etched in a solution of ammonium hydroxide and hydrogen peroxide for 5 and 10 min to selectively dissolve Zn and Cu-Zn based phases from the sample surface. The recovered etched sample after 5 and 10 min were named as SE-5 min and SE-10 min respectively. The two etched samples showed presence of porous microstructure (Figure 6.7 a-d). In case of SE-5 min sample surface showed residual Zn on the surface with appearance of clogged pores while SE-10 min sample surface was porous with no residual Zn. The average ligament size of SE-10 min was about 10 nm (n=30).

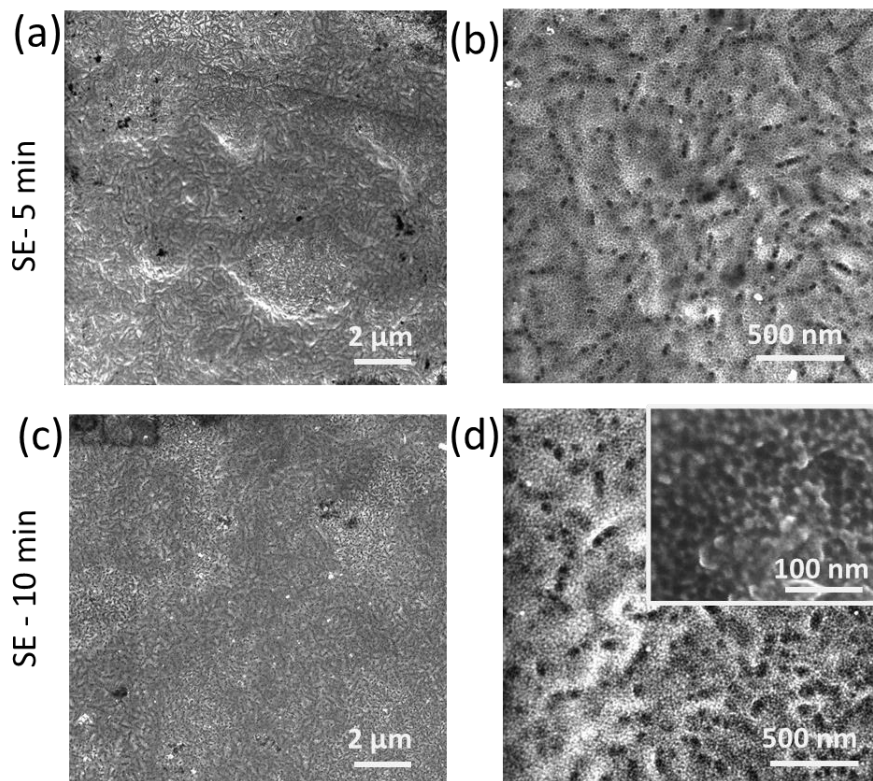


Figure 6.7. FESEM images of sample etched with ammonium hydroxide and hydrogen peroxide after (a-b) 5 min and (c-d) 10 min.

Further SE-10 min sample was analyzed using EDS to measure the chemical composition of the sample surface. Table 6.1 shows that the etched sample were free from Zn on the surface (Figure 6.8 a) and the chemical composition was similar to the nominal composition of as-quenched ribbon sample. The XRD of as-quenched ribbon and Zn-ED-HT-SE-10 min sample showed broad peak representative of amorphous structure (Figure 6.8 b). This confirms the amorphous structure of the ribbon sample after the treatment.

The penetration depth of the two techniques, namely XRD and EDS, is limited to a few microns or tens of microns [348,349]. However, the anticipated thickness of the np-Ti layer is in the order of a few nanometers. Consequently, using these techniques alone may not enable the

differentiation of surface structure properties from those of the bulk material. To address this limitation and gain a more comprehensive understanding, further in-depth studies are imperative. Techniques such as transmission electron microscopy (TEM), selected area electron diffraction (SAED), and X-ray photoelectron spectroscopy (XPS) should be employed. These methods offer higher resolution and sensitivity, allowing for a detailed examination of the surface characteristics and providing insights into the properties of the thin Ti np layer.

Table 6.1. EDS of sample etched in ammonium hydroxide and hydrogen peroxide for 10 min (n=7).

Concentration (at %)	Ti	Fe	Cu	Zr	Ag	Sn
Nominal Composition	40	3	40	11	3	3
Zn-ED-HT-SE - 10 min	40.7 ± 0.1	3.0 ± 0.0	39.7 ± 0.4	10.3 ± 0.3	3.1 ± 0.1	2.9 ± 0.0

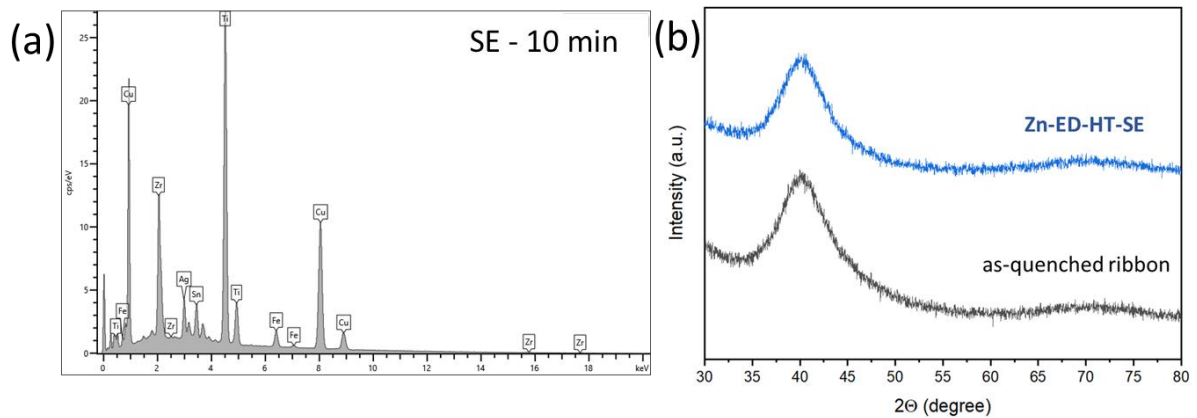


Figure 6.8. (a) EDS analysis of sample etched for 10 min (b) XRD of as-quenched ribbon and Zn-ED-HT-SE-10 min sample.

Conclusion

Solid state diffusion treatment was studied using electrodeposition of pure Zn on an amorphous ribbon. The parameters used were -1.3V for 60 sec using 1M of ZnSO₄.7H₂O solution. The samples with heat treatment at 300°C for 24 h resulted in formation of diffusion layer rich in Cu-Zn phases such as CuZn₅ and CuZn₂. The samples were successfully etched using a solution of ammonium hydroxide and hydrogen peroxide for 10 min to recover nanostructured and Cu depleted sample surface. This study presents the possibility of using Zn for solid state selective element dissolution of Cu from Ti-Cu based amorphous alloy.

Chapter VII

SUMMARY AND OUTLOOK

The culmination of extensive research in the dissertation reveals groundbreaking insights into the $\text{Ti}_{40}\text{Cu}_{40}\text{Zr}_{11}\text{Fe}_3\text{Sn}_3\text{Ag}_3$ composition, showcasing promising Glass-Forming Ability (GFA) with fully amorphous ribbon formation. This dissertation showcases a series of transformative studies, each exploring distinct dealloying techniques on this amorphous alloy, offering significant contributions to development of efficient biomaterials.

Nitric Acid Chemical Dealloying (CD): The exploration of dealloying using 14.6 M nitric acid at 70 °C for 72 hours demonstrated improved properties of the amorphous ribbon, enhancing the ROS activity. The sample produced from the treatment named etched 72-h displayed increased cell proliferation and differentiation response, coupled with limited and non-harmful Cu ion release. This technique exhibits promise in achieving enhanced biocompatible properties for potential implantable materials.

Ammonia-Based Chemical Dealloying (CD): The breakthrough in ammonia-based dealloying, represents a major achievement. The surface modification of amorphous ribbon led to the formation of finer porosities and ligaments, showcasing the controllability of this method additionally controlled Cu etching, morphological variations were achieved by changing process parameters such as immersion time, stirring the solution and solution concentration. In particular, DS-60min-NS (DS, 5:1:4 volume ratio of NH_4OH , H_2O_2 , H_2O , for 60 min in non-stirred condition) sample surface exhibited hydrophilic interaction, enhancing the reactive oxygen species (ROS) production, promising hemocompatibility, cytocompatibility (Soas-2 and HOb cells), and demonstrated efficacy against *Pseudomonas aeruginosa* bacteria adhesion and biofilm formation. DS-60min-NS, exhibits significant promise in combating bacteria adhesion and biofilm formation without compromising cytocompatibility.

Electrochemical Dealloying (ECD): The innovative electrochemical surface treatment strategy utilizing 5 M nitric acid at 60°C for 1 hour at (0.75, 1, 1.25 V) resulted in the successful generation of Cu-depleted nanostructured oxide surfaces. Maintaining the pseudo-passive potential range was crucial for achieving the desired np structure. Notably, the process provided insights into tailoring surface characteristics, offering potential applications in diverse fields.

Solid-State Dealloying (SSD): The study introduced the possibility of using zinc for solid-state selective element dissolution, presenting a novel approach to dealloying. The electrodeposition of pure zinc on an amorphous ribbon, followed by heat treatment at 300 °C for 24 hours, resulted in a diffusion layer rich in Cu-Zn phases. The recovery of nanostructured and Cu-depleted surfaces after etching in a solution of 1:1 vol ration of NH_4OH , H_2O_2 for 10 min presents an intriguing avenue for further exploration.

A groundbreaking patent has been filed, centered around the innovative ammonia-based dealloying solution. This patented solution has demonstrated remarkable efficacy, particularly in the treatment of the $\text{Ti}_{40}\text{Cu}_{40}\text{Zr}_{11}\text{Fe}_3\text{Sn}_3\text{Ag}_3$ alloy. This ammonia-based treatment extends beyond amorphous ribbon, ESR 14: Yohan Douest in BIOREMIA, at Anthogyr SAS during his research collaboration at UNITO, performed successful etching of $\text{Ti}_{40}\text{Zr}_{10}\text{Cu}_{36}\text{Pd}_{14}$ bulk metallic glass plates and rods, offering promising results in terms of corrosion resistance, hemocompatibility and cytocompatibility. Notably, the modified surfaces exhibit unique topographical features and altered chemical compositions with surface layer rich on Pd-oxide. This collaborative venture signifies a strategic partnership between the University of Torino and Anthogyr SAS, France, a dental implant company in exploring the unique potential of ammonia-based treatment on dental alloys. The patent filing underscores the significant advancements achieved in surface modification techniques and their potential transformative impact on the field of biomaterials.

While the achieved results present promising avenues, the outlook emphasizes the need for in-depth investigations to fully comprehend the potential biomedical applications of dealloyed samples. The variations in morphology with changing solution concentrations and the extent of Cu depletion require atomistic-level evaluation, potentially through computational models. Further exploration is necessary to understand the long-term effects, cell differentiation, beyond the initial three-day period and antibacterial studies using other bacteria strains. Each dealloying technique such as CD, ECD and SSD demands analysis for understanding their potential biomedical applications of the modified surfaces which involves:

1. Comprehensive assessment of corrosion properties, cytocompatibility and antibacterial properties of samples produced through various dealloying techniques.
2. Nitric acid dealloyed samples and ammonia-based dealloyed samples require cell studies with extended incubation and cell differentiation assessments for long-term cytocompatibility studies. Assessment of antibacterial activity using different strains of bacteria.
3. Electrochemical dealloyed samples require further in-depth characterization of surface layer, wettability, and AFM of np structures along with biocompatibility tests.
4. Solid-state dealloyed samples require investigation of surface layer through HR-TEM, SAED, and XPS for analysis of surface property for a comprehensive understanding of the surface composition.

Overall, this dissertation highlights the efficacy of various dealloying techniques in tailoring surface characteristics. This research represents a significant stride toward innovative biomaterials, setting the stage for impactful advancements in the biomedical field.

LIST OF PUBLICATIONS AND PATENTS

Publications:

- Kirti Tiwari, Andreu Blanquer, Cristina Pavan, Maura Tomatis, Federico Scaglione, Gianluca Fiore, Francesco Turci, Carme Nogués, Paola Rizzi, “Surface Modification of $Ti_{40}Cu_{40}Zr_{11}Fe_3Sn_3Ag_3$ Amorphous Alloys for Enhanced Biocompatibility in Implant Applications” Under review in Journal of Materials Research and Technology.
- Kirti Tiwari, Christine Joy, Nora Fernandez, Cristina Pavan, Marina Roshchina, Federico Scaglione, Gianluca Fiore, Martin Hantusch, Annett Gebert, Francesco Turci, Paola Rizzi, “Surface Nanostructuring of $Ti_{40}Cu_{40}Zr_{11}Fe_3Sn_3Ag_3$ Amorphous Alloy by Alkaline Chemical Treatment potential use as Biocompatible Material” submitted to Journal of Material Science and Technology.
- Kirti Tiwari, Andreu Blanquer, David Zermeno, Cristina Pavan, Maura Tomatis, Federico Scaglione, Gianluca Fiore, Francesco Turci, Brian Rodriguez, Tadhg O Croinin, Carme Nogues, Paola Rizzi, “Biocompatibility and Antibacterial Efficacy of Etched $Ti_{40}Cu_{40}Zr_{11}Fe_3Sn_3Ag_3$ Amorphous Alloy for Biomedical Implants” submitted to ACS Applied Materials and Interface.
- Kirti Tiwari, Sara Micol, Gianluca Fiore, Federico Scaglione, Paola Rizzi, “Investigating Evolution of Morphology Using a Novel Solid-State Dealloying of $Ti_{40}Cu_{40}Zr_{11}Fe_3Sn_3Ag_3$ Amorphous Alloy” in preparation.
- Kirti Tiwari, Nora Fernández Navas, Marina Roshchina, Martin Hantusch, Annett Gebert, Paola Rizzi, “Electrochemical selective etching of copper from $Ti_{40}Cu_{40}Zr_{11}Fe_3Sn_3Ag_3$ amorphous alloy using nitric acid” in preparation.
- N. Fernández Navas, C.J. Querebillo, K. Tiwari, M. Hantusch, V. Shtefan, N. Pérez, P. Rizzi, M. Zimmermann, A. Gebert, “Electrochemical surface nanostructuring of $Ti_{47}Cu_{38}Fe_{2.5}Zr_{7.5}Sn_2Si_1Ag_2$ metallic glass for improved corrosion resistance” under review in Advanced Engineering Materials.
- Yohan Douest, Kirti Tiwari, Paula Milena Giraldo-Osorno, Jules Galipaud, Thierry Douillard, Nicholas Blanchard, Anders Palmquist, Nicolas Courtois, Damien Fabrègue, Jérôme Chevalier, Paola Rizzi, Benoit Ter-Ovanessian, “Nanotopographical design and corrosion resistance improvement of $Ti_{40}Zr_{10}Cu_{36}Pd_{14}$ amorphous alloy using selective etching” in preparation.
- Kirti Tiwari, Federico Scaglione, Deepti Raj, Paola Rizzi, “Advances in dealloying of Ti and its alloys for biomedical application”, review paper in preparation.

Patent:

- Effective surface modification technique for dealloying titanium based bulk metallic glass for biomedical implant application, submitted a European patent (submission no. 1000514521).

ACKNOWLEDGEMENTS

I would like to take this opportunity to express my heartfelt gratitude and appreciation to all the remarkable individuals and organizations who have been instrumental in making my doctoral journey a truly enriching and fulfilling experience. Their support, guidance, and contributions have played an invaluable role in the successful completion of this dissertation.

I extend my heartfelt gratitude to the members of my PhD jury for graciously agreeing to evaluate and contribute to the examination of this thesis.

I am profoundly grateful to my supervisor Prof. Paola Rizzi, whose unwavering support, guidance, and mentorship have been instrumental in shaping this research. Her expertise, patience, and dedication have made a significant impact on both my work and personal development. Her mentorship has been invaluable throughout my doctoral journey, shaping my research trajectory and fostering my academic growth. Her commitment to excellence, keen insights, and meticulous attention to detail have elevated the quality of my work. I am thankful for her dedication, approachability, and encouragement, which have empowered me to reach new heights. Her profound impact on my professional development and personal growth is immeasurable.

I am deeply grateful for the funding from the European Union's Horizon 2020 research and innovation programme under the Marie Skłodowska-Curie grant agreement No. 861046. For Project BIOREMIA - European Training Network BIOfilm-RESistant Materials for hard tissue Implant Applications.

The BIOREMIA project holds a special place in my heart, and I extend my sincere appreciation to senior researchers and the 14 Early-Stage Researchers (ESR) named according to the ESR number, Yannick Fortouna, Ludovico Andrea Alberta, Aleksandra Bartkowska, Fei-Fan Cai, Miguel Brito Costa, Tim Kreuz, John Michael Ahmed Escobar Hernandez, Adnan Akman, David Zermeño Pérez, Adam Turner, Paula Milena Giraldo Osorno, Juan José Londoño Rueda, Yohan Douest, Sebastião Mollet Barros, involved in this exceptional research initiative. I am truly grateful for the collaborative environment we shared. Their passion, dedication, and commitment to advancing scientific knowledge have been a constant inspiration. I will cherish the memories made in this consortium over the 3 years.

I would like to extend my heartfelt thanks to Dr. Mariana Calin, the project coordinator and Anne Hönemann, the project manager of BIOREMIA, for their unwavering dedication, tireless efforts, and consistent support throughout this project. Her guidance, organization of training sessions, soft skills development programs, and regular meetings have not only facilitated a dynamic research environment but have also nurtured my personal and professional growth.

To all my colleagues in the University of Turin, from MET group and the TBM group, I extend my heartfelt thanks for their support, friendship, and stimulating discussions.

I express my profound gratitude to Dr. Gianluca Fiore and Dr. Federico Scaglione for their invaluable contributions to our research, specifically in conducting experiments and facilitating data acquisition. Their prompt and unwavering assistance throughout the entire process was instrumental in ensuring the smooth progress and accuracy of our study. Moreover, their expert opinions and insights provided invaluable guidance, enriching our findings, and further validating the credibility of our research. I'm immensely grateful for their expertise, dedication, and unwavering support. In particular, I am grateful to Prof. Francesco Turci and Dr. Cristina Pavan for their valuable insights and assistance, which have greatly contributed to the success of this research.

I would like to express my deepest appreciation and gratitude to the students Sara Micol, Marian Gabriela Vargas Guerrero, and Aiste Miliute whom I assisted with their MSc thesis project. Their unwavering commitment, hard work, and intellectual contributions have significantly shaped the trajectory and outcomes of my PhD research. Their presence and collaboration were a constant source of inspiration.

I would like to express my sincere appreciation to the University of Turin (UNITO) for providing me with the necessary resources, facilities, and opportunities to pursue my research. I am especially grateful to the UNITO office for their constant support, guidance, and assistance with bureaucratic matters, ensuring a smooth and seamless progress in my doctoral studies and stay in Italy.

During my secondments, I had the privilege of working at two exceptional institutions, where I was surrounded by outstanding researchers and professionals. At Leibniz Institute for Solid State and Materials Research Dresden (IFW), Germany, I extend my deepest appreciation to Dr. Annett Gebert, Christine Joy Querebillo Nora Fernandez and IKM group. Their warm welcome, exceptional expertise, and willingness to collaborate were truly remarkable. The outstanding PhD students, postdocs, technicians, and experts within the group made my time there truly invaluable.

Likewise, at Universitat Autònoma de Barcelona (UAB), Spain, I would like to express my gratitude to Prof. Carme Nogués, Prof. Jordi Sort Viñas, Dr. Andreu Blanquer, and the PhD students in their group. Their warm embrace, collaborative spirit, and generous sharing of knowledge have significantly enriched my research experience and contributed to my personal and academic growth.

My sincere appreciation goes to Prof. Tadhg Ó Cróinín and Dr. Brian Rodriguez at UCD Dublin for their invaluable expertise in the field of Microbiology, and their enthusiastic willingness to collaborate. A special thanks to Prof Christina Lekka and Maria Evanthia Nousia at University of Ioannina (UOI), Greece and her incredible team for performing interesting DFT calculations on my experimental work. I would like to thank Dr. Nicolas Courtois at Anthogyr SAS (Anthogyr), France and the legal team working on the joint patent.

I want to extend my deepest gratitude to my loving parents Nirjala, Balram, Geetha, and Manivasagam for their unwavering support, understanding, and belief in me have been a constant source of motivation and inspiration. Their presence in my life has provided the

balance and strength needed to overcome challenges and reach new heights. I am truly grateful for their love, encouragement, and unwavering belief in my abilities. Thank you mummy, papa, amma and appa. I want to extend my heartfelt appreciation to my loving husband Vignesh, for his unwavering help and support throughout my PhD journey. His constant encouragement, understanding, and belief in my abilities has been a source of strength during the challenging times. He has been my pillar of support, patiently listening to me and offering words of encouragement. His belief in my capabilities and sacrifices to accommodate my plans have been crucial for me to carry out my PhD. I am truly grateful for his love, patience, and unwavering support, which has played an integral role in my academic achievements.

I am incredibly grateful for my sweet siblings, Sruti and Harshit for being the coolest siblings and always making me laugh out loud even when I'm so far from them, their love and support always kept me motivated. My best friends in India, Soumya and Priya who are my support system, thank you for your love and encouragement. My friends and *La mia nonna italiana, signora Gianna*, in Italy who have been there for me throughout my PhD journey. Their presence has brought joy, laughter, and a sense of belonging to my life. Thank you for being amazing friends. I'm thankful to Aleksandra-my polish sister for always being there for me and creating the best memories.

In the end, thank you all for the exceptional contributions and for being an integral part of this remarkable journey with me.

Embarking on a PhD is like embarking on a marathon. It requires dedication, perseverance, and the ability to keep pushing forward even when faced with challenges. But just like a marathon, the journey is not only about reaching the finish line; it's about the personal growth, resilience, and determination that one develops along the way.

BIBLIOGRAPHY

- [1] N. Patel, P. Gohil, A Review on Biomaterials : Scope , Applications & Human Anatomy Significance, (2012).
- [2] S. Bauer, P. Schmuki, K. von der Mark, J. Park, Engineering biocompatible implant surfaces: Part I: Materials and surfaces, *Prog Mater Sci* 58 (2013) 261–326.
<https://doi.org/10.1016/J.PMATSCI.2012.09.001>.
- [3] M. Ariff, M. Ariffin, S. Kim, F. Dakhelallah Al-Shalawi, A. Hanim Mohamed Ariff, D.-W. Jung, M. Khairol Anuar Mohd Ariffin, C. Looi Seng Kim, D. Brabazon, M. Obaid Al-Osaimi, Biomaterials as Implants in the Orthopedic Field for Regenerative Medicine: Metal versus Synthetic Polymers, *Polymers* 2023, Vol. 15, Page 2601 15 (2023) 2601.
<https://doi.org/10.3390/POLYM15122601>.
- [4] M. Oudrhiri, C. Rherib, M. Oulja, A. Assermouh, C. Mahraoui, N.E. Hafidi, Requirements for Selection/Development of a Biomaterial, *Biomed J Sci Tech Res* 14 (2019) 001–006.
<https://doi.org/10.26717/BJSTR.2019.14.002554>.
- [5] M.A. Hussein, A.S. Mohammed, N. Al-Aqeeli, Wear Characteristics of Metallic Biomaterials: A Review, *Materials* 2015, Vol. 8, Pages 2749-2768 8 (2015) 2749–2768.
<https://doi.org/10.3390/MA8052749>.
- [6] C. Nogués, A. Blanquer, L. Barrios, E. Ibañez, Assessment of metallic alloys biocompatibility, *Biomaterials in Clinical Practice: Advances in Clinical Research and Medical Devices* (2017) 461–475. https://doi.org/10.1007/978-3-319-68025-5_16.
- [7] F.A. Shah, P. Thomsen, A. Palmquist, Osseointegration and current interpretations of the bone-implant interface, *Acta Biomater* 84 (2019) 1–15.
<https://doi.org/10.1016/j.actbio.2018.11.018>.
- [8] M. Riool, L. De Boer, V. Jaspers, C.M. Van Der Loos, W.J.B. Van Wamel, G. Wu, P.H.S. Kwakman, S.A.J. Zaat, Staphylococcus epidermidis originating from titanium implants infects surrounding tissue and immune cells, *Acta Biomater* 10 (2014) 5202–5212.
<https://doi.org/10.1016/J.ACTBIO.2014.08.012>.
- [9] H.J. Busscher, H.C. Van Der Mei, G. Subbiahdoss, P.C. Jutte, J.J.A.M. Van Den Dungen, S.A.J. Zaat, M.J. Schultz, D.W. Grainger, Biomaterial-associated infection: locating the finish line in the race for the surface, *Sci Transl Med* 4 (2012).
<https://doi.org/10.1126/SCITRANSLMED.3004528>.
- [10] I. Armentano, C.R. Arciola, E. Fortunati, D. Ferrari, S. Mattioli, C.F. Amoroso, J. Rizzo, J.M. Kenny, M. Imbriani, L. Visai, The interaction of bacteria with engineered nanostructured polymeric materials: a review, *ScientificWorldJournal* 2014 (2014).
<https://doi.org/10.1155/2014/410423>.

- [11] K.P. Rumbaugh, K. Sauer, Biofilm dispersion, *Nature Reviews Microbiology* 2020 18:10 18 (2020) 571–586. <https://doi.org/10.1038/s41579-020-0385-0>.
- [12] Y.X. Ma, C.Y. Wang, Y.Y. Li, J. Li, Q.Q. Wan, J.H. Chen, F.R. Tay, L.N. Niu, Considerations and Caveats in Combating ESKAPE Pathogens against Nosocomial Infections, *Advanced Science* 7 (2020) 1901872. <https://doi.org/10.1002/ADVS.201901872>.
- [13] M. Sarraf, E. Rezvani Ghomi, S. Alipour, S. Ramakrishna, N. Liana Sukiman, A state-of-the-art review of the fabrication and characteristics of titanium and its alloys for biomedical applications, *Bio-Design and Manufacturing* 2021 5:2 5 (2021) 371–395. <https://doi.org/10.1007/S42242-021-00170-3>.
- [14] K. Prasad, O. Bazaka, M. Chua, M. Rochford, L. Fedrick, J. Spoor, R. Symes, M. Tieppo, C. Collins, A. Cao, D.M. Id, K.K. Ostrikov, K. Bazaka, *Metallic Biomaterials : Current Challenges and Opportunities*, (n.d.). <https://doi.org/10.3390/ma10080884>.
- [15] S. Thanka Rajan, B. Subramanian, A. Arockiarajan, A comprehensive review on biocompatible thin films for biomedical application, *Ceram Int* 48 (2022) 4377–4400. <https://doi.org/10.1016/J.CERAMINT.2021.10.243>.
- [16] J. Schroers, G. Kumar, T.M. Hodges, S. Chan, T.R. Kyriakides, Bulk metallic glasses for biomedical applications, *JOM* 61 (2009) 21–29. <https://doi.org/10.1007/S11837-009-0128-1/METRICS>.
- [17] Y. An, Y. Tian, C. Wei, Y. Tao, B. Xi, S. Xiong, J. Feng, Y. Qian, Dealloying: An effective method for scalable fabrication of 0D, 1D, 2D, 3D materials and its application in energy storage, *Nano Today* 37 (2021) 101094. <https://doi.org/10.1016/J.NANTOD.2021.101094>.
- [18] *Metallic Glass | Orbray Co., Ltd.*, (n.d.). <https://orbray.com/en/product/jewel/material/bmg.html> (accessed September 14, 2023).
- [19] W.L. Johnson, Bulk glass-forming metallic alloys: science and technology, *MRS Bull* 24 (1999) 42–56. <https://doi.org/10.1557/S0883769400053252>.
- [20] M. Chen, A brief overview of bulk metallic glasses, *NPG Asia Mater* 3 (2011) 82–90. <https://doi.org/10.1038/asiamat.2011.30>.
- [21] A.I. Salimon, M.F. Ashby, Y. Bréchet, A.L. Greer, Bulk metallic glasses: what are they good for?, *Materials Science and Engineering: A* 375–377 (2004) 385–388. <https://doi.org/10.1016/J.MSEA.2003.10.167>.
- [22] C. Zhang, D. Ouyang, S. Pauly, L. Liu, 3D printing of bulk metallic glasses, *Materials Science and Engineering: R: Reports* 145 (2021) 100625. <https://doi.org/10.1016/J.MSER.2021.100625>.
- [23] S. Jayalakshmi, M. Gupta, *Amorphous Alloys/Bulk Metallic Glasses (BMG)*, *SpringerBriefs in Materials* (2015) 59–83. https://doi.org/10.1007/978-3-319-15016-1_3/COVER.

- [24] K.R. Lim, J.H. Na, J.M. Park, W.T. Kim, D.H. Kim, Enhancement of plasticity in Ti-based metallic glass matrix composites by controlling characteristic and volume fraction of primary phase, *J Mater Res* 25 (2010) 2183–2191. <https://doi.org/10.1557/JMR.2010.0277/METRICS>.
- [25] (PDF) Sustainable Manufacturing Process for Bulk Metallic Glasses Production Using Rapid Solidification with Melt Spinning Technique, (n.d.). https://www.researchgate.net/publication/273146021_Sustainable_Manufacturing_Process_for_Bulk_Metallic_Glasses_Production_Using_Rapid_Solidification_with_Melt_Spinning_Technique?channel=doi&linkId=54fac22c0cf23e66f032c6e8&showFulltext=true (accessed September 14, 2023).
- [26] C. Rong, B. Shen, Nanocrystalline and nanocomposite permanent magnets by melt spinning technique, *Chinese Physics. B* 27 (2018). <https://doi.org/10.1088/1674-1056/27/11/117502>.
- [27] X. Wang, Surface crystallization in Mg-based bulk metallic glass during copper mold casting, *Advances in Materials Science and Engineering 2014* (2014). <https://doi.org/10.1155/2014/798479>.
- [28] M. Calin, A. Gebert, A.C. Ghinea, P.F. Gostin, S. Abdi, C. Mickel, J. Eckert, Designing biocompatible Ti-based metallic glasses for implant applications, *Materials Science and Engineering: C* 33 (2013) 875–883. <https://doi.org/10.1016/J.MSEC.2012.11.015>.
- [29] S. Tantavisut, B. Lohwongwatana, A. Khamkongkao, A. Tanavalee, P. Tangpornprasert, P. Ittiravivong, The novel toxic free titanium-based amorphous alloy for biomedical application, *Journal of Materials Research and Technology* 7 (2018) 248–253. <https://doi.org/10.1016/j.jmrt.2017.08.007>.
- [30] D. Fakult, T. Universit, G. Doktoringenieur, Ni-free Ti-based Bulk Metallic Glasses : Glass Forming Ability and Mechanical Behavior, (1982).
- [31] Z. Liu, L. Huang, W. Wu, X. Luo, M. Shi, P.K. Liaw, W. He, T. Zhang, Novel low Cu content and Ni-free Zr-based bulk metallic glasses for biomedical applications, *J Non Cryst Solids* 363 (2013) 1–5. <https://doi.org/10.1016/j.jnoncrysol.2012.09.026>.
- [32] S. Pang, Y. Liu, H. Li, L. Sun, Y. Li, T. Zhang, New Ti-based Ti–Cu–Zr–Fe–Sn–Si–Ag bulk metallic glass for biomedical applications, *J Alloys Compd* 625 (2015) 323–327. <https://doi.org/10.1016/J.JALLCOM.2014.07.021>.
- [33] T. Wang, Y.D. Wu, J.J. Si, Y.H. Cai, X.H. Chen, X.D. Hui, Novel Ti-based bulk metallic glasses with superior plastic yielding strength and corrosion resistance, *Materials Science and Engineering: A* 642 (2015) 297–303. <https://doi.org/10.1016/J.MSEA.2015.05.060>.
- [34] P. Gong, L. Deng, J. Jin, S. Wang, X. Wang, K. Yao, Review on the Research and Development of Ti-Based Bulk Metallic Glasses, *Metals* 2016, Vol. 6, Page 264 6 (2016) 264. <https://doi.org/10.3390/MET6110264>.
- [35] A. Liens, A. Etienne, P. Rivory, S. Balvay, J.M. Pelletier, S. Cardinal, D. Fabrègue, H. Kato, P. Steyer, T. Munhoz, J. Adrien, N. Courtois, D.J. Hartmann, J. Chevalier, On the Potential of Bulk

- Metallic Glasses for Dental Implantology: Case Study on Ti₄₀Zr₁₀Cu₃₆Pd₁₄, *Materials (Basel)* 11 (2018). <https://doi.org/10.3390/MA11020249>.
- [36] S.L. Zhu, X.M. Wang, A. Inoue, Glass-forming ability and mechanical properties of Ti-based bulk glassy alloys with large diameters of up to 1 cm, *Intermetallics (Barking)* 16 (2008) 1031–1035. <https://doi.org/10.1016/J.INTERMET.2008.05.006>.
- [37] P. Gong, L. Deng, J. Jin, S. Wang, X. Wang, K. Yao, Review on the Research and Development of Ti-Based Bulk Metallic Glasses, *Metals* 2016, Vol. 6, Page 264 6 (2016) 264. <https://doi.org/10.3390/MET6110264>.
- [38] S. Bera, P. Ramasamy, D. Şopu, B. Sarac, J. Zálešák, C. Gammer, M. Stoica, M. Calin, J. Eckert, Tuning the glass forming ability and mechanical properties of Ti-based bulk metallic glasses by Ga additions, *J Alloys Compd* 793 (2019) 552–563. <https://doi.org/10.1016/J.JALLCOM.2019.04.173>.
- [39] S. Zhu, X. Wang, F. Qin, A. Inoue, Glass-Forming Ability and Thermal Stability of Ti-Zr-Cu-Pd-Si Bulk Glassy Alloys for Biomedical Applications, (n.d.). <https://doi.org/10.2320/matertrans.48.163>.
- [40] Y. Liu, G. Wang, H. Li, S. Pang, K. Chen, T. Zhang, TiCuZrFeSnSiSc bulk metallic glasses with good mechanical properties for biomedical applications, *J Alloys Compd* 679 (2016) 341–349. <https://doi.org/10.1016/J.JALLCOM.2016.03.224>.
- [41] Y. Liu, S. Pang, H. Li, Q. Hu, B. Chen, T. Zhang, Formation and properties of Ti-based Ti–Zr–Cu–Fe–Sn–Si bulk metallic glasses with different (Ti + Zr)/Cu ratios for biomedical application, *Intermetallics (Barking)* 72 (2016) 36–43. <https://doi.org/10.1016/J.INTERMET.2016.01.007>.
- [42] T. Hanawa, Research and development of metals for medical devices based on clinical needs, *Sci Technol Adv Mater* 13 (2012). <https://doi.org/10.1088/1468-6996/13/6/064102>.
- [43] J. Li, N. Yu, H. Jiang, J. Leng, H. Geng, Effects of annealing temperature on dealloying of Ti–Cu Alloy, *Corros Sci* 91 (2015) 95–100. <https://doi.org/10.1016/J.CORSCI.2014.11.002>.
- [44] I. McCue, E. Benn, B. Gaskey, J. Erlebacher, Dealloying and Dealloyed Materials, *Annu Rev Mater Res* 46 (2016) 263–286. <https://doi.org/10.1146/annurev-matsci-070115-031739>.
- [45] F. Scaglione, F. Celegato, P. Rizzi, L. Battezzati, A comparison of de-alloying crystalline and amorphous multicomponent Au alloys, *Intermetallics (Barking)* 66 (2015) 82–87. <https://doi.org/10.1016/J.INTERMET.2015.06.022>.
- [46] M. Li, J. Liu, C. Wang, Y. Liu, Y. Sun, C. Qin, Z. Wang, Y. Li, L. Liu, S. Liu, Controllable nanoporous copper synthesized by dealloying metallic glasses: New insights into the tuning pore structure and applications, *Chemical Engineering Journal* 427 (2022). <https://doi.org/10.1016/J.CEJ.2021.130861>.
- [47] J. Erlebacher, An Atomistic Description of Dealloying Porosity Evolution, the Critical Potential, and Rate-Limiting Behavior, *J Electrochem Soc* 151 (2004) C614. <https://doi.org/10.1149/1.1784820>.

- [48] F. Scaglione, F. Celegato, P. Rizzi, L. Battezzati, A comparison of de-alloying crystalline and amorphous multicomponent Au alloys, *Intermetallics (Barking)* 66 (2015) 82–87. <https://doi.org/10.1016/J.INTERMET.2015.06.022>.
- [49] E. Vassileva, L. Mihaylov, L. Lyubenova, T. Spassov, F. Scaglione, P. Rizzi, Porous metallic structures by dealloying amorphous alloys, *J Alloys Compd* 969 (2023) 172417. <https://doi.org/10.1016/J.JALLCOM.2023.172417>.
- [50] J. Lan, M. Peng, P. Liu, D. Chen, X. Xu, M. Luo, Y. Tan, M. Chen, Scalable synthesis of nanoporous boron for high efficiency ammonia electrosynthesis, *Materials Today* 38 (2020) 58–66. <https://doi.org/10.1016/J.MATTOD.2020.04.012>.
- [51] Z. Wang, P. Liu, J. Han, C. Cheng, S. Ning, A. Hirata, T. Fujita, M. Chen, Engineering the internal surfaces of three-dimensional nanoporous catalysts by surfactant-modified dealloying, *Nature Communications* 2017 8:1 8 (2017) 1–8. <https://doi.org/10.1038/s41467-017-01085-3>.
- [52] M. Hadden, D. Martinez-Martin, K.T. Yong, Y. Ramaswamy, G. Singh, Recent Advancements in the Fabrication of Functional Nanoporous Materials and Their Biomedical Applications, *Materials* 15 (2022). <https://doi.org/10.3390/ma15062111>.
- [53] W. Ma, K. Yin, H. Gao, J. Niu, Z. Peng, Z. Zhang, Alloying boosting superior sodium storage performance in nanoporous tin-antimony alloy anode for sodium ion batteries, *Nano Energy* 54 (2018) 349–359. <https://doi.org/10.1016/J.NANOEN.2018.10.027>.
- [54] J. Snyder, K. Livi, J. Erlebacher, Dealloying Silver/Gold Alloys in Neutral Silver Nitrate Solution: Porosity Evolution, Surface Composition, and Surface Oxides, *J Electrochem Soc* 155 (2008) C464. <https://doi.org/10.1149/1.2940319>.
- [55] G. Scandura, P. Kumari, G. Palmisano, G.N. Karanikolos, J. Orwa, L.F. Dumée, Nanoporous Dealloyed Metal Materials Processing and Applications—A Review, *Ind Eng Chem Res* 62 (2023) 1736–1763. https://doi.org/10.1021/ACS.IECR.2C03952/ASSET/IMAGES/LARGE/IE2C03952_0001.JPEG.
- [56] J. Erlebacher, Dealloying of Silver/Gold/(Platinum) Alloys, *ECS Meeting Abstracts MA2007-02* (2007) 852–852. <https://doi.org/10.1149/ma2007-02/13/852>.
- [57] A. Abbas, S. Abbas, X. Wang, Nanoporous copper: fabrication techniques and advanced electrochemical applications, *Corrosion Reviews* 34 (2016) 249–276. <https://doi.org/10.1515/CORRREV-2016-0023>.
- [58] S. J. F. T. C. MW, E. J, Oxygen reduction in nanoporous metal-ionic liquid composite electrocatalysts, *Nat Mater* 9 (2010) 904–907. <https://doi.org/10.1038/NMAT2878>.
- [59] A.J. Smith, T. Tran, M.S. Wainwright, Kinetics and mechanism of the preparation of Raney® copper, *Journal of Applied Electrochemistry* 1999 29:9 29 (1999) 1085–1094. <https://doi.org/10.1023/A:1003637410133>.

- [60] C. Xu, Y. Li, F. Tian, Y. Ding, Dealloying to Nanoporous Silver and Its Implementation as a Template Material for Construction of Nanotubular Mesoporous Bimetallic Nanostructures, *ChemPhysChem* 11 (2010) 3320–3328. <https://doi.org/10.1002/CPHC.201000313>.
- [61] M. Hakamada, M. Mabuchi, Fabrication of nanoporous palladium by dealloying and its thermal coarsening, *J Alloys Compd* 479 (2009) 326–329. <https://doi.org/10.1016/J.JALLCOM.2008.12.078>.
- [62] L. Sun, C.-L. Chien, P.C. Searson, Fabrication of Nanoporous Nickel by Electrochemical Dealloying, (2004). <https://doi.org/10.1021/cm0497881>.
- [63] H. Liu, X. Wang, J. Wang, H. Xu, W. Yu, X. Dong, H. Zhang, L. Wang, High electrochemical performance of nanoporous Fe₃O₄/CuO/Cu composites synthesized by dealloying Al-Cu-Fe quasicrystal, *J Alloys Compd* 729 (2017) 360–369. <https://doi.org/10.1016/J.JALLCOM.2017.09.111>.
- [64] A. Chauvin, W. Xia Cha Heu, P.Y. Tessier, A.A. El Mel, Impact of the morphology and composition on the dealloying process of co-sputtered silver–aluminum alloy thin films, *Phys Status Solidi B Basic Res* 253 (2016) 2167–2174. <https://doi.org/10.1002/PSSB.201600604>.
- [65] I. McCue, B. Gaskey, P.A. Geslin, A. Karma, J. Erlebacher, Kinetics and morphological evolution of liquid metal dealloying, *Acta Mater* 115 (2016) 10–23. <https://doi.org/10.1016/j.actamat.2016.05.032>.
- [66] I. McCue, A. Karma, J. Erlebacher, Pattern formation during electrochemical and liquid metal dealloying, *MRS Bull* 43 (2018) 27–34. <https://doi.org/10.1557/MRS.2017.301>.
- [67] J.D. Harrison, C. Wagner, The attack of solid alloys by liquid metals and salt melts, *Acta Metallurgica* 7 (1959) 722–735. [https://doi.org/10.1016/0001-6160\(59\)90178-6](https://doi.org/10.1016/0001-6160(59)90178-6).
- [68] T. Wada, H. Kato, Surface improvement for biocompatibility of ti-6al-4v by dealloying in metallic melt, *Interface Oral Health Science 2014: Innovative Research on Biosis-Abiosis Intelligent Interface* (2015) 93–101. https://doi.org/10.1007/978-4-431-55192-8_8.
- [69] M. Tsuda, T. Wada, H. Kato, Kinetics of formation and coarsening of nanoporous α -titanium dealloyed with Mg melt, *J Appl Phys* 114 (2013). <https://doi.org/10.1063/1.4821066>.
- [70] T. Wada, A.D. Setyawan, K. Yubuta, H. Kato, Nano- to submicro-porous β -Ti alloy prepared from dealloying in a metallic melt, *Scr Mater* 65 (2011) 532–535. <https://doi.org/10.1016/j.scriptamat.2011.06.019>.
- [71] X. Guo, C. Zhang, Q. Tian, D. Yu, Liquid metals dealloying as a general approach for the selective extraction of metals and the fabrication of nanoporous metals: A review, *Mater Today Commun* 26 (2021) 102007. <https://doi.org/10.1016/j.mtcomm.2020.102007>.
- [72] T. Song, H.P. Tang, Y. Li, M. Qian, Liquid metal dealloying of titanium-tantalum (Ti-Ta) alloy to fabricate ultrafine Ta ligament structures: A comparative study in molten copper (Cu) and Cu-based alloys, *Corros Sci* 169 (2020). <https://doi.org/10.1016/j.corsci.2020.108600>.

- [73] T. Wada, P.A. Geslin, H. Kato, Preparation of hierarchical porous metals by two-step liquid metal dealloying, *Scr Mater* 142 (2018) 101–105. <https://doi.org/10.1016/j.scriptamat.2017.08.038>.
- [74] L. Lai, B. Gaskey, A. Chuang, J. Erlebacher, A. Karma, Topological control of liquid-metal-dealloyed structures, *Nat Commun* 13 (2022) 1–10. <https://doi.org/10.1038/s41467-022-30483-5>.
- [75] I. McCue, M.J. Demkowicz, Alloy Design Criteria for Solid Metal Dealloying of Thin Films, *JOM* 69 (2017) 2199–2205. <https://doi.org/10.1007/S11837-017-2571-8>.
- [76] M.A. Atwater, L.N. Guevara, K.A. Darling, M.A. Tschopp, Solid State Porous Metal Production: A Review of the Capabilities, Characteristics, and Challenges, *Adv Eng Mater* 20 (2018). <https://doi.org/10.1002/adem.201700766>.
- [77] T. Wada, K. Yubuta, H. Kato, Evolution of a bicontinuous nanostructure via a solid-state interfacial dealloying reaction, *Scr Mater* 118 (2016) 33–36. <https://doi.org/10.1016/J.SCRIPTAMAT.2016.03.008>.
- [78] I. McCue, M.J. Demkowicz, Alloy Design Criteria for Solid Metal Dealloying of Thin Films, *JOM* 69 (2017) 2199–2205. <https://doi.org/10.1007/s11837-017-2571-8>.
- [79] Y. Shi, L. Lian, Y. Liu, N. Xing, A novel solid-state dealloying method to prepare ultrafine ligament nanoporous Ti, *Applied Physics A* 2019 125:10 125 (2019) 1–10. <https://doi.org/10.1007/S00339-019-2984-Z>.
- [80] K.E. O., Diffusion of Zinc in Alpha Brass, *Trans. AIME* 147 (1942) 104–110. <https://doi.org/10.2320/MATERIA.34.461>.
- [81] S.A. D., Zinc diffusion in alpha brass, *Trans. AIME* 171 (1947) 130–142. <https://cir.nii.ac.jp/crid/1572261550635469696> (accessed June 20, 2023).
- [82] Z. Lu, C. Li, J. Han, F. Zhang, P. Liu, H. Wang, Z. Wang, C. Cheng, L. Chen, A. Hirata, T. Fujita, J. Erlebacher, M. Chen, Three-dimensional bicontinuous nanoporous materials by vapor phase dealloying, *Nature Communications* 2018 9:1 9 (2018) 1–7. <https://doi.org/10.1038/s41467-017-02167-y>.
- [83] J. Han, C. Li, Z. Lu, H. Wang, Z. Wang, K. Watanabe, M. Chen, Vapor phase dealloying: A versatile approach for fabricating 3D porous materials, *Acta Mater* 163 (2019) 161–172. <https://doi.org/10.1016/J.ACTAMAT.2018.10.012>.
- [84] R.W. Balluffi, B.H. Alexander, Dimensional changes normal to the direction of diffusion, *J Appl Phys* 23 (1952) 953–956. <https://doi.org/10.1063/1.1702357>.
- [85] R.W. Balluffi, B.H. Alexander, Development of Porosity during Diffusion in Substitutional Solid Solutions, *J Appl Phys* 23 (2004) 1237. <https://doi.org/10.1063/1.1702040>.

- [86] Z. Lu, C. Li, J. Han, F. Zhang, P. Liu, H. Wang, Z. Wang, C. Cheng, L. Chen, A. Hirata, T. Fujita, J. Erlebacher, M. Chen, Three-dimensional bicontinuous nanoporous materials by vapor phase dealloying, *Nat Commun* 9 (2018). <https://doi.org/10.1038/S41467-017-02167-Y>.
- [87] Y. Shi, Y. Wang, W. Yang, J. Qin, Q. Bai, Z. Zhang, Vapor phase dealloying-driven synthesis of bulk nanoporous cobalt with a face-centered cubic structure, *CrystEngComm* 23 (2021) 6526–6532. <https://doi.org/10.1039/D1CE00883H>.
- [88] Z. Lu, F. Zhang, D. Wei, J. Han, Y. Xia, J. Jiang, M. Zhong, A. Hirata, K. Watanabe, A. Karma, J. Erlebacher, M. Chen, Vapor phase dealloying kinetics of MnZn alloys, *Acta Mater* 212 (2021) 116916. <https://doi.org/10.1016/J.ACTAMAT.2021.116916>.
- [89] A. Pinna, G. Pia, M.F. Casula, F. Delogu, E. Sogne, A. Falqui, L. Pilia, Fabrication of nanoporous Al by vapor-phase dealloying: Morphology features, mechanical properties and model predictions, *Applied Sciences (Switzerland)* 11 (2021) 6639. <https://doi.org/10.3390/APP11146639/S1>.
- [90] M. Chen, J. Mandal, Q. Ye, A. Li, Q. Cheng, T. Gong, T. Jin, Y. He, N. Yu, Y. Yang, A Scalable Dealloying Technique to Create Thermally Stable Plasmonic Nickel Selective Solar Absorbers, *ACS Appl Energy Mater* 2 (2019) 6551–6557. https://doi.org/10.1021/ACSAEM.9B01112/SUPPL_FILE/AE9B01112_SI_001.PDF.
- [91] Y. Fukuzumi, T. Wada, H. Kato, Surface Improvement for Biocompatibility of Ti-6Al-4V by Dealloying in Metallic Melt, *Interface Oral Health Science 2014: Innovative Research on Biosis-Abiosis Intelligent Interface* (2015) 93–101. https://doi.org/10.1007/978-4-431-55192-8_8.
- [92] I.V. Okulov, S.-H. Joo, A.V. Okulov, A.S. Volegov, B. Luthringer, R. Willumeit-Römer, L. Zhang, L. Mädler, J. Eckert, H. Kato, Surface Functionalization of Biomedical Ti-6Al-7Nb Alloy by Liquid Metal Dealloying, *Nanomaterials* 2020, Vol. 10, Page 1479 10 (2020) 1479. <https://doi.org/10.3390/NANO10081479>.
- [93] I. V. Okulov, A. V. Okulov, I. V. Soldatov, B. Luthringer, R. Willumeit-Römer, T. Wada, H. Kato, J. Weissmüller, J. Markmann, Open porous dealloying-based biomaterials as a novel biomaterial platform, *Materials Science and Engineering: C* 88 (2018) 95–103. <https://doi.org/10.1016/J.MSEC.2018.03.008>.
- [94] A. V. Okulov, A.S. Volegov, J. Weissmüller, J. Markmann, I. V. Okulov, Dealloying-based metal-polymer composites for biomedical applications, *Scr Mater* 146 (2018) 290–294. <https://doi.org/10.1016/J.SCRIPTAMAT.2017.12.022>.
- [95] I. V. Okulov, A. V. Okulov, A.S. Volegov, J. Markmann, Tuning microstructure and mechanical properties of open porous TiNb and TiFe alloys by optimization of dealloying parameters, *Scr Mater* 154 (2018) 68–72. <https://doi.org/10.1016/J.SCRIPTAMAT.2018.05.029>.
- [96] S.A. Berger, I. Okulov, Open porous $\alpha + \beta$ titanium alloy by liquid metal dealloying for biomedical applications, *Metals (Basel)* 10 (2020) 1–11. <https://doi.org/10.3390/met10111450>.

- [97] T. Wada, A.D. Setyawan, K. Yubuta, H. Kato, Nano- to submicro-porous β -Ti alloy prepared from dealloying in a metallic melt, *Scr Mater* 65 (2011) 532–535. <https://doi.org/10.1016/J.SCRIPTAMAT.2011.06.019>.
- [98] N.T. Panagiotopoulos, A. Moreira Jorge, I. Rebai, K. Georgarakis, W.J. Botta, A.R. Yavari, Nanoporous titanium obtained from a spinodally decomposed Ti alloy, *Microporous and Mesoporous Materials* 222 (2016) 23–26. <https://doi.org/10.1016/J.MICROMESO.2015.09.054>.
- [99] F. Saba, E. Garmroudi-Nezhad, F. Zhang, L. Wang, Fabrication, mechanical property and in vitro bioactivity of hierarchical macro-/micro-/nano-porous titanium and titanium molybdenum alloys, *J Mater Res* 35 (2020) 2597–2609. <https://doi.org/10.1557/JMR.2020.123>.
- [100] I. V. Okulov, J. Weissmüller, J. Markmann, Dealloying-based interpenetrating-phase nanocomposites matching the elastic behavior of human bone, *Sci Rep* 7 (2017) 1–7. <https://doi.org/10.1038/s41598-017-00048-4>.
- [101] I.V. Okulov, J. Wilmers, S.H. Joo, S. Bargmann, H.S. Kim, H. Kato, Anomalous compliance of interpenetrating-phase composite of Ti and Mg synthesized by liquid metal dealloying, *Scr Mater* 194 (2021) 1–5. <https://doi.org/10.1016/j.scriptamat.2020.113660>.
- [102] F. Zhang, P. Li, J. Yu, L. Wang, F. Saba, G. Dai, S. He, Fabrication, formation mechanism and properties of three-dimensional nanoporous titanium dealloyed in metallic powders, *J Mater Res* 32 (2017) 1528–1540. <https://doi.org/10.1557/JMR.2017.19>.
- [103] B. Kang, X. Chen, P. Liu, Facile fabrication of nanoporous structure on β titanium alloy to eliminate stress shielding for bone implant, *Journal of Vacuum Science & Technology B* 40 (2022) 050601. <https://doi.org/10.1116/6.0001962>.
- [104] L. Wang, Y. Xu, S. Yu, T. Bai, W. Zhou, Z. Yu, L. Zhou, Improvement on biosafety and bioactivity of Ti–6Al–4V alloys by construction the three-dimensional grid structure through electrochemical dealloying, *Journal of Materials Research and Technology* 17 (2022) 546–559. <https://doi.org/10.1016/j.jmrt.2022.01.002>.
- [105] L. Wang, W. Zhou, Z. Yu, S. Yu, L. Zhou, Y. Cao, M. Dargusch, G. Wang, An in Vitro Evaluation of the Hierarchical Micro/Nanoporous Structure of a Ti3Zr2Sn3Mo25Nb Alloy after Surface Dealloying, *ACS Appl Mater Interfaces* 13 (2021) 15017–15030. <https://doi.org/10.1021/acsami.1c02140>.
- [106] S.L. Zhu, J.L. He, X.J. Yang, Z.D. Cui, L.L. Pi, Ti oxide nano-porous surface structure prepared by dealloying of Ti–Cu amorphous alloy, *Electrochem Commun* 13 (2011) 250–253. <https://doi.org/10.1016/J.ELECOM.2010.12.025>.
- [107] J. Jayaraj, B.J. Park, D.H. Kim, W.T. Kim, E. Fleury, Nanometer-sized porous Ti-based metallic glass, *Scr Mater* 55 (2006) 1063–1066. <https://doi.org/10.1016/J.SCRIPTAMAT.2006.07.054>.

- [108] J. Jayaraj, J.M. Park, P.F. Gostin, E. Fleury, A. Gebert, L. Schultz, Nano-porous surface states of Ti-Y-Al-Co phase separated metallic glass, *Intermetallics (Barking)* 17 (2009) 1120–1123. <https://doi.org/10.1016/J.INTERMET.2009.05.008>.
- [109] T. Wada, K. Yubuta, A. Inoue, H. Kato, Dealloying by metallic melt, *Mater Lett* 65 (2011) 1076–1078. <https://doi.org/10.1016/j.matlet.2011.01.054>.
- [110] J. Huang, J. Wang, X. Su, W. Hao, T. Wang, Y. Xia, G. Da, Y. Fan, Biocompatibility of nanoporous TiO₂ coating on NiTi alloy prepared via dealloying method, *J Nanomater* 2012 (2012). <https://doi.org/10.1155/2012/731592>.
- [111] M. Chembath, J.N. Balaraju, M. Sujata, Surface characteristics, corrosion and bioactivity of chemically treated biomedical grade NiTi alloy, *Materials Science and Engineering: C* 56 (2015) 417–425. <https://doi.org/10.1016/J.MSEC.2015.06.051>.
- [112] D. Zang, H. Yi, Z. Gu, L. Chen, D. Han, X. Guo, S. Wang, M. Liu, L. Jiang, Interfacial Engineering of Hierarchically Porous NiTi/Hydrogels Nanocomposites with Exceptional Antibiofouling Surfaces, *Advanced Materials* 29 (2017) 1602869. <https://doi.org/10.1002/ADMA.201602869>.
- [113] A. Chuang, J. Erlebacher, Challenges and opportunities for integrating dealloying methods into additive manufacturing, *Materials* 13 (2020). <https://doi.org/10.3390/MA13173706>.
- [114] S.L. Zhu, X.M. Wang, F.X. Qin., A. Inoue, A new Ti-based bulk glassy alloy with potential for biomedical application, *Materials Science and Engineering: A* 459 (2007) 233–237. <https://doi.org/10.1016/J.MSEA.2007.01.044>.
- [115] Y. Liu, G. Wang, H. Li, S. Pang, K. Chen, T. Zhang, TiCuZrFeSnSiSc bulk metallic glasses with good mechanical properties for biomedical applications, *J Alloys Compd* 679 (2016) 341–349. <https://doi.org/10.1016/J.JALLCOM.2016.03.224>.
- [116] S. Pang, Y. Liu, H. Li, L. Sun, Y. Li, T. Zhang, New Ti-based Ti–Cu–Zr–Fe–Sn–Si–Ag bulk metallic glass for biomedical applications, *J Alloys Compd* 625 (2015) 323–327. <https://doi.org/10.1016/J.JALLCOM.2014.07.021>.
- [117] S. Zhu, X. Wang, F. Qin, A. Inoue, Glass-Forming Ability and Thermal Stability of Ti–Zr–Cu–Pd–Si Bulk Glassy Alloys for Biomedical Applications, *Mater Trans* 48 (2007) 163–166. <https://doi.org/10.2320/MATERTRANS.48.163>.
- [118] S.L. Zhu, X.M. Wang, A. Inoue, Glass-forming ability and mechanical properties of Ti-based bulk glassy alloys with large diameters of up to 1 cm, *Intermetallics (Barking)* 16 (2008) 1031–1035. <https://doi.org/10.1016/J.INTERMET.2008.05.006>.
- [119] Y.B. Wang, H.F. Li, Y. Cheng, Y.F. Zheng, L.Q. Ruan, In vitro and in vivo studies on Ti-based bulk metallic glass as potential dental implant material, *Materials Science and Engineering: C* 33 (2013) 3489–3497. <https://doi.org/10.1016/J.MSEC.2013.04.038>.

- [120] Y. Liu, S. Pang, H. Li, Q. Hu, B. Chen, T. Zhang, Formation and properties of Ti-based Ti-Zr-Cu-Fe-Sn-Si bulk metallic glasses with different (Ti + Zr)/Cu ratios for biomedical application, *Intermetallics (Barking)* 72 (2016) 36–43. <https://doi.org/10.1016/j.intermet.2016.01.007>.
- [121] W. Yang, Y. Liu, N. Hua, S. Pang, Y. Li, P.K. Liaw, T. Zhang, Formation and properties of biocompatible Ti-based bulk metallic glasses in the Ti – Cu – Zr – Fe – Sn – Si – Ag system, *J Non Cryst Solids* 571 (2021) 121060. <https://doi.org/10.1016/j.jnoncrysol.2021.121060>.
- [122] R. Kokubun, W. Wang, S. Zhu, G. Xie, S. Ichinose, S. Itoh, K. Takakuda, In vivo evaluation of a Ti-based bulk metallic glass alloy bar, *Biomed Mater Eng* 26 (2015) 9–17. <https://doi.org/10.3233/BME-151546>.
- [123] M.D. Demetriou, A. Wiest, D.C. Hofmann, W.L. Johnson, B. Han, N. Wolfson, G. Wang, P.K. Liaw, Amorphous metals for hard-tissue prosthesis, *JOM* 62 (2010) 83–91. <https://doi.org/10.1007/S11837-010-0038-2/METRICS>.
- [124] T. Xue, S. Attarilar, S. Liu, J. Liu, X. Song, L. Li, B. Zhao, Y. Tang, Surface modification techniques of titanium and its alloys to functionally optimize their biomedical properties: Thematic review, *Front Bioeng Biotechnol* 8 (2020) 1261. <https://doi.org/10.3389/FBIOE.2020.603072/BIBTEX>.
- [125] V.K. Manivasagam, K.C. Papat, Hydrothermally treated titanium surfaces for enhanced osteogenic differentiation of adipose derived stem cells, *Materials Science and Engineering: C* 128 (2021) 112315. <https://doi.org/10.1016/J.MSEC.2021.112315>.
- [126] J. Vishnu, V. K Manivasagam, V. Gopal, C. Bartomeu Garcia, P. Hameed, G. Manivasagam, T.J. Webster, Hydrothermal treatment of etched titanium: A potential surface nano-modification technique for enhanced biocompatibility, *Nanomedicine* 20 (2019) 102016. <https://doi.org/10.1016/J.NANO.2019.102016>.
- [127] V.K. Manivasagam, G. Perumal, H.S. Arora, K.C. Papat, Enhanced antibacterial properties on superhydrophobic micro-nano structured titanium surface, *J Biomed Mater Res A* 110 (2022) 1314–1328. <https://doi.org/10.1002/JBM.A.37375>.
- [128] A. Kurup, P. Dhatrak, N. Khasnis, Surface modification techniques of titanium and titanium alloys for biomedical dental applications: A review, *Mater Today Proc* 39 (2021) 84–90. <https://doi.org/10.1016/J.MATPR.2020.06.163>.
- [129] P. Pesode, S. Barve, Surface modification of titanium and titanium alloy by plasma electrolytic oxidation process for biomedical applications: A review, *Mater Today Proc* 46 (2021) 594–602. <https://doi.org/10.1016/J.MATPR.2020.11.294>.
- [130] W.L. Johnson, *Bulk Glass-Forming Metallic Alloys : Science and Technology*, 1 (2021).
- [131] J. Schroers, G. Kumar, T.M. Hodges, S. Chan, T.R. Kyriakides, Bulk metallic glasses for biomedical applications, *JOM* 2009 61:9 61 (2009) 21–29. <https://doi.org/10.1007/S11837-009-0128-1>.

- [132] A. Phys, J.S. Saini, metallic glasses with superior glass-forming ability and processability Rare-earth and precious-metal free Cu-based metallic glasses with superior glass-forming ability and processability, 011901 (2020). <https://doi.org/10.1063/1.5131645>.
- [133] M. Miller, P. Liaw, Bulk metallic glasses: An overview, 2008. <https://doi.org/10.1007/978-0-387-48921-6>.
- [134] M. Chen, A brief overview of bulk metallic glasses, NPG Asia Materials 2011 3:9 3 (2011) 82–90. <https://doi.org/10.1038/asiamat.2011.30>.
- [135] P. Meagher, E.D.O. Cearbhail, J.H. Byrne, D.J. Browne, Bulk Metallic Glasses for Implantable Medical Devices and Surgical Tools, (2016) 5755–5762. <https://doi.org/10.1002/adma.201505347>.
- [136] H. Yan, Y. Liu, S. Pang, Glass formation and properties of Ti-based bulk metallic glasses as potential biomaterials with Nb additions, Rare Metals 37 (2018) 831–837. <https://doi.org/10.1007/s12598-015-0664-5>.
- [137] M. Calin, A. Gebert, A. Cosmina, P. Flaviu, S. Abdi, C. Mickel, J. Eckert, Designing biocompatible Ti-based metallic glasses for implant applications, Materials Science & Engineering C 33 (2013) 875–883. <https://doi.org/10.1016/j.msec.2012.11.015>.
- [138] M.M. Khan, A. Nemati, Z.U. Rahman, U.H. Shah, H. Asgar, W. Haider, Recent Advancements in Bulk Metallic Glasses and Their Applications: A Review, Critical Reviews in Solid State and Materials Sciences 43 (2018) 233–268. <https://doi.org/10.1080/10408436.2017.1358149>.
- [139] C.A. Grillo, M.A. Reigosa, M.F. Lorenzo de Mele, Effects of copper ions released from metallic copper on CHO-K1 cells, Mutation Research/Genetic Toxicology and Environmental Mutagenesis 672 (2009) 45–50. <https://doi.org/10.1016/J.MRGENTOX.2008.09.012>.
- [140] P. Wang, Y. Yuan, K. Xu, H. Zhong, Y. Yang, S. Jin, K. Yang, X. Qi, Biological applications of copper-containing materials, Bioact Mater 6 (2021) 916–927. <https://doi.org/10.1016/J.BIOACTMAT.2020.09.017>.
- [141] S. Moniri Javadhesari, S. Alipour, M.R. Akbarpour, Biocompatibility, osseointegration, antibacterial and mechanical properties of nanocrystalline Ti-Cu alloy as a new orthopedic material, Colloids Surf B Biointerfaces 189 (2020) 110889. <https://doi.org/10.1016/j.colsurfb.2020.110889>.
- [142] P.F. Gostin, O. Addison, A.P. Morrell, Y. Zhang, A.J.M.C. Cook, A. Liens, M. Stoica, K. Ignatyev, S.R. Street, J. Wu, Y.L. Chiu, A.J. Davenport, In Situ Synchrotron X-Ray Diffraction Characterization of Corrosion Products of a Ti-Based Metallic Glass for Implant Applications, Adv Healthc Mater 7 (2018). <https://doi.org/10.1002/ADHM.201800338>.
- [143] P.F. Gostin, D. Eigel, D. Grell, J. Eckert, E. Kerscher, A. Gebert, Comparing the pitting corrosion behavior of prominent Zr-based bulk metallic glasses, J Mater Res 30 (2015) 233–241. <https://doi.org/10.1557/JMR.2014.371>.

- [144] J. Fornell, E. Pellicer, N. Van Steenberge, S. González, A. Gebert, S. Suriñach, M.D. Baró, J. Sort, Improved plasticity and corrosion behavior in Ti–Zr–Cu–Pd metallic glass with minor additions of Nb: An alloy composition intended for biomedical applications, *Materials Science and Engineering: A* 559 (2013) 159–164. <https://doi.org/10.1016/J.MSEA.2012.08.058>.
- [145] F.X. Qin, G.Q. Xie, X.M. Wang, T. Wada, M. Song, K. Furuya, M. Yoshimura, M. Tsukamoto, A. Inoue, Microstructure and electrochemical properties of PVD TiN, (Ti, Al) N-coated Ti-based bulk metallic glasses, *Mater Trans* 50 (2009) 1313–1317. <https://doi.org/10.2320/MATERTRANS.ME200820>.
- [146] T. Shirai, H. Tsuchiya, T. Shimizu, K. Ohtani, Y. Zen, K. Tomita, Prevention of pin tract infection with titanium-copper alloys, *J Biomed Mater Res B Appl Biomater* 91B (2009) 373–380. <https://doi.org/10.1002/JBM.B.31412>.
- [147] T. Zhang, H. Men, S.J. Pang, J.Y. Fu, C.L. Ma, A. Inoue, Effects of a minor addition of Si and/or Sn on formation and mechanical properties of Cu-Zr-Ti bulk metallic glass, *Materials Science and Engineering A* 449–451 (2007) 295–298. <https://doi.org/10.1016/j.msea.2005.12.102>.
- [148] C. Wang, N. Hua, Z. Liao, W.E.I. Yang, S. Pang, P.K. Liaw, T.A.O. Zhang, Ti-Cu-Zr-Fe-Sn-Si-Ag-Pd Bulk Metallic Glasses with Potential for Biomedical Applications, *Metallurgical and Materials Transactions A* 52 (2021) 1559–1567. <https://doi.org/10.1007/s11661-021-06183-y>.
- [149] Y. Liu, H. Wang, S. Pang, Ti – Zr – Cu – Fe – Sn – Si – Ag – Ta bulk metallic glasses with good corrosion resistance as potential biomaterials, *Rare Metals* 39 (2020) 688–694. <https://doi.org/10.1007/s12598-018-1124-9>.
- [150] Y. Liu, S. Pang, H. Li, Q. Hu, B. Chen, T. Zhang, Intermetallics Formation and properties of Ti-based Ti e Zr e Cu e Fe e Sn e Si bulk metallic glasses with different (Ti p Zr)/ Cu ratios for biomedical application, *Intermetallics (Barking)* 72 (2016) 36–43. <https://doi.org/10.1016/j.intermet.2016.01.007>.
- [151] P. Gong, L. Deng, J. Jin, S. Wang, X. Wang, K. Yao, Review on the research and development of Ti-based bulk metallic glasses, *Metals (Basel)* 6 (2016). <https://doi.org/10.3390/met6110264>.
- [152] S. Pang, Y. Liu, H. Li, L. Sun, Y. Li, T. Zhang, New Ti-based Ti-Cu-Zr-Fe-Sn-Si-Ag bulk metallic glass for biomedical applications, *J Alloys Compd* 625 (2015) 323–327. <https://doi.org/10.1016/j.jallcom.2014.07.021>.
- [153] Y.S. Kim, S.H. Hong, H.J. Park, J.T. Kim, H.J. Jeong, Y.S. Na, K.R. Lim, J.M. Park, K.B. Kim, Crystallization and phase transformation behavior of TiCu-based bulk metallic glass composite with B₂ particles, *J Alloys Compd* 707 (2017) 87–91. <https://doi.org/10.1016/j.jallcom.2016.12.110>.
- [154] A. Concustell, Á. Révész, S. Surinach, L.K. Varga, G. Heunen, M.D. Baró, Microstructural evolution during decomposition and crystallization of the Cu₆₀Zr₂₀Ti₂₀ amorphous alloy, *J Mater Res* 19 (2004) 505–512. <https://doi.org/10.1557/jmr.2004.0062>.
- [155] S. Hamar-Thibault, C.H. Allibert, New phases in the ternary Cu-Ti-Sn system, *J Alloys Compd* 317 (2001) 363–366. [https://doi.org/10.1016/S0925-8388\(00\)01439-0](https://doi.org/10.1016/S0925-8388(00)01439-0).

- [156] J.C. Schuster, M. Naka, T. Shibayanagi, Crystal structure of CuSn₃Ti₅ and related phases, *J Alloys Compd* 305 (2000) L1. [https://doi.org/10.1016/S0925-8388\(00\)00737-4](https://doi.org/10.1016/S0925-8388(00)00737-4).
- [157] A. Hynowska, A. Blanquer, E. Pellicer, J. Fornell, S. Suriñach, M.D. Baró, A. Gebert, M. Calin, J. Eckert, C. Nogués, E. Ibáñez, L. Barrios, J. Sort, Nanostructured Ti-Zr-Pd-Si-(Nb) bulk metallic composites: Novel biocompatible materials with superior mechanical strength and elastic recovery, *J Biomed Mater Res B Appl Biomater* 103 (2015) 1569–1579. <https://doi.org/10.1002/jbm.b.33346>.
- [158] A. Liens, B. Ter-ovanessian, N. Courtois, D. Fabregue, T. Wada, H. Kato, J. Chevalier, Effect of alloying elements on the microstructure and corrosion behavior of TiZr-based bulk metallic glasses, *Corros Sci* 177 (2020) 108854. <https://doi.org/10.1016/j.corsci.2020.108854>.
- [159] H. Men, T. Zhang, Glass Formation and Thermal Stability of Bulk Glassy Cu – Zr – Ti – Sn – Si Alloys Intensity (a . u .) Heat flow (a . u .) Temperature , T / K Temperature , T / K, 46 (2005) 1692–1694.
- [160] R. Rosenkranz, G. Frommeyer, W. Smarsly, Microstructures and properties of high melting point intermetallic Ti₅Si₃ and Ti₅i₂ compounds, ELSEVIER SEQUOIA S.A., 1992. <https://doi.org/10.1016/B978-1-85166-822-9.50048-0>.
- [161] S. Abdi, S. Oswald, P.F. Gostin, A. Helth, J. Sort, M.D. Baró, M. Calin, L. Schultz, J. Eckert, A. Gebert, Designing new biocompatible glass-forming Ti_{75-x}Zr₁₀Nb_xSi₁₅ (x = 0, 15) alloys: Corrosion, passivity, and apatite formation, *J Biomed Mater Res B Appl Biomater* 104 (2016) 27–38. <https://doi.org/10.1002/jbm.b.33332>.
- [162] F. Scaglione, A. Gebert, L. Battezzati, Dealloying of an Au-based amorphous alloy, *Intermetallics (Barking)* 18 (2010) 2338–2342. <https://doi.org/10.1016/j.intermet.2010.08.005>.
- [163] H. Gao, Z. Li, S. Zhou, G. Zhang, N. Cui, The improvement of surface quality and thickness stability of Fe₇₈Si₉B₁₃ melt-spun ribbons by melt overheating, *Progress in Natural Science: Materials International* 29 (2019) 556–560. <https://doi.org/10.1016/J.PNSC.2019.08.012>.
- [164] J. Lario, A. Amigó, F. Segovia, V. Amigó, Surface Modification of Ti-35Nb-10Ta-1.5Fe by the Double Acid-Etching Process, *Materials* 11 (2018). <https://doi.org/10.3390/MA11040494>.
- [165] K.R. Williams, K. Gupta, M. Wasilik, Etch rates for micromachining processing - Part II, *Journal of Microelectromechanical Systems* 12 (2003) 761–778. <https://doi.org/10.1109/JMEMS.2003.820936>.
- [166] J. Li, N. Yu, H. Jiang, J. Leng, H. Geng, Effects of annealing temperature on dealloying of Ti – Cu Alloy, *Corros Sci* 91 (2015) 95–100. <https://doi.org/10.1016/j.corsci.2014.11.002>.
- [167] Z. Zhao, J. Xu, P.K. Liaw, B. Wu, Y. Wang, One-step formation and photocatalytic performance of spindle-like TiO₂ nanorods synthesized by dealloying amorphous Cu₅₀Ti₅₀ alloy, *Corros Sci* 84 (2014) 66–73. <https://doi.org/10.1016/j.corsci.2014.03.014>.

- [168] N. Wang, Y. Pan, S. Wu, E. Zhang, W. Dai, Rapid synthesis of rutile TiO₂ nano-flowers by dealloying Cu₆₀Ti₃₀Y₁₀ metallic glasses, *Appl Surf Sci* 428 (2018) 328–337. <https://doi.org/10.1016/j.apsusc.2017.09.041>.
- [169] W. Wang, Z. Qiao, Y. Zhao, G. Xie, S. Yan, Z. Pang, Y. Chen, H. Yang, M. Zhang, Y. Zhang, W. Li, Y. Jiang, Z. Yu, Z. Zhang, SO₂-ion induced synthesis of 3D porous hydrangea-shaped anatase TiO₂ as high performance anode material for lithium/sodium-ion batteries, *Journal of Porous Materials* 1 (2023) 1–9. <https://doi.org/10.1007/S10934-022-01416-W/FIGURES/7>.
- [170] S. Zhu, G. Xie, X. Yang, Z. Cui, A thick hierarchical rutile TiO₂ nanomaterial with multilayered structure, *Mater Res Bull* 48 (2013) 1961–1966. <https://doi.org/10.1016/j.materresbull.2013.01.049>.
- [171] S.L. Zhu, J.L. He, X.J. Yang, Z.D. Cui, L.L. Pi, Ti oxide nano-porous surface structure prepared by dealloying of Ti-Cu amorphous alloy, *Electrochem Commun* 13 (2011) 250–253. <https://doi.org/10.1016/j.elecom.2010.12.025>.
- [172] E.M. Paschalidou, F. Scaglione, A. Gebert, S. Oswald, P. Rizzi, L. Battezzati, Partially and fully de-alloyed glassy ribbons based on Au: Application in methanol electro-oxidation studies, *J Alloys Compd* 667 (2016) 302–309. <https://doi.org/10.1016/j.jallcom.2016.01.181>.
- [173] N. Fernández-Navas, C.J. Querebillo, K. Tiwari, M. Hantusch, V. Shtefan, N. Pérez, P. Rizzi, M. Zimmermann, A. Gebert, Electrochemical Surface Nanostructuring of Ti₄₇Cu₃₈Fe_{2.5}Zr_{7.5}Sn₂Si₁Ag₂ Metallic Glass for Improved Corrosion Resistance, (n.d.). <https://doi.org/10.2139/SSRN.4603396>.
- [174] S. Hasani, P. Rezaei-Shahreza, A. Seifoddini, M. Hakimi, Enhanced glass forming ability, mechanical, and magnetic properties of Fe₄₁Co₇Cr₁₅Mo₁₄Y₂C₁₅B₆ bulk metallic glass with minor addition of Cu, *J Non Cryst Solids* 497 (2018) 40–47. <https://doi.org/10.1016/J.JNONCRY SOL.2018.05.021>.
- [175] M. Shi, R. Li, J. Wang, Z. Liu, X. Luo, T. Zhang, Effects of minor Cu addition on glass-forming ability and magnetic properties of FePCBCu alloys with high saturation magnetization, *Philosophical Magazine* 93 (2013) 2182–2189. <https://doi.org/10.1080/14786435.2013.765986>.
- [176] C.H. Lin, C.H. Chen, Y.S. Huang, C.H. Huang, J.C. Huang, J.S.C. Jang, Y.S. Lin, In-vivo investigations and cytotoxicity tests on Ti/Zr-based metallic glasses with various Cu contents, *Materials Science and Engineering: C* 77 (2017) 308–317. <https://doi.org/10.1016/J.MSEC.2017.03.228>.
- [177] E. Brooks, M. Tobias, K. Krautsak, M. Ehrensberger, The influence of cathodic polarization and simulated inflammation on titanium electrochemistry, *J Biomed Mater Res B Appl Biomater* 102 (2014) 1445–1453. <https://doi.org/10.1002/JBM.B.33123>.
- [178] M. Prestat, D. Thierry, Corrosion of titanium under simulated inflammation conditions: clinical context and in vitro investigations, *Acta Biomater* 136 (2021) 72–87. <https://doi.org/10.1016/J.ACTBIO.2021.10.002>.

- [179] S.T. Rajan, A. Arockiarajan, Thin film metallic glasses for bioimplants and surgical tools: A review, *J Alloys Compd* 876 (2021) 159939. <https://doi.org/10.1016/J.JALLCOM.2021.159939>.
- [180] J. Ye, B. Li, M. Li, Y. Zheng, S. Wu, Y. Han, ROS induced bactericidal activity of amorphous Zn-doped titanium oxide coatings and enhanced osseointegration in bacteria-infected rat tibias, *Acta Biomater* 107 (2020) 313–324. <https://doi.org/10.1016/J.ACTBIO.2020.02.036>.
- [181] Y.B. Wang, H.F. Li, Y. Cheng, Y.F. Zheng, L.Q. Ruan, In vitro and in vivo studies on Ti-based bulk metallic glass as potential dental implant material, *Materials Science and Engineering: C* 33 (2013) 3489–3497. <https://doi.org/10.1016/J.MSEC.2013.04.038>.
- [182] G. Cerqueni, A. Scalzone, C. Licini, P. Gentile, M. Mattioli-Belmonte, Insights into oxidative stress in bone tissue and novel challenges for biomaterials, *Materials Science and Engineering: C* 130 (2021) 112433. <https://doi.org/10.1016/J.MSEC.2021.112433>.
- [183] C. Catanio Bortolan, F. Copes, M. Shekargoftar, V. de Oliveira Fidelis Sales, C. Paternoster, L. Contri Campanelli, N. Giguère, D. Mantovani, Electrochemical and in vitro biological behaviors of a Ti-Mo-Fe alloy specifically designed for stent applications, *Biomaterials and Biosystems* 10 (2023) 100076. <https://doi.org/10.1016/J.BBIOSY.2023.100076>.
- [184] S. Thanka Rajan, A. Bendavid, B. Subramanian, Cytocompatibility assessment of Ti-Nb-Zr-Si thin film metallic glasses with enhanced osteoblast differentiation for biomedical applications, *Colloids Surf B Biointerfaces* 173 (2019) 109–120. <https://doi.org/10.1016/J.COLSURFB.2018.09.041>.
- [185] Y. Harada, Y. Ikuhara, The Latest Analytical Electron Microscope and its Application to Ceramics, *Handbook of Advanced Ceramics: Materials, Applications, Processing, and Properties: Second Edition* (2013) 3–21. <https://doi.org/10.1016/B978-0-12-385469-8.00001-0>.
- [186] O. Çakir, H. Temel, M. Kiyak, Chemical etching of Cu-ETP copper, *J Mater Process Technol* 162–163 (2005) 275–279. <https://doi.org/10.1016/j.jmatprotec.2005.02.035>.
- [187] M. Chembath, J.N. Balaraju, M. Sujata, Surface characteristics, corrosion and bioactivity of chemically treated biomedical grade NiTi alloy, *Mater Sci Eng C Mater Biol Appl* 56 (2015) 417–425. <https://doi.org/10.1016/J.MSEC.2015.06.051>.
- [188] O. Cakir, Photochemical Machining of Copper and its Alloys Photochemical Machining of Copper and its Alloys Orhan ÇAKIR Yildiz Technical University , Department of Mechanical Engineering , 3rd International Conference on Advanced Manufacturing Technology (ICAMT 20, (2016) 1–7.
- [189] J. Tian, K. Xu, J. Hu, S. Zhang, G. Cao, G. Shao, Durable self-polishing antifouling Cu-Ti coating by a micron-scale Cu/Ti laminated microstructure design, *J Mater Sci Technol* 79 (2021) 62–74. <https://doi.org/10.1016/j.jmst.2020.11.038>.
- [190] M. Hattori, Y. Oda, EQCM analysis of titanium corrosion in peroxide- or fluoride-containing solutions, *Bull Tokyo Dent Coll* 54 (2013) 135–140. <https://doi.org/10.2209/TDCPUBLICATION.54.135>.

- [191] X. Yue, R. Hu, J. Qi, Y. Sui, Y. He, Q. Meng, F. Wei, Y. Ren, Y. Zhao, Three-dimensional nanoporous copper with tunable structure prepared by dealloying titanium–copper–cobalt metallic glasses for supercapacitors, *Micro Nano Lett* 15 (2020) 283–286. <https://doi.org/10.1049/MNL.2019.0627>.
- [192] D. v. Nazarov, E.G. Zemtsova, A. Yu. Solokhin, R.Z. Valiev, V.M. Smirnov, Modification of the surface topography and composition of ultrafine and coarse grained titanium by chemical etching, *Nanomaterials* 7 (2017) 1–15. <https://doi.org/10.3390/nano7010015>.
- [193] D.A. Luke, Etching of Copper With Sulphuric Acid/Hydrogen Peroxide Solutions., *Transactions of the Institute of Metal Finishing* 62 (1984) 81–87. <https://doi.org/10.1080/00202967.1984.11870677>.
- [194] A. Ketabchi, K. Komm, M. Miles-Rossouw, D.A.D. Cassani, F. Variola, Nanoporous Titanium Surfaces for Sustained Elution of Proteins and Antibiotics, *PLoS One* 9 (2014) e92080. <https://doi.org/10.1371/JOURNAL.PONE.0092080>.
- [195] F. Scaglione, P. Rizzi, F. Celegato, L. Battezzati, Synthesis of nanoporous gold by free corrosion of an amorphous precursor, *J Alloys Compd* 615 (2014) S142–S147. <https://doi.org/10.1016/J.JALLCOM.2014.01.239>.
- [196] P. Wang, X. Yi, Y. Lu, H. Yu, J. Yu, In-situ synthesis of amorphous H₂TiO₃-modified TiO₂ and its improved photocatalytic H₂-evolution performance, *J Colloid Interface Sci* 532 (2018) 272–279. <https://doi.org/10.1016/j.jcis.2018.07.139>.
- [197] N. Wang, Y. Pan, W. Dai, S. Wu, Y. an Zhu, E. Zhang, Dealloying synthesis of SnO₂–TiO₂ solid solution and composite nanoparticles with excellent photocatalytic activity, *Appl Surf Sci* 457 (2018) 200–207. <https://doi.org/10.1016/j.apsusc.2018.06.225>.
- [198] S.L. Zhu, J.L. He, X.J. Yang, Z.D. Cui, L.L. Pi, Ti oxide nano-porous surface structure prepared by dealloying of Ti-Cu amorphous alloy, *Electrochem Commun* 13 (2011) 250–253. <https://doi.org/10.1016/j.elecom.2010.12.025>.
- [199] H. Fan, Z. Guo, Bioinspired surfaces with wettability: Biomolecule adhesion behaviors, *Biomater Sci* 8 (2020) 1502–1535. <https://doi.org/10.1039/c9bm01729a>.
- [200] M. Osorio, A. Cañas, J. Puerta, L. Díaz, T. Naranjo, I. Ortiz, C. Castro, Ex Vivo and In Vivo Biocompatibility Assessment (Blood and Tissue) of Three-Dimensional Bacterial Nanocellulose Biomaterials for Soft Tissue Implants, *Scientific Reports* 2019 9:1 9 (2019) 1–14. <https://doi.org/10.1038/s41598-019-46918-x>.
- [201] V.K. Manivasagam, K.C. Popat, Improved Hemocompatibility on Superhemophobic Micro–Nano-Structured Titanium Surfaces, *Bioengineering* 2023, Vol. 10, Page 43 10 (2022) 43. <https://doi.org/10.3390/BIOENGINEERING10010043>.
- [202] C. Pavan, M.J. Sydor, C. Bellomo, R. Leinardi, S. Cananà, R.L. Kendall, E. Rebba, M. Corno, P. Ugliengo, L. Mino, A. Holian, F. Turci, Molecular recognition between membrane epitopes and nearly free surface silanols explains silica membranolytic activity, *Colloids Surf B Biointerfaces* 217 (2022) 112625. <https://doi.org/10.1016/J.COLSURFB.2022.112625>.

- [203] J. Fu, Y. Su, Y. Qin, Y. Zheng, Y. Wang, D. Zhu, Biomaterials Evolution of metallic cardiovascular stent materials : A comparative study among stainless steel , magnesium and zinc, Biomaterials 230 (2020) 119641. <https://doi.org/10.1016/j.biomaterials.2019.119641>.
- [204] V.K. Manivasagam, M. Sankar, · Caterina, B. Garcia, J. Vishnu, · Kaushik Chatterjee, · Satyam Suwas, G. Manivasagam, · Thomas, J. Webster, C.B. Garcia, K. Chatterjee, S. Suwas, T.J. Webster, Surface-modified WE43 magnesium alloys for reduced degradation and superior biocompatibility, In Vitro Models 2022 1:3 1 (2022) 273–288. <https://doi.org/10.1007/S44164-022-00016-X>.
- [205] V.K. Manivasagam, K.C. Papat, In Vitro Investigation of Hemocompatibility of Hydrothermally Treated Titanium and Titanium Alloy Surfaces, ACS Omega 5 (2020) 8108–8120. <https://doi.org/10.1021/acsomega.0c00281>.
- [206] F756 Standard Practice for Assessment of Hemolytic Properties of Materials, (n.d.). <https://www.astm.org/f0756-17.html> (accessed November 28, 2023).
- [207] M.Y. Bai, Y.C. Chang, J.P. Chu, Preclinical studies of non-stick thin film metallic glass-coated syringe needles, Sci Rep 10 (2020) 1–11. <https://doi.org/10.1038/s41598-020-77008-y>.
- [208] R. Wang, Y. Wang, J. Yang, J. Sun, L. Xiong, Influence of heat treatment on the mechanical properties, corrosion behavior, and biocompatibility of Zr56Al16Co28 bulk metallic glass, J Non Cryst Solids 411 (2015) 45–52. <https://doi.org/10.1016/J.JNONCRY SOL.2014.12.018>.
- [209] V.K. Manivasagam, R.M. Sabino, P. Kantam, K.C. Papat, Surface modification strategies to improve titanium hemocompatibility: A comprehensive review, Mater Adv 2 (2021) 5824–5842. <https://doi.org/10.1039/d1ma00367d>.
- [210] D. Zhou, L. Shao, D.R. Spitz, Reactive Oxygen Species in Normal and Tumor Stem Cells, Adv Cancer Res 122 (2014) 1–67. <https://doi.org/10.1016/B978-0-12-420117-0.00001-3>.
- [211] H.L. Yang, L. Zou, A.N. Juaim, C.X. Ma, M.Z. Zhu, F. Xu, X.N. Chen, Y.Z. Wang, X.W. Zhou, Copper release and ROS in antibacterial activity of Ti-Cu alloys against implant-associated infection, Rare Metals 42 (2023) 2007–2019. <https://doi.org/10.1007/s12598-022-02242-4>.
- [212] P.A. Mouthuy, S.J.B. Snelling, S.G. Dakin, L. Milković, A.Č. Gašparović, A.J. Carr, N. Žarković, Biocompatibility of implantable materials: An oxidative stress viewpoint, Biomaterials 109 (2016) 55–68. <https://doi.org/10.1016/j.biomaterials.2016.09.010>.
- [213] E. Scarcello, A. Herpain, M. Tomatis, F. Turci, P.J. Jacques, D. Lison, Hydroxyl radicals and oxidative stress: the dark side of Fe corrosion, Colloids Surf B Biointerfaces 185 (2020) 110542. <https://doi.org/10.1016/j.colsurfb.2019.110542>.
- [214] J. Li, A.N. Pham, R. Dai, Z. Wang, T.D. Waite, Recent advances in Cu-Fenton systems for the treatment of industrial wastewaters: Role of Cu complexes and Cu composites, J Hazard Mater 392 (2020). <https://doi.org/10.1016/J.JHAZMAT.2020.122261>.

- [215] F. Turci, M. Tomatis, I.G. Lesci, N. Roveri, B. Fubini, The iron-related molecular toxicity mechanism of synthetic asbestos nanofibres: a model study for high-aspect-ratio nanoparticles, *Chemistry* 17 (2011) 350–358. <https://doi.org/10.1002/CHEM.201001893>.
- [216] M.P. Pachamuthu, S. Karthikeyan, R. Maheswari, A.F. Lee, A. Ramanathan, Fenton-like degradation of Bisphenol A catalyzed by mesoporous Cu/TUD-1, *Appl Surf Sci* 393 (2017) 67–73. <https://doi.org/10.1016/J.APSUSC.2016.09.162>.
- [217] S.A. Yashnik, O.P. Taran, T.A. Surovtsova, A.B. Ayusheev, V.N. Parmon, Cu- and Fe-substituted ZSM-5 zeolite as an effective catalyst for wet peroxide oxidation of Rhodamine 6 G dye, *J Environ Chem Eng* 10 (2022) 107950. <https://doi.org/10.1016/J.JECE.2022.107950>.
- [218] B. Applications, W. Zhou, A. Gulino, C.J. Querebillo, A Review on Nano Ti-Based Oxides for Dark and Photocatalysis: From Photoinduced Processes to Bioimplant Applications, *Nanomaterials* 2023, Vol. 13, Page 982 13 (2023) 982. <https://doi.org/10.3390/NANO13060982>.
- [219] Z. Liu, T. Wang, X. Yu, Z. Geng, Y. Sang, H. Liu, In situ alternative switching between Ti⁴⁺ and Ti³⁺ driven by H₂O₂ in TiO₂ nanostructures: mechanism of pseudo-Fenton reaction, *Mater Chem Front* 1 (2017) 1989–1994. <https://doi.org/10.1039/C7QM00163K>.
- [220] L.D. Sánchez, S.F.M. Taxt-Lamolle, E.O. Hole, A. Krivokapić, E. Sagstuen, H.J. Haugen, TiO₂ suspension exposed to H₂O₂ in ambient light or darkness: Degradation of methylene blue and EPR evidence for radical oxygen species, *Appl Catal B* 142–143 (2013) 662–667. <https://doi.org/10.1016/J.APCATB.2013.05.017>.
- [221] V.N. Shetti, P. Manikandan, D. Srinivas, P. Ratnasamy, Reactive oxygen species in epoxidation reactions over titanosilicate molecular sieves, *J Catal* 216 (2003) 461–467. [https://doi.org/10.1016/S0021-9517\(02\)00119-7](https://doi.org/10.1016/S0021-9517(02)00119-7).
- [222] P. Tengvall, I. Lundström, L. Sjöqvist, H. Elwing, L.M. Bjursten, Titanium-hydrogen peroxide interaction: model studies of the influence of the inflammatory response on titanium implants, *Biomaterials* 10 (1989) 166–175. [https://doi.org/10.1016/0142-9612\(89\)90019-7](https://doi.org/10.1016/0142-9612(89)90019-7).
- [223] D.H. Kim, A.D. Bokare, M.S. Koo, W. Choi, Heterogeneous catalytic oxidation of As(III) on nonferrous metal oxides in the presence of H₂O₂, *Environ Sci Technol* 49 (2015) 3506–3513. <https://doi.org/10.1021/ES5056897>.
- [224] H.H. Kim, H. Lee, D. Lee, Y.J. Ko, H. Woo, J. Lee, C. Lee, A.L.T. Pham, Activation of Hydrogen Peroxide by a Titanium Oxide-Supported Iron Catalyst: Evidence for Surface Fe(IV) and Its Selectivity, *Environ Sci Technol* 54 (2020) 15424–15432. <https://doi.org/10.1021/ACS.EST.0C04262>.
- [225] P. Mahmoudi, M.R. Akbarpour, H.B. Lakeh, F. Jing, M.R. Hadidi, B. Akhavan, Antibacterial Ti–Cu implants: A critical review on mechanisms of action, *Mater Today Bio* 17 (2022) 100447. <https://doi.org/10.1016/j.mtbio.2022.100447>.

- [226] S.H. Chang, B.Y. Chen, J.X. Lin, Toxicity assessment and selective leaching characteristics of Cu-Al-Ni shape memory alloys in biomaterials applications, *J Appl Biomater Funct Mater* 14 (2016) e59–e64. <https://doi.org/10.5301/jabfm.5000245>.
- [227] B. Cao, Y. Zheng, T. Xi, C. Zhang, W. Song, K. Burugapalli, H. Yang, Y. Ma, Concentration-dependent cytotoxicity of copper ions on mouse fibroblasts in vitro: effects of copper ion release from TCu380A vs TCu220C intra-uterine devices, *Biomed Microdevices* 14 (2012) 709–720. <https://doi.org/10.1007/S10544-012-9651-X>.
- [228] R.P. Singh, S. Kumar, R. Nada, R. Prasad, Evaluation of copper toxicity in isolated human peripheral blood mononuclear cells and its attenuation by zinc: ex vivo, *Mol Cell Biochem* 282 (2006) 13–21. <https://doi.org/10.1007/S11010-006-1168-2>.
- [229] A. Yamamoto, R. Honma, M. Sumita, Cytotoxicity evaluation of 43 metal salts using murine fibroblasts and osteoblastic cells, *J Biomed Mater Res* 39 (1998) 331–340. [https://doi.org/10.1002/\(SICI\)1097-4636\(199802\)39:2](https://doi.org/10.1002/(SICI)1097-4636(199802)39:2).
- [230] A. Blanquer, E. Pellicer, A. Hynowska, L. Barrios, E. Ibáñez, M.D. Baró, J. Sort, C. Nogués, In vitro biocompatibility assessment of Ti₄₀Cu₃₈Zr₁₀Pd₁₂ bulk metallic glass, *J Mater Sci Mater Med* 25 (2014) 163–172. <https://doi.org/10.1007/S10856-013-5041-Z>.
- [231] J. Wei, T. Igarashi, N. Okumori, T. Igarashi, T. Maetani, B. Liu, M. Yoshinari, Influence of surface wettability on competitive protein adsorption and initial attachment of osteoblasts, *Biomedical Materials* 4 (2009) 045002. <https://doi.org/10.1088/1748-6041/4/4/045002>.
- [232] E.M. Czekanska, M.J. Stoddart, J.R. Ralphs, R.G. Richards, J.S. Hayes, A phenotypic comparison of osteoblast cell lines versus human primary osteoblasts for biomaterials testing, *J Biomed Mater Res A* 102 (2014) 2636–2643. <https://doi.org/10.1002/JBM.A.34937>.
- [233] Z. Zhao, T. Kou, L. Zhang, S. Zhai, W. Wang, Y. Wang, Dealloying induced N-doping in spindle-like porous rutile TiO₂ for enhanced visible light photocatalytic activity, *Corros Sci* 137 (2018) 204–211. <https://doi.org/10.1016/j.corsci.2018.03.049>.
- [234] S.L. Zhu, J.L. He, X.J. Yang, Z.D. Cui, L.L. Pi, Ti oxide nano-porous surface structure prepared by dealloying of Ti-Cu amorphous alloy, *Electrochem Commun* 13 (2011) 250–253. <https://doi.org/10.1016/j.elecom.2010.12.025>.
- [235] S.C. Pinho, C. Ribeiro, C.A. Ferraz, M.F. Almeida, Copper, zinc, and nickel recovery from printed circuit boards using an ammonia–ammonium sulphate system, *J Mater Cycles Waste Manag* 23 (2021) 1456–1465. <https://doi.org/10.1007/S10163-021-01226-3/FIGURES/6>.
- [236] J.I. Fisher, J. Halpern, Corrosion of Copper-Gold Alloys by Oxygen-Containing Solutions of Ammonia and Ammonium Salts, *J Electrochem Soc* 103 (1956) 282. <https://doi.org/10.1149/1.2430311>.
- [237] J. Halpern, Kinetics of the Dissolution of Copper in Aqueous Ammonia, *J Electrochem Soc* 100 (1953) 421. <https://doi.org/10.1149/1.2780873>.

- [238] D. V. Nazarov, E.G. Zemtsova, R.Z. Valiev, V.M. Smirnov, Specific features of etching of ultrafine- and coarse-grained titanium in base and acid solutions of hydrogen peroxide, *Russian Journal of Applied Chemistry* 89 (2016) 334–336. <https://doi.org/10.1134/S1070427216020269/METRICS>.
- [239] D. V. Nazarov, E.G. Zemtsova, A. Yu. Solokhin, R.Z. Valiev, V.M. Smirnov, Modification of the Surface Topography and Composition of Ultrafine and Coarse Grained Titanium by Chemical Etching, *Nanomaterials (Basel)* 7 (2017). <https://doi.org/10.3390/NANO7010015>.
- [240] X. Yuan, Y. Kang, J. Zuo, Y. Xie, L. Ma, X. Ren, Z. Bian, Q. Wei, K. Zhou, X. Wang, Z. Yu, Micro/nano hierarchical structured titanium treated by NH₄OH/H₂O₂ for enhancing cell response, *PLoS One* 13 (2018). <https://doi.org/10.1371/JOURNAL.PONE.0196366>.
- [241] M. Biały, M. Hasiak, A. Łaszcz, Review on Biocompatibility and Prospect Biomedical Applications of Novel Functional Metallic Glasses, *Journal of Functional Biomaterials* 2022, Vol. 13, Page 245 13 (2022) 245. <https://doi.org/10.3390/JFB13040245>.
- [242] T. Xue, S. Attarilar, S. Liu, J. Liu, X. Song, L. Li, B. Zhao, Y. Tang, Surface modification techniques of titanium and its alloys to functionally optimize their biomedical properties: Thematic review, *Front Bioeng Biotechnol* 8 (2020) 603072. <https://doi.org/10.3389/FBIOE.2020.603072/BIBTEX>.
- [243] A.M. Holban, C. Farcasiu, O.C. Andrei, A.M. Grumezescu, A.T. Farcasiu, Surface Modification to Modulate Microbial Biofilms—Applications in Dental Medicine, *Materials* 14 (2021). <https://doi.org/10.3390/MA14226994>.
- [244] Y.Z. Wan, S. Raman, F. He, Y. Huang, Surface modification of medical metals by ion implantation of silver and copper, *Vacuum* 81 (2007) 1114–1118. <https://doi.org/10.1016/J.VACUUM.2006.12.011>.
- [245] A. Cochis, B. Azzimonti, C. Della Valle, E. De Giglio, N. Bloise, L. Visai, S. Cometa, L. Rimondini, R. Chiesa, The effect of silver or gallium doped titanium against the multidrug resistant *Acinetobacter baumannii*, *Biomaterials* 80 (2016) 80–95. <https://doi.org/10.1016/j.biomaterials.2015.11.042>.
- [246] L. Rimondini, C. Della Valle, A. Cochis, B. Azzimonti, R. Chiesa, The biofilm formation onto implants and prosthetic materials may be contrasted using Gallium (3+), *Key Eng Mater* 587 (2014) 315–320. <https://doi.org/10.4028/www.scientific.net/KEM.587.315>.
- [247] Y. Kaneko, M. Thoendel, O. Olakanmi, B.E. Britigan, P.K. Singh, The transition metal gallium disrupts *Pseudomonas aeruginosa* iron metabolism and has antimicrobial and antibiofilm activity, *Journal of Clinical Investigation* 117 (2007) 877–888. <https://doi.org/10.1172/JCI30783>.
- [248] C.H. Goss, Y. Kaneko, L. Khuu, G.D. Anderson, S. Ravishankar, M.L. Aitken, N. Lechtzin, G. Zhou, D.M. Czyn, K. McLean, O. Olakanmi, H.A. Shuman, M. Teresi, E. Wilhelm, E. Caldwell, S.J. Salipante, D.B. Hornick, R.J. Siehnel, L. Becker, B.E. Britigan, P.K. Singh, Gallium disrupts

- bacterial iron metabolism and has therapeutic effects in mice and humans with lung infections, *Sci Transl Med* 10 (2018) 1–12. <https://doi.org/10.1126/scitranslmed.aat7520>.
- [249] A. Cochis, B. Azzimonti, R. Chiesa, L. Rimondini, M. Gasik, Metallurgical Gallium Additions to Titanium Alloys Demonstrate a Strong Time-Increasing Antibacterial Activity without any Cellular Toxicity, *ACS Biomater Sci Eng* 5 (2019) 2815–2820. <https://doi.org/10.1021/acsbio.3b00147>.
- [250] E. Xiang, M.N. Gómez-Cerezo, Y. Ali, S.S. Ramachandra, N. Yang, M. Dargusch, C.S. Moran, S. Ivanovski, A. Abdal-Hay, Surface Modification of Pure Zinc by Acid Etching: Accelerating the Corrosion Rate and Enhancing Biocompatibility and Antibacterial Characteristics, *ACS Appl Mater Interfaces* (2022). <https://doi.org/10.1021/acsaami.2c00918>.
- [251] Q. Shen, Y. Qi, Y. Kong, H. Bao, Y. Wang, A. Dong, H. Wu, Y. Xu, Advances in Copper-Based Biomaterials With Antibacterial and Osteogenic Properties for Bone Tissue Engineering, *Front Bioeng Biotechnol* 9 (2022) 1–9. <https://doi.org/10.3389/fbioe.2021.795425>.
- [252] F. Heidenau, W. Mittelmeier, R. Detsch, M. Haenle, F. Stenzel, G. Ziegler, H. Gollwitzer, A novel antibacterial titania coating: Metal ion toxicity and in vitro surface colonization, *J Mater Sci Mater Med* 16 (2005) 883–888. <https://doi.org/10.1007/S10856-005-4422-3/METRICS>.
- [253] P. Pędziwiatr, F. Mikołajczyk, D. Zawadzki, K. Mikołajczyk, A. Bedka, Decomposition of hydrogen peroxide - kinetics and review of chosen catalysts, *Acta Innovations* (2018) 45–52. <https://doi.org/10.32933/ACTAINNOVATIONS.26.5>.
- [254] N. Fairley, V. Fernandez, M. Richard-Plouet, C. Guillot-Deudon, J. Walton, E. Smith, D. Flahaut, M. Greiner, M. Biesinger, S. Tougaard, D. Morgan, J. Baltrusaitis, Systematic and collaborative approach to problem solving using X-ray photoelectron spectroscopy, *Applied Surface Science Advances* 5 (2021) 100112. <https://doi.org/10.1016/J.APSADV.2021.100112>.
- [255] F.M. Fowkes, THE INTERFACE SYMPOSIUMS Attractive Forces at Interfaces Calculation of a new prop-erty unifies several previously unrelated fields of surface chemistry and permits rapid determination of several de-sign variables. Most note-worthy of these are the heats and free energies of adsorption, 10 (2023) 21. <https://pubs.acs.org/sharingguidelines> (accessed October 12, 2023).
- [256] D.K. Owens, R.C. Wendt, Estimation of the surface free energy of polymers, *J Appl Polym Sci* 13 (1969) 1741–1747. <https://doi.org/10.1002/APP.1969.070130815>.
- [257] M. Li, T. Yin, Y. Wang, F. Du, X. Zou, H. Gregersen, G. Wang, Study of biocompatibility of medical grade high nitrogen nickel-free austenitic stainless steel in vitro, *Materials Science and Engineering: C* 43 (2014) 641–648. <https://doi.org/10.1016/J.MSEC.2014.06.038>.
- [258] Y. Haishima, C. Hasegawa, Y. Nomura, T. Kawakami, T. Yuba, T. Shindo, K. Sakaguchi, T. Tanigawa, K. Inukai, M. Takenouchi, K. Isama, A. Matsuoka, S. Niimi, Development and performance evaluation of a positive reference material for hemolysis testing, *J Biomed Mater Res B Appl Biomater* 102 (2014) 1809–1816. <https://doi.org/10.1002/JBM.B.33169>.

- [259] J. Fu, Y. Su, Y.X. Qin, Y. Zheng, Y. Wang, D. Zhu, Evolution of metallic cardiovascular stent materials: A comparative study among stainless steel, magnesium and zinc, *Biomaterials* 230 (2020) 119641. <https://doi.org/10.1016/J.BIOMATERIALS.2019.119641>.
- [260] C. Pavan, G. Escolano-Casado, C. Bellomo, S. Cananà, M. Tomatis, R. Leinardi, L. Mino, F. Turci, Nearly free silanols drive the interaction of crystalline silica polymorphs with membranes: Implications for mineral toxicity, *Front Chem* 10 (2023) 1092221. <https://doi.org/10.3389/FCHEM.2022.1092221/BIBTEX>.
- [261] M.C. Biesinger, L.W.M. Lau, A.R. Gerson, R.S.C. Smart, Resolving surface chemical states in XPS analysis of first row transition metals, oxides and hydroxides: Sc, Ti, V, Cu and Zn, *Appl Surf Sci* 257 (2010) 887–898. <https://doi.org/10.1016/j.apsusc.2010.07.086>.
- [262] J.C. Dupin, D. Gonbeau, P. Vinatier, A. Levasseur, Systematic XPS studies of metal oxides, hydroxides and peroxides, *Physical Chemistry Chemical Physics* 2 (2000) 1319–1324. <https://doi.org/10.1039/a908800h>.
- [263] S. Oswald, P.F. Gostin, A. Helth, S. Abdi, L. Giebeler, H. Wendrock, M. Calin, J. Eckert, A. Gebert, XPS and AES sputter-depth profiling at surfaces of biocompatible passivated Ti-based alloys: Concentration quantification considering chemical effects, *Surface and Interface Analysis* 46 (2014) 683–688. <https://doi.org/10.1002/sia.5437>.
- [264] M.C. Biesinger, Advanced analysis of copper X-ray photoelectron spectra, *Surface and Interface Analysis* 49 (2017) 1325–1334. <https://doi.org/10.1002/sia.6239>.
- [265] J. Pan, D. Thierry, C. Leygraf, Hydrogen peroxide toward enhanced oxide growth on titanium in PBS solution: Blue coloration and clinical relevance, (n.d.). [https://doi.org/10.1002/\(SICI\)1097-4636\(199603\)30:3](https://doi.org/10.1002/(SICI)1097-4636(199603)30:3).
- [266] J. Pan, D. Thierry, C. Leygraf, Electrochemical impedance spectroscopy study of the passive oxide film on titanium for implant application, *Electrochim Acta* 41 (1996) 1143–1153. [https://doi.org/10.1016/0013-4686\(95\)00465-3](https://doi.org/10.1016/0013-4686(95)00465-3).
- [267] D. Guspita, A. Ulianas, Optimization of complex NH₃ with Cu²⁺ ions to determine levels of ammonia by UV-Vis spectrophotometer, *J Phys Conf Ser* 1481 (2020) 012040. <https://doi.org/10.1088/1742-6596/1481/1/012040>.
- [268] W.C. Vosburgh, G.R. Cooper, Complex Ions. I. The Identification of Complex Ions in Solution by Spectrophotometric Measurements, *J Am Chem Soc* 63 (1941) 437–442. https://doi.org/10.1021/JA01847A025/ASSET/JA01847A025.FP.PNG_V03.
- [269] D.F. Evans, M.W. Upton, Studies on singlet oxygen in aqueous solution. Part 4. The 'spontaneous' and catalysed decomposition of hydrogen peroxide, *Journal of the Chemical Society, Dalton Transactions* (1985) 2525–2529. <https://doi.org/10.1039/DT9850002525>.
- [270] Z.M. Galbács, L.J. Csányi, Alkali-induced decomposition of hydrogen peroxide, *Journal of the Chemical Society, Dalton Transactions* (1983) 2353–2357. <https://doi.org/10.1039/DT9830002353>.

- [271] O. Špalek, J. Balej, I. Paseka, Kinetics of the decomposition of hydrogen peroxide in alkaline solutions, *Journal of the Chemical Society, Faraday Transactions 1: Physical Chemistry in Condensed Phases* 78 (1982) 2349–2359. <https://doi.org/10.1039/F19827802349>.
- [272] X. Ge, A. Sumboja, D. Wu, T. An, B. Li, F.W.T. Goh, T.S.A. Hor, Y. Zong, Z. Liu, Oxygen Reduction in Alkaline Media: From Mechanisms to Recent Advances of Catalysts, *ACS Catal* 5 (2015) 4643–4667. https://doi.org/10.1021/ACSCATAL.5B00524/ASSET/IMAGES/LARGE/CS-2015-005246_0016.JPEG.
- [273] J.I. Fisher, J. Halpern, Corrosion of Copper-Gold Alloys by Oxygen-Containing Solutions of Ammonia and Ammonium Salts, *J Electrochem Soc* 103 (1956) 282. <https://doi.org/10.1149/1.2430311/XML>.
- [274] Q. Luo, R.A. Mackay, S. V. Babu, Copper Dissolution in Aqueous Ammonia-Containing Media during Chemical Mechanical Polishing, *Chemistry of Materials* 9 (1997) 2101–2106. <https://doi.org/10.1021/CM970168S>.
- [275] S. Nakayama, T. Notoya, T. Osakai, A Mechanism for the Atmospheric Corrosion of Copper Determined by Voltammetry with a Strongly Alkaline Electrolyte, *J Electrochem Soc* 157 (2010) C289. <https://doi.org/10.1149/1.3465636/XML>.
- [276] R.W. Lane, H.J. McDonald, Kinetics of the Reaction between Copper and Aqueous Ammonia, *J Am Chem Soc* 68 (1946) 1699–1704. https://doi.org/10.1021/JA01213A005/ASSET/JA01213A005.FP.PNG_V03.
- [277] A. Aracena, J. Pino, O. Jerez, Mechanism and Kinetics of Malachite Dissolution in an NH₄OH System, *Metals* 2020, Vol. 10, Page 833 10 (2020) 833. <https://doi.org/10.3390/MET10060833>.
- [278] Q. Zheng, R. Wang, T. Wu, B. Liu, S. Wang, Effect of Ammonium Citrates as an Auxiliary Complexing Agent in TSV Copper Film CMP, *ECS Journal of Solid State Science and Technology* 11 (2022) 054008. <https://doi.org/10.1149/2162-8777/AC6D71>.
- [279] A. Aracena, A. Valencia, O. Jerez, Ammoniacal System Mechanisms for Leaching Copper from Converter Slag, *Metals* 2020, Vol. 10, Page 712 10 (2020) 712. <https://doi.org/10.3390/MET10060712>.
- [280] R.W. Lane, H.J. McDonald, Kinetics of the Reaction between Copper and Aqueous Ammonia, *J Am Chem Soc* 68 (1946) 1699–1704. <https://doi.org/10.1021/ja01213a005>.
- [281] A. ARACENA, F. PÉREZ, D. CARVAJAL, Leaching of cuprite through NH₄OH in basic systems, *Transactions of Nonferrous Metals Society of China (English Edition)* 28 (2018) 2545–2552. [https://doi.org/10.1016/S1003-6326\(18\)64901-5](https://doi.org/10.1016/S1003-6326(18)64901-5).
- [282] T. Sun, M. Wang, A comparative study on titania layers formed on Ti, Ti-6Al-4V and NiTi shape memory alloy through a low temperature oxidation process, *Surf Coat Technol* 205 (2010) 92–101. <https://doi.org/10.1016/J.SURFCOAT.2010.06.019>.

- [283] C. Mahr, P. Kundu, A. Lackmann, D. Zanaga, K. Thiel, M. Schowalter, M. Schwan, S. Bals, A. Wittstock, A. Rosenauer, Quantitative determination of residual silver distribution in nanoporous gold and its influence on structure and catalytic performance, *J Catal* 352 (2017) 52–58. <https://doi.org/10.1016/j.jcat.2017.05.002>.
- [284] A. Wittstock, V. Zielasek, J. Biener, C.M. Friend, M. Bäumer, Nanoporous gold catalysts for selective gas-phase oxidative coupling of methanol at low temperature, *Science* 327 (2010) 319–322. <https://doi.org/10.1126/SCIENCE.1183591>.
- [285] M. Karthega, N. Rajendran, Hydrogen peroxide treatment on Ti–6Al–4V alloy: A promising surface modification technique for orthopaedic application, *Appl Surf Sci* 256 (2010) 2176–2183. <https://doi.org/10.1016/J.APSUSC.2009.09.069>.
- [286] I. Lauria, T.N. Kutz, F. Böke, S. Rütten, D. Zander, H. Fischer, Influence of nanoporous titanium niobium alloy surfaces produced via hydrogen peroxide oxidative etching on the osteogenic differentiation of human mesenchymal stromal cells, *Materials Science and Engineering: C* 98 (2019) 635–648. <https://doi.org/10.1016/J.MSEC.2019.01.023>.
- [287] O. Janson, S. Gururaj, S. Pujari-Palmer, M. Karlsson Ott, M. Strømme, H. Engqvist, K. Welch, Titanium surface modification to enhance antibacterial and bioactive properties while retaining biocompatibility, *Materials Science and Engineering: C* 96 (2019) 272–279. <https://doi.org/10.1016/J.MSEC.2018.11.021>.
- [288] X. Liu, P.K. Chu, C. Ding, Surface modification of titanium, titanium alloys, and related materials for biomedical applications, *Materials Science and Engineering: R: Reports* 47 (2004) 49–121. <https://doi.org/10.1016/J.MSER.2004.11.001>.
- [289] J. Xu, J. Zhang, Y. Shi, J. Tang, D. Huang, M. Yan, M.S. Dargusch, Surface Modification of Biomedical Ti and Ti Alloys: A Review on Current Advances, *Materials* 15 (2022). <https://doi.org/10.3390/MA15051749>.
- [290] T. Xue, S. Attarilar, S. Liu, J. Liu, X. Song, L. Li, B. Zhao, Y. Tang, Surface modification techniques of titanium and its alloys to functionally optimize their biomedical properties: Thematic review, *Front Bioeng Biotechnol* 8 (2020) 1261. <https://doi.org/10.3389/FBIOE.2020.603072/BIBTEX>.
- [291] V.K. Manivasagam, R.M. Sabino, P. Kantam, K.C. Papat, Surface modification strategies to improve titanium hemocompatibility: a comprehensive review, *Mater Adv* 2 (2021) 5824–5842. <https://doi.org/10.1039/D1MA00367D>.
- [292] L. Ponsonnet, K. Reybier, N. Jaffrezic, V. Comte, C. Lagneau, M. Lissac, C. Martelet, Relationship between surface properties (roughness, wettability) of titanium and titanium alloys and cell behaviour, *Materials Science and Engineering C* 23 (2003) 551–560. [https://doi.org/10.1016/S0928-4931\(03\)00033-X](https://doi.org/10.1016/S0928-4931(03)00033-X).
- [293] R.A. Gittens, L. Scheideler, F. Rupp, S.L. Hyzy, J. Geis-Gerstorfer, Z. Schwartz, B.D. Boyan, A review on the wettability of dental implant surfaces II: Biological and clinical aspects, *Acta Biomater* 10 (2014) 2907–2918. <https://doi.org/10.1016/j.actbio.2014.03.032>.

- [294] V.K. Manivasagam, K.C. Papat, In Vitro Investigation of Hemocompatibility of Hydrothermally Treated Titanium and Titanium Alloy Surfaces, *ACS Omega* 5 (2020) 8108–8120. <https://doi.org/10.1021/acsomega.0c00281>.
- [295] M. Larrañaga-Altuna, A. Zabala, I. Llavori, O. Pearce, D.T. Nguyen, J. Caro, H. Mescheder, J.L. Endrino, G. Goel, W.N. Ayre, R.K. Seenivasagam, D.K. Tripathy, J. Armstrong, S. Goel, Bactericidal surfaces: An emerging 21st-century ultra-precision manufacturing and materials puzzle, *Appl Phys Rev* 8 (2021). <https://doi.org/10.1063/5.0028844>.
- [296] M. Larrañaga-Altuna, A. Zabala, I. Llavori, O. Pearce, D.T. Nguyen, J. Caro, H. Mescheder, J.L. Endrino, G. Goel, W.N. Ayre, R.K. Seenivasagam, D.K. Tripathy, J. Armstrong, S. Goel, Bactericidal surfaces: An emerging 21st-century ultra-precision manufacturing and materials puzzle, *Appl Phys Rev* 8 (2021). <https://doi.org/10.1063/5.0028844>.
- [297] A. Rudawska, E. Jacniacka, Analysis for determining surface free energy uncertainty by the Owen-Wendt method, *Int J Adhes Adhes* 29 (2009) 451–457. <https://doi.org/10.1016/J.IJADHADH.2008.09.008>.
- [298] M. Weber, H. Steinle, S. Golombek, L. Hann, C. Schlensak, H.P. Wendel, M. Avci-Adali, Blood-Contacting Biomaterials: In Vitro Evaluation of the Hemocompatibility, *Front Bioeng Biotechnol* 6 (2018). <https://doi.org/10.3389/fbioe.2018.00099>.
- [299] J. Shi, Y. Hedberg, M. Lundin, I. Odnevall Wallinder, H.L. Karlsson, L. Möller, Hemolytic properties of synthetic nano- and porous silica particles: the effect of surface properties and the protection by the plasma corona, *Acta Biomater* 8 (2012) 3478–3490. <https://doi.org/10.1016/J.ACTBIO.2012.04.024>.
- [300] L. Huang, C. Pu, R.K. Fisher, D.J.H. Mountain, Y. Gao, P.K. Liaw, W. Zhang, W. He, A Zr-based bulk metallic glass for future stent applications: Materials properties, finite element modeling, and in vitro human vascular cell response, *Acta Biomater* 25 (2015) 356–368. <https://doi.org/10.1016/J.ACTBIO.2015.07.012>.
- [301] M. Jafary-Zadeh, G.P. Kumar, P.S. Branicio, M. Seifi, J.J. Lewandowski, F. Cui, A Critical Review on Metallic Glasses as Structural Materials for Cardiovascular Stent Applications, *J Funct Biomater* 9 (2018). <https://doi.org/10.3390/JFB9010019>.
- [302] G. Grass, C. Rensing, M. Solioz, Metallic copper as an antimicrobial surface, *Appl Environ Microbiol* 77 (2011) 1541–1547. <https://doi.org/10.1128/AEM.02766-10>.
- [303] L. Wang, Y. Fu, Q. Li, Z. Wang, EPR Evidence for Mechanistic Diversity of Cu(II)/Peroxygen Oxidation Systems by Tracing the Origin of DMPO Spin Adducts, *Environ Sci Technol* 56 (2022) 8796–8806. <https://doi.org/10.1021/ACS.EST.2C00459>.
- [304] C. Molteni, H.K. Abicht, M. Solioz, Killing of Bacteria by Copper Surfaces Involves Dissolved Copper, *Appl Environ Microbiol* 76 (2010) 4099. <https://doi.org/10.1128/AEM.00424-10>.
- [305] C.E. Santo, N. Taudte, D.H. Nies, G. Grass, Contribution of Copper Ion Resistance to Survival of *Escherichia coli* on Metallic Copper Surfaces, *Appl Environ Microbiol* 74 (2008) 977. <https://doi.org/10.1128/AEM.01938-07>.

- [306] C.E. Santo, D. Quaranta, G. Grass, Antimicrobial metallic copper surfaces kill *Staphylococcus haemolyticus* via membrane damage, *Microbiologyopen* 1 (2012) 46–52. <https://doi.org/10.1002/MBO3.2>.
- [307] R. Hong, T.Y. Kang, C.A. Michels, N. Gadura, Membrane Lipid Peroxidation in Copper Alloy-Mediated Contact Killing of *Escherichia coli*, *Appl Environ Microbiol* 78 (2012) 1776. <https://doi.org/10.1128/AEM.07068-11>.
- [308] R. Nandakumar, C.E. Santo, N. Madayiputhiya, G. Grass, Quantitative proteomic profiling of the *Escherichia coli* response to metallic copper surfaces, *Biometals* 24 (2011) 429–444. <https://doi.org/10.1007/S10534-011-9434-5>.
- [309] M. Ölander, N. Handin, P. Artursson, Image-Based Quantification of Cell Debris as a Measure of Apoptosis, *Anal Chem* 91 (2019) 5548–5552. https://doi.org/10.1021/ACS.ANALCHEM.9B01243/ASSET/IMAGES/LARGE/AC-2019-01243H_0005.JPEG.
- [310] S. Huh, D.F.E. Ker, H. Su, T. Kanade, Apoptosis detection for adherent cell populations in time-lapse phase-contrast microscopy images, *Med Image Comput Comput Assist Interv* 15 (2012) 331–339. https://doi.org/10.1007/978-3-642-33415-3_41.
- [311] D.J. Taatjes, B.E. Sobel, R.C. Budd, Morphological and cytochemical determination of cell death by apoptosis, *Histochem Cell Biol* 129 (2008) 33–43. <https://doi.org/10.1007/S00418-007-0356-9/FIGURES/4>.
- [312] E.M. Czekanska, M.J. Stoddart, J.R. Ralphs, R.G. Richards, J.S. Hayes, A phenotypic comparison of osteoblast cell lines versus human primary osteoblasts for biomaterials testing, *J Biomed Mater Res A* 102 (2014) 2636–2643. <https://doi.org/10.1002/jbm.a.34937>.
- [313] A. Yamamoto, R. Honma, A. Tanaka, M. Sumita, Generic tendency of metal salt cytotoxicity for six cell lines, (1999). [https://doi.org/10.1002/\(SICI\)1097-4636\(19991205\)47:3](https://doi.org/10.1002/(SICI)1097-4636(19991205)47:3).
- [314] A. Biesiekierski, J. Wang, M. Abdel-Hady Gepreel, C. Wen, A new look at biomedical Ti-based shape memory alloys, *Acta Biomater* 8 (2012) 1661–1669. <https://doi.org/10.1016/J.ACTBIO.2012.01.018>.
- [315] T. Yamazaki, A. Yamazaki, Y. Hibino, S.A. Chowdhury, Y. Yokote, Y. Kanda, S. Kunii, H. Sakagami, H. Nakajima, J. Shimada, Biological Impact of Contact with Metals on Cells, *In Vivo (Brooklyn)* 20 (2006) 605–611. <https://iv.iarjournals.org/content/20/5/605> (accessed December 3, 2023).
- [316] A. Blanquer, E. Pellicer, A. Hynowska, L. Barrios, E. Ibáñez, M.D. Baró, J. Sort, C. Nogués, *In vitro* biocompatibility assessment of Ti₄₀Cu₃₈Zr₁₀Pd₁₂ bulk metallic glass, *J Mater Sci Mater Med* 25 (2014) 163–172. <https://doi.org/10.1007/s10856-013-5041-z>.
- [317] A. Milheiro, K. Nozaki, C.J. Kleverlaan, J. Muris, H. Miura, A.J. Feilzer, *In vitro* cytotoxicity of metallic ions released from dental alloys, *Odontology* 104 (2016) 136–142. <https://doi.org/10.1007/S10266-014-0192-Z>.

- [318] H. Chai, L. Guo, X. Wang, Y. Fu, J. Guan, L. Tan, L. Ren, K. Yang, Antibacterial effect of 317L stainless steel contained copper in prevention of implant-related infection in vitro and in vivo, *J Mater Sci Mater Med* 22 (2011) 2525–2535. <https://doi.org/10.1007/s10856-011-4427-z>.
- [319] W.S. da Cruz Nizer, V. Inkovskiy, Z. Versey, N. Stempel, E. Cassol, J. Overhage, Oxidative Stress Response in *Pseudomonas aeruginosa*, *Pathogens* 10 (2021). <https://doi.org/10.3390/PATHOGENS10091187>.
- [320] Y. Cheng, G. Feng, C.I. Moraru, Micro- and Nanotopography Sensitive Bacterial Attachment Mechanisms: A Review, *Front Microbiol* 10 (2019). <https://doi.org/10.3389/FMICB.2019.00191>.
- [321] C.M. Bhadra, V. Khanh Truong, V.T.H. Pham, M. Al Kobaisi, G. Seniutinas, J.Y. Wang, S. Juodkakis, R.J. Crawford, E.P. Ivanova, Antibacterial titanium nano-patterned arrays inspired by dragonfly wings, *Scientific Reports* 2015 5:1 5 (2015) 1–12. <https://doi.org/10.1038/srep16817>.
- [322] M. Lorenzetti, I. Dogša, T. Stošicki, D. Stopar, M. Kalin, S. Kobe, S. Novak, The influence of surface modification on bacterial adhesion to titanium-based substrates, *ACS Appl Mater Interfaces* 7 (2015) 1644–1651. <https://doi.org/10.1021/AM507148N>.
- [323] A.G. Gristina, Biomaterial-Centered Infection: Microbial Adhesion Versus Tissue Integration, *Science* (1979) 237 (1987) 1588–1595. <https://doi.org/10.1126/SCIENCE.3629258>.
- [324] L. Liu, Z. Liu, K.C. Chan, H.H. Luo, Q.Z. Cai, S.M. Zhang, Surface modification and biocompatibility of Ni-free Zr-based bulk metallic glass, *Scr Mater* 58 (2008) 231–234. <https://doi.org/10.1016/J.SCRIPTAMAT.2007.09.040>.
- [325] Y. Zeng, B. Gaskey, E. Benn, I. McCue, G. Greenidge, K. Livi, X. Zhang, J. Jiang, J. Elebacher, Electrochemical dealloying with simultaneous phase separation, *Acta Mater* 171 (2019) 8–17. <https://doi.org/10.1016/j.actamat.2019.03.039>.
- [326] Z. Zhao, J. Xu, C. Shang, R. Ye, Y. Wang, Dealloying-driven synthesis of sea-urchin like titanate nanowires and hierarchically porous anatase TiO₂ nanospindles with enhanced photocatalytic performance, *Corros Sci* 98 (2015) 651–660. <https://doi.org/10.1016/j.corsci.2015.06.007>.
- [327] S.L. Zhu, J.L. He, X.J. Yang, Z.D. Cui, L.L. Pi, Ti oxide nano-porous surface structure prepared by dealloying of Ti–Cu amorphous alloy, *Electrochem Commun* 13 (2011) 250–253. <https://doi.org/10.1016/J.ELECOM.2010.12.025>.
- [328] M.J.N. Pourbaix, Atlas of electrochemical equilibria in aqueous solutions, *J Electroanal Chem Interfacial Electrochem* (1974) 644. https://books.google.com/books/about/Atlas_of_Electrochemical_Equilibria_in_A.html?id=QjxRAAAAMAAJ (accessed February 21, 2023).
- [329] K.A. Persson, B. Waldwick, P. Lazic, G. Ceder, Prediction of solid-aqueous equilibria: Scheme to combine first-principles calculations of solids with experimental aqueous states, *Phys Rev*

- B Condens Matter Mater Phys 85 (2012) 235438.
<https://doi.org/10.1103/PHYSREVB.85.235438/FIGURES/10/MEDIUM>.
- [330] O.P. Abolusoro, E.T. Akinlabi, Tribocorrosion Measurements and Behaviour in Aluminium Alloys: An Overview, *J Bio Tribocorros* 6 (2020) 1–13. <https://doi.org/10.1007/S40735-020-00393-4/FIGURES/8>.
- [331] M.C. Biesinger, L.W.M. Lau, A.R. Gerson, R.S.C. Smart, Resolving surface chemical states in XPS analysis of first row transition metals, oxides and hydroxides: Sc, Ti, V, Cu and Zn, *Appl Surf Sci* 257 (2010) 887–898. <https://doi.org/10.1016/J.APSUSC.2010.07.086>.
- [332] M.C. Biesinger, Advanced analysis of copper X-ray photoelectron spectra, *Surface and Interface Analysis* 49 (2017) 1325–1334. <https://doi.org/10.1002/SIA.6239>.
- [333] F.U. Renner, M. Oezaslan, *Dealloying on the atomic scale*, Elsevier, 2018.
<https://doi.org/10.1016/B978-0-12-409547-2.14060-0>.
- [334] T. Wada, K. Yubuta, A. Inoue, H. Kato, Dealloying by metallic melt, *Mater Lett* 65 (2011) 1076–1078. <https://doi.org/10.1016/J.MATLET.2011.01.054>.
- [335] A. Chuang, J. Erlebacher, Challenges and Opportunities for Integrating Dealloying Methods into Additive Manufacturing, *Materials* 2020, Vol. 13, Page 3706 13 (2020) 3706.
<https://doi.org/10.3390/MA13173706>.
- [336] C. Zhao, K. Kisslinger, X. Huang, M. Lu, F. Camino, C.H. Lin, H. Yan, E. Nazaretski, Y. Chu, B. Ravel, M. Liu, Y.C.K. Chen-Wiegart, Bi-continuous pattern formation in thin films: Via solid-state interfacial dealloying studied by multimodal characterization, *Mater Horiz* 6 (2019) 1991–2002. <https://doi.org/10.1039/c9mh00669a>.
- [337] F. Zhang, P. Li, J. Yu, L. Wang, F. Saba, G. Dai, S. He, Fabrication, formation mechanism and properties of three-dimensional nanoporous titanium dealloyed in metallic powders, *J Mater Res* 32 (2017) 1528–1540. <https://doi.org/10.1557/jmr.2017.19>.
- [338] I. McCue, S. Xiang, K. Xie, M.J. Demkowicz, The Effect of Microstructure Morphology on Indentation Response of Ta/Ti Nanocomposite Thin Films, *Metall Mater Trans A Phys Metall Mater Sci* 51 (2020) 5677–5690. <https://doi.org/10.1007/s11661-020-05969-w>.
- [339] C. Zhao, K. Kisslinger, X. Huang, J. Bai, X. Liu, C.H. Lin, L.C. Yu, M. Lu, X. Tong, H. Zhong, A. Pattammattel, H. Yan, Y. Chu, S. Ghose, M. Liu, Y.C.K. Chen-Wiegart, Design nanoporous metal thin films: Via solid state interfacial dealloying, *Nanoscale* 13 (2021) 17725–17736.
<https://doi.org/10.1039/d1nr03709a>.
- [340] Y. Tan, Z. Lu, Z. Li, X. Tao, Y. Ouyang, Y. Du, Investigation on diffusion characteristics and mechanical properties of Ti–Zn system, *Intermetallics (Barking)* 154 (2023) 107794.
<https://doi.org/10.1016/j.intermet.2022.107794>.
- [341] C.M. Eastman, Q. Zhang, J.C. Zhao, Diffusion Coefficients and Phase Equilibria of the Cu–Zn Binary System Studied Using Diffusion Couples, *J Phase Equilibria Diffus* 41 (2020) 642–653.
<https://doi.org/10.1007/s11669-020-00831-3>.

- [342] K. Liu, W. Ding, X. Tao, H. Chen, Y. Ouyang, Y. Du, Diffusional behaviors and mechanical properties of Cu–Zn system, *J Alloys Compd* 812 (2020) 152141. <https://doi.org/10.1016/j.jallcom.2019.152141>.
- [343] R. Davalos-Monteiro, Observations of corrosion product formation and stress corrosion cracking on brass samples exposed to ammonia environments, *Materials Research* 22 (2019) 1–10. <https://doi.org/10.1590/1980-5373-MR-2018-0077>.
- [344] Z.A. Mahmud,) Gabriel Gordillo,) Liliana Gassa,) Carlos, V. D´alkaine, Control of zinc plating solutions, determining the optimum concentration of thiourea additive by electrochemical techniques, (n.d.).
- [345] J. Zheng, L.A. Archer, Controlling electrochemical growth of metallic zinc electrodes: Toward affordable rechargeable energy storage systems, *Sci Adv* 7 (2021). <https://doi.org/10.1126/SCIADV.ABE0219>.
- [346] Y. Wang, A.S. Hall, Room-Temperature Synthesis of Intermetallic Cu-Zn by an Electrochemically Induced Phase Transformation, *Chemistry of Materials* 33 (2021) 7309–7314. <https://doi.org/10.1021/acs.chemmater.1c01678>.
- [347] M.Y. Hacıbrahimoğlu, M. Bedir, A. Yavuz, Structural and Corrosion Study of Uncoated and Zn-Cu Coated Magnesium-Based Alloy, *Metals* 2016, Vol. 6, Page 322 6 (2016) 322. <https://doi.org/10.3390/MET6120322>.
- [348] W. Wisniewski, C. Genevois, E. Veron, M. Allix, Experimental evidence concerning the significant information depth of X-ray diffraction (XRD) in the Bragg-Brentano configuration, *Powder Diffr* 38 (2023) 139–144. <https://doi.org/10.1017/S0885715623000052>.
- [349] D. Martín, D. Moro, G. Ulian, G. Valdrè, Monte Carlo SEM-EDS Nano-Microanalysis Strategy of Historical Mineral Pigments: The Simulation of the Egyptian Blue from Pompeii (Italy) as an Example, *Minerals* 2020, Vol. 10, Page 807 10 (2020) 807. <https://doi.org/10.3390/MIN10090807>.